



UNIVERSITÄT HAMBURG
DEUTSCHES ELEKTRONEN-SYNCHROTRON DESY



High-Resolution and In-Solution Hard X-ray Ptychography at the Ptychographic Nano-Analytical Microscope PtyNAMi

Dissertation

zur Erlangung des Doktorgrades
an der Fakultät für Mathematik,
Informatik und Naturwissenschaften
Fachbereich Physik
der Universität Hamburg

vorgelegt von
KARL MARTIN SEYRICH

Hamburg
2020

The work described in this thesis is done at the Photon Science division of Deutsches Elektronen-Synchrotron, a Research Centre of the Helmholtz Association.

Gutachter/in der Dissertation:	Prof. Dr. Christian Schroer Prof. Dr. Dorota Koziej
Zusammensetzung der Prüfungskommission:	Prof. Dr. Christian Schroer Prof. Dr. Dorota Koziej Prof. Dr. Daniela Pfannkuche Prof. Dr. Edgar Weckert Jun.-Prof. Dr. Peter Modregger
Vorsitzende der Prüfungskommission:	Prof. Dr. Daniela Pfannkuche
Datum der Disputation:	26.02.2021
Vorsitzender Fach-Promotionsausschusses PHYSIK:	Prof. Dr. Günter Hans Walter Sigl
Leiter des Fachbereichs PHYSIK:	Prof. Dr. Wolfgang Hansen
Dekan der Fakultät MIN:	Prof. Dr. Heinrich Graener

Zusammenfassung

Röntgenmikroskopie zeichnet sich gegenüber der optischen Mikroskopie durch eine höhere räumliche Auflösung aus und kann, im Gegensatz zur Elektronenmikroskopie, auch auf dickere Proben und Probenumgebungen angewendet werden. Sie eignet sich somit hervorragend zur In-situ-Bildgebung nanoskopischer Probensysteme, wie sie beispielsweise in der Chemie und den Biowissenschaften von hoher Relevanz sind.

Ptychographie ist eine linsenlose, rechnergestützte Mikroskopiemethode, welche die abbildende Wirkung der Objektivlinse eines Mikroskops durch einen Algorithmus zur Phasenrückgewinnung des kohärenten Wellenfeldes ersetzt. Dieses Verfahren erlaubt es, die räumliche Auflösung eines ptychographischen Mikroskops weit über die Grenzen der verwendeten Röntgenoptiken zu steigern.

Wesentliche limitierende Faktoren aktueller ptychographischer Mikroskope im Röntgenbereich sind Nanopositionierfehler und Vibrationen. Diese werden in der vorliegenden Arbeit mittels laserinterferometrischer Methoden an dem Ptychographischen Nano-Analytischen Mikroskop (PtyNAMi, P06, PETRA III) charakterisiert; hierbei werden die auftretenden Messungenauigkeiten genau betrachtet. Weiterhin wird ein schwingungsoptimierter Aufbau für zweidimensionale Messungen vorgestellt, der isotrope Probenschwingungen von 1 nm im QMW erreicht.

Ein weiterer Aspekt der instrumentellen Verbesserungen ist die Unterdrückung des Messuntergrundes auf dem Detektor durch die Verwendung einer fensterlosen Vakuumflugstrecke. Mittels dieser beiden instrumentellen Optimierungen gelang es, mikroskopische Bilder mit 10 nm Höchstauflösung aufzunehmen.

Eine Besonderheit der Ptychographie ist die hohe Überbestimmung des Datensatzes zur Phasenrückgewinnung, welche zahlreiche Erweiterungen des ptychographischen Modells zur Beschreibung experimenteller Modellabweichungen zulässt. So lässt sich unter anderem ein Objekt, dessen Ausdehnung entlang der optischen Achse die Schärfentiefe des Mikroskops überschreitet, virtuell in mehrere Bildebenen aufteilen.

Diese sogenannte Mehrschichtptychographie ist erforderlich zur Abbildung von Nanoteilchen während ihrer Synthese in Lösung in Fällen, in denen sich die Partikel an beiden durchstrahlten Wänden des In-situ-Reaktors bilden. Ein solcher Reaktor, der mit der ptychographischen Bildgebung kompatibel ist, wird konzipiert und erprobt.

In einem Demonstrationsversuch wird die Nukleation und das Wachstum von Kupfer- und Kupferoxidnanoteilchen in geheiztem Benzylalkohol untersucht. Über einen Zeitraum von 20 Stunden konnte die Entwicklung individueller Nanoteilchen mit einer räumlichen Auflösung von 70 nm und einer zeitlichen Auflösung von 22 Minuten in zwei Bildebenen abgebildet werden. Die hierbei auftretenden Bildartefakte sind Teil einer weiterführenden Diskussion zu den Nachteilen der Mehrschichtptychographie.

Abstract

X-ray microscopy is characterized by its high spatial resolution, exceeding that of visible light microscopy, while also being able to penetrate thick samples and sample enclosures that are inaccessible to electron microscopy. With these characteristics, x-ray microscopy excels in in-situ imaging of nanoscopic sample systems that are highly relevant in fields such as chemistry and life sciences.

Ptychography is a lensless, computational microscopy technique in which the objective lens of the microscope is replaced with an algorithm to retrieve the phases of the coherent wave field. With this approach, the spatial resolution achieved in a ptychographic microscope can widely exceed that of the used x-ray focusing optics.

One of the limiting factors of current ptychographic microscopes are nanopositioning errors and vibrations. Using laser-interferometry, these factors are studied in this thesis at the Ptychographic Nano-Analytical Microscope (PtyNAMi, P06, PETRA III) with particular attention to the occurring measurement uncertainties. In addition, an ultra-stable setup for two-dimensional measurements, that exhibits isotropic vibrations in the order of 1 nm rms, is presented.

Further improvement of the instrumentation is achieved by placing the area detector into a windowless and evacuated detector device, thereby suppressing the incoherent scattering background. With both of these instrumentational optimizations, ptychographic imaging with 10 nm resolution is demonstrated.

A distinct advantage of ptychography is the high degree of overdetermination in the data set that permits extensions of the ptychographic model to describe experimental imperfections. For samples that extend along the optical axis beyond the depth-of-field of the microscope, several independent virtual object planes can be modeled, reconstructing all of them from a single measurement.

This *multi-slice* ptychography is required when imaging the synthesis of nanoparticles in solution in cases in which the forming particles adhere to both windows of the in situ cell. Such an in situ cell, that is designed to be compatible with hard x-ray ptychographic imaging, is designed and commissioned.

In a first demonstration, the nucleation and growth of copper and copper oxide nanoparticles in heated benzyl alcohol is imaged. For a period of 20 h, the growth of individual nanoparticles was imaged with a spatial resolution of 70 nm and a temporal resolution of 22 minutes in two image planes. The observed imaging artifacts are part of an overarching discussion about the disadvantages of multi-slice ptychography.

Contents

Zusammenfassung / Abstract	3
Abbreviations	8
1 Introduction	11
1.1 X-ray microscopy	11
1.2 A brilliant future	12
1.3 About this thesis	13
2 Ptychography	15
2.1 The ideal ptychographic model	15
2.1.1 The forward model	16
2.1.2 Phase retrieval	17
2.2 Beyond the ideal model	20
2.2.1 Multi-slice ptychography	21
2.2.2 Virtually enlarged probes	24
2.2.3 Position refinement	26
2.2.4 Intensity refinement	27
2.2.5 Partially coherent illumination	28
2.3 Spatial resolution	29
2.3.1 Transversal resolution	29
2.3.2 Longitudinal resolution	31
2.3.3 Resolution criteria	32
2.4 Summary	34
3 Instrumentation	35
3.1 Beamline P06 at PETRA III	35
3.1.1 PETRA	35
3.1.2 Beamline P06	36
3.2 PtyNAMi in the P06 nanoprobe endstation	39
3.2.1 Mechanical design	39
3.2.2 X-ray optical design	42
3.2.3 Summary	44

4	In situ cell for ptychography in heated solution	47
4.1	Sample System	47
4.2	Design and requirements	48
4.2.1	Requirements	48
4.2.2	Design	49
4.2.3	Effects on the microscope	51
5	Laser-interferometric position measurement	53
5.1	Motivation	53
5.2	Interferometer hardware	55
5.2.1	Interferometer controllers	55
5.2.2	Interferometer heads	55
5.3	Retroreflectors	56
5.3.1	Ball lens retroreflectors	57
5.3.2	Measuring geometry	58
5.3.3	Determining the interferometer angles	59
5.3.4	Comparison to cylinder reflector	60
5.3.5	Abbe error	61
5.3.6	Extension to the third dimension	62
5.4	Vibration measurements	62
5.4.1	Comparison to seismometers	62
5.4.2	Vibration of the interferometer reference	64
5.4.3	Repeatability of vibration measurements	64
5.4.4	Vibration spectra	66
5.4.5	Quantitative analysis	69
5.4.6	Histograms	71
5.5	The influence of air	73
5.5.1	Edlén correction	73
5.5.2	Air fluctuations	74
5.5.3	Helium	74
5.6	Periodic measurement error	75
5.6.1	Phase quadrature	75
5.6.2	Linear test measurement	76
5.6.3	Ptychographic scans	77
5.6.4	Outlook: Interference Spectroscopy	80
5.7	Ptychographic test measurements	80
5.7.1	Microchip test structure	80
5.7.2	Siemens star test pattern	81
5.8	Summary	83

6	The in-vacuum detector device	85
6.1	PtyNAMi detector device	85
6.1.1	Detector requirements	85
6.1.2	Incoherent background scattering	86
6.1.3	Mechanical design	87
6.1.4	Beamstops	88
6.2	Background measurements	88
6.2.1	Evacuated flight path and beamstop	88
6.2.2	Position of the entrance window	91
6.2.3	Influence of the in situ cell	93
6.3	Summary	95
7	High-resolution ptychography	97
7.1	Upsampling and diffractive optics	97
7.2	Transversal resolution of single-slice reconstructions	99
7.2.1	Fourier Ring Correlation	99
7.2.2	Line profiles	103
7.2.3	Discussion	104
7.3	Multi-slice measurements	105
7.3.1	Finding the slice distance	105
7.3.2	Reconstruction with four slices	107
7.3.3	Multi-slicing artifacts	109
7.3.4	Multi-slice FRC	112
7.4	Summary	113
8	In-solution ptychography	115
8.1	Ptychographic time series of a chemical reaction	115
8.1.1	Temporal resolution	115
8.1.2	Sample drifts	116
8.1.3	Experimental observations	117
8.1.4	Beam damage	120
8.2	Low frequency artifacts and intensity refinement	121
8.2.1	Single-slice measurement	123
8.2.2	Multi-slice measurement	125
8.3	Spatial resolution	127
8.3.1	Transversal resolution	127
8.3.2	Depth of field	129
8.4	Summary	131
9	Outlook	133

Appendices	135
A Monochromator vibrations	137
B Coordinate transformation for laser-interferometry	139
B.1 General problem	139
B.2 Two-dimensional case	140
C Homodyne Phase Quadrature	143
D Carbon deposition and beam damage	145
Bibliography	145
Experimental Data	159
List of publications	162
Danksagung	163
Eidesstattliche Versicherung	167

List of Abbreviations

AC	Alternating Current
ADC	Analog-to-digital Converter
ASIC	Application-Specific Integrated Circuit
CAD	Computer-Aided Design
CC	Channel Cut
CCD	Charge Coupled Device
CDI	Coherent Diffractive Imaging
CHyN	Center for Hybrid Nanostructures
CMOS	Complementary Metal Oxide Semiconductor
cSAXS	Coherent Small Angle X-ray Scattering (a beamline at SLS)
CRL	Compound Refractive Lens
DC	Direct Current
DCM	Double Crystal Monochromator
DESY	Deutsches Elektronen-Synchrotron DESY, A Research Centre of the Helmholtz Association
DFB	Distributed Feedback Laser
DOF	Depth of Field Depth of Focus
DPC	Differential Phase Contrast
ePIE	extended Ptychographic Iterative Engine
ESRF-EBS	European Synchrotron Radiation Facility - Extremely Brilliant Source
EXAFS	Extended X-ray Absorption Fine Structure
FEM	Finite Element Method
FFT	Fast Fourier Transformation
FPGA	Field-Programmable Gate Array
FRC	Fourier Ring Correlation
FWHM	Full Width at Half Maximum
FZP	Fresnel Zone Plate
GPU	Graphics Processing Unit
HERA	Hadron-Elektron-Ring-Anlage
KB	Kirkpatrick-Baez

KIT	Karlsruher Institut für Technologie
LASER	Light Amplification by Stimulated Emission of Radiation
LPTEM	Liquid Phase Transmission Electron Microscopy
LUT	Look-Up Table
MLL	Multilayer Laue Lens
μ XRF	Micro X-ray Fluorescence
NFL	Nano-Focusing lens
OSA	Order-Sorting Aperture
PETRA	Positronen-Elektronen-Tandem-Ring-Anlage
PID	Proportional-Integral-Derivative
PRTF	Phase Retrieval Transfer Function
PTFE	Polytetrafluoroethylene (Teflon)
PtyNAMi	Ptychographic Nano-Analytical Microscope
PXCT	Ptychographic X-ray Computed Tomography
QBPM	Quadrant Beam Position Monitor
QMW	Quadratischer Mittelwert
rms	root mean square
SAXS	Small Angle X-ray Scattering
SEM	Scanning Electron Microscopy
SLS	Swiss Light Source
SNR	Signal-to-Noise Ratio
STXM	Scanning Transmission X-ray Microscopy
TEM	Transmission Electron Microscopy
UHV	Ultra High Vacuum
UPS	Uninterruptible Power Supply
WAXS	Wide Angle X-ray Scattering
XANES	X-ray Absorption Near-Edge Structure
XES	X-ray Emission Spectroscopy
XFEL	X-ray Free Electron Laser
XRF	X-ray Fluorescence

Chapter 1

Introduction

1.1 X-ray microscopy

Scientists often find it difficult to explain their work to laymen. Personally, I do not experience this difficulty as I work in the field of *x-ray microscopy*. Everyone knows X-rays, medical practitioners use them to look *through* the human body. And everyone knows microscopes, they are used to look at *small* objects. Therefore, x-ray microscopy combines both traits and looks *through* the *small* objects.

Looking through objects does not only eliminate the necessity to cut samples open, it also permits to place the sample in an enclosure providing suitable environmental conditions. In these *in situ* experiments, samples are measured *in their place*, meaning under conditions that mimic those of their relevant application or natural environment. Such conditions can include elevated or lowered temperature and pressure, liquid or gaseous chemical reagents, magnetic fields and many others. In situ experiments yield much more valuable scientific insight, but they are also more difficult to perform. In this thesis, particles in a container filled with a heated, pressurized solvent are imaged.

In addition to its penetrating properties, the interaction of X-rays with atoms permits to probe atomic properties of the sample. The wavelength of the emitted fluorescence photons identifies the chemical species of an atom, the shape of their absorption edges reveals information of their surrounding local electronic structure. Furthermore, wide angle diffraction permits to measure locally crystal structure, orientation, stress, grain sizes and more. In *multi-modal* x-ray microscopy, several of these contrasts are measured in parallel to completely characterize a sample system.

So x-ray microscopes can penetrate samples and sample enclosures, imaging highly relevant properties with a variety of contrasts, but the advantages do not end there. In the 19th century, the pioneers of the visible light microscopy soon realized that the resolving power of a microscope is limited by the wavelength of light. Essentially, the Abbe resolution limit says that a light wave cannot image anything that is smaller than its wavelength. This fundamental resolution barrier is not relevant in x-ray microscopes

as X-rays have wavelengths of nanometers and below. With that, the resolving power of state-of-the-art x-ray microscopes exceed that of their visible light counterparts a hundredfold.

However, there are also disadvantages to x-ray microscopy. Even though the field of x-ray optics has experienced a rapid succession of breakthroughs over the last 25 years, the best x-ray optics available today cannot compete with their visible light counterparts. Therefore, the best x-ray lens is no lens at all. Lensless coherent imaging techniques replace the image-forming objective lens with a digital phase retrieval algorithm. *Ptychography* is one of these lensless imaging techniques that has gained considerable global popularity over the last decade.

There remains, unfortunately, a major technological and economical challenge to x-ray microscopy in general and coherent imaging in particular: The x-ray source. Different to the x-ray tubes used in simple absorption radiography, the x-ray source has to possess a high brilliance, meaning that a large number of photons has to be emitted from a small source, into a small solid angle within a small energy bandwidth. As of today, sufficient brilliance can only be reached by large-scale accelerator-based light sources that are many hundreds of meters in size and cost many hundreds of million euros to build.

Learning these facts while visiting DESY, many visitors do not understand how public funds are used to build such expensive machines and some downright refuse to believe that there is not only one, but many of these synchrotron radiation sources around the world. The facts are that synchrotron radiation sources, with the UV and x-ray light they produce, are such powerful and versatile tools for science and industry that all of the 14 world's largest economies operate one or several of them [1, 2].

1.2 A brilliant future

Soon after having started my work at DESY, at the PETRA III synchrotron radiation source, I learned that there are several generations of sources and PETRA III was the most brilliant source of the third generation. There was, however, already much talk about the upcoming fourth generation of electron storage rings. These would solve the problem of the highly asymmetric source size of the third generation sources by switching from dipole magnets to a multi-bend achromat lattice design, resulting in a 100× flux gain for the microscopy techniques [3].

In March of 2016, I attended the Fifth Diffraction Limited Storage Ring Workshop hosted at DESY. During the three days of the event, representatives of the synchrotrons around the world introduced their extensive upgrade programs, one-upping each other with their ambitious plans. It was only then I realized what an immense leap forward the diffraction limited storage ring would be.

But the best x-ray source in the world is ineffective if not paired with an equally

capable microscope. Whenever microscopes approach the nanometer resolution mark, as electron microscopes and atomic force microscopes did, vibrations start to become a major concern. My work to measure, understand and improve the vibrations at our present setup PtyNAMi at P06 benefits our users today; but it is more importantly a piece of guidance for the design of future instruments at PETRA IV. While we do not know yet precisely how these microscopes will look like and what performance they will reach, there is one thing that is certain: A brilliant future lies ahead.

1.3 About this thesis

This thesis does not follow the practice to print précis of textbook content, starting from the Maxwell equations, covering wave equations, coherence, Fraunhofer diffraction, Fourier transforms, interaction of X-rays with matter and so forth. Every reader either knows these topics already, or if not, they will not understand them by reading a one-pager here.

The standard introduction to synchrotron x-ray physics is Als-Nielsen [4]. A standard textbook about wave optics is Hecht [5], more details are explained by Goodman [6]. Champeney [7] and Butz [8] discuss the properties of the Fourier transform. All relevant topics are also contained in a recently published book by Chris Jacobsen [9].

The body of the thesis is structured into three parts:

Part I, spanning the chapters 2 and 3, is the introductory part written for readers that are not experts in the field. Chapter 2 takes the part of a theory chapter and explains the ptychographic model and phase retrieval algorithm, the extensions of the algorithm as well as the concepts of numerical aperture and depth of field. Chapter 3 is an introduction to the instrumentation at the beamline P06 and PtyNAMi. The components of the instrument are listed and their function is summarized.

Part II, consisting of chapters 4 to 6, focuses in more detail on certain aspects of the instrumentation. The short chapter 4 introduces the in situ cell build for imaging of particles in liquid. The cell is introduced early in the thesis as it has implications for the following aspects of the instrumentation.

Chapter 5, about laser-interferometry, can be considered in many ways the heart of the thesis. My work in this field goes back to my Master's thesis [10] and continued all throughout my doctoral studies. As such, it summarizes at many instances my findings over the years instead of presenting individual measurements.

Concluding the instrumentation part, chapter 6 shows some results obtained with the new in-vacuum detector device at PtyNAMi.

In **Part III**, ptychographic measurements of copper and copper oxide nanoparticles are presented. All of these measurements have been performed in collaboration with Lukas Grote who works in the group of Prof. Dorota Koziej at the Center for Hybrid Nanostructures (CHyN).

In chapter 7, copper oxide cubes are measured *ex situ* as a resolution benchmark in both single-slice and multi-slice measurements. The artifacts introduced by multi-slicing and upsampling to the ptychographic reconstruction are analyzed and their impact on quantitative imaging is discussed.

In the final chapter 8, copper particles are grown and imaged successfully *in situ*. As this is one of the first ptychographic imaging experiments through a liquid, there are parts of the image formation process that are not fully understood; several variants of the ptychographic phase retrieval are compared.

The appendices contain additional points that I considered to be of particular interest and therefore removed from the main part. Appendix A has more details on the monochromator vibrations at P06. In appendix B, the coordinate transformation used with the laser-interferometers is derived. Appendix C reproduces the working principle of homodyne phase quadrature interferometry from [10]. Finally, appendix D shows the effect of carbon deposition and the beam damage associated with it as well as the *in situ* cell that was employed as a helium enclosure to solve the problem.

As this thesis shows data measured in a dozen different beamtimes, the table on page 159 lists the beamtime IDs for all figures in the thesis.

In the text, the pronoun *we* is often used. Sometimes it refers to me and my fellow coworkers, but most often it means me and *you*, the reader. At some points, when I made decisions on my own or arrive at conclusions that are more opinion than evidence-based, the pronoun changes to *I*.

Chapter 2

Ptychography

The microscopy technique *Ptychography* was originally conceived by Walther Hoppe and his students in 1969 [11–14]. The name was formed in the tradition of holography and tomography as a compound of the greek $\pi\tau\upsilon\chi\acute{\eta}$ (*ptyche*, "to fold") and $\gamma\rho\acute{\alpha}\phi\epsilon\iota\nu$ (*graphein*, "to write"). The term *folding* refers to the German name *Faltung* for the convolution operation.

Hoppe used the convolution of the probe beam with the crystal reflexes in Fourier space to directly solve the phase problem in electron crystallography. He even envisioned the imaging of aperiodic objects with ptychography, though it was deemed computationally unfeasible at the time. Half a century later, we now have the computational means to solve ptychograms in minutes.

In this chapter, we introduce at first ptychography in the most simple form before concerning ourselves with a number of extensions of the algorithm which are used to take experimental imperfections into account. In the later half of the chapter, we discuss the limits of the spatial resolution achievable in ptychography including different methods to estimate the resolution of experimental data.

Readers interested in a more in-depth discussion of fundamentals and more variants of ptychography should also refer to a recently published book chapter by John Rodenburg and Andrew Maiden [15].

2.1 The ideal ptychographic model

Ptychography consists of two parts: In the forward model, we describe how the beam interacts with the sample and propagates to the detector. The phase retrieval algorithm permits us to solve the inverse problem, i.e. to deduce the sample and probe fields from the images on the detector.

2.1.1 The forward model

The idealized model starts with an incoming probe beam, the illumination, that we describe with a complex function $P(\mathbf{r}) : \mathbb{R}^2 \mapsto \mathbb{C}$. This complex-valued field is orthogonal to the optical axis of our physical microscope. By choosing this type of function, we assume that the beam is perfectly coherent, i.e. it consists of a single monochromatic mode, and does not change with time.¹ The assumption of a scalar wave field limits us to the description of diffraction occurring at small angles with respect to the optical axis.

The physical interpretation of the complex field $P(\mathbf{r})$ is that at every point \mathbf{r} we can define the amplitude of the probe wave A_P and the phase of the probe wave ϕ_P so that

$$P(\mathbf{r}) = A_P(\mathbf{r}) \cdot \exp[i \cdot \phi_P(\mathbf{r})]. \quad (2.1)$$

In a similar fashion, we describe the object, i.e. the sample of interest in our microscope, with a complex function $O(\mathbf{r}) : \mathbb{R}^2 \mapsto \mathbb{C}$. The modulus A_O of $O(\mathbf{r})$ describes the transmission of the object. $A_O = 0$ describes complete absorption of the probe beam, $A_O = 1$ describes perfect transmission, everything in between is considered partial absorption. The phase ϕ_O of the object function $O(\mathbf{r})$ describes a phase shift introduced to the probe beam by the object.²

With the physical interpretation of both complex fields in mind, we can express the *exit wave* ψ , i.e. the wave field immediately after the interaction with the sample, as a simple multiplication:

$$\psi(\mathbf{r}) = P(\mathbf{r}) \cdot O(\mathbf{r}) = A_P \cdot A_O \cdot \exp[i(\phi_P + \phi_O)] \quad (2.2)$$

With this interaction model we assume that the sample is so thin that no propagation effects occur within the sample volume; the object can be described as a parallel projection along the beam axis. Furthermore, we disregard all incoherent and inelastic scattering processes.

Finally, the exit wave field has to propagate to the area detector, we can express this with a general free space propagator \mathcal{P} :

$$\Psi = \mathcal{P}[\psi] \quad (2.3)$$

The propagator can be the Fresnel-propagator \mathcal{N} in the near-field or the Fraunhofer propagator, i.e. the Fourier-transformation \mathcal{F} , in the far-field regime [9, sec. 4.3]. At the detector, the phase of the complex wave cannot be detected; the detected intensity

¹In general, the discussion in this chapter holds for all types of probes, including visible light, UV, X-rays and electrons, but all examples shown and further discussion are from the hard x-ray regime.

²The relation of transmission and phase shift to physical properties such as the complex refractive index and the electron density is described in [4, ch. 1] and [16, ch. 2].

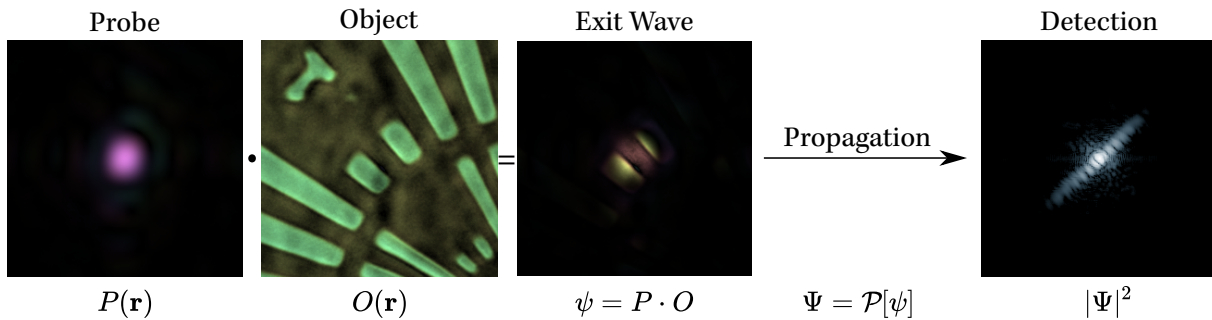


Figure 2.1: The forward model in the most simple, idealized form. The brightness encodes the amplitude of the wave, the phase is expressed by the hue of the color. The diffraction pattern on the detector is not shown in color since the phase cannot be detected.

pattern is the squared modulus of the wave:

$$I = |\Psi|^2 = |\mathcal{P}[P \cdot O]|^2 \quad (2.4)$$

In the case of far-field ptychography we consider the intensity pattern to be detected in the Fourier domain; we then write the intensity distribution as a function of spatial frequencies: $I(\mathbf{q})$. As only far-field ptychography was performed in this work, we will adapt this notation in the following.

When the probe function has a large extent in space, the interference pattern $I(\mathbf{q})$ will be so finely structured that the interference speckles cannot be resolved on real-world detectors with their technologically limited pixel sizes. Therefore, the probe beam is usually produced by focusing optics and the object is positioned near the focus.

This forward model is also illustrated in figure 2.1, where the wave fields are exemplified with real data.

2.1.2 Phase retrieval

If we were able to measure the full phase information of the propagated wave Ψ , we would be able to propagate the wave field back and, with an educated guess of our probe function, obtain an estimation of the object function $O(\mathbf{r})$. Since we cannot measure the phase of Ψ this is not possible. In fact, since we want to calculate two complex-valued fields, but only measure a single real-valued field, only a quarter of the necessary information is available to us. Clearly, this problem is not solvable in the general case.³

2.1.2.1 Scanning scheme

In order to obtain a stable solution in the general case we need to measure more information. This is achieved by scanning the probe beam over the sample so that we acquire a number of diffraction patterns I_i at different lateral offsets \mathbf{R}_i . If the positions

³This does not mean that single-shot coherent imaging is impossible in all cases. In CDI, an isolated object can be reconstructed from a far-field diffraction pattern, and with inline holography the back-propagation can be performed in the near field [17, 18].



Figure 2.2: By scanning the sample with overlapping illuminations the diffraction patterns are gradually changing, thereby encoding shared information.

\mathbf{R}_i were chosen such that the probes never overlapped, we would create a number of independent unsolvable problems, but by scanning with an overlap, we can generate a single, coupled, and thus solvable problem.

Such a scanning scheme is shown in fig. 2.2. Here, we recorded four diffraction patterns at probe positions with vertical overlap, and in consequence, the four respective diffraction patterns show a gradual change of the diffraction signal.

While four diffraction patterns are theoretically enough, the sample is scanned in a grid pattern in practice, collecting at least 100 diffraction patterns. Such a scanning scheme can be combined with complementary scanning microscopy contrasts in a simultaneous measurement [19]. When a larger field of view is required, the scanning grid can be extended, in some cases to up to several million points [20].

The experimental data measured in ptychography thus consists of a number of diffraction patterns I_i and their respective relative offsets \mathbf{R}_i . It is not a coincidence that, in the instrumentation part of this thesis, we have dedicated chapters (5 and 6) that discuss the data quality of those two measurands in detail.

2.1.2.2 Iterative Algorithm

Retrieving the complex object and probe functions is done with an iterative algorithm, the *extended Ptychographic Iterative Engine* (ePIE)⁴ [21]. The algorithm is shown in figure 2.3 and begins with initial guesses for the object and probe functions. The initial object can be completely empty while the beam size and curvature of field of the probe should be roughly estimated.

The forward model is then calculated as described above. In the detector plane, an updated propagated wave field Ψ' is generated by keeping the current guess of the phase, but replacing the modulus with the square root of the measured diffraction

⁴Several alternative algorithms exist [15], but only ePIE was used in this work.

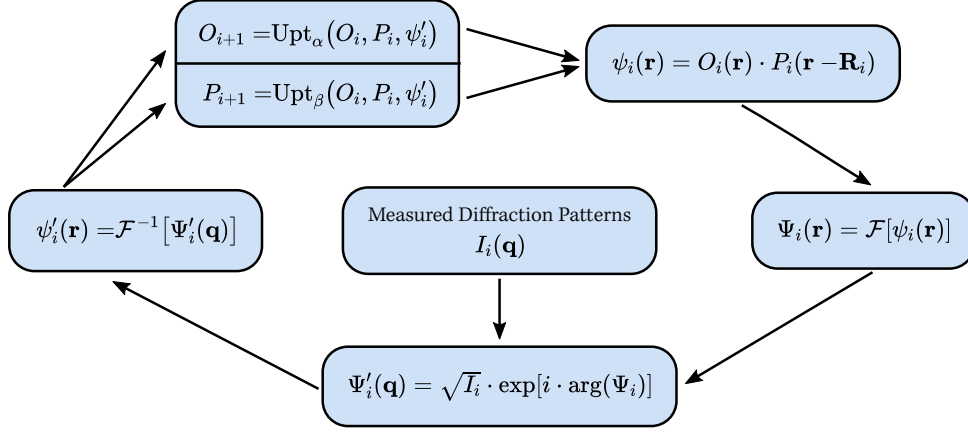


Figure 2.3: Algorithm to iteratively solve the phase problem in ptychography with ePIE. After backpropagation into the sample plane, the update of the exit wave ψ' is applied to both the probe and object function, completing one subiteration of the algorithm.

The update function is in general in the form of

$$O_{i+1} = O_i + \alpha \cdot \frac{P_i}{\max|P_i|^2} (\psi'_i - \psi_i) \quad P_{i+1} = P_i + \beta \cdot \frac{O_i}{\max|O_i|^2} (\psi'_i - \psi_i) \quad (2.5)$$

where α and β are free parameters to control the update strength and the maximum in the denominator is used to avoid numerical instabilities. An iteration of ePIE is completed when this cycle has been executed for all diffraction patterns I_i of the ptychographic scan, a typical reconstruction using ePIE is run for several hundred iterations. The convergence of the algorithm can be monitored with the error sum

$$E = \sum_i \left\| |\Psi_i| - \sqrt{I_i} \right\|_2. \quad (2.6)$$

2.1.2.3 *ptycho*

The constant forth- and backpropagation between the sample and the detector plane, with restraints being applied in both planes, is a hallmark of phase retrieval algorithms. With that in mind, we can understand why these techniques only became feasible in the 2000s: The requirement to calculate the propagation, i.e. the Fourier transform, many thousands of times was just not computationally feasible before. Even today, high-end professional GPUs are still required to handle larger data sets while small scans can also be evaluated on laptops.

The ptychograms in this thesis were calculated with *ptycho*, a group-internal ptychography code initially written by Wolfgang Hönig [22] in 2010. Robert Hoppe [23] and Tobias Witt [24] continued the development until 2016 and Felix Wittwer maintains the code until the present day. As *ptycho* is written in Nvidia CUDA, it requires compatible GPUs to run. For this, the resources of the Maxwell cluster at DESY were used, the majority of the reconstructions were run on Nvidia Tesla P100 cards.

2.1.2.4 Results

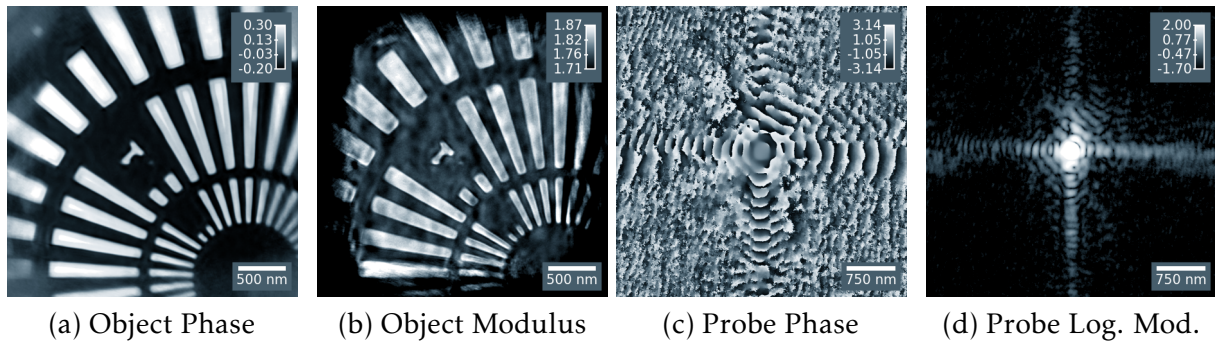


Figure 2.4: Result of a ptychographic reconstruction: The complex probe and object functions are reconstructed in both modulus and phase. The logarithm of the modulus of the probe is shown so that the reconstructed features beyond the focus spot are visible.

The results of a ptychographic reconstruction are shown in figure 2.4. We have four scalar, real-valued fields: the phase and modulus of the complex probe and object functions. The sample scanned is a Siemens star, a microscopic test pattern in wide use for ptychographic test measurements.

The superior image quality obtained in the phase image of the object in comparison to the modulus is evident. This is an overarching observation that holds for almost all ptychographic reconstructions as well as most other imaging techniques. For weakly absorbing objects, the reconstructed modulus is often extremely noisy, but the phase shift still yields a usable image.

Looking at the reconstructed probe, we can understand why the probe beam cannot be simply modeled but has to be reconstructed as an independent field. The x-ray focus is highly structured. In the case here, we see that the aperture slits of the focusing optics cause diffraction in the focus plane decaying over four orders of magnitude. The knowledge of this complex probe field in the object plane makes ptychography one of the most valuable tools for the characterization and development of x-ray optics [25, 26].

Even though the probe beam may be 100 nm in size, the 50 nm lines and spaces in the center of the Siemens star are perfectly resolved. The ptychographic reconstruction algorithm performs a complex-valued deconvolution of probe and object that renders probe size, lens aberrations and other optical imperfections irrelevant as long as the diffraction speckles on the detector can still be resolved. The achievable spatial resolution is limited by other factors that we discuss in section 2.3.

2.2 Beyond the ideal model

The ptychographic model described above does never hold perfectly in any experiment. Samples are never infinitesimally thin, the incident beam is neither fully coherent nor completely stable over time and the sample cannot be positioned with infinite precision.

To account for these imperfections, a number of extensions to the ptychographic model and reconstruction algorithm have been developed by various groups over the last years. The following list is not complete; we limit ourselves to methods used on the data presented within this work.

All of these extensions of the algorithm have in common that they introduce additional degrees of freedom to the model. If too many degrees of freedom are added, the reconstruction becomes unstable and fails. Deciding how many extensions to use, with which strength and for how many iterations, is therefore often a question of experience and trial-and-error. Furthermore, the computational effort increases greatly. In a series of benchmarks run in May 2018, reconstructing a test data set with the basic algorithm presented above on Nvidia Tesla P100 cards only took four minutes, while the same data set required 22 hours of computing time on identical hardware with multi-slicing, upsampling and position refinement enabled.

2.2.1 Multi-slice ptychography

By describing the interaction of sample and probe beam with a simple multiplication, we neglect all propagation effects inside the sample volume, or in other words, we assume that the sample volume lies within the depth-of-field (DOF) of the microscope. When performing Ptychographic X-ray Computed Tomography (PXCT) on large volumes, this assumption does not hold necessarily [27].

Furthermore, the process of the sample creation may intrinsically result in multiple objects planes [28]. In chapter 7, we image nanoparticles that were grown on a substrate completely immersed in solution, consequently both sides of the substrate are covered. In the following chapter 8, we grow such particles in situ, with the particles covering both walls of the reaction container. In such an experiment, we cannot avoid growing particles on both the entrance and exit window of the container and thus creating objects at two planes along the beam.

Such situations can be modeled by introducing two independent object functions $O_1(\mathbf{r})$ and $O_2(\mathbf{r})$ such as shown in figure 2.5. The exit wave function ψ_1 is propagated with a near-field propagator⁵ to the second object plane, where it is multiplied with the second object function $O_2(\mathbf{r})$. The resulting second exit wave function ψ_2 is then propagated to the detector plane as usual.

Only a second object plane was introduced in this example, but the generalization to an arbitrary number of object planes is trivial. We just introduce n independent object functions $O_i(\mathbf{r})$ and $n-1$ near-field propagators \mathcal{N}_i between them. The maximum number of slices reconstructed in this work is four, but in literature reconstructions with over 30 slices in the visible light regime have been reported [29].

⁵*ptycho* implements the propagation as the *Angular Spectrum Propagation* [23]. This implementation keeps the pixel size constant and requires no prior knowledge of the wave curvature.

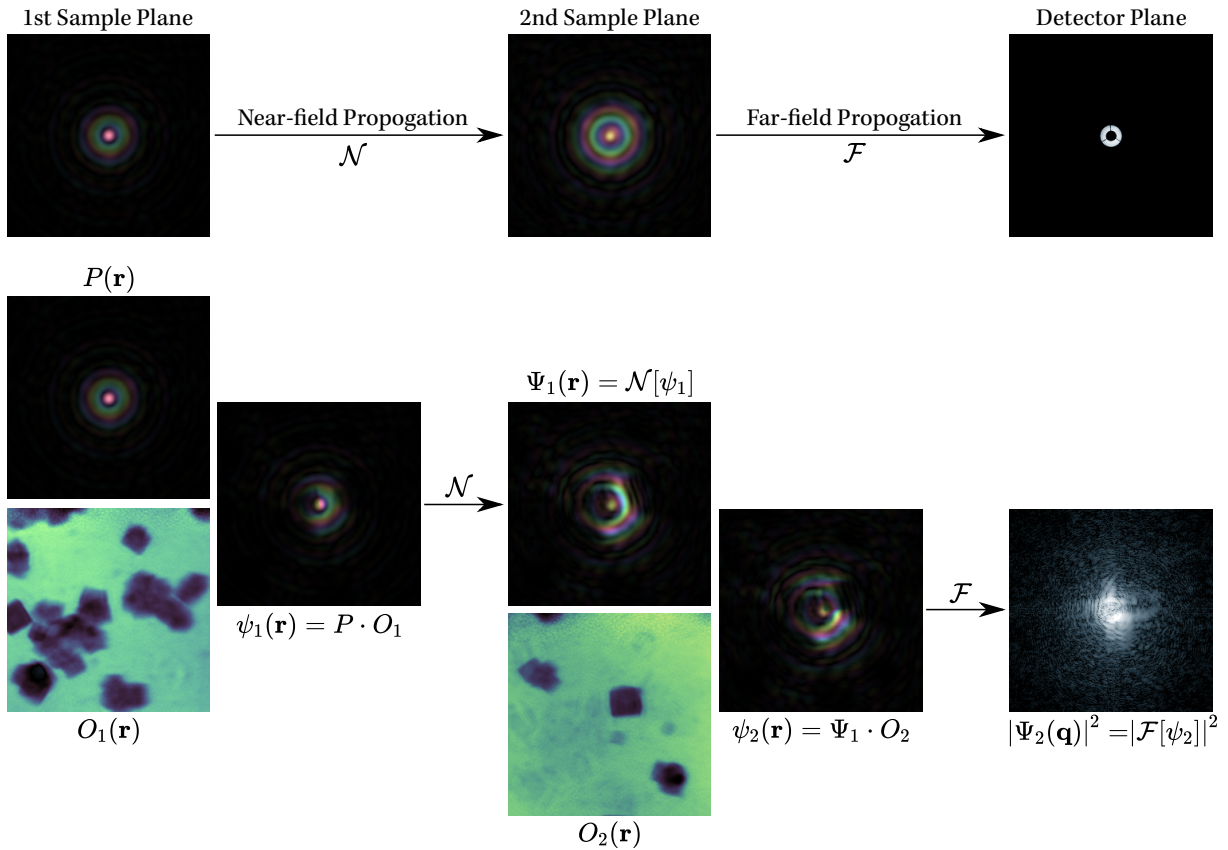


Figure 2.5: A more complex forward model that takes two object planes into account. On the top, the effect of the near-field propagator \mathcal{N} and the far-field propagator \mathcal{F} on the illumination without object is demonstrated. On the bottom, the effect of two object planes is simulated. These objects are the reconstructed slices of real measurements, but their scattering power has been increased in the simulation to increase the visibility of the scattering signal.

The modified reconstruction algorithm for two object slices is outlined in figure 2.6. Just as the forward model contains two propagators and multiplications of the probe field with the objects, the backpropagation is now done in two steps, updating the object and probe functions in each plane. Essentially, the algorithms of near-field ptychography and far-field ptychography are just linked together.

In practice, it is not advisable to initialize all object planes at the beginning of a multi-slice reconstruction. Instead, a conventional single-slice reconstruction should first be performed in the slice that contains the strongest scatterers so that an approximate solution is found. After some iterations, the second slice can be added, thereby minimizing the instabilities introduced by the additional degrees of freedom.

Figure 2.7 shows such a two-step reconstruction. Here, the reconstruction begins with the second object, i.e. the first object is empty and not updated. After 100 iterations, the first object is added to the modified ePIE algorithm. With two object planes, the convergence is now much slower. At 1000 iterations, the reconstruction is considered complete; the two object slices are now clearly separated.

The distance of the slices in multi-slice ptychography has to be known with an accuracy smaller than the DOF. For the reconstructions presented in this work, the

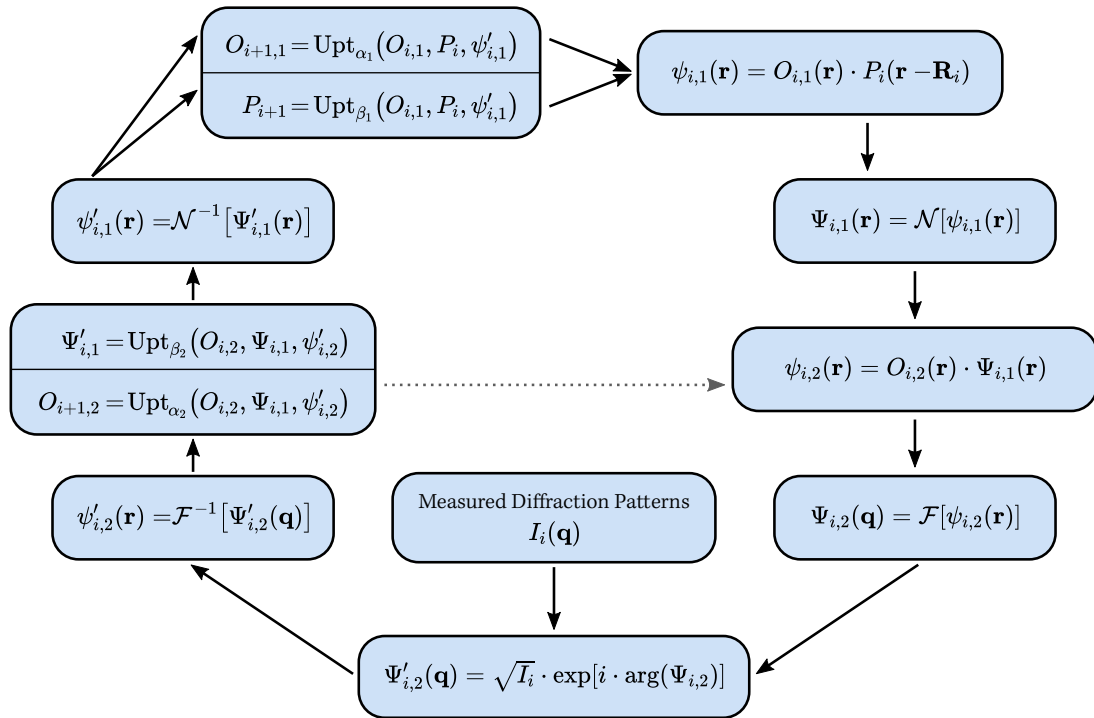


Figure 2.6: A modified version of ePIE to reconstruct two independent object planes [30].

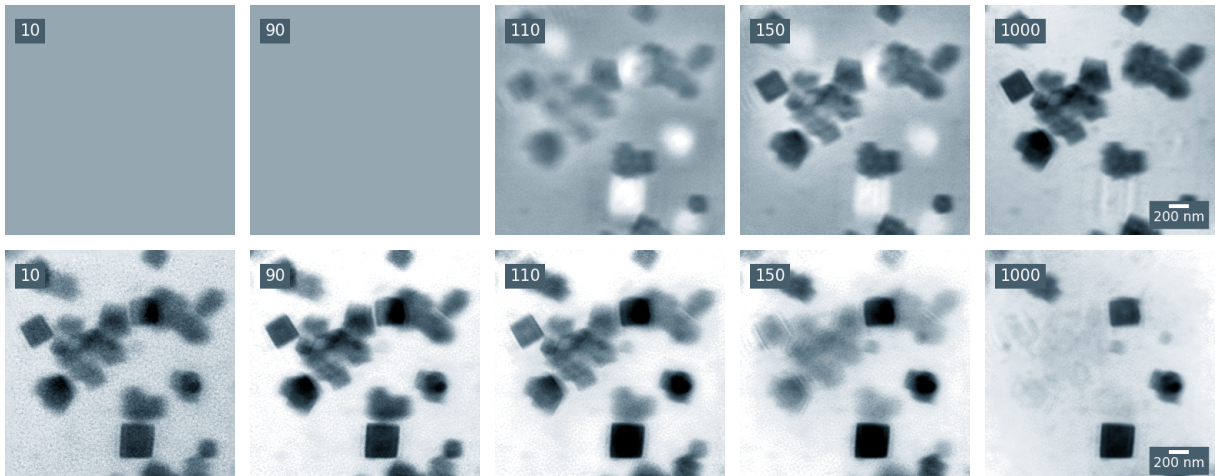


Figure 2.7: Iterations of a ptychographic multi-slice reconstruction. The top row shows the upstream object plane, the bottom row the downstream image plane. The number of the iteration is denoted in the top left corner of each frame. For the first 100 iterations the conventional single-slice algorithm is used, from iteration 100 onward both object slices are updated.

distances have been determined manually by running reconstruction with several distance settings. However, an autofocusing variant of the algorithm has been reported in literature [31]. In chapter 7, we will attempt to find an objective measure to determine the best distance.

2.2.2 Virtually enlarged probes

As we have discussed above, the probe size in the sample plane has to be small enough so that the pixel detector can resolve the interference speckles. More precisely, the size D_p of the digitized field $P(\mathbf{r})$ is limited by the pixel size p_x and distance d of the detector for a given wave length λ to

$$D_p = \frac{\lambda \cdot d}{p_x}. \quad (2.7)$$

According to the Nyquist-theorem, the probe should be confined to the inner 50% of this field to be sufficiently sampled [32], further decreasing the maximum probe size to $D_p/2$. If this is the case, the smallest interference speckles on the detector are sampled by at least two detector pixels.

In many experimental situations this is not fulfilled:

1. The sample may be positioned deliberately out of focus to scan a given area with fewer steps and more overlap. This is a common procedure when ptychography is not measured in parallel with other complementary contrasts.
2. The multiple image planes of the sample cannot be positioned along the beam caustic such that the probe is small enough in *all* planes along the beam.
3. The focus is not clean, i.e. the majority of the intensity may be concentrated in a small focus area, but the remaining intensity is distributed in a large area around the focus as is the case in the illumination of fig. 2.4d.

In such cases, the reconstruction quality can be improved by dividing each detector pixel into $n \times n$ virtual subpixels, thereby virtually increasing the size of the probe field, and with that the largest possible size of the probe, by a factor n . In this case, we say that the reconstruction is n times *upsampled* or *upscaled* [33, 34].

In the ePIE algorithm, the update step in the detector plane has to be modified; the sum of all virtual subpixels now has to be matched to the number of photons in the measured diffraction pattern.

In figure 2.8 we see an application of a virtual enlarged probe. Here, the probe is aberrated and extends outside the probe field. The undersampling of the diffraction pattern results in interference at the edges of the reconstructed probe and mirror

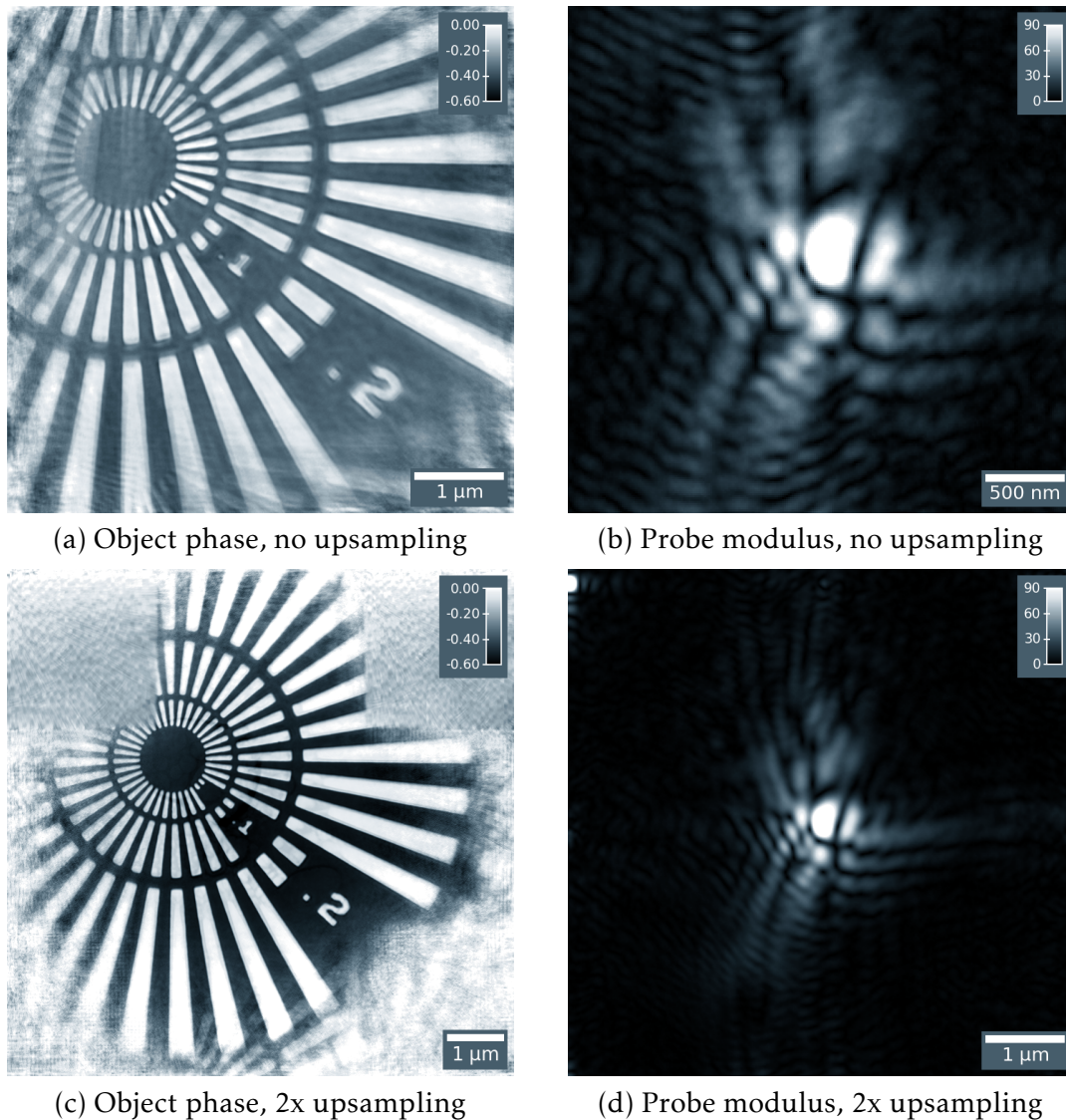


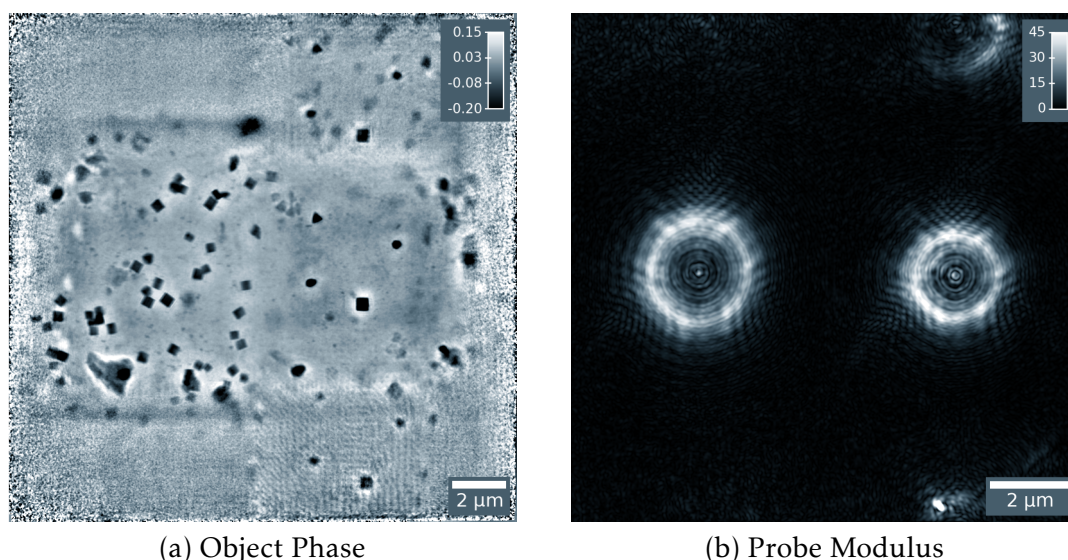
Figure 2.8: Example of the application of a virtually enlarged probe. a,b) Conventional reconstruction. c,d) Same data set reconstructed with 2x upsampling, i.e. each detector pixel is divided into 2×2 virtual subpixels. The probe moduli are shown in linear color scale.

artifacts in the reconstructed object. By virtually doubling the probe size, both probe and object can be reconstructed with nearly flawless image quality.

With such results, this modification of the algorithm may seem miraculous at first, but it is certainly not without pitfalls. The complete freedom to distribute the measured intensity among the virtual subpixels in any pattern can lead to various sampling artifacts. In particular, high-frequency artifacts can lead to several copies of the probe.⁶

In figure 2.9, an object with two object planes has been reconstructed without using the multi-slice algorithm, but a virtual enlarged probe was used as the sample was positioned out of focus. During the reconstruction, the probe split into two probes, both roughly reconstructing the object of their respective object plane. From the point

⁶Readers that have difficulty to understand these Fourier aliasing artifacts may think of a virtual diffraction grating present on the detector that splits the backpropagated beam into several beams in the sample plane.



(a) Object Phase

(b) Probe Modulus

Figure 2.9: Example of upsampling artifacts in a reconstruction with a virtually enlarged illumination. A high-pass filter with a cut-off wavelength of $1\ \mu\text{m}$ was applied to a) suppress long-range image artifacts that made the image contrast unsuitable for printing.

of the ptychographic model, this is nonsense and does not describe the experimental conditions at all.

Especially if the scanned area is smaller than the enlarged field of the probe, reconstructions become unstable. As a consequence, the result of the reconstruction strongly fluctuates with the order of the diffraction patterns in the subiterations. Reconstructions have then to be repeated multiple times until a qualitatively correct result is obtained. However, such a reconstruction will still not represent quantitative data.

With these characteristics, virtually enlarging the probe is certainly a double-edged sword. In the beamtime that I describe in chapter 7, the experiment was set up such that scans could only be reconstructed using upsampling. The result was a greatly increased effort in performing the data evaluation and ultimately failure to obtain the quantitative data desired. In summary, I strongly recommend designing the experimental geometry such that the conventional algorithm suffices.

2.2.3 Position refinement

As will be discussed in the next chapters, the relative positioning of the sample with respect to the focused beam is of great importance. As a general rule of thumb, the spatial resolution in a ptychographic reconstruction cannot be better than the precision with which the relative positions of the beam on the sample are known for every exposure [35].

As ptychography is scanned with overlapping probes, the positions can be improved algorithmically. This procedure is called *position refinement* or *position correction* [36].

Before the refinement step, the object has to be reconstructed with the initial positions. At the refinement step, the forward model is calculated for a number of positions

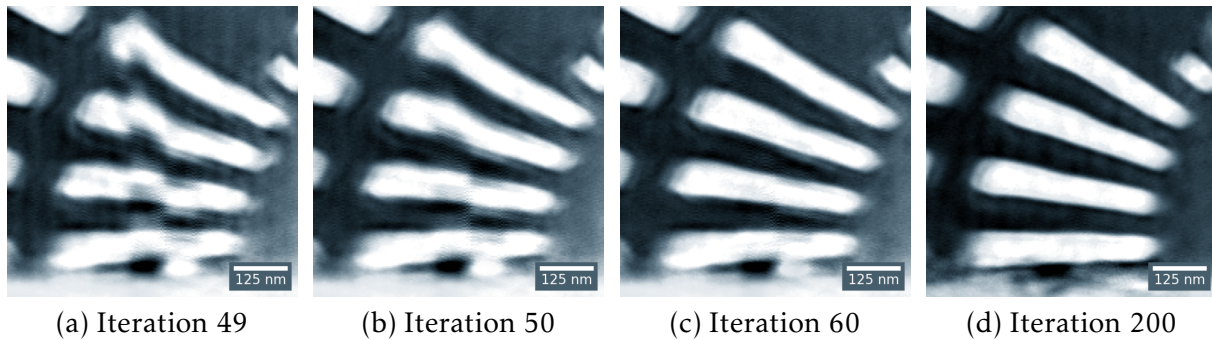


Figure 2.10: Demonstration of algorithmic position refinement on a ptychographic scan of the Siemens star with vertical position errors. The ptychographic reconstruction algorithm is run normally for (a) 49 iterations, in (b) iteration 50 a brute-force search of positions with a maximum jump width of five pixels is performed. This position search is repeated in (c) iteration 60 and every tenth following iteration until the final result in (d) iteration 200 is reached. These figures show a small region of interest, the full reconstructed object is shown in figure 5.14c.

in the vicinity of the initial offset vector \mathbf{R}_i . For each of these positions, the exit wave is propagated to the detector and the error sum (equation 2.6) is calculated; the offset vector with the smallest error sum is taken as the new position. This neighborhood search is performed for every scan position sequentially.

After the positions of all scan points have been refined once, the conventional algorithm should be run for some iterations. The example of position refinement in fig. 2.10 shows a typical configuration: The first position refinement is done in iteration 50 and then every 10 iterations until the end of the reconstruction.

Position refinement works well on local positioning errors such as shown in the example, but it struggles to correct global errors such as rotation, shearing or stretching of the entire position field. These global deformations are hard to solve since the positions are refined in sequence and usually require a large number of iterations. In addition, over-use of position refinement can also introduce global deformations, especially in cases where the sample has no strong features and the overlap of the probes is small.

The weak point of position refinement is its dependency on the features of the object. With benevolent test patterns, such as the Siemens star, positions can usually be retrieved from strongly distorted initial positions, while weakly scattering or sparse samples see hardly any improvement.

Indifferent to these drawbacks, position refinement is one of the most useful and widely used additions to the ptychographic algorithm.

2.2.4 Intensity refinement

In general, the ptychographic model assumes that the probe function is identical at all positions on the sample. This assumption is intrinsically flawed at synchrotron radiation sources as the beam current in the storage ring is steadily decaying and periodically refilled.

The standard method to account for beam intensity fluctuations is to normalize all diffraction patterns with the incoming beam intensity I_0 . However, as I_0 is measured upstream of the focusing optics in the flat beam (cf. fig. 3.5 on p. 43), the beam intensity in the focus does not perfectly correlate with I_0 . Even though intensity fluctuations are usually less than 1%, they can have a strong impact on the quality of the reconstructed object.

In such cases, the normalization of each measured diffraction pattern can be fitted in the reconstruction algorithm. Instead of simply replacing the modulus of $\Psi(\mathbf{q})$ with the measured \sqrt{I} , the measured diffraction pattern is normalized to fit the overall number of photons in the current estimate of the probing beam [23, p. 39]. This procedure works best when the thickness of the sample is homogeneous on the global scale, e.g. wedge-shaped samples are not suitable. We will see a demonstration of this intensity refinement in figure 8.5 on page 124.

Intensity refinement works best when the probe is large and the scan has a large overlap. In contrast, concurrent use with multi-slicing leads to instabilities and should be avoided.

2.2.5 Partially coherent illumination

Among our model assumptions, the least true is probably that we have a fully coherent probe in our experiment. The coherent fraction of synchrotron radiation sources in the hard x-ray regime is limited; a trade-off between the degree of partial coherence and flux is always necessary.⁷

The effects of partial coherence can be included in the ptychographic model by a multi-mode decomposition of $P(\mathbf{r})$ into several (orthogonal) modes $P_j(\mathbf{r})$. These modes are in itself fully coherent but mutually incoherent. The forward model is then calculated for each mode individually; the intensity on the detector is modeled at the weighted incoherent sum $\sum_j c_j |\Psi_j|$ of the individual contributions. For more details and examples see [38].

The support of multi-mode probes is not very developed in *ptycho* and they cannot be used in conjunction with multi-slicing. For this reason, multiple probes could not be used to treat the experimental data presented in this thesis. Changing to a different code base was considered, but none offered all the other features required at the same time. Nevertheless, we mention this approach here as some reconstructions show clear evidence that multi-mode probes could further improve the reconstructions.

⁷Fourth generation storage rings bring an enormous improvement in this regard but still require trade-offs at energies above 10 keV [37].

2.3 Spatial resolution

In microscopy we talk a lot about resolution. Resolution may not be everything that a microscope has to offer, but it is certainly the key figure. Here, we first discuss the theoretical limits of the achievable resolution in far-field ptychography before introducing a few methods to estimate the resolution achieved in a measurement.

2.3.1 Transversal resolution

The *transversal* or *lateral* resolution is defined as the smallest distance in the object plane that two point sources can be apart while still being recognizable as separate⁸ [39]. With this definition in mind, we can immediately conclude that in a digital pixel image the resolution can never be better than twice the pixel size.

One of the fundamental results of wave optics found by Ernst Abbe [40] is that the spatial resolution δ of a microscope is limited by the wavelength λ of the light wave and the numerical aperture NA of the objective

$$\delta \geq \frac{\lambda}{\text{NA}} \quad \text{with} \quad \text{NA} = n \cdot \sin \alpha \quad (2.8)$$

where α is half the opening angle of the objective and $n \approx 1$ for measurements in air or vacuum. As the wave lengths of x-rays are on the atomic scale ($\lambda = 1 \text{ \AA}$ at 12.4 keV), an x-ray microscope could reach atomic resolution if the necessary x-ray optics were available. In reality, the performance of x-ray lenses is limited by small numerical apertures, limited efficiency and aberrations [41].

For this reason, we choose to replace the objective lens with the pixel detector in the experiment, turning it into a virtual objective with the ptychography algorithm. This virtual lens has no aberrations, can have a much larger aperture and has nearly perfect efficiency.⁹ Still, we cannot circumvent the limitations of Abbe's law and the question arises how the effective numerical aperture of this virtual lens is defined.

In figure 2.11, we see a simplified sketch of the optical scheme in the microscope. The numerical aperture NA_{Lens} of the focusing optics defines the theoretical limit of the focus spot size and with that the resolution limit achievable with conventional scanning microscopy contrasts such as transmission (STXM) or fluorescence (μXRF). The detector also collects signal scattered at higher angles, therefore, it has a larger numerical aperture NA_{Det} . Consequently, ptychography achieves higher spatial resolution than the conventional scanning microscopy methods.

If we take simply the distance D from the sample to the detector, the detector pixel size p_x and the number of pixels in row N , we get with equation 2.8 the theoretical

⁸Depending on the precise definition of the resolution criteria and the experimental setup, a factor between 1/2 and 2 can be added to most of the following equations. See [9, ch. 4] for more details.

⁹Given that we use a photon-counting detector suitable for the photon energy [42, p. 3].

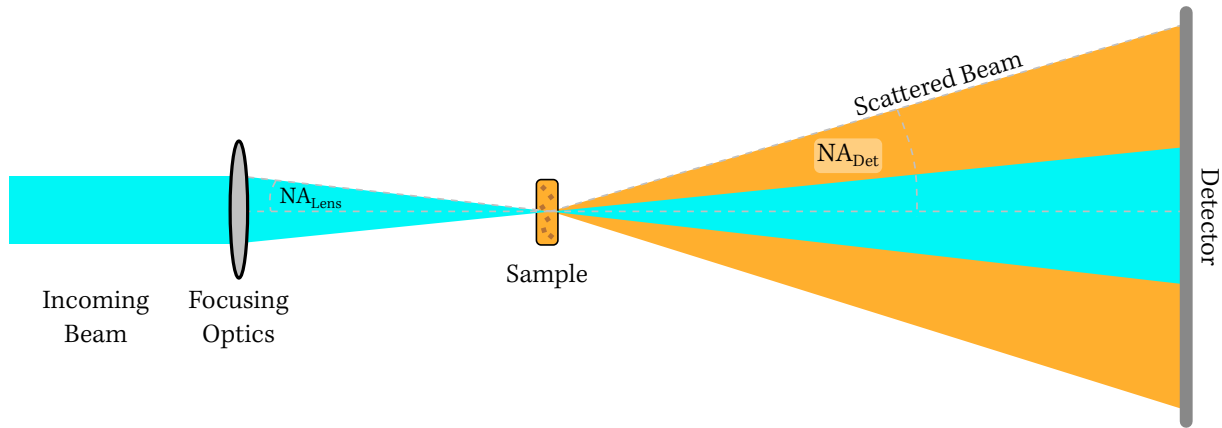


Figure 2.11: The numerical aperture of the virtual lens, i.e. the area detector, is in general much larger than the NA of the x-ray focusing optics.

resolution limit¹⁰

$$\delta_{\text{Det}} = 2 \frac{\lambda D}{N p_x} = 2 \delta_p. \quad (2.9)$$

This result is exactly twice the pixel size δ_p of the ptychographic reconstruction.

According to equation 2.9, we can improve the resolution arbitrarily by using a bigger detector or moving the detector closer. In a real measurement, this is not the case, as the signal scattered of non-periodic objects decreases quickly towards higher scattering angles (Porod's law: $I \sim q^{-4}$ [43–45]). At a certain scattering angle, the scattered signal becomes too weak to be detected over the noise in the diffraction pattern, limiting the effective numerical aperture NA_{eff} that has to be used in Abbe's law.

In figure 2.12, we see a diffraction pattern with the resolution equivalents of the respective effective apertures. In the center, we see, in bright yellow, the direct image of the focusing optics in the 70 nm virtual aperture, meaning that the focus spot size is around 70 nm, or worse in the presence of lens aberrations. The scattered signal in red extends far beyond the 70 nm aperture but falls to the single photon level around the 10 nm mark. Depending on the beam intensity, the scattering properties of the sample and the noise on the detector, the effective numerical aperture changes, and with that the resolution limit of the ptychographic microscope.

As the beam intensity is mainly defined by the electron storage ring and the sample is set by our research question, the only variable that the instrumentation can address is the noise on the detector; we have a separate chapter about this topic (chapter 6). We need to emphasize again that Abbe's law using the effective numerical aperture gives us a theoretical resolution limit. Many experimental problems, e.g. vibrations or incoherence, can still decrease the resolution obtained in the final result.

¹⁰In the hard x-ray range, the small angle approximations of the trigonometric functions hold well.

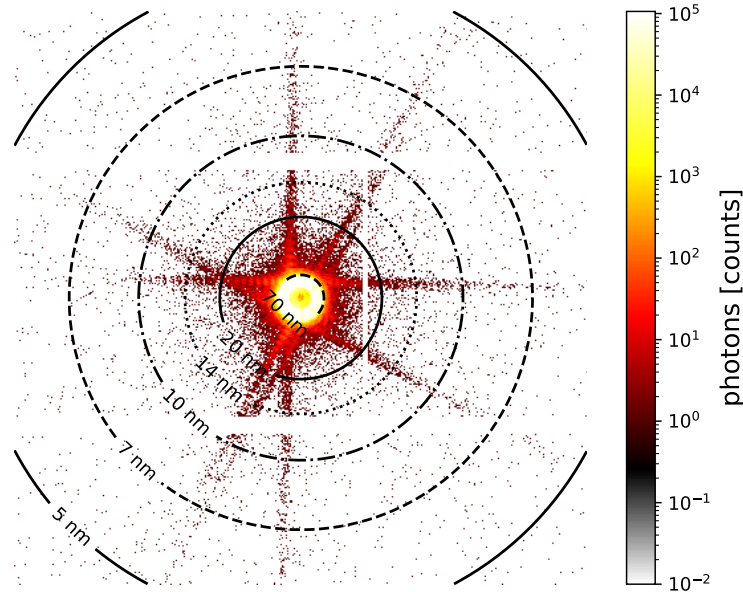


Figure 2.12: A measured diffraction pattern on the far-field area detector with resolution markings of the corresponding virtual numerical aperture. The resolution numbers marks the pixel size δ_p in the ptychographic reconstruction. This definition is intuitive as it relates the NA to the focus size of the corresponding focused beam, but the smallest resolvable features are twice as large.

2.3.2 Longitudinal resolution

The longitudinal resolution, also called axial resolution or referred to as depth-of-field (DOF), is the smallest distance along the optical axis at which two point sources can be distinguished. Worded differently, it is the length along the optical axis in which an object has to lie to be considered optically thin. If a large or a small DOF is considered desirable depends on the application.

Similar to Abbe's law, the DOF can be expressed in terms of λ and NA [9]:

$$\text{DOF} = \frac{2\lambda}{\text{NA}^2} \quad (2.10)$$

Identical to our discussion of the transversal resolution, the NA of the ptychographic microscope that has to be used in this equation is the effective NA determined by the scattering signal on the detector. With equation 2.8 we can express the DOF in terms of the transversal resolution δ

$$\text{DOF} = 2\frac{\delta^2}{\lambda} \quad (2.11)$$

which agrees with the result obtained from considerations of the Ewald sphere [46] but is more conservative than definitions used by other authors [47] derived from empirical studies. Considering the problem from the other end, namely that we force an object of thickness $T > \text{DOF}$ to reconstruct with the conventional ePIE algorithm without

multi-slicing, we expect the transversal spatial resolution to be limited to

$$\delta_{\max} = \sqrt{\frac{1}{2}\lambda T}. \quad (2.12)$$

In chapters 7 and 8, we confirm on experimental data these relations between longitudinal and transversal resolution in ptychography. We will also arrive at the conclusion that equation 2.11 is indeed overly conservative and that the true observed DOF is 2.6 times larger.

Contrary to a conventional microscope, the distance between the sample and detector does *not* have to be known or adjusted with the precision of the DOF. The necessary relative accuracy of the detector distance is instead related to the number of resolution elements in the image.

2.3.3 Resolution criteria

Determining the resolution of a ptychogram is surprisingly difficult. There are a number of established methods that are presented here, but all of them have disadvantages and the results do not necessarily agree. In consequence, we have to speak of a *resolution estimation* and always state exactly which method and criteria were used.

2.3.3.1 Known features

Measuring resolution test charts is a widespread method to determine the resolution of an optical system. The Siemens star is one of such test patterns, however, the performance of our ptychographic microscope has surpassed the 50 nm lines and spaces resolution limit of our Siemens star. Therefore, it cannot fulfill its original purpose anymore.

On real samples, features can be matched with higher resolution images obtained from electron microscopy. Such feature matching yields a lower bound of the resolution and is often subjective.

2.3.3.2 Edge profiles

Edge profiles are one of the more direct methods to assess resolution. A line profile through a sharp edge in the object is plotted, the width is determined either by fitting a Gaussian error function or taking the distance from the 10% to the 90% point of the edge. This method only assesses the resolution at the single point in the image in a single direction. If the edge in the object is not a perfect step function, the image resolution is underestimated.

2.3.3.3 Fourier methods

There are several methods that use the Fourier space to estimate the resolution.

An upper bound of the resolution estimate is given by the signal-to-noise ratio (SNR) of the diffraction signal on the detector and thus by the effective numerical aperture (see section 2.3.1). In order to evaluate the SNR correctly, the detector images have to be binned to match the size of the diffraction speckles [48].

The Phase Retrieval Transfer Function (PRTF) correlates the measured diffraction patterns $I_i(\mathbf{q})$ with the intensity of the modeled wave $|\Psi(\mathbf{q})|^2$ [38, 49]. This is a measure of how well the phase retrieval algorithm is capable of reproducing the signal collected on the detector, but not necessarily of how well the object is reconstructed.

A general method of resolution estimation in conventional microscopy is the Power Spectrum Density (PSD) in which the amplitudes of the Fourier transform of the reconstructed object are regarded [50]. This method assumes that the resolution of the object is limited by white, uncorrelated noise in the pixels of the image. For ptychography such an assumption does not hold in the general case as the results presented in chapter 7 show.

2.3.3.4 Fourier ring correlation

The Fourier ring correlation (FRC) estimates the global average resolution by evaluating the similarity of two images of the same object in Fourier space [51]. Taking the complex Fourier transformations $F_1(\mathbf{k})$ and $F_2(\mathbf{k})$ of the images, the correlation is

$$\text{FRC}_{12}(k) = \frac{\sum_{|\mathbf{k}'|=k} [F_1(\mathbf{k}') \cdot \overline{F_2(\mathbf{k}')}] }{\sqrt{\sum_{|\mathbf{k}'|=k} |F_1(\mathbf{k}')|^2 \cdot \sum_{|\mathbf{k}'|=k} |F_2(\mathbf{k}')|^2}}. \quad (2.13)$$

The calculation of this correlation function may be simple, but the choice of the cut-off threshold is not. If two independent measurements are correlated, the one-bit criterion is used, i.e. the threshold is set at 1/3. If only a single measurement is available, the data set can be split (e.g. into odd and even numbered diffraction patterns) and the less conservative half-bit criterion is used with a threshold at $\text{FRC} = 0.1716$.¹¹ The validity of these thresholds is still under discussion in the literature [52, 53].

The FRC evaluations in this thesis are computed with a program written by Maik Kahnt that is based on the algorithm presented in [54]. The evaluations of split data sets in chapters 7 and 8 were performed by first reconstructing the full data set of a scan with position refinement. Afterwards, the scan is divided into even and odd-numbered scan positions. As all evaluated scans have an odd number of positions per line, this results in a checkerboard pattern for the positions of the divided scans. Both divided data sets are then reconstructed again from empty probe and object fields, but using the refined positions of the full data set reconstruction. These positions are not further refined during the reconstruction of the divided data sets.

¹¹The thresholds stated are only valid far from $k = 0$, the shape of the cut-off curve is defined in [51].

2.4 Summary

We have seen that ptychography is a combination of scanning microscopy with coherent imaging in which the objective lens is replaced with a virtual lens and a phase retrieval algorithm. This reconstruction algorithm does not require prior knowledge of neither the probe beam nor the object and reconstructs both of them in modulus and phase. The achievable lateral and axial resolution is not limited by the size of the probe beam, instead, the effective numerical aperture defined by the scattering signal on the detector has to be regarded. Several competing methods exist to estimate the achieved resolution.

Ptychography works under strong model assumptions that are not always fulfilled in experiments. To this end, several modifications of the phase retrieval algorithms have been introduced that take thick samples, large probes, displacement errors, intensity fluctuations and partial coherence into account.

Chapter 3

Instrumentation

In this chapter we describe the scientific instrumentation that is required to perform high resolution hard x-ray ptychography, taking the storage ring PETRA III, the beamline P06 and the instrument PtyNAMi as the examples.

3.1 Beamline P06 at PETRA III

3.1.1 PETRA

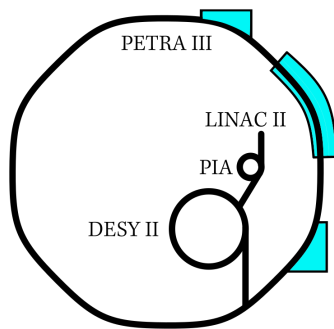
The particle accelerator PETRA was built in the 1970s as an experiment in high energy physics. The circumference of 2.3 km made PETRA the largest accelerator ring worldwide at the time [55]. In 1979, the Gluon was discovered here in three-jet events of electron-positron collisions [56].

A decade later the storage ring was remodeled into the PETRA II ring, a preaccelerator for electrons, positrons and protons for HERA. In 1995, the first undulator was placed into PETRA II, marking the beginning of photon science at PETRA [57]. When HERA was shutdown in 2007, PETRA was remodeled again into the dedicated synchrotron radiation source PETRA III; the operation started in 2009.

Figure 3.1 depicts the electron accelerator chain and a few key parameters of the storage ring. At first, the electrons emitted by the electron gun are preaccelerated with the LINAC II. The PIA ring was primarily used to accumulate a sufficient number of converted positrons and can be bypassed today. The electrons are then guided into the synchrotron DESY II where they are accelerated to the final energy of 6 GeV.

The electron bunches are then transferred to the PETRA III ring where they are stored to produce synchrotron radiation. As PETRA III supports top-up operation, a single electron bunch in the storage ring can be refilled without dumping the entire ring. In this manner, fluctuations of the beam current are limited to 1 %.

As PETRA III reuses the ring structure of former high energy experiments, it has the largest circumference of any synchrotron radiation source in the world by a wide



PETRA III Parameters

Electron Energy	6 GeV
Current	100 mA
Circumference	2304 m
Number of bunches	40 - 960
Horizontal emittance	1300 pm rad
Vertical emittance	10 pm rad

Figure 3.1: The electron acceleration path from the linear accelerator to the synchrotron DESY II and the storage ring PETRA III, with the key parameters of the storage ring [3, p. 24].

margin. In combination with the moderately high electron energy of 6 GeV, PETRA III is the most brilliant synchrotron light source of the third generation in the hard x-ray regime [37]. These characteristics of the storage ring are essential for coherent imaging in the hard x-ray regime.

However, there remains a strong asymmetry between the horizontal and vertical size of the electron bunches. In consequence, a large fraction of the x-ray beam cannot be used in coherent and scanning microscopy applications. Fourth generation synchrotron sources solve this problem by installing a refined lattice structure using multi-bend achromats to focus the electron bunch more strongly, thereby increasing the usable fraction of the beam by two orders of magnitude in such applications [58]. The new storage rings of the fourth generation, MAX-IV [59] and ESRF-EBS [60], have already surpassed PETRA III in recent years. The PETRA IV project at DESY aims to install such a lattice structure in the PETRA storage ring within the 2020s.

3.1.2 Beamline P06

The Hard X-ray Micro-Probe and Nano-Probe Beamline P06 is located in a central position in the Max-von-Laue hall, the main experimental hall at PETRA III. The beamline shares a sector with the beamline P05; this is achieved by having two independent undulators of 2 m length each with a canting angle of 5 mrad between them [61]. Within this shared sector, P06 has its optics hutch immediately behind the frontend. Downstream of the optics hutch the beam propagates freely for 42 m since the space is entirely occupied by P05 hutches. The micro-probe and nano-probe hutches are then located at the far end of the beamline.

A sketch of the beamline layout with all functional components is shown in figure 3.2. In the following, a short description of each of these components is given. The beamline is also described in more detail in [19, 61, 62].

3.1.2.1 Frontend

In the front end, the x-ray beam is emitted by the electron beam inside the undulator. The detailed physics of this process is documented in literature [4, ch. 2]. A dipole

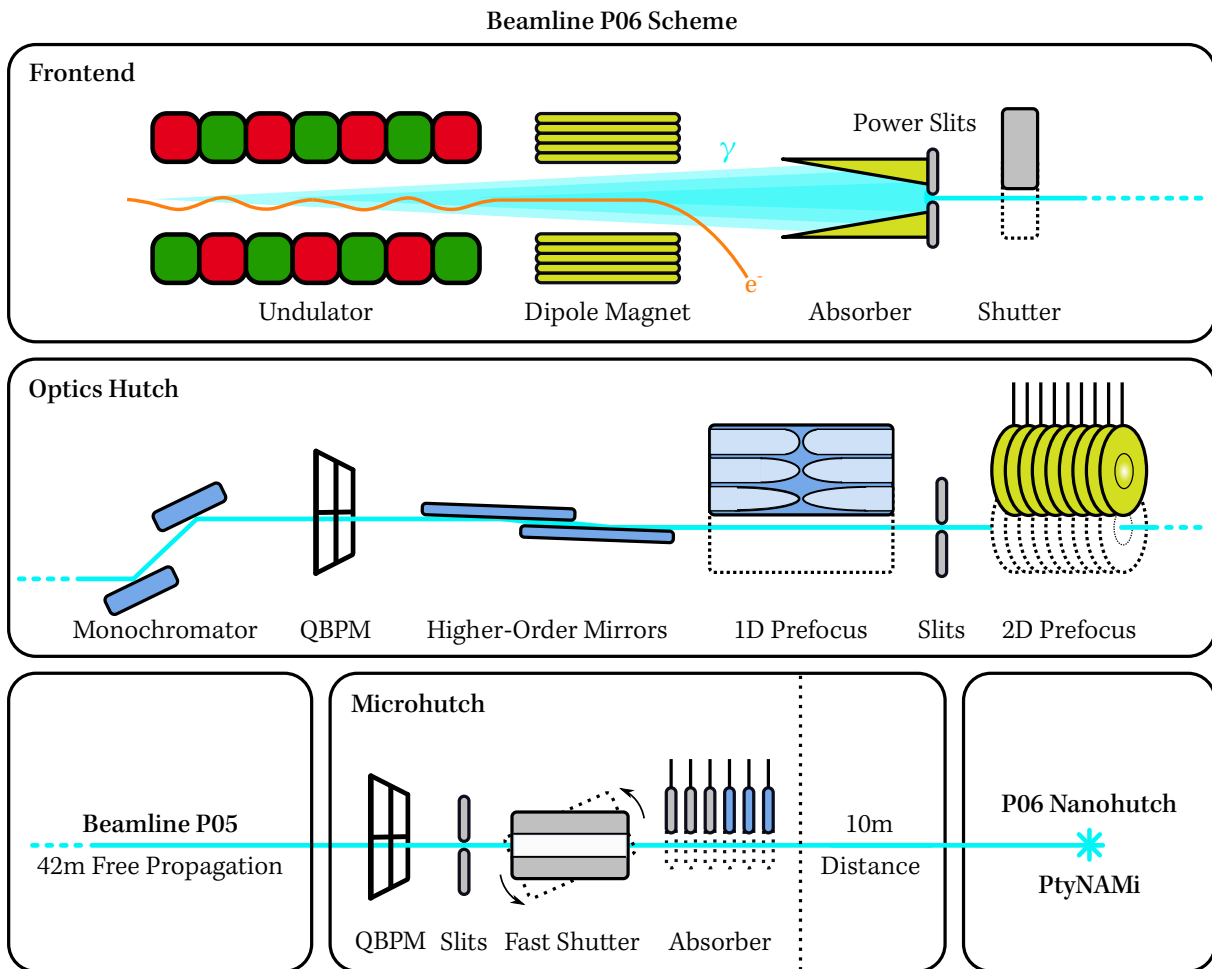


Figure 3.2: Schematic of components in the P06 beamline. The schematic is simplified, not to scale and mixes top and side view. Retractable alignment screens are omitted completely.

magnet is used to separate electron and x-ray beam.

The overall power of electromagnetic radiation emitted in the undulator is in the order of kilowatts [63, p. 214]. For radiation safety, the photons outside the central cone are immediately absorbed by water-cooled copper absorbers and tungsten slits. Finally, there is a vacuum and beam shutter to separate the frontend from the rest of the photon beamline.

3.1.2.2 Optics Hutch

The first element in the optics hutch is the monochromator which uses two silicon crystals to reflect a specific wavelength, and higher orders of it, via a 111 Bragg reflection. The selected x-ray energy can be changed by rotating the crystal pair. As all wave lengths that are not reflected are absorbed, the monochromator has to be cooled with liquid nitrogen.

The monochromators are available in two variants, installed next to each other: As a double-crystal monochromator (DCM) in which two separate crystals have individual degrees of freedom and as a channel-cut (CC) in which both reflecting crystal surfaces are manufactured into the same piece of silicon.

The DCM can use the additional degrees of freedom to adapt the gap between the crystal surfaces, keeping the beam height constant when changing the photon energy. On the CC the beam height depends on the selected photon energy, but the reduced complexity of the mechanics reduces vertical beam vibrations.¹ Additionally, the DCM can serve a wider energy range between 2.4 keV and 50 keV, while CC is limited to a range from 6 keV to 18 keV due to the geometry of the channel cut into the crystal.

Using a monochromator is mandatory to maintain radiation-safe operation of the beamline. The following elements in the optics hutch are optional and can be inserted and retracted from the beam as needed.

The next device is a quadrant beam position monitor (QBPM). This device consists of a thin nickel or titanium foil in the beam and four large area photon diodes around it to detect x-ray fluorescence photons. From the ratio of the four signals, the center of mass of the beam in the transversal plane can be estimated [64]. In combination with a second QBPM in the micro hutch, the pointing of the beam can be monitored.

Downstream of the monochromator, the beam can still contain higher orders of the photon energy. These can be filtered with a pair of flat silicon mirrors. As the critical angle of total reflection decreases with higher photon energy, the mirrors are aligned such that the order of the target photon energy (i.e. the first undulator order up to 9 keV and the third order above) is totally reflected, but higher orders are not. The mirrors have regions on them coated with chromium and platinum as well as a bare silicon region to provide different low-pass energy cut-offs. At a reflection angle of 2.5 mrad, the cut-off energies at 12 keV, 20 keV and 30 keV.

The next two components are both used for prefocusing. Prefocusing is a powerful tool that can be used to balance coherence and photon flux at the experimental endstation. For experiments that require flux but not coherence, such as XRF, the beam can be prefocused onto the aperture of the focusing optics in the experimental hutch. In the other case, when the degree of coherence on a given aperture needs to be increased, the beam can be strongly prefocused to generate a secondary source, thereby reducing the flux density, but increasing the transversal coherence length [61].

Since the emittance of the storage ring is much smaller in the vertical direction, a set of 1D focusing cylinder lenses can be used to symmetrize the coherence volume at the endstation, resulting in additional photon flux without significant loss in coherence. Additionally, a set of lens interferometers can be inserted at this position to measure the source size [65, 66].

Uniform two-dimensional prefocusing is enabled by a transfocator equipped with beryllium lenses [67]. This device holds six cartridges with sets of rotationally symmetric parabolic lenses that can be individually inserted into the beam. The wide variety of possible lens combinations covers a large energy range and experimental scenarios.

¹More details of the monochromator vibrations are presented in the appendix A.

A set of horizontal and vertical slits complete the components in the optics hutch. Thereafter, the beamline P05 is set up, so that the beam cannot be further manipulated for the next 42 m of propagation distance.

3.1.2.3 Microhutch

At the entrance of the microhutch we find the second QBPM that is necessary to obtain information about the pointing, i.e. the angular alignment of the beam. Immediately behind the QBPM another pair of slits are located.

The fastshutter is used to block the x-ray beam from entering the experiment between data acquisition periods, in particular when moving the sample to the next scan position in step scanning mode. This measure to minimize beam damage is important as the experimental results in chapter 8 will show.

The final component before the PtyNAMi setup in the nanohutch is a set of attenuators made of silicon and aluminium filters. Beam attenuation is primarily used during alignment to avoid damaging components with the intense direct beam.

Downstream of the attenuators the micro-probe setup is situated. The components of this setup are removed from the beam path when the nano probe is in operation. The PtyNAMi setup is located in the nanohutch after another 10 m of free propagation.

3.2 PtyNAMi in the P06 nanoprobe endstation

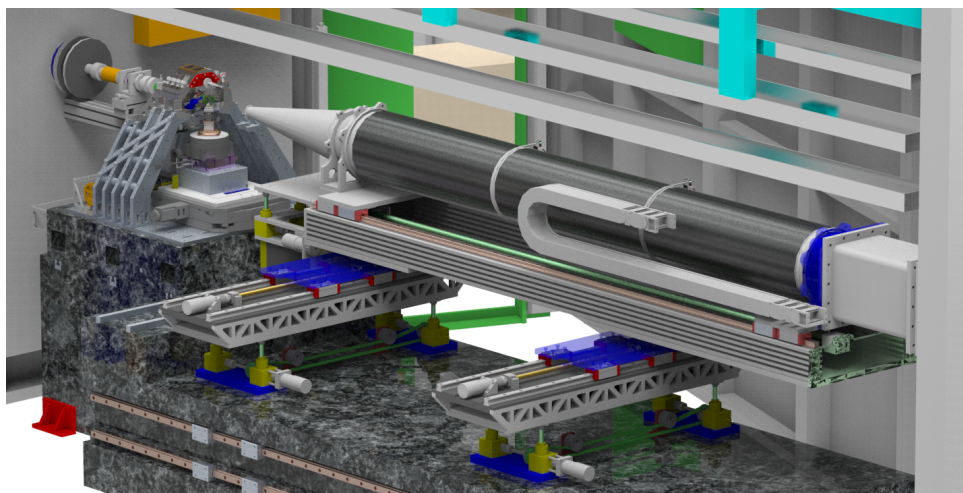
The Ptychographic Nano-Analytical Microscope (PtyNAMi) is the upgraded nanoprobe setup at the P06 beamline. Its primary advantages over the previous setup are increased mechanical stability, monitored by laser-interferometry, the windowless in-vacuum area detector, a dedicated bench for near detectors and a more convenient and flexible alignment of the x-ray optics.

3.2.1 Mechanical design

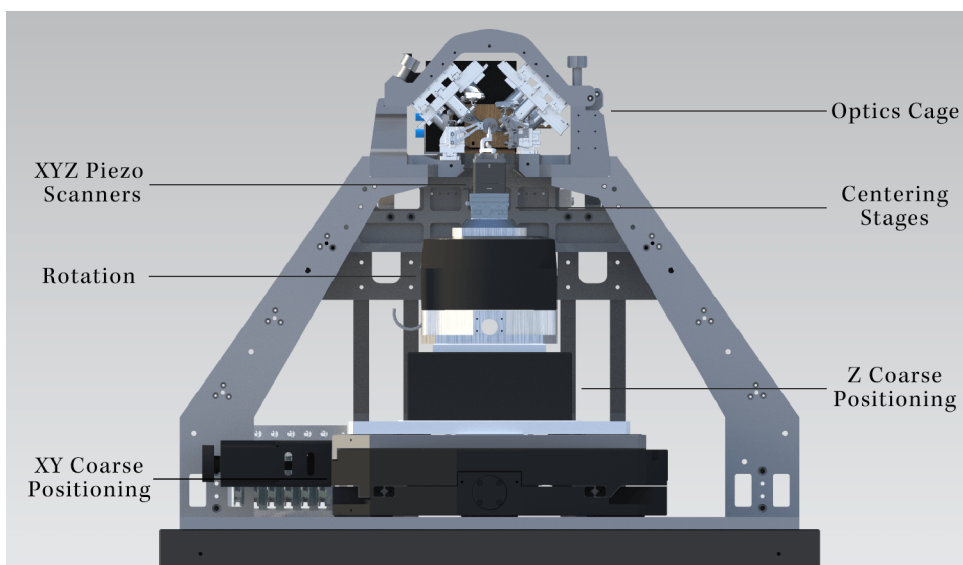
Figure 3.3 shows CAD renderings of the setup. As can be seen in fig. 3.3a, the setup is built on two separate granite blocks. The first and smaller block holds the scanner unit that comprises the x-ray optics and the sample positioning stages; the larger, second block, situated downstream of the first, supports the detector device. An additional fluorescence detector that is not shown here can be mounted on separate table next to the scanner unit.

3.2.1.1 Tomography sample positioning tower

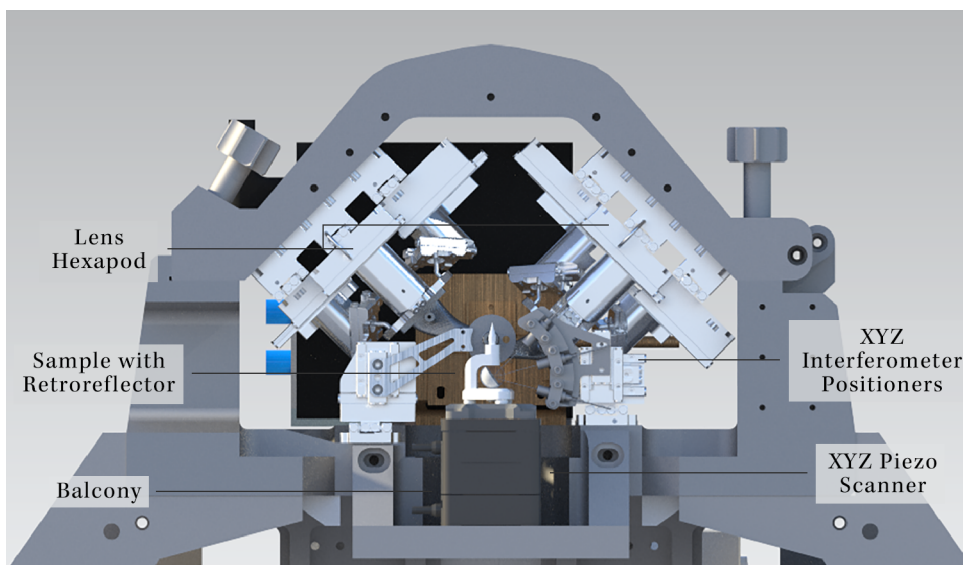
The rendering in fig. 3.3b shows the microscope in a configuration for tomographic measurements. A tower of sample positioning stages is mounted on the base plate. The x-ray optics and laser-interferometric references are mounted in a cage machined from



(a) Overview of PtyNAMi



(b) Tomography configuration



(c) Ultra-stable 2D configuration

Figure 3.3: Components of PtyNAMi a) Overview of the setup without near detectors and off-axis detector. b) Sample tower for 3D measurements including coarse alignment and rotation stages. c) Ultra-stable setup for 2D measurements directly attached to lens cage. Rendering: a) Ralph Döhrmann b,c) Stephan Botta.

Invar.² This lens cage is lifted to the sample height by a frame of titanium profiles.

Starting from the bottom of the sample tower, the three coarse translational degrees of freedom, realized with stepper motors, move the rotation axis into the x-ray focus. The air-bearing rotation stage is mounted on top.

As the center of the sample volume has to coincide with the rotation axis within sub-micrometer precision, a pair of piezo-electric slip-stick stages are placed on top of the rotation stage to align the sample to the rotation axis. During data taking, the feedback loop of these centering stages are turned off to reduce vibrations.

On the top of the tower we find the three piezo-electric translation stages that are used to scan the sample. The minimal repeatable step size of these stages is in the single nanometer range, but the travel range is limited to 100 μm for each direction. In total, we count nine stages in the tower and there is no motorized goniometer.

3.2.1.2 Ultra-stable 2D setup

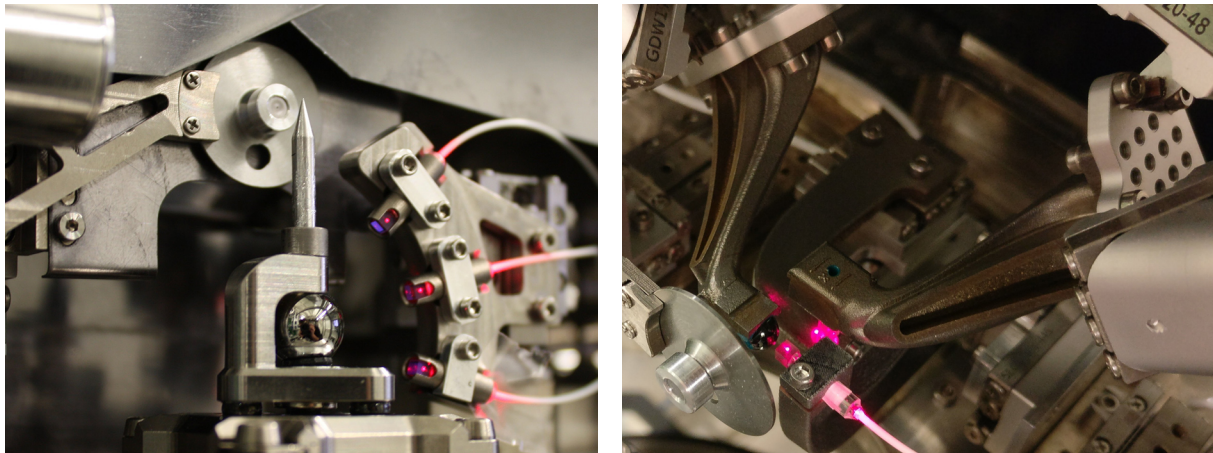
An alternative setup for 2D measurements at increased stability is shown in figure 3.3c. Here, the coarse translation stages as well as the rotation and the centering stages are omitted; the sample scanner is instead directly mounted to the lens cage. In consequence, the sample cannot be rotated any more. As there are no stepper motors for coarse alignment, once a sample is mounted, a region of interest on the sample can only be chosen within the 100 μm travel range of the piezo scanners.

Different regions on the sample can only be reached by manually remounting the sample. The sample pin can be screwed at different heights into the holder, and elongated holes permit the piezo scanner to be mounted at different horizontal positions relative to the lens cage. Given these difficulties to find a specific region on the sample, this setup is mostly suitable for large and flat samples on which one region is as interesting as another, e.g. nanoparticles on a substrate or a periodically repeating semiconductor.

As much as this configuration is limiting and time-consuming it gains in mechanical stability. Whereas on the tomography tower typical horizontal vibrations are 10 nm rms, this ultra-stable setup is an order of magnitude better at 1 nm rms.

Independent of the configuration, samples are mounted on pins of 3 mm diameter. This mount, including the ball lens retroreflector underneath, is shown in figure 3.4a. The working principle of the ball lens and the laser-interferometer on the right-hand side of it are described in chapter 5.

²Invar is the trademark name of a low thermal expansion nickel-iron alloy. It was discovered by Charles Édouard Guillaume, who received the Nobel Prize in physics in 1920 [68, p. 122].



(a) Sample position with interferometers

(b) Lens interferometers

Figure 3.4: Laser-interferometers in PtyNAMi a) Sample position with ball lens and sample interferometers. b) X-ray focusing optics on 3D-printed titanium mounts with lens interferometers. Photographs by Maik Kahnt.

3.2.1.3 Lens cage

Upstream of the sample position, inside the lens cage, the x-ray optics are located as shown in the photograph 3.4b. A large variety of refractive and diffractive focusing optics can be mounted on the slip-stick driven hexapods that are hanging under 45° from the ceiling of the lens cage. With the hexapod stages, the focusing optics can be aligned in all six degrees of freedom with micrometer precision.

In order to accommodate different geometries and focal distances, the x-ray optics are mounted on 3D-printed arms made of titanium. These arms are individually designed for every x-ray optical element and can also accommodate ball lens retroreflectors.

Interferometers designed to measure the vibration of the x-ray nanofocusing optics are mounted on the bottom of the lens cage and positioned with a stack of linear slip-stick stages. Similar to the x-ray optics, the interferometer optics are also mounted on 3D-printed titanium parts. These lens interferometers are considered optional and are not always installed due to space limitations.

3.2.2 X-ray optical design

In figure 3.2 we have seen how the x-ray beam is transported and conditioned in the beamline. Figure 3.5 shows how the beam is further manipulated inside the x-ray microscope. The details of this configuration depend on the type of focusing optics used, here a setup of Fresnel Zone Plates (FZPs), that were used for the high resolution measurements presented in chapter 7, is shown.

3.2.2.1 I_0 monitoring

After the x-ray beam exits the beamline vacuum and enters the PtyNAMi setup in air, its intensity is measured with an ionization chamber. In such a chamber, x-ray photons

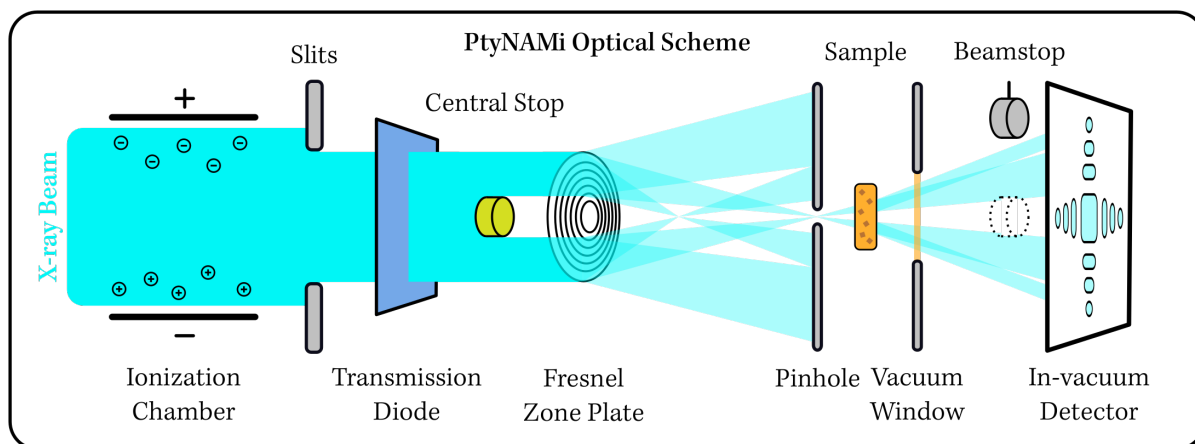


Figure 3.5: Schematic (not to scale) of the optical components in the PtyNAMi setup for a ptychography configuration using FZPs.

ionize molecules of the filling gas, the resulting free charge carriers are collected with an electric potential. The electric current is then measured by an amperemeter.

In the next step, the beam is confined to the aperture of the focusing optics using a slit system. Keeping the beam clean by absorbing any rays that are not going through the microscope optics is essential; any stray radiation in the instrument contributes to additional background noise on the detectors, deteriorating the quality of the experimental results.

Downstream of the aperture slits, the beam intensity is measured again with a transmission diode. This is necessary as the ratio of intensity in the complete beam to the intensity on the aperture may change, in particular in the case of drifts of components in the optics hutch.

3.2.2.2 Focusing optics

At this point, the details of the setup diverge depending on the type of focusing optics employed.

When using FZPs there are multiple orders of diffraction of which all but the primary one have to be absorbed [9, pp. 216-230]. This is achieved by having a small pinhole of 30 μm diameter close to the focus of the primary order. In this configuration, the pinhole is also referred to as the Order Sorting Aperture (OSA).

However, there is still the zero-order beam, i.e. photons that are not diffracted by the zone plate, that can pass the pinhole in large quantities. A central stop of least the size of the pinhole has to be aligned in front of the zone plate to block this unwanted radiation.

In configurations with Nano-Focusing Lenses,³ the central stop and zone plate are

³The term Nano-Focusing Lens (NFL) refers to one-dimensionally focusing cylinder lenses that are etched into a substrate, most commonly silicon [69]. The term does not refer to all types of optics generating a nano-focus in general.

replaced by the horizontally and vertically focusing lenses, respectively. The pinhole remains in place, but is not called OSA in this configuration.

With Multilayer Laue Lenses (MLLs), the horizontal and vertical lenses can either be preassembled on a single substrate [70] or mounted individually on both hexapods [71]. As MLLs can reach extremely short working distances (< 1 mm), it can be impossible to place the OSA in the focus. In this situation, an L-shaped wedge is used to absorb unwanted orders further downstream.

The sample is placed downstream of the pinhole. When x-ray fluorescence is measured simultaneously with ptychography, a silicon drift detector [72] is placed orthogonal to the beam at the sample position.

3.2.2.3 Detector device

Downstream of the sample, the detector device is situated on a second granite. The detector device comprises an evacuated flight tube, a bench of near detectors and a platform for an off-axis Bragg detector.

For ptychography experiments, the scattered beam directly enters the vacuum of the flight tube. After a propagation distance of about 3.5 m, the beam reaches the photon-counting area detector without passing through any additional windows. An optional beamstop can be employed to absorb the central part of the beam. These components are discussed in detail in chapter 6.

The near detector bench houses two optical microscopes that are primarily used for the alignment of the x-ray microscope as well as space to mount an area detector close to the sample position for WAXS measurements. The separate near detector bench allows these detectors to be moved in and out the beam without entering the hutch.

The first microscope is a visible light microscope that looks upstream on the sample position. It is useful to mark the beam position when changing the sample and aligning the center of rotation for tomography. When working with focusing optics with extremely short working distances, its short depth of field can also be used to position optical elements along the beam axis correctly.

The second microscope consists of a thin scintillator screen and an attached visible light microscope. A revolver mechanism allows to choose between three scintillators and three matched objectives. This microscope is used to observe the flat beam, in particular when aligning the x-ray optics. When PtyNAMi is reconfigured as a full-field microscope it can also be used as the primary detector.

3.2.3 Summary

PtyNAMi is a fairly flexible experiment that offers a variety of optics in different energy ranges, several options for sample mounts and environments and a pool of detectors that can be positioned with some freedom. The possibility to use several detectors in

parallel makes PtyNAMi particularly attractive for multi-modal measurements; the possibility to mount focusing optics on custom 3d-printed mounts on hexapods enables the characterization and development of various types of x-ray optics.

A challenge in the design of PtyNAMi was the combination of this flexibility with the high demands on stability. To this end, laser-interferometers were added to the setup as a permanent installation and a specialized ultra-stable mode was envisioned.

Chapter 4

In situ cell for ptychography in heated solution

Several experiments have been reported in literature that performed ptychography under cryogenic conditions [73] or under gaseous reagents [74] as well as in magnetic fields [75]. In this chapter, we describe a novel in situ cell designed to image with hard x-ray ptychography the nucleation and growth of nanoparticles in a heated solution.

The project to build such a cell was headed by Lukas Grote working in the group of Dorota Koziej and received strong engineering support from Ralph Döhrmann. In the design phase of the cell, my own contributions were limited to advice on design aspects that would optimize the performance in the x-ray microscope. During the experiments at the beamline, I conducted and evaluated the imaging experiment while Lukas and his team handled the chemical aspects of the experiment.

4.1 Sample System

The chemical synthesis of interest is based on the precursor copper acetylacetonate dissolved in benzyl alcohol. Under pressure-tight conditions, the solution is heated to 155 °C to initiate the reaction. In the time frame of hours, the nucleation and growth of Cu₂O cubes occur (see fig. 4.1a). These nanocubes form on the walls of the container and on a kapton substrate placed in the solution.

The growth continues until cube sizes between 200 nm and 500 nm are reached. At this point, the Cu₂O reduces to metallic copper; in the same process the cubic particles are getting rounded. In the final hours of the synthesis, the particles are fusing together until they form a homogeneous copper foil (fig. 4.1c).

The reaction pathway as described above was determined by lab experiments and scanning electron microscopy (SEM) as well as non-imaging diffraction and spectroscopy synchrotron experiments [76, 77]. As we will see in chapter 8, the reactions observed during the in situ imaging experiments grew Cu₂O cubes of the expected size

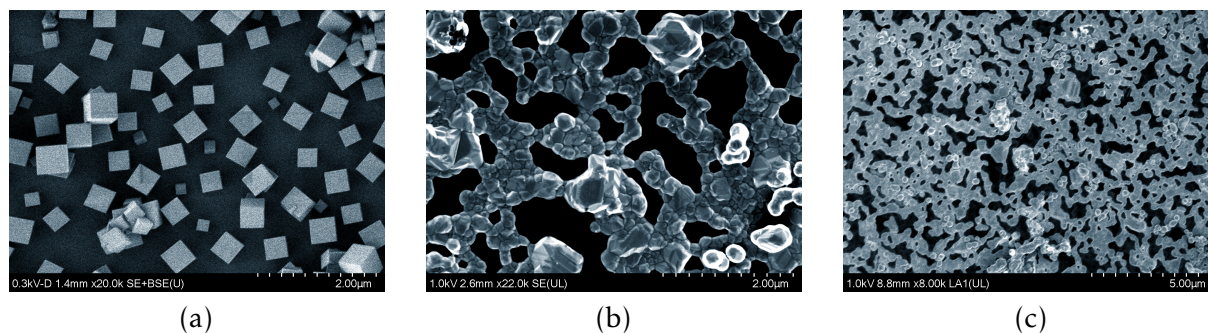


Figure 4.1: SEM images of expected reaction obtained by aborting synthesis after a given run time. a) Synthesized at 180 °C for 40 min. b,c) Synthesized at 140 °C for 73 h in a large volume container. The difference in temperature lead to reaction times different to those mentioned in the main text. SEM images by Lukas Grote.

but then took a completely different path.

This sample system offered three distinct advantages that made it the preferred choice for a first attempt of ptychography in solution:

1. The reaction takes place in a suitable time frame. On the one hand, recording a single ptychographic scan, i.e. one frame in the time series, takes several minutes. On the other hand, synchrotron beamtime is usually limited to a few days. As such, a reaction time of a few hours is ideal and we were able to average one run per day of beamtime including overheads.
2. The Cu_2O cubes grow to relatively large sizes, have sharp edges and often lie flat on the substrate. These factors lead to an overall strong scattering signal. As the scattering background introduced by the solution in the beam path was unknown, a strong signal from the sample was beneficial.
3. The reaction has the interesting property that a change of oxidation state is expected to be directly linked to a change of the morphology of the particles. Ptychography can directly determine the morphology; the reconstructed projection of the electron density gives an indication of the oxidation state. Complementary WAXS signals can be acquired simultaneously for confirmation.¹

4.2 Design and requirements

4.2.1 Requirements

One of the major challenges during the design of the enclosure was the observation that the reaction requires a minimum volume of about 1 mL; smaller volumes could take a different reaction pathway. For this reason, it was not possible to adapt miniaturized chip-based liquid containers which are commercially available for liquid phase

¹In the measurements presented here no WAXS signal was acquired, but the feasibility has been recently demonstrated.

transmission electron microscopy (LPTEM) [78] as their volume is in the nanoliter range.

From considerations of the absorption in the relevant energy range² and the divergence of the beam (the probe must be sufficiently small on both walls of the container, see section 2.2.2), the design goal was set for a maximum of 1 mm of solution in the x-ray path between the entrance and the exit windows of the container. Consequently, the reactor had to be thin along the beam axis but extended laterally to the beam. To withstand the elevated pressure inside the sealed reactor, and assure a homogeneous temperature distribution, the reactor has to be enclosed in a metal housing.

As the sample volume and its entire enclosure has to be heated to 155 °C for extended periods of time, a heat isolation base has to be included in the design. According to the manufacturer of the piezo scanner, the piezo-electric properties are irreversibly altered at 80 °C and "approaching this [temperature] can cause serious detrimental effects to the accuracy and performance of the piezo stage" [79]. Therefore, the design goal was set that the base temperature should never exceed 50 °C.

Additional factors to take into account are mass and thermal expansion. Heavy loads, in particular with an elevated center of mass, lead to increased motion dead time when step scanning. We initially calculated up to 500 nm thermal drifts for a titanium construction being heated by a PID-controller of 1 °C stability, but the heater turned out to be an order of magnitude more stable.

4.2.2 Design

The components and assembly of the in situ cell is shown in figure fig. 4.2. The inner frame around the reaction volume (4.2a) is made of Invar. The top of the frame has a small recess that fits a glass capillary for filling the cell. The windows for the cell are cut from 125 µm thick kapton sheets; a PTFE frame is sandwiched between them. In this manner, the reagents inside the cell only contact kapton, PTFE and the glass capillary; they do not contact the metal surfaces. The assembled and filled reaction chamber is shown in fig. 4.2b.

The inner reaction container has to be filled and sealed in an inert gas atmosphere to avoid the inclusion of water and oxygen. The containers were prepared under argon in the labs of the Center for Hybrid Nanostructures (CHyN) situated in the vicinity of PETRA III. The remaining assembly can be done at the beamline.

The kapton windows are held in their shape by the heating covers that are also machined from Invar (fig. 4.2c). These heating covers have a convex parabolic profile, reducing the inner distance of the windows in the center to 1 mm.

A recess on one of the edges of the heating cover is shaped to accept a temperature

²The considered photon energy range was from 9 keV (resonant measurements on copper) to 18 keV.

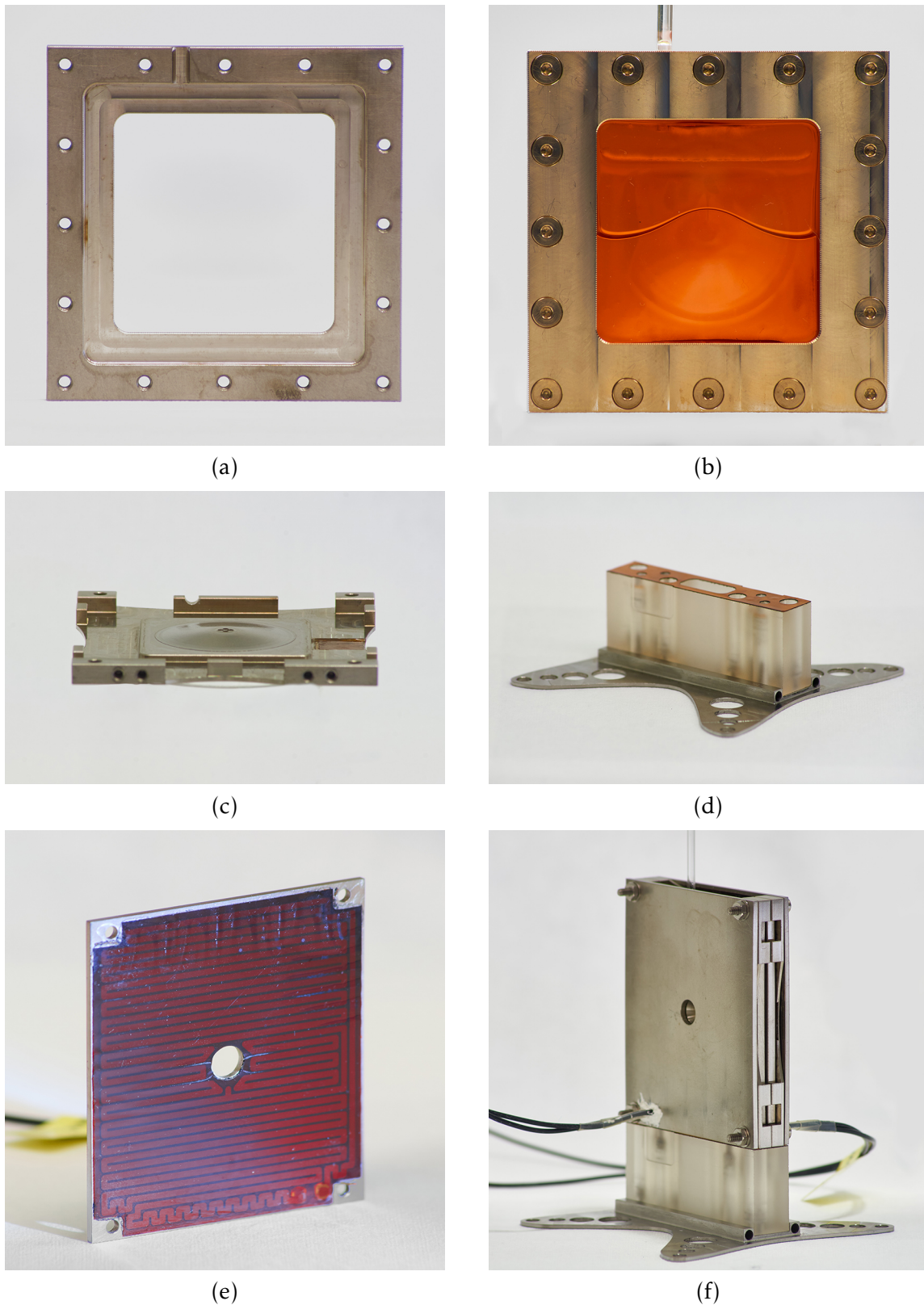


Figure 4.2: Components of the in situ cell for ptychography in solution. a) Innermost Invar frame. b) Assembled reaction chamber with kapton windows and glass capillary. c) Invar heating cover with parabolic profile. d) Zerodur isolating base. e) Kapton heating element on a titanium plate. f) Assembled in situ cell (without temperature probes and cooling gas tube).

probe connected to the PID-controller. The heating elements (fig. 4.2e) are directly attached to the heating covers. They consist of a custom-made copper spiral, embedded in kapton, that is attached to a plate of titanium. The heat isolation base is connected to the Invar heating cover and not to the heating elements, so that thermal expansion of the heating elements is uncritical and titanium can be used to save weight.

The thermal isolation of the heated components to the motor stack below is achieved by a block of Zerodur, a glass ceramic trademarked by Schott that embeds nanocrystals into a glass matrix [80]. Its key characteristic is an extremely low thermal expansion coefficient of $\alpha < 10^{-7} \text{K}^{-1}$ that mitigates thermal drifts. Zerodur is a moderately good heat insulator at $\lambda = 1.46 \text{W m}^{-1} \text{K}$. As this ceramic is brittle and can chip when in direct contact with metal, a piece of laser-cut kapton is used as a separator.

The Zerodur isolation block is screwed into a titanium base plate. The inclusion of a feed-through permits active cooling with a gas stream (fig. 4.2d). The effectiveness of the heat isolation and cooling measures can be monitored with a temperature probe on the base; with the active cooling the base temperature never exceeded 40 °C. The fully assembled in situ cell is shown in figure 4.2f.

4.2.3 Effects on the microscope

When designing this in situ cell, we had several concerns about aspects that may prevent us from obtaining the desired results:

First, we were concerned that the heat input into the microscope may lead to the x-ray optics drifting out of alignment. This problem never occurred in PtyNAMi and only to a minor degree during the experiments conducted at cSAXS at the Swiss Light Source.

Second, how well does the nanopositioning work with a sample environment that weighs about 220 g instead of the usual 35 g and has several cables and a tube attached? Preliminary testing with a dummy weight showed that the stability and accuracy of the nanopositioner is not impaired, but reaching the target position after moving a step takes about 100 ms longer. The cables and tubes had no detrimental effect when attached with strain relief to the microscope.

Third, how much background scattering is added by the additional 250 μm of kapton and 1 mm of organic solvent in the beam? We analyse this question in chapter 6; a moderate increase of the scattering background is observed there.

Chapter 5

Laser-interferometric position measurement

In this chapter we discuss the interferometric position and vibration measurement system extensively. Our discussion begins with the motivation to install such a system and a description of the hardware. Afterwards we will discuss the vibration measurements in detail and close with the major measurement error sources.

Some of the more mathematical discussions, that are probably not of interest for the majority of the readers, can be found in the appendices.

5.1 Motivation

In scanning microscopy in general, the local properties of the sample are probed with a focused beam. Many of such local measurements are then combined to display an image of the sample. In doing so, there are two major measurement errors that can occur:

- The position of the beam on the sample changes during the accumulation of signal, i.e. the sample and beam vibrate. In this case, the measured property is averaged over the total illuminated area. Sharp features in the sample are blurred and the spatial resolution of the image is reduced.
- The position of the beam on the sample is offset by an unknown amount. The signal may be accumulated from a single spot, but the displayed image shows artefacts since the signal cannot be attributed to the correct location. The resulting image may be rotated, stretched, sheared or generally distorted in more complicated manners.

As we will see on the following pages, the interferometer solution presented here deals well with the first point but solves the second challenge only partially.

Traditionally, imaging systems can be characterized by measuring known test patterns. From contrast variations, the module transfer function and with that the resolution of the system can be measured; distortions are visible in the images of regular grids [81, ch. 3]. The Siemens star (c.f. fig. 5.14) is a popular test patterns to quickly assess the resolution of a microscope.

In scanning x-ray microscopy, with its reliance on micromechanics to move the sample from point to point, the imaging artifacts are of a different kind. The image resolution is often not isotropic as the mechanical systems are stiffer in one direction than the other. Depending on the working principle of the positioning stage, more problems can arise, such as inconsistent performance over the available range or non-orthogonal motion.

These positioning errors can still be assessed with a test pattern such as the Siemens star: As it has sharp edges in all directions, anisotropic resolution is easily detectable (for an example see figure 5.14c). Missing steps will result in steps or jumps of the edges. Non-orthogonality leads to a distortion of the concentric rings.

However, there are more challenges remaining. As the image is not recorded at a single point in time, the image quality is rarely completely homogeneous within an image. The vibrations at the facility may change abruptly, e.g. as doors are shut and people walk by. The vibration background also changes in general, especially at a synchrotron facility where many user groups are permanently installing new setups.

As the sample has to move during scanning, the characteristics of the nano-positioning may change with the physical properties of the sample. It is unreasonable to characterize the performance of the scanning microscope with a light-weight test pattern when the measurement of the real sample is performed in a heavy liquid cell with multiple additional cables and tubes attached to it. Clearly, an external positioning reference is necessary in such a situation.

In ptychography, further challenges arise. The signal is not simply an integration over the illuminated area, it is a coherent diffraction pattern from which the real-space image has to be reconstructed by a non-linear algorithm. This can have both beneficial and detrimental effects.

On the one hand, small position deviations can be corrected algorithmically (see section 2.2.3). On the other hand, the algorithm can converge to a completely wrong solution, making the interpretation non-trivial, or it does not converge at all. In particular, distinguishing between positioning problems and beam stability problems can be challenging without adequate diagnostics.

For all of these reasons, it is not sufficient to characterize the vibration and motion of a scanning x-ray microscope once, instead, they have to be constantly monitored during the experiment. Laser-interferometry is the ideal tool for this purpose as it is completely contact-free and thereby not interfering with the mechanical system. At the same time,

the resolution of the distance measurement can be below a single nanometer, covering even the most demanding scanning x-ray microscopy applications in the foreseeable future.

As the position of the focused x-ray beam on the sample is not only determined by the motion of the sample but also of the focusing optics, such a system should also be capable of monitoring the x-ray focusing optics. In combination with the QBPMs in the beamline monitoring changes of the beam direction, every factor that contributes to a change of the focus position on the sample should ideally be accounted for.

Performing scanning microscopy without any external monitoring of the nanopositioning stages' motion essentially means to blindly trust one of the most critical components in the experimental setup.

5.2 Interferometer hardware

From the start of the project, it was clear that a commercial interferometry system had to be integrated into PtyNAMi. Building a custom system was not feasible given the lack of experience with visible light optics in the group and the requirement that the setup had to be operated by non-expert users.

5.2.1 Interferometer controllers

In the end, two different systems by two manufacturers¹ were used. Both use homodyne phase quadrature [82] with a laser wavelength of 1535 nm [83]. These systems are so similar that optical components can be freely exchanged between the systems.

Both systems consist of a controller unit that integrates a control computer with an FPGA, the laser source and detectors. The FPGA performs the quadrature demodulation at an internal frequency of 10 MHz, however, data cannot be streamed continuously via the USB or Ethernet interfaces at this rate. Stable data streaming² is possible at sampling rates up to 100 kHz. This is not a real-world limitation since all vibration frequencies ever observed in the setup were below 10 kHz.

5.2.2 Interferometer heads

The distance sensing optics, the interferometer heads, are attached via optical fibers to the control unit. These fibers can be tens of meters in length so that the controller unit

¹The two systems are the Attocube FPS3010 and the Smaract PicoScale. The FPS3010 is lacking a trigger input that is necessary to synchronize the position measurement with the rest of the beamline components, in particular for fast continuous scanning. The PicoScale gives the user access to the raw and corrected quadrature signal (see fig. 5.12, 5.13) that is valuable for debugging purposes. The FPS3010 has a better alignment mode with access to quantitative signal strength values.

²These high data rates, in combination with the advanced triggering system of the PicoScale, also permits to measure in a continuous motion with up to a kilohertz acquisition rate, enabling experiments that would otherwise simply take too long [84]. In this work, the rapidness of the data acquisition is not our primary concern.

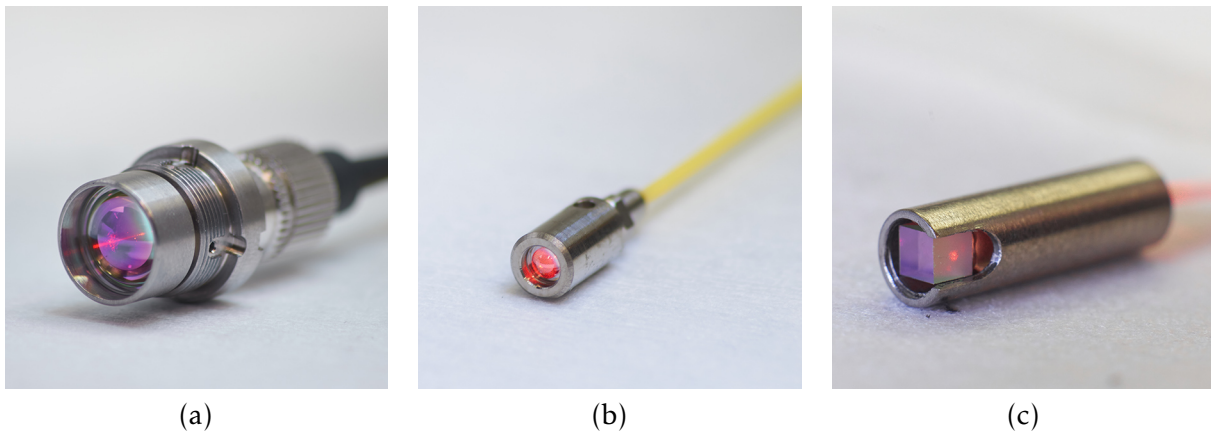


Figure 5.1: Interferometer heads, i.e. fiber exit optics of the interferometers. a) Large head with 14 mm diameter with collimating optics. b) Small head with 4 mm diameter and a focal length of nominally 8 mm. c) Collimating head of 4 mm diameter and beam splitter cube in the head. This type is used for regular operation in PtyNAMi.

can be placed outside the experimental hutch, eliminating a heat and vibration source in the hutch. As the reference path of the interferometer is integrated directly into the interferometer head, changes of the optical path length inside the optical fiber do not affect the measurement.

Three different types of these interferometer heads are shown in figure 5.1. Interferometer heads can be either focusing or collimating. Collimating heads can work in a wide range of distances from the reflector target whereas focusing heads also need to be aligned longitudinally, often with sub-millimeter precision [85]. On the flip side, collimating heads only have a small angular acceptance, often less than 0.1° [86] and therefore need a well-aligned mirror or a retroreflector as a target. Focusing heads can have angular acceptances of over 1° and can therefore also be used on convex reflective surfaces.

A hybrid of both types is a cylinder lens head which is focusing in one dimension and collimated in the other [87]. These specialized interferometer heads are built to measure rotating cylinder surfaces.

The heads installed in PtyNAMi are all collimating heads as in figure 5.1c. This type of head, with the openly visible beam splitter cube in the front, is in particular useful during alignment in tight spaces as the beam reflection is also visible from the side. For the lens interferometers, due to space constraints, this head is used without the protective titanium housing (c.f. fig. 3.4b).

5.3 Retroreflectors

Interferometric displacement measurements always measure the relative distance changes between the interferometer heads and a reflector target. Since the objects of interest, i.e. the sample and the focusing optics, are not reflective in general, a suitable reflector must be placed as close as possible to them. Any relative motion

between the reflector and sample will result in an immediate measurement error.

Plane mirrors or corner-cube retroreflectors made from plane mirror pieces can be used as targets for 2D-measurements, but in applications of 3D microscopy the sample with the attached reflector has to be rotated as well. For a complete tomogram, a rotation of 180° is required and within that range blind spots should be avoided. In some cases, such as fluorescence tomography with strong self absorption [88], a full rotation of 360° is needed. In general, there are also techniques such as SAXS tensor-tomography [89] that require tilting the rotation axis, but these cannot be performed at PtyNAMi as there is not tilting stage.³

A common approach to build a reflector for such applications is a large polished metal cylinder or a spherical equator disk on which the sample is mounted [90–93]. However, an alternative solution using ball lens retroreflectors was developed for PtyNAMi [10, 94]. There are advantages and disadvantages to both designs.

5.3.1 Ball lens retroreflectors

Ball lens retroreflectors consist of a homogeneous glass sphere with a refractive index as close as possible to $n = 2$. Such spheres can be bought as of-the-shelf components⁴ since they are used for coupling into optical fibers and the manufacturing of endoscopes.

For a ball lens of $n = 2$ in air with a refractive index $n \approx 1$, the focal length of the ball lens is equal to its diameter. In consequence, a parallel beam hitting the ball lens close to its center will be focused onto the backside of the glass-air interface of the sphere. This interface is orthogonal to the optical axis through the center of the sphere. The beam is therefore reflected back and emitted as a parallel beam again, i.e. the beam is retroreflected. Figure 5.2 shows the beam path inside a ball lens.

Since the ball lens is rotationally completely symmetric the retroreflection works from any orientation. However, this spherical shape has a disadvantage in that the ball lens is spherically aberrated. In consequence, beams coming in farther from the optical axes are increasingly poorly retroreflected.

In practice, the backside of the ball lens is coated with metal by sputter deposition⁵ to suppress transmission through the ball lens and enhance the reflected fraction. This limits the acceptance of the reflector to one hemisphere, a limitation that is not severe in application.

³While there is no motorized goniometer to tilt the sample and rotation axis an optional wedge can be used to perform laminography.

⁴The ball lenses for this project were purchased from Edmund Optics and are manufactured from OHARA S-LAH79 glass with a refractive index of $n = 1.95518$ at $\lambda = 1550\text{nm}$ [95]. It is beneficial to have the refractive index deviate from $n = 2$ in the negative direction as it negates the spherical aberration partially [10].

⁵The coating materials gold, silver and chromium were tested. There was not a notable difference in signal strength, but chromium adheres best to the glass and is therefore more scratch-resistant.

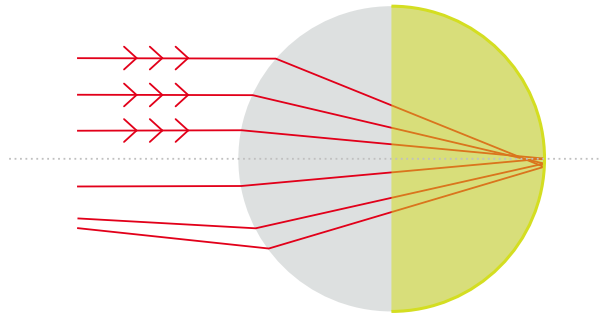


Figure 5.2: Ray optics simulation of retroreflection in a ball lens with $n = 2$. Three parallel beams are entering the ball lens in the top half and are focused to the backside of the ball lens. The reflective metallic coating is indicated in yellow. The innermost beam is reflected nearly parallel, while the outer beams experience spherical aberration. Simulation with [96], image first published in [10].

The spherical aberration of the lens together with the offset of the reflected beam limit the acceptance range of the retroreflector. The transversal working range in which the target can be moved without realignment further depends on the type, size and distance of the interferometer heads. As the signal degradation is a continuous process, the effective acceptance area also depends on the signal quality one is willing to accept.

Early tests under ideal conditions, i.e. with the large interferometer head of fig. 5.1a in close vicinity, have shown that about 10 % of the ball lens diameter can be used before the signal becomes so weak that the signal evaluation fails. In PtyNAMI, smaller interferometer heads are used with a longer working distance. Furthermore, measuring with weak signals on the detection threshold is not recommended, so that for a ball lens with a 1 cm diameter a few hundred micrometers of usable measuring range remain.

5.3.2 Measuring geometry

A single interferometer head is not sufficient to track the motion of the sample in two or three dimensions. Several interferometer beams have to be used, and these beams must intersect in the center of the ball lens. When the interferometer beams are not perfectly aligned, the experimentally usable area shrinks to the overlap of the individual acceptance areas.

Mounting the interferometer heads with the necessary tolerances can be challenging, often paper shims or adhesive tape has to be used to correct for angular deviations (compare lowest interferometer in fig. 3.4a). A reproducible alignment device using flexure hinges was developed by Mirko Landmann [97] but has not been tested yet.

There are several possible configurations of the coated ball lens and the interferometer axes around it (fig. 5.3, also [10, p. 39]). Mathematically, an arbitrary small opening angle between two interferometer axes is sufficient to calculate the motion of the target in a two-dimensional plane, but in a real experiment with measurement uncertainties, the results are more precise when the two axes span a wider angle, ideally 90° . The available space at the sample position does not allow this ideal configuration.

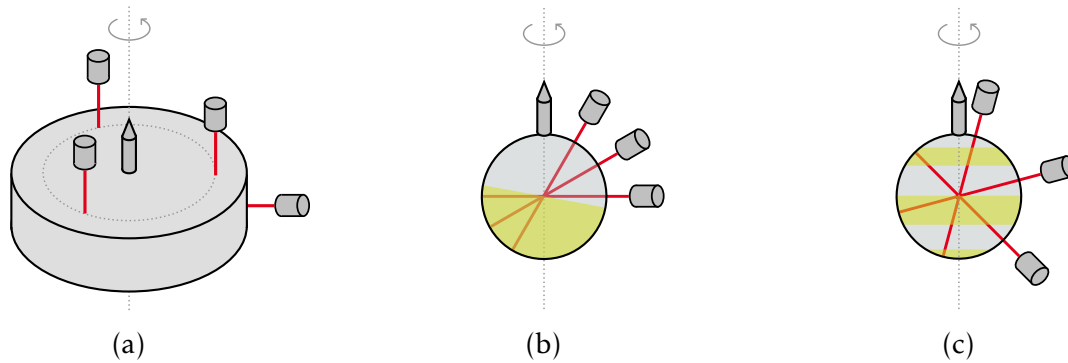


Figure 5.3: Geometries of interferometer beams and reflectors for tomography measurements. a) A large, polished metal cylinder. Interferometers measure the vertical motion on several point on the cylinder face, the horizontal motion is measured on the curved cylinder surface. b) Retroreflective ball lens with one hemisphere coated with reflective material. c) Alternative ball lens design with stripped reflective coating that enables full rotation of the sample.

The final design consists of three interferometer axes with an opening angle of 30° between them, so that the outer axes span a total angle of 60° , see figure 5.3b. Having a third backup interferometer axis is important as the signal is sometimes lost or corrupted without apparent reason. The data pipeline implemented is such that the sample position is calculated three times separately for each pair of interferometer axes (bottom - top, bottom - mid and mid - top). The position calculated from the outer axes (bottom - top) is used as the default, but the positions calculated from two alternative combinations are always available as a backup.

Referring to figure 5.3b again, we can see that the equator between the coated and uncoated halves is tilted about 15° so that the bottom interferometer axis along the horizontal plane does not hit the edge of the coating. If the ball lens is rotated about $\pm 80^\circ$, the bottom interferometer loses its signal and the remaining projections of the tomogram have to be measured with only two active interferometer axes. This compromise proved to work well.

An alternative geometry with signal at all rotation angles and wide spread of the interferometer axes is shown in figure 5.3c. The concept requires a more complex sputtering coating in stripes that has not been manufactured so far.

5.3.3 Determining the interferometer angles

Indifferent of the geometry, the angles of the interferometer axes have to be known precisely.

The relative angles between the interferometers can be obtained numerically by performing a scan and calculating the positions from all three combinations of interferometer axes for several guesses of the angles. After moving the center of mass of the calculated point clouds to the origin, an error metric is established from the sum of the euclidean distances of the positions. The angles are then quickly found by a two-dimensional optimization.

The result obtained from this method is that, to the precision of 0.05° , the relative angles are always the nominal value of 30° , even after reassembling the device.

Finding the absolute angle is more involved. Initially, the absolute angle was simply determined from the motion of the sample scanner along the coordinate axes [10]. However, it was soon realized that this is not reliable as the axes of the scanner stages are not perfectly orthogonal to each other. In fact, it was discovered with laser-interferometry that one of the scanning stages that had been used for years has a huge tilt of 6.3° on its z-axis, the effect of which can be seen in some older publications [25, 98].

The absolute angles can be determined precisely by measuring ptychograms of the siemens star in a tomography setup at opposite angles, e.g. at 0° and 180° [73]. Again, the positions are calculated for several guesses of the absolute angle, and both ptychograms are reconstructed for each of the guesses. After flipping one of the reconstructions and aligning them an error metric is again calculated and a search for the optimum is performed. Even though this method is both experimentally and computationally expensive it delivers the best results.

5.3.4 Comparison to cylinder reflector

The alternative to the ball lens is a large, polished metal cylinder or spherical equator disk, such as shown in fig. 5.3a. The top of the cylinder is used as a flat mirror for vertical position measurements; the cylinder side reflects in horizontal direction. The cylinder is not a retro-reflector, in fact the rounded cylinder sides are the straight opposite. In consequence, such a setup is sensitive to motions along the curve, i.e. in the direction of the x-ray beam. For this reason, the cylinder works better when it has a larger diameter, with the disadvantage of a heavier mass that has to be moved by the piezo scanners.

A clear advantage of the cylinder is that it permits to directly measure along the coordinate axes. The absence of the coordinate transformation is in particular advantageous when the interferometer signal is used as feedback for a control loop. With the ball lens design, a software solution has not sufficiently low latency to perform the necessary coordinate transformation. Dedicated real-time hardware, FPGA or ASIC, has to be used instead.

The cylinder is better suitable for measuring the full 360° rotation. Since the sample pin on top of the ball lens has to be held in place by a metal support, a certain angular range is not accessible.⁶ In contrast, the sample can be mounted easily to a metal

⁶There is the possibility to glue the sample mount directly to the ball lens as shown in fig. 5.4b. However, despite using specialized adhesives for this use case and building a dedicated alignment tool, the sample pin receptacle could never be glued stable and in the correct angular orientation. Therefore, a 360° tomogram can only be measured with the current ball lens setup by removing the sample and remounting it in a different orientation.

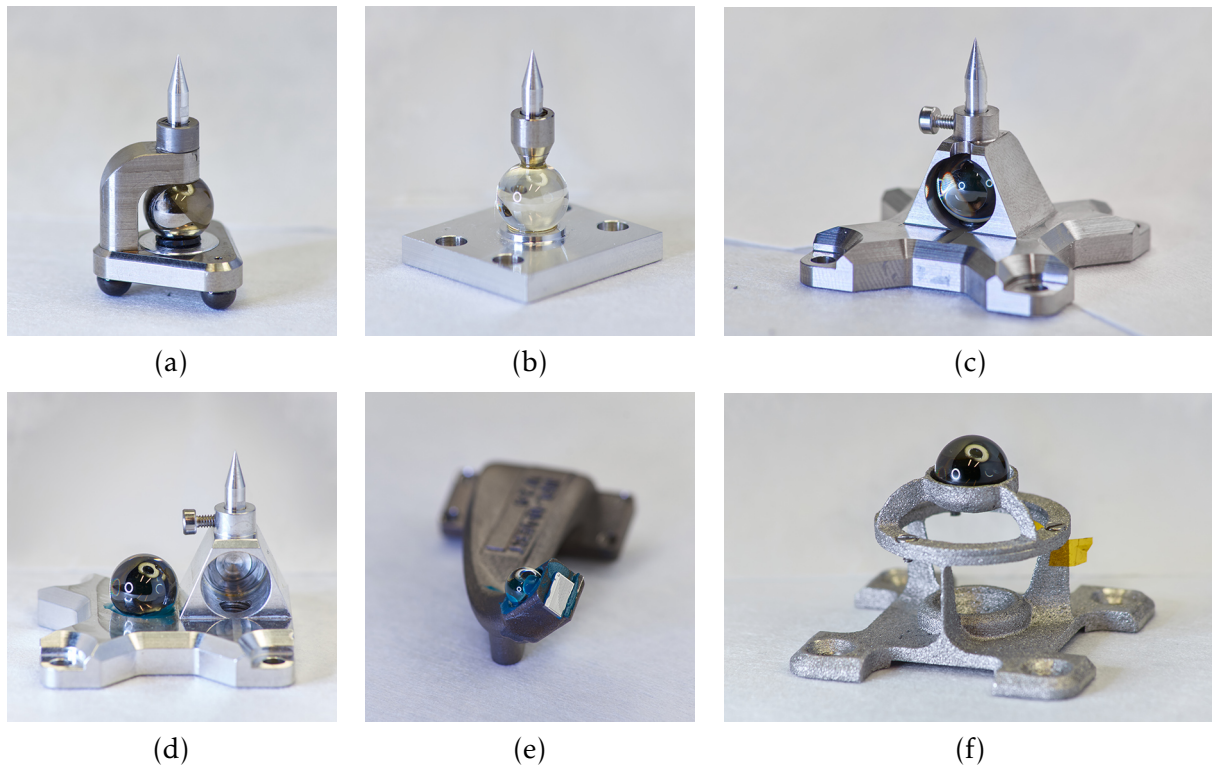


Figure 5.4: Integration of ball lenses into mounts. a) Kinematic sample mount that is commonly used for tomography measurements. b) Prototype of sample mount directly glued to ball lens. c) Sample mount with enclosed ball lens for 2D measurements. d) Acentric sample mount for use with x-ray optics of very short working distance. In this configuration the ball lens is glued downstream of the sample position to avoid collisions of the x-ray optics with the interferometer heads. e) 5 mm ball lens next to x-ray optics (NFLs) on a 3D-printed titanium lens holder. f) Sample holder for laminography measurements.

cylinder and there is no necessity for an additional structural support.

An additional advantage of ball lenses are the relatively low cost and small size. They can be easily glued to various sample and lens mounts, providing a fast method of enabling interferometry on custom user setups. Figure 5.4 shows a variety of use cases of ball lenses at P06.

5.3.5 Abbe error

The piezo scanners in PtyNAMi are specified to an angular error of $6 \mu\text{rad}$ (xy-stage) and $15 \mu\text{rad}$ (z-stage) [99, 100]. Considering that the sample is mounted about 3 cm above the ball lens, this may result in an Abbe error [101] of up to 630 nm. Upon request, the manufacturer clarified that this angular error is specified from one end of the travel range to the other and has a linear relation in between them, so that the full Abbe error is accumulated over the $100 \mu\text{m}$ travel range.

The remaining local deviations from the linear increase of the angular error are small, but could not be quantified so far. This is an inherent weakness of the ball lens design; angular deviations cannot be detected with a single ball lens, and using multiple ball lenses nullifies many of the advantages.

With a cylinder reflector, several vertical interferometer axes can be pointed at the flat top surface. With these multiple measurements of the vertical displacement at different points, the wobble of the rotation stage and other tilting effects can be observed.

In contrast, ball lenses allow the entire sample tower to be tilted on purpose, rendering the ball lens the perfect reflector for tensor-tomography SAXS and laminography. Laminography with interferometric tracking was successfully performed at PtyNAMI using the sample holder shown in fig. 5.4f.

5.3.6 Extension to the third dimension

Up until now, the discussed configurations only track the sample in a two-dimensional plane perpendicular to the beam direction. This is completely reasonable as vibrations along the beam direction are only influencing the measurement when they are in the order of the depth of field (DOF) or larger. As of today, the DOF of both the focusing optics and the ptychographic reconstructions are above the micrometer threshold and with that at least a factor 10 larger than the horizontal vibrations.

However, the DOF is decreasing continuously with the improvement of the spatial resolution of the microscope. Both MLLs with high numerical apertures [102] and high-resolution ptychography as presented here already approach the micrometer mark in DOF. Furthermore, efforts are made to increase the field of view by fast scanning or novel optical schemes [103]. For large viewing fields, parasitic motions in beam direction can no longer be neglected.

In the future, especially at fourth-generation sources, vibrations and positioning errors along the beam axis will gain in relevance and three-dimensional interferometric tracking will be necessary. Fortunately, both the cylinder reflector and the ball lens can be used for three-dimensional measurements by adding an out-of-plane interferometer axis. As a angular span of 30° has proven sufficient to calculate to motion along the coordinate axes, it is not necessary to install an interferometer directly in beam direction.

5.4 Vibration measurements

With their high spatial resolution, high sampling rate and non-invasive operation, the interferometer system is the ideal tool to characterize vibrations of sample and optics.

5.4.1 Comparison to seismometers

It may seem surprising that interferometers are chosen as the tool to study vibrations since seismometers are the first method that comes to mind. Laser-interferometers and seismometers are not to be seen as competing tools but rather as complementary with the ability to confirm each others' results. In fact, seismometers were used a lot in

the early phase of the project but phased out as interferometry proved to be a reliable method.

Seismometers consist of a spring-loaded magnet inside a coil winding and measure a signal proportional to the acceleration of the device, weighted by a frequency-dependent response curve. Even though these acceleration measurements may be integrated twice to obtain the displacement over time, the diminishing response at lower frequencies introduce large ambiguities to the calculation. In consequence, the measured acceleration values cannot be integrated to obtain quantitative displacement information.

In contrast, laser-interferometers measure the displacement directly and have a perfectly flat frequency responsive curve over the spectrum.⁷ The disadvantage is that the measured displacement is always relative to a reference, i.e. the interferometer head. Vibrations of the target reflector and the interferometer head mount cannot be distinguished. In particular, when measuring generally stable targets, such as the base granite, the vibrations of the interferometer head mount can easily exceed those of the target. Here, seismometers, that do not have to rely on external references, are at a clear advantage.

Another differentiating factor is the mass of the device. The mass of a system is one of the deciding factors that determine resonant frequencies and frequency responses in general. It is therefore futile to characterize the vibrations of a sample scanner that holds sample mounts with a mass of less than 30 g by putting a seismometer with a mass of 150 g on it. In comparison, reflectors can be very light-weight and can be integrated into the sample mount.

A further complication of seismographic measurements is the reliance on (weak) electric signals. Practically all vibration measurements at PtyNAMi show that the dominating contributions to the vibration spectrum are arising from the power grid frequency of 50 Hz and its higher orders. At the same time, the seismometer setup⁸ is extremely susceptible to electric interference. Connected to a conventional power circuit, useful measurements cannot be performed at all. Switching over to a clean, dampened power circuit, such as is available at P06, the spectrum is still strongly dominated by the grid frequencies; running the amplifiers on DC batteries brings some further improvement.

Ultimately, the problem remains that the power grid is the major cause of vibrations at PtyNAMi and also a major source of measurement uncertainties of these vibrations when using seismometers. Therefore, both effects cannot be distinguished with confidence.

⁷For measurements in air, low frequencies (< 1 Hz) are disturbed, see section 5.5. Measurements at extremely high frequencies (> 100 kHz) suffer from increased noise [104].

⁸This setup consisted of four seismometer (KB12VD, IDS Innomic GmbH), four individual amplifiers (M68D1, Metra Mess- und Frequenztechnik in Radebeul e. K.), an analogue-to-digital converter (IOtech, Personal Daq 3005) and a Dell laptop connected via USB.

Despite these challenges, seismometers are still a valuable complementary tool. While interferometers are used to directly measure the nano-positioning mechanics at the heart of the setup, seismometers can be used on the ground and the granite to monitor the vibration background. However, they are not a permanent part of the setup.

5.4.2 Vibration of the interferometer reference

A prominent challenge when measuring vibrations with interferometers is that the measurement is always relative. Therefore, a characterization of the interferometer head mount is essential.

Fortunately, there is a straightforward method to characterize the vibration of the interferometer head mount at PtyNAMI. From comparisons of the ultra-stable 2D setup with the tomography setup we see that horizontal vibrations are smaller by a full order of magnitude on the ultra-stable setup (see table 5.1 on page 70). In consequence, as the interferometer head mount is identical in both configurations, the measurement error from the interferometer head mount can be at maximum 10 % in the tomography configuration.⁹

In additional commissioning done by Patrik Wiljes, the piezo-scanner on the ultra-stable setup was replaced by a metal block dummy to assess the contribution of the head mount further. Averaged over intervals of 1 s, the remaining vibrations were measured at 0.33 nm horizontal rms and 0.76 nm vertical rms. Since these numbers still contain vibrations of the dummy block and air fluctuations, we can safely conclude that the contribution of the interferometer head mount is in the low Ångström range and therefore not relevant for all following discussions.

5.4.3 Repeatability of vibration measurements

The most prevalent challenge for meaningful vibration measurements, indifferent to the used method or device, is repeatability. The first vibration measurements using laser-interferometers at P06 were conducted in summer of 2015 on the predecessor setup of PtyNAMI; with the installation of PtyNAMI in 2016 interferometric vibration measurement became a standard tool that was used during the majority of the beamtimes from this point.

In 2017, I developed a tool that auto-generates vibration spectra and histograms for each scan and presents them in hyper-linked documents. This permits us to navigate the thousands of vibrations measurements taken over the last four years somewhat

⁹At least in theoretical considerations, there remains the possibility that motions of the lens cage in its entirety form a sizable contribution to the observed vibration spectra. While a small contribution is certainly present, the major influences can clearly be attributed to the sample tower from comparing the vibration spectra in figure 5.5.

quickly, even though the underlying data format has changed several times due to changes of the control software.

From this wealth of data, we can clearly see that vibrations are subject to change without prior notice. In general, these changes of the vibration background are not surprising as the Max-von-Laue hall is densely packed with beamlines in user operation that require frequent change of experimental configuration and equipment.

In the immediate vicinity of P06 the soft x-ray beamline P04 is situated that operates a considerable number of scroll pumps to maintain the UHV. Since P04 has no permanent end station open to user operation, the setup is modified several times per month. The beamline that shares its sector with P06, the full-field microscopy beamline P05, has a granite table of 9 t which is fully motorized and scannable in five degrees of freedom [105]. The neighbour on the other side, P07, researches engineering-sized samples at high energies up to 200 keV [106]. Every single opening and closing of their heavy fast shutter is visible in the vibration data.

Looking outside the experimental hall, three completely new major buildings¹⁰ have been built in the immediate vicinity of the Max-von-Laue hall during the last four years. While the more aggressive construction steps, such as breaking the frozen ground with excavators and compacting the soil, resulted in vibrations of several microns and with that in the halt of data taking, minor vibration sources were present during the entirety of the construction periods.

But not all the changes of vibrations are coming from the exterior of the beamline, also seemingly extraneous details, such as the torque with which certain screws are fastened, can lead to major changes in the vibration spectrum. At several times, the appearance and disappearance of new and very distinct peaks in the vibration spectrum were observed without any attributable cause. Once, without any changes of the setups at neither P06 nor the neighboring beamlines, the vibrations increased by 50 % from Saturday night to Sunday night.

Such observations demonstrate why vibration monitoring must be an integral part of the experimental detectors and not a one-off measurement that is referenced for years. The interferometric devices that measures the vibrations have great repeatability, but the vibrations present in the setup are constantly changing.

In this situation, the selection of data to present here is a delicate matter. Easily, an overly positive or negative image could be painted from a selection bias. At the same time, presenting the data in its entirety may fill an additional volume. In the following, the data examples were chosen to represent an average case as far as possible and the discussion focuses on aspects of the data that were observed over and over again.

Despite the seemingly random changes in the vibration data, the key characteristics

¹⁰Max-Planck-Institut für Struktur und Dynamik der Materie, Centre for Structural Systems Biology, and Centre for X-ray and Nano Science.

of the vibration, such as the dominant influence of the grid frequency and order-of-magnitude difference between the tomography and ultra-stable setup, were constantly observed.

5.4.4 Vibration spectra

Figure 5.5 shows averaged vibration spectra of four experimental configurations. These spectra are calculated from step scans: At each point of the scan, a time series of position values are measured with the interferometers. Each time series is then individually Fourier-transformed, and the amplitudes of the Fourier components are averaged over all scan positions.

The orange curve shows a typical spectrum for the full sample tower used for tomography measurements. The horizontal spectrum is dominated by a large and sharp peak precisely at 100 Hz, i.e. the rectified grid frequency of 50 Hz (see fig. 5.6). There are a few sharp peaks around the central 100 Hz peak, but their amplitudes are below 1 nm. There are two broadened double peaks around 180 Hz and 230 Hz as well as a flat band around 400 Hz. The vertical spectrum shows features at higher frequencies, in particular a characteristic peak at 620 Hz. Besides that peak, the vertical spectrum consists of a lot white noise and not a lot of structure.

The green spectrum was measured on the same day and with the same configuration as the tomography reference, but with the difference that the air-bearing rotation stage was settled, i.e. the air was turned off. Immediately the 100 Hz peak grows above everything else while the broadened double peak disappears. Here we see a strong indication that the setup is subjected to strong excitations at 100 Hz from the ground, and with increasing stiffness of the setup, this excitation is more directly visible. The air cushion inside the air-bearing rotation stage decreases the stiffness and therefore the peak is less pronounced. Further tests, that are not presented here, confirmed this hypothesis.

The presence of strong 100 Hz excitations can be primarily attributed to the design and construction of the experimental hutches. The hutch doors are held shut by electromagnets which do not use a flat DC current but the rectified 50 Hz AC grid frequency (see fig. 5.6). Deactivating the electromagnet on the secondary door of the P06 nanohutch reduced the 100 Hz peak by about a third, but the remaining magnets cannot be deactivated due to safety regulations.

Additionally, FEM simulations performed by Torben Reuß [107] showed that the metal walls of the hutch have resonances in the 100 Hz region, turning the experimental hutch effectively into an echo chamber for this vital frequency. Reuß' research also revealed that vibrations are transmitted to the sample through both acoustic and solid-borne sound at about equal proportions.

The black curve in figure 5.5 shows data obtained with the ultra-stable 2D setup,

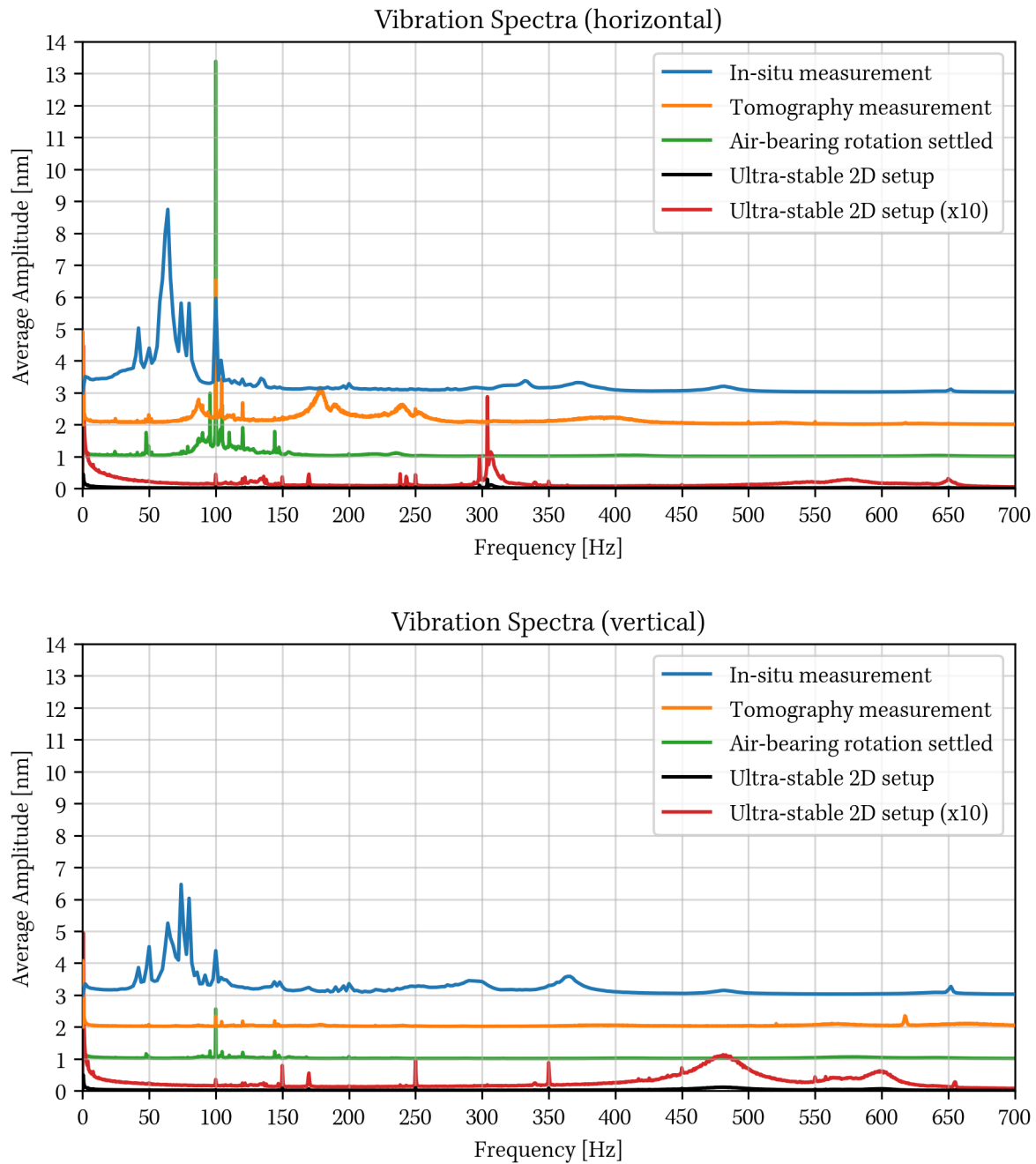


Figure 5.5: Examples of vibration spectra measured by laser-interferometry. Spectra are calculated from ptychographic scans in step-scanning mode. The spectra are offset by 1 nm for better visibility. The tomography measurement (in orange) shows the standard configuration at PtyNAMi used for most experiments. The green curve is taken under identical conditions, only the air-bearing rotation stage was deactivated and settled. The blue spectrum was measured with the in-situ cell described in 4.2. The spectrum of the ultra-stable setup (black) appears to be completely flat and is therefore multiplied by 10 (red).

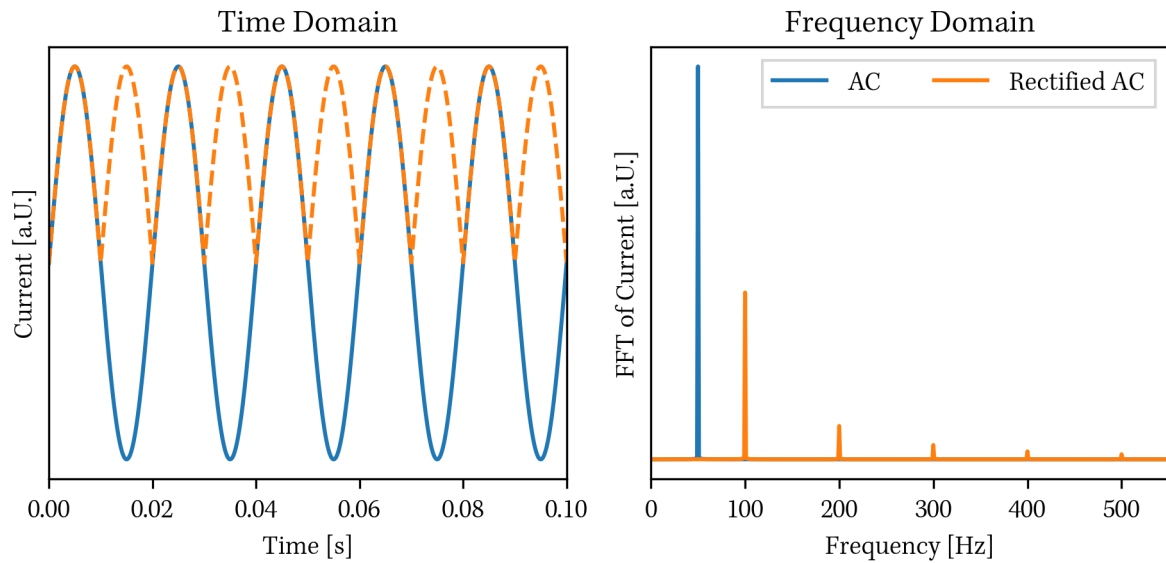


Figure 5.6: Simulation: A rectified 50 Hz sinusoidal oscillation results in a 100 Hz oscillation and higher harmonics of it. Such primitive rectification is implemented on the circuit-board level in the holding magnets of the PETRA III experimental hutch doors.

but since the vibrations are greatly reduced, the graph is barely visible over the abscissa. Therefore, the red curve shows the spectrum amplified by a factor 10. We observe that the major contributions of the spectrum are shifted towards higher frequencies as all large stages have been eliminated from the sample tower. A distinct peak in the spectrum appears just above 300 Hz that corresponds very well to FEM simulations of the PtyNAMi lens cage frame performed by Ralph Döhrmann in which a ground mode at 318 Hz was predicted.

A closer look at the vertical spectrum reveals more influences of the power grid frequency. While the 100 Hz is barely visible anymore, we see clear peaks at 150 Hz, 250 Hz and 350 Hz as well as tiny contributions at 450 Hz and 550 Hz. The most likely conclusion is that the same excitation from the ground is still present, but the susceptible frequency range of the setup has shifted. Yet it is not understood why the multiple of 100 Hz show no contribution, especially when regarding the peaks around 300 Hz in the horizontal spectrum. In the end, this lack of insight is a purely academic nuisance as the vibrations of a single nanometer rms have no practical implication at all.

The spectrum in blue shows the case in which the in situ cell described in chapter 4 is mounted on the sample tower. In this situation the vibration measurement is less reliable as both the mount of the interferometer heads and the mount of the ball lens retroreflector had to be extended to reach around the large in situ cell, resulting in an unknown amount of additional vibrations of the reference. However, the data quality still suffices to recognize certain trends.

Both the horizontal and vertical spectrum clearly show a shift towards lower frequencies. This is not surprising as the in situ cell has a mass of 220 g, differing from the

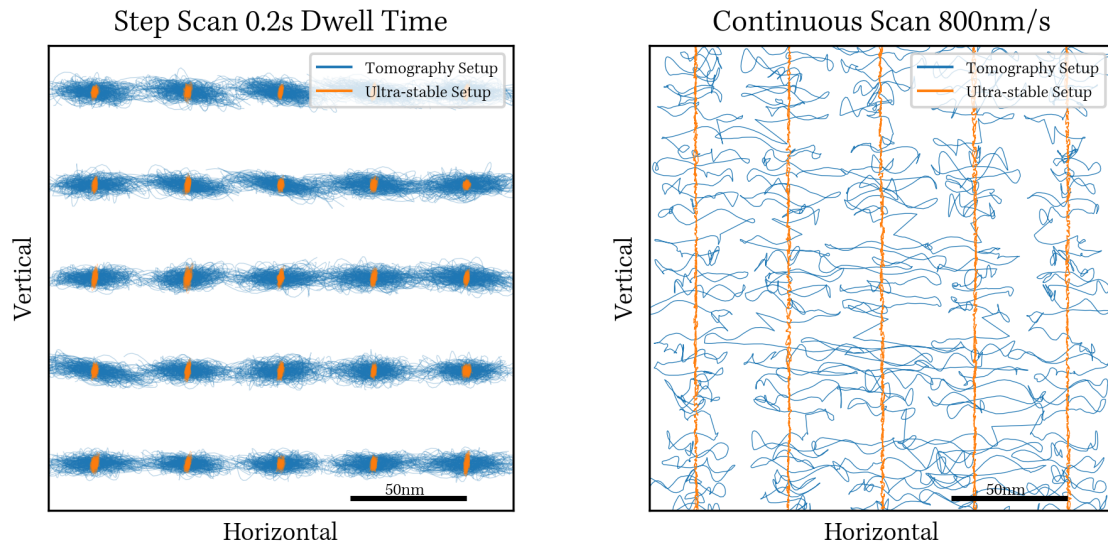


Figure 5.7: Traces of sample motion during ptychography scans as measured by interferometers. Tomography setup (blue) and ultra-stable 2D setup (orange) as well as step scanning (left) and continuous scanning (right) are compared. Step scanning was done with 100 nm step width and 0.2 s dwell time. During continuous scanning, the sample was moved with 800 nm s^{-1} in vertical direction through the beam.

30 g mass of the cinematic mount and lowering the resonant frequencies of the sample tower in consequence. The 100 Hz peak is reduced and exceeded by peaks in the 60 Hz to 80 Hz region. The 100 Hz excitations in the experimental hutch are still present, but the setup is less susceptible at this frequency with the increased mass.

5.4.5 Quantitative analysis

In figure 5.7 we see the point clouds of step and continuous scans on both the tomography and the ultra-stable setup. While the points are very dense for the step scan, we can clearly follow the path of the sample in the continuous scans.

Such point clouds are visually interesting to look at and give a first impression of the vibrations, especially when they are animated in a video [108–110]. They are, however, not very suitable for quantitative analysis of vibrations.

Whenever discussing vibration measurements, the most-used statistical measures are rms values, i.e. the average quadratic distance from the center of mass. Rms values are a valid measure of the width of a distribution, especially since they take all measured points into account. However, rms values also have the tendency to produce a small number that may result in an overly positive perception of the stability.

The table 5.1 lists four additional statistical measures for the distribution of position values. Two of them are calculated from quantiles: The 50% value is the distance between the upper and the lower quartile. Similarly, the 95% value is calculated as the distance between the 97.5% and 2.5%-quantiles. The range is simply the distance between the maximum and the minimum of the distribution. These statistical measures

Horizontal	rms	50%	fwhm	95%	range	fwhm/rms	95%/50%	95%/fwhm
Tomography	10.9	14.3	26	42.7	84.9	238%	299%	164%
Air off	10.4	16.7	30	37.1	60.4	288%	222%	124%
Ultra-stable	0.8	1.1	2	3.1	5.8	250%	282%	155%
In-situ cell	9.9	13.1	22	38.7	61.4	222%	295%	175%

Vertical	rms	50%	fwhm	95%	range	fwhm/rms	95%/50%	95%/fwhm
Tomography	3.4	4.5	8	12.5	24.1	235%	277%	156%
Air off	2.3	3.3	6	8.7	15.8	260%	264%	145%
Ultra-stable	1.2	1.6	4	4.6	8.9	333%	288%	115%
In-situ cell	6.2	8.4	14	24.5	38.7	226%	291%	175%

Table 5.1: Quantitative measures of vibrations, all quantities are in nanometer. The 50% and 95% values mark the average width of the central interval in which 50% resp. 95% of the values lie. FWHM values have been calculated for histograms with a bin size of 1 nm, therefore they are only precise to 1 nm. The range is average distance of the outermost points of the point clouds.

are calculated for each scan point individually and are then averaged.

The Full-Width at Half-Maximum (FWHM) is another measure that is popular in the x-ray microscopy community, in particular for the characterisation of foci [71, 111]. For a distribution of points it has to be calculated via histograms such as shown in figure 5.8. The FWHM is obtained from the lowest and highest (i.e. the leftmost and the rightmost) points of the distribution that represent half the density of the histogram bin with the highest density. As such, the exact value of the FWHM depends the choice of bins of the histogram, especially for small number of position points that result in a less smooth histogram. In general, the FWHM is not the best choice for the characterization of vibrations and has only been included here to illustrate this point.

Studying the values of table 5.1 in more detail, we see that even though the rms values of the horizontal vibration only changes from 10.9 nm to 10.4 nm when settling the air-bearing rotation stage, the other statistical measures show significant differences. These differences are also expressed as relative changes on the right-hand side of the table. We see that measures that discard outer points in their calculation (50%, FWHM) are more favorable in the air-bearing case while the measures that also take these points far from the center of mass into account are smaller in the settled case.

This example, measured on a single setup with only a single variable changed, nicely illustrates the necessity to discuss more statistical measures than the rms. Let us assume that we are given the task to decide if the air-bearing rotation stage should be settled when no rotation is needed to reduce vibrations. Deciding on the basis of the rms value, we arrive at the conclusion that there is almost no difference. However, when we base our decision on the 50% and 95% values, we arrive at definite, but opposite conclusions. The answer to our question is *yes*, *no* and *doesn't matter* at the same time.

Giving a general answer to the question which of these measures is to be considered

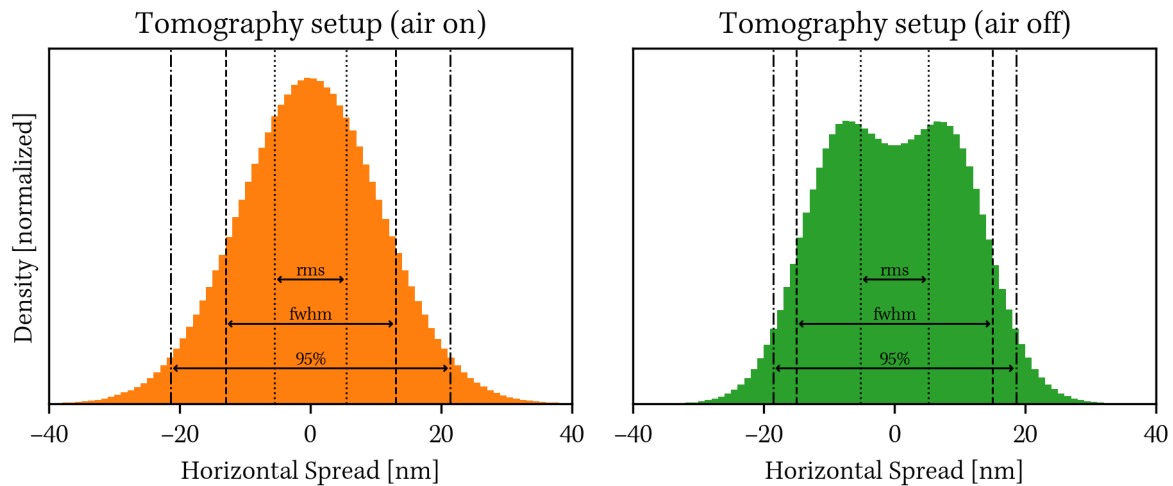


Figure 5.8: Horizontal vibration data of fig. 5.5 displayed as histograms. The distributions of individual scan points were aligned according to their center of mass and averaged. The statistical parameters are visualized with respect to the distribution.

with priority over the others is certainly not trivial. It may depend on the scanning microscopy technique used and the nature of the sample.

Let us consider an XRF scan of a sample where we want to measure small amounts of an element, but in the vicinity there is a large accumulation of this element. Even if the sample and beam vibrations leave the beam stable on our spot of interest for the vast majority of time, a short burst of vibration to the large accumulation may still degrade the signal, therefore, the range of the vibration is the most significant value. On a different sample, with a more homogeneous distribution of material, we might favor a broad distribution with a sharp peak in its center instead.

5.4.6 Histograms

When discussing values such as in table 5.1 it is still not clear how constant the vibrations are from point to point during a scan. Are they all on the same, constant level, indicating constant external excitations that affect the setup identically at all times? Or is the vibration background much lower, but sporadic external excitations cause much higher vibrations on isolated scan points?

One of the more convenient ways to answer these questions is to plot a histogram of the statistical measures in question over the individual scan points such as is done in figure 5.9. As can be seen in the data of the tomography setup, the distributions of the rms and 50% values are narrow. Over the relative long dwell time of 5 s per scan point, the random nature of the vibrations average to a consistent value and changes of the external excitations did not occur.

The scan on the ultra-stable setup was recorded with a dwell time of 2 s, in consequence, the distributions have a larger relative spread. We observe a very typical asymmetry of the distribution with a sharp fall-off from the maximum towards smaller

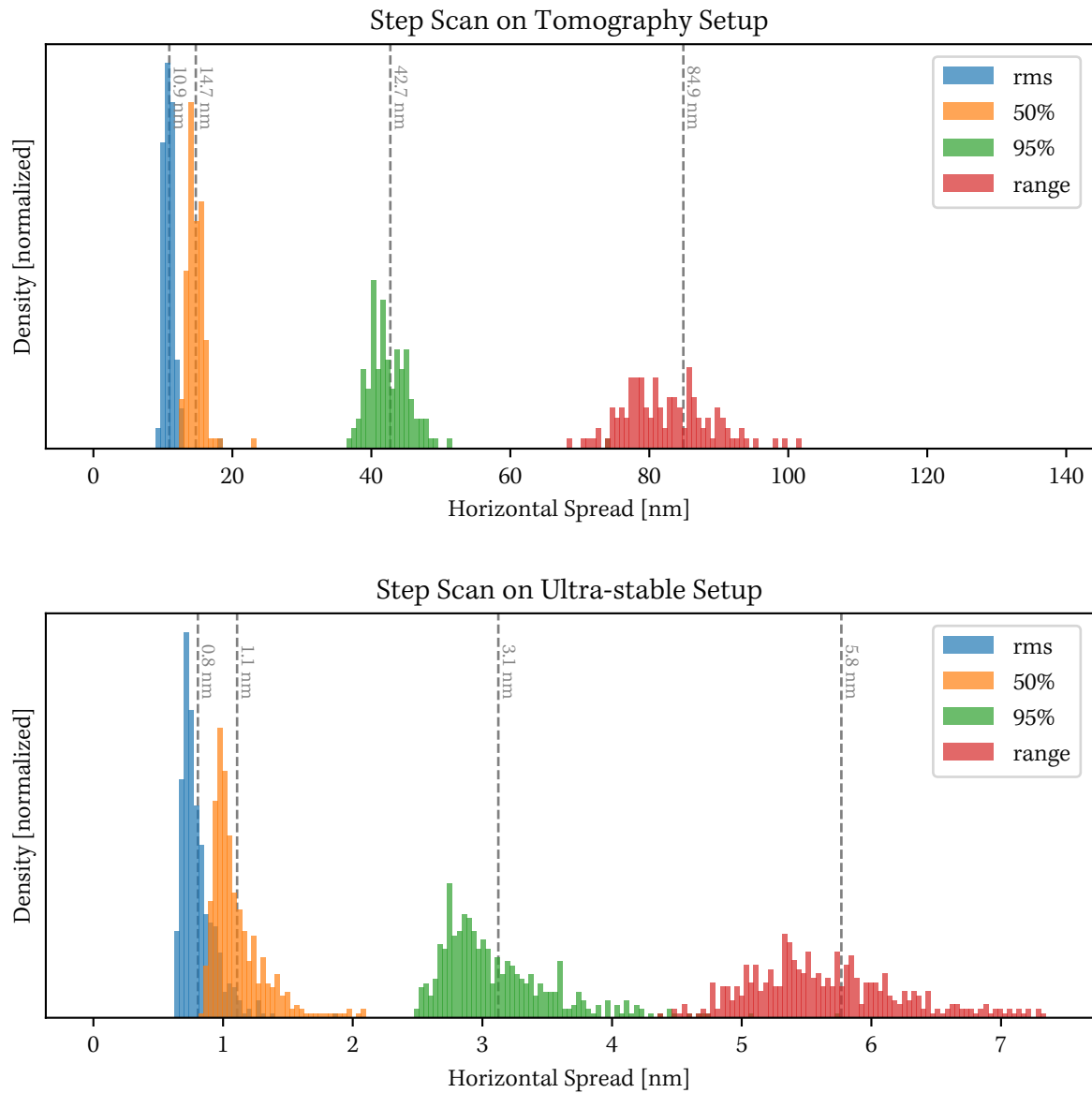


Figure 5.9: Evaluation of the vibrations present during a single scan via histograms of rms and quantile distances as histograms. These histograms are shown here as they are automatically produced at the beamline. The abscissa is scaled such that 98% of the range values are in the visible range. This is done to prevent a single point of large vibration to compress the histograms too much. The vertical dashed lines mark the average of the four distributions.

values but a long tail towards higher values. This indicates a ground noise level below which the vibrations never fall, and a tendency of excitation events to negatively influence some points.

The pixel size in the reconstructed high-resolution ptychograms in chapter 7 measured on the ultra-stable setup is 6.6 nm. Therefore, all 95% intervals lie well within a single pixel and even most peak-to-peak ranges do not leave a single pixel of the reconstruction. With these results, vibrations of the sample are truly a non-issue on the ultra-stable setup, at least until the upgrade to PETRA IV is completed.

Histograms like these have proven very effective in evaluating the vibrations present during a scan on a glance. Therefore, I have written software for the P06 beamline to show such histograms together with the vibrations spectra automatically after every scan. This vibration data is bundled with the signals from all other detectors of the beamline and presented to the operator as a preliminary data evaluation in a web browser. Having such a software in place when using interferometers to monitor vibrations is crucial, there is no point in noticing harmful vibration sources after the data taking is finished.

5.5 The influence of air

One of the disadvantages of the interferometry at PtyNAMi is certainly that it is housed in air. Therefore, the beams of the laser-interferometers have to travel through air, making the measurement susceptible for any changes of the refractive index of the air between the interferometer head and the reflector.

5.5.1 Edlén correction

At the beginning of the interferometry project, most attention was paid to the influences of temperature, humidity and pressure on the refractive index of air [10]. These dependencies have been described in the literature in detail, the Edlén-corrections [112, 113] give a formula to calculate the corrected refractive index. The manufacturers of the interferometer systems offer optional "weather stations", i.e. small units that measure temperature, humidity and air pressure and report them to the controller to automatically perform this correction.¹¹

However, with progression of the project, it was realized that the effect of the Edlén-correction is small, even negligible in most cases. The P06 nanohutch is temperature stable to the centikelvin [94], resulting in a complete flat readout of the temperature sensor. Humidity and pressure changes are measurable but do not produce a measurably harmful effect.

¹¹But neither system gives access to the value of the refractive index that was calculated that way.

5.5.2 Air fluctuations

A much more harmful and definitely noticeable influence are air fluctuations. The air currents in the experimental hutch are reduced as much as possible; the air conditioning uses large fabric diffusers to distribute the chilled air over the full length of the hutch. Furthermore, all components with active cooling fans are banned from the hutch and must be connected via long cables and tubes from the outside.

Nevertheless, there are still air fluctuations in the hutch that possibly arise from motor blocks and the air-bearing stage. The consequence of these fluctuations are low-frequency contributions to the interferometer signal, typically of 1 Hz and below. A rule of thumb that was established between PtyNAMI and other experiments [114] at DESY using similar interferometry devices is that 1 cm of travel distance in air adds about 1 nm to the rms signal. The specific value depends of course on the details of the experimental setup.

A possibility to minimize this effect is to shield the optical path of the interferometer. This can be done easily by putting small plastic tips on the front of the interferometer heads that are obtained from cutting up pipettes (see fig. D.3d on page 146). As these shielding parts must not touch the sample mount and still have to leave sufficient clearance for rotation and other motions, about a centimeter of unshielded air path still remains.

The effect of air fluctuations can also be seen clearly when the heated in situ cell is in use. Over a dwell time of effectively 6 s, the horizontal rms value increased from 12.4 nm to 21.8 nm when the heating was turned on. A more detailed analysis of the air flow around the in situ cell inside the setup was performed by Mirko Landmann [115].

Since the typical dwell times are only fractions of a second, these fluctuations do not immediately appear as vibrations in the measurement but rather as a distortion of the position grid.

5.5.3 Helium

Another source of change of the refractive index is the usage of helium. Helium has a refractive index of $n_{\text{He}} = 1.000036$ which is an order of magnitude closer to 1 than that of air ($n_{\text{air}} = 1.000293$) [5]. The distance from the beam exit of the interferometer heads to the retroreflector is about 2.5 cm, resulting in a total optical path length difference of about 6.5 μm between measurements performed in pure air and in pure helium.

In consequence, any experimental setup that works with open helium disturbs the interferometric measurement catastrophically. An attempt to build a helium tent around the entire microscope unit resulted in optical path length fluctuations in the range of 1 μm during a single scan, another setup that tried to use a helium dome with minimal helium throughput on top of the sample still experienced fluctuations of several hundred nanometers despite shielding components around the air path.

The only workable solution that allows a helium atmosphere around the sample with parallel interferometry operation is a completely gas-tight sample enclosure such as the one shown in figure D.3.

5.6 Periodic measurement error

The interferometers used in the PtyNAMi setup are based on the homodyne phase quadrature principle [116, 117]. In consequence, the measured position signal suffers from a periodic error [118] that is one of the major limiting factors of the current interferometer setup. An in-depth explanation of the homodyne phase quadrature is given in appendix C, here we focus on the consequences.

5.6.1 Phase quadrature

In a simple Michelson interferometer,¹² the displacement of the target reflector results in a sinusoidal modulation of an intensity signal. Such a signal is of limited usefulness, as at the minima and maxima of the sine curve the sensitivity of small changes is zero and a change in direction of the mirror displacement cannot be detected. A second, phase-shifted signal, such the cosine of the displacement, should therefore be measured at the same time to eliminate these blind spots.

This second signal can be obtained with various methods, e.g. using multiple laser wavelengths (heterodyne interferometer) or splitting into multiple reference beams (e.g. via polarization). With homodyne phase quadrature, only a single laser and a single reference arm are required; instead, the number of waves in the path length difference is constantly varied by either oscillation of the reference mirror or wavelength modulation of the laser source. While physical oscillations are limited to a bandwidth in the kilohertz regime, distributed feedback (DFB) lasers can be modulated with several megahertz [117] and permit much more compact interferometer heads.

When the wavelength is modulated with a frequency ω , the observed interference pattern has time-dependent components of ω and 2ω modulation. As is shown in appendix C, these components are proportional to the sine and cosine of the displacement in an approximation with small wavelength modulations.

With both sine and cosine at hand, the interferometer output can be displayed as a circle such as shown in figure 5.10. In polar coordinates, the displacement can be

¹²In literature, especially in materials published by manufacturers of such interferometer devices, there is often a distinction made between sensing heads using Michelson geometry and heads using a Fabry-Pérot geometry. This distinction is made as the Fabry-Pérot geometry is protected by European patents [119, 120]. The Michelson geometry is not covered by those patents, a possibly relevant Japanese patent is expired [121]. For distance sensing applications, the étalon of the Fabry-Pérot interferometer is produced with a low reflectivity so that the finesse is close to one, i.e. only the first order reflection needs to be taken into account. In this case, the interference signal exhibits the same sinusoidal dependency on the distance as a Michelson interferometer and both types can be considered mathematically equivalent in the phase quadrature scheme [10, 122].

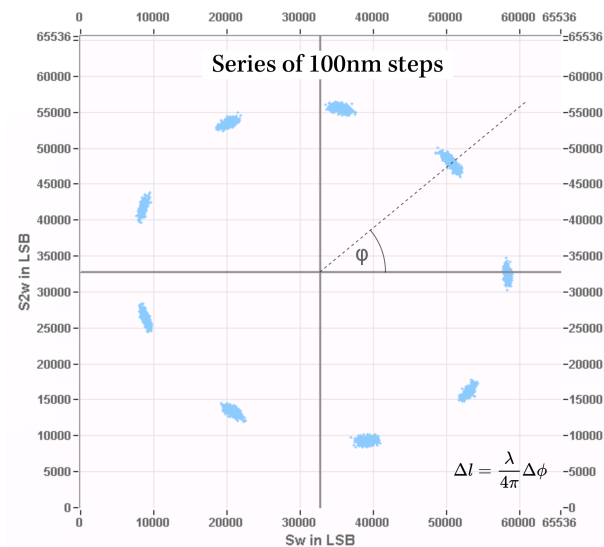


Figure 5.10: Homodyne quadrature signal as displayed in the control software of the Smaract PicoScale. This figure was created from an overlay of multiple screen shots. When moving the reflector target in 100 nm steps, the point cloud of the quadrature signal moves from one position to the next. In this representation, the displacement of the reflector target is determined directly from the angle φ .

determined from the angular position on the circle; as the target moves, the full circle is traced out. A full rotation around the circle equals a displacement of half the laser wavelength, in our case $\lambda/2 = 767.5$ nm.

In real-world measurement, the obtained signal is not a perfect circle. In a first approximation of the measurement error, the sine and cosine signal have different amplitudes and the phase-offset is not precisely $\pi/2$, deforming the circle into an ellipse. The commercial interferometer controllers expect the occurrence of such an error and fit the resulting ellipse correspondingly. However, the signal is usually visibly distorted beyond the simple elliptical case.

The correction algorithms programmed into the FPGAs of the interferometer controllers are not disclosed by the manufacturers. With the Attocube FPS3010 this process is a complete black box to the user as only the final displacement is output. In contrast, the Smaract PicoScale permits to stream the quadrature signal before and after the correction step alongside the position data, permitting more insight into the signal processing chain.

5.6.2 Linear test measurement

In figure 5.11 the periodic error was measured in a dedicated metrology laboratory outside the beamline on a damped optical table. In this one-dimensional scan, a piezo-positioner was moved in 50 nm steps over a distance of 5 μ m, positions measured with the interferometers as well as the internal stage encoders were pulled repeatedly. A linear function was fitted to the data and subtracted to account for the motion of the positioner.

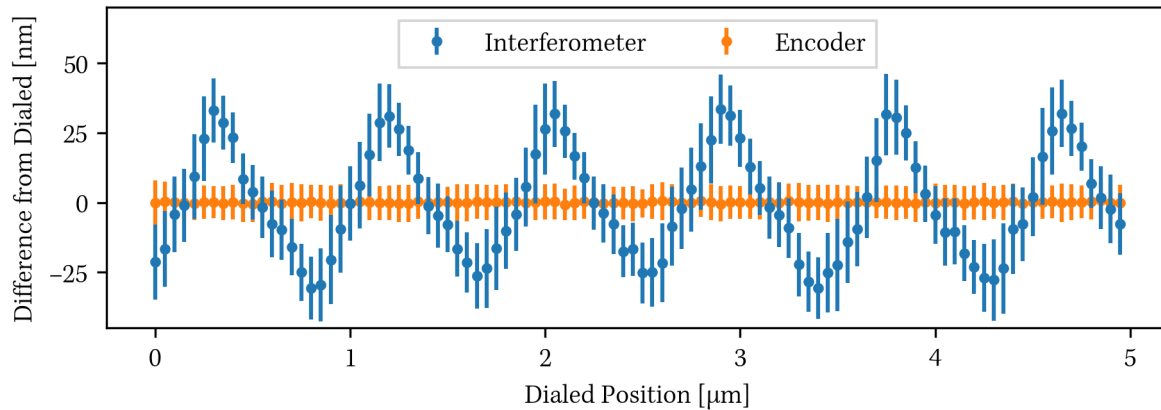


Figure 5.11: Measurement of the systemic periodic error of the Attocube FPS3010 under ideal conditions on an optical table. The piezo positioner was driven in 50 nm steps over an 5 μm range, encoder and interferometer values for were acquired for 5 s at each position. The errors bars indicate the rms values. A linear function was fitted and subtracted from both interferometer and encoder positions.

The resulting encoder values are completely flat as expected. In contrast, the interferometer positions show a clear triangular wave form with an amplitude of about ± 25 nm. The period¹³ of this error is $\lambda/2$. Repeating this measurement several times results in exactly the same curve within the error bars. When the alignment of the interferometer optics is changed and the alignment procedure of the controller is rerun, i.e. an automatic procedure during which the controller tries to optimize amplification and demodulation settings, the shape and amplitude of the error changes, yet the period remains the same. Depending on the alignment, the amplitude of the periodic error varies between 10 nm in the best case up to 40 nm in the worst case.

The nature of this measurement error must not be confused with an absolute measurement uncertainty or repeatability error of 25 nm. The interferometer still remains capable to reliably detect displacements of a single nanometer given sufficiently stable conditions. In fact, in complete isolation on an air-damped optical table, peak-to-peak vibrations of only a few hundred picometers have been measured.

The periodic error introduces a *relative* measurement uncertainty for distances up to $\lambda/4$. In the case of the data in figure 5.11, the relative error from a minimum to a maximum of the error curve amounts to 50 nm over the half-period of 383.75 nm, i.e. about 13%. Measuring larger distances will decrease this high relative error again as the periodic error averages to zero over full period of the quadrature signal.

5.6.3 Ptychographic scans

The figures 5.12 and 5.13 show the positions of two ptychographic scans acquired during user beamtimes at PtyNAMi. As the installed interferometer was the PicoScale,

¹³In this measurement, the period appears to be larger as the interferometer axis and the direction of motion of the nano-positioner were not parallel. When taking this geometric factor into account, the period matches $\lambda/2$ exactly.

we can also plot the "raw" and "corrected" quadrature signal, i.e. the quadrature signal before and after the fitting of the ellipse. These quadrature signals are streamed and saved in parallel to the processed position values and are automatically plotted along the vibration analysis in the software package that I developed for the beamline P06.

The first scan in figure 5.12 is a continuous scan recorded as one projection of a tomogram. This projection was measured at a moderately high speed of $1.25 \mu\text{m s}^{-1}$ in vertical direction. The raw quadrature shows a very reasonable shape that has no major deviations from a circle; furthermore, the signal is consistent over the entire region of the scan.

In contrast, the corrected signal exhibits an unexpected behavior: While the majority of the points are projected on a perfect circle as they should be, for a part of the scan the correction completely fails and produces a strongly eccentric ellipse that is cut-off on the sine axis on both ends of the 16 bit integer range of the signal.

The result is immediately visible in the calculated positions: While in the left half of the scan the densely packed positions fill the plane homogeneously and a periodic distortion is only faintly visible, the position distortions are extreme in the third quarter of the scan; a strong wave-like pattern is visible. If we were to draw a wave vector \mathbf{k} on these waves it would be colinear with the direction of the distorted interferometer axis. This sudden change in the corrected output is remarkable as we can clearly see in the raw signal that there is no sudden change in signal quality, meaning that there is no obvious physical reason for this behaviour.

It should be noted that each of the three interferometer axes used for the sample tracking record their individual quadrature signal and apply the correction algorithm independently. As a result, even in a case of a spontaneous misfitting as in this example, it is not necessary to repeat the measurement as usable positions can be calculated from the two remaining intact interferometer channels.

The second scan in figure 5.13 is a high dose scan which was aimed at reaching high spatial resolution. With only $0.5 \mu\text{m}$ by $0.5 \mu\text{m}$, the scanned area is small, the resulting quadrature signal does not even show a closed trajectory as the measured displacement does not reach the 765 nm period. As the interferometer axis is nearly parallel to the slow scan direction, the arc segment is also not sampled multiple times during the scan but only once.

The consequence is that the error correction algorithm has difficulties to fit the shape of the entire ellipse as it is never completely sampled, thus, the corrected signal looks worse than raw signal and the positions are strongly distorted to the point where they are unusable for high resolution reconstructions.

This failure to perform any useful ellipse fitting was observed on all occasions when attempts were made to scan slowly with high photon dose. The periodic error is thus least prominent when the sample is scanned very quickly and in the presence of large

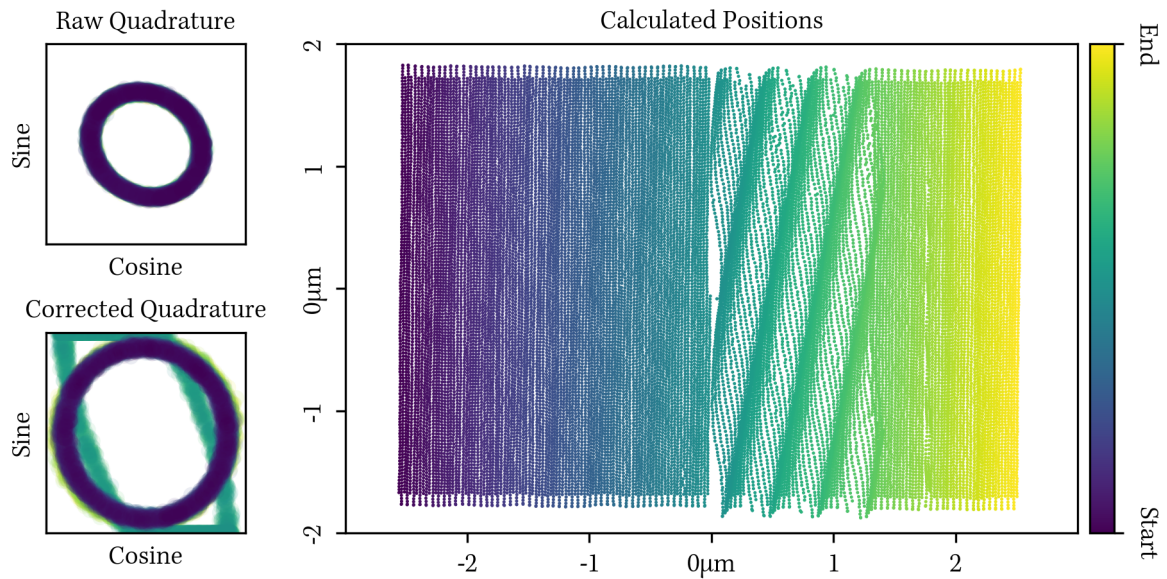


Figure 5.12: Spontaneous appearance of a strong periodic error during a continuous scan measured at 50 Hz in 204 by 140 steps in an area of $5.1 \mu\text{m}$ by $3.5 \mu\text{m}$. The average position of each acquisition time window is plotted. The color gradient indicates the order of acquisition of the data points.

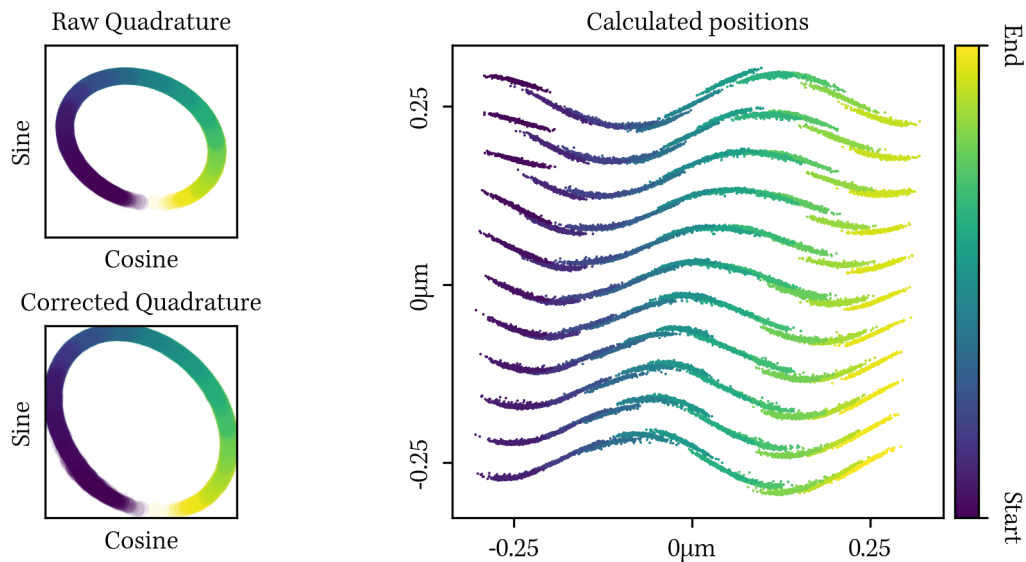


Figure 5.13: Typical periodic error of a high-dose step scan measured in 10 by 10 steps in an area of $0.5 \mu\text{m}$ by $0.5 \mu\text{m}$ with a dwell time of 1 s. The expected plot is a perfect regular grid, or when accounting for the horizontal sample vibrations, parallel horizontal lines. Per scan position several points are plotted to give an indication of the vibrations during exposure. The color gradient indicates the order of acquisition of the data points.

vibrations; it is most prevalent when the sample stands stable and is moved in small steps.

In consequence, the effective resolution of position data and x-ray data are in an unfortunate inverse relation.

5.6.4 Outlook: Interference Spectroscopy

The root cause of the periodic error is that the wavelength modulation is small¹⁴ and as such the full period of the quadrature signal cannot be sampled when the target is too stable.

During the preparation of this manuscript, a novel interferometer came to market that modulates the DFB laser with a far greater amplitude, sampling the entire ellipse several times in a single sweep.¹⁵ Since several sinusoidal modulations of the interference are sampled with each sweep, a sine function can be fitted directly to the signal; determining the angle on the ellipses is no longer necessary. This procedure effectively eliminates the periodic error.

A first test of this device at PtyNAMi was successful in that the interferometer controller is compatible with the existing optics. Position measurements similar to those presented in figures 5.11 and 5.13 could be performed without an observable periodic error. After these promising preliminary results, the device has to be integrated now into the control system of the beamline to allow for systematic testing.

5.7 Ptychographic test measurements

After having discussed the results obtained with the interferometers in detail, we are now taking a look at how these results apply to ptychographic reconstructions.

5.7.1 Microchip test structure

In figure 5.14a and 5.14b we see two reconstructions of a ptychography scan of a planar semiconductor structure (detailed description of this sample in [125]). During the scan, the setup was suffering from a large vertical drift.¹⁶ Both ptychograms were reconstructed with algorithmic position refinement, however, the initial positions were given from encoder values in 5.14a and interferometer positions in 5.14b.

In the reconstruction initialized with encoder positions the field of view is rectangular, but the horizontally planar structures are reconstructed as a staircase shape. From

¹⁴The quantitative amplitude of the modulation is not disclosed.

¹⁵quDIS by qutools GmbH [123]. The working principle is patented [124], the patent is not limited to certain sensor head geometries.

¹⁶The drift was caused by settling of the air-bearing stage. Turning off the constant stream of pressurized air induces a temperature change in the sample tower. Thermal drifts such as the one shown here do not occur during normal operation of PtyNAMi.

the left to the right of the image, there are about eleven steps on the staircase, but the sample was scanned in 40 steps across that were continuously descending due to the vertical drift. The positions refinement algorithm has accumulated the positions of four diffraction patterns on average to form a piece-wise flat edge, but it fails to align these sections of the image correctly.

Using positions obtained from interferometers as the initial guess, the field of view is sheared into a parallelogram and the layers of the semiconductor are reconstructed correctly. The interferometer successfully detected the vertical drift present in the setup. Upon closer inspection, in particular of the isolated features in the bottom half of the image, we can see that the features are not perfectly on a horizontal line. This distortion of the image is caused by the periodic error.

5.7.2 Siemens star test pattern

In figure 5.14c we see a ptychographic reconstruction of the Siemens star that suffers from strong vibration and positioning errors. This image is the full field of view of figure 2.10 in which a strong position correction was applied. We see that on top of the center hole, the horizontal 50 nm lines and spaces are hardly resolved, while the vertical lines and spaces are. This is a direct consequence of the anisotropic nature of the sample vibrations.

The figures 5.14d to 5.14f show the same test pattern measured on the ultra-stable setup. A single measurement is reconstructed three times with different positions while all other reconstruction parameters are identical.

In all three reconstructions, all features of the test pattern are clearly reconstructed. As the smallest features present are 50 nm in size this is not a challenge. We are interested in more subtle differences between the images, such as the homogeneity of the background and the edges.

In figure 5.14d the reconstruction is initialized with nominal encoder positions that are not refined during the reconstruction. Looking at the edges of the stripes, especially in lower left quarter of the image, we can see that they are not perfectly straight. Furthermore, there are bright and dark halos around the edges, giving a further indication that the positions are not correct.

The improvement introduced by using interferometer positions (fig. 5.14e) is minimal to non-existent. While in some areas of the image artifacts are reduced, in others they are increased.¹⁷ Only using position refinement (fig. 5.14f) yields a definitive improvement. Here, most of the halos are resolved and the background is more homogeneous.

¹⁷This argument only holds for step scans. For continuous scans, encoder positions are not available at PtyNAMi; interferometer positions are then a necessary part of the experiment. In consequence, fast continuous scans of large sample areas at low to intermediate resolution are only possible with interferometers.

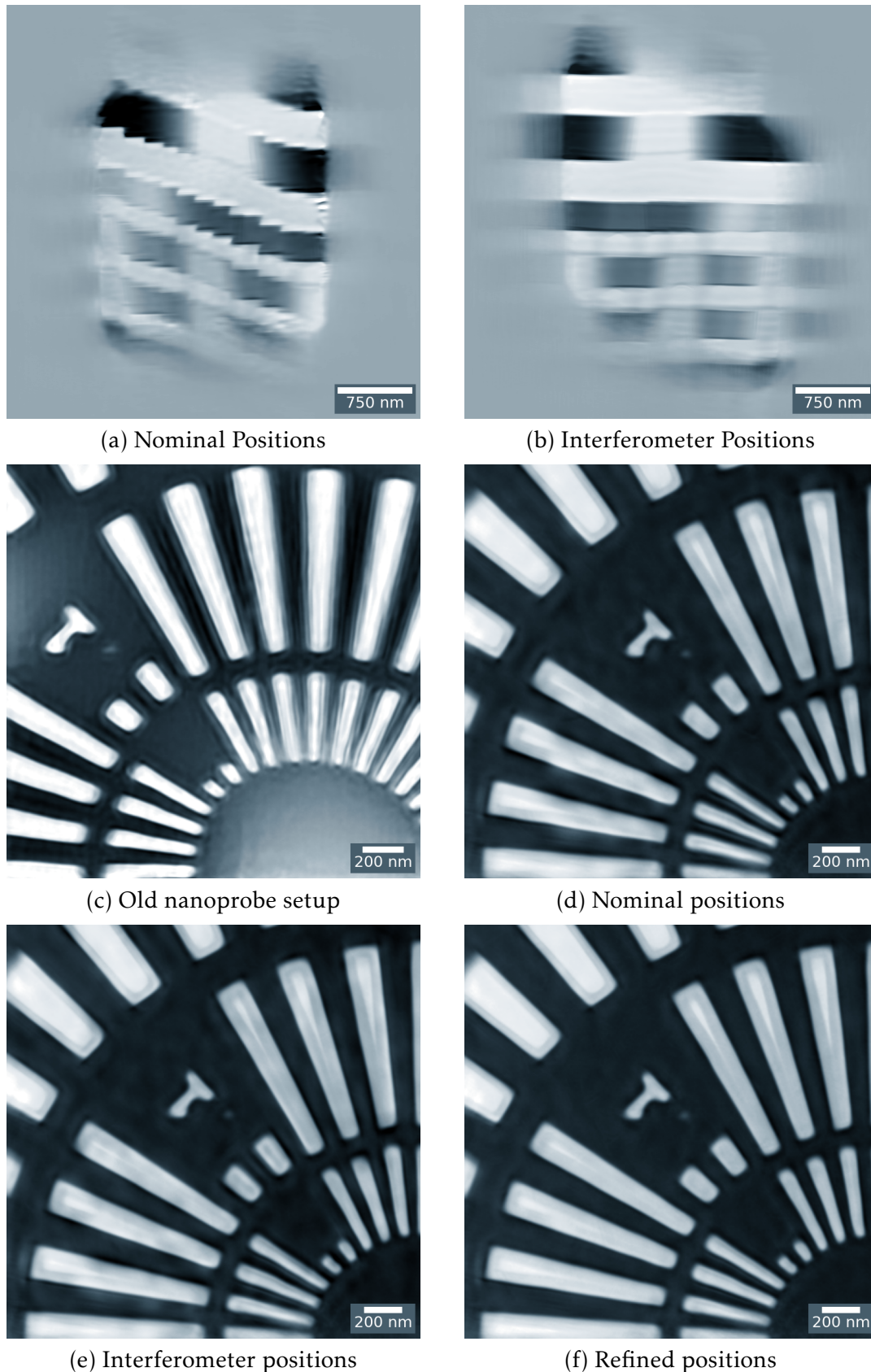


Figure 5.14: Phase shift images reconstructed with ptychography a,b) Microchip measured during strong vertical drift. Positions are algorithmically refined, but initial positions are from a) nominal positions and b) interferometer positions. c) Siemens Star test pattern measured on old nanoprobe setup with significant horizontal vibrations, reconstructed with position refinement. d-f) Same test pattern measured on ultra-stable setup and reconstructed with d) nominal positions without refinement e) interferometer positions without refinement f) algorithmically refined positions.

It is important to keep in mind that the position of the focused beam on the sample does not only depend on the position of the sample but also on the motion of the focusing optics and the pointing of the x-ray beam coming out of the beamline. The algorithmic positions refinement can account for all three of these error sources so the improvement of the reconstruction is not surprising. Even in a hypothetical case of perfect interferometric position measurement, the algorithmic refinement might still produce superior results.

5.8 Summary

We can summarize the findings of the interferometer system in four points:

1. The interferometers are an excellent system to study and monitor vibrations. All relevant frequencies and length scales are covered, the system is non-invasive and can be used in most experimental configurations. An ultra-stable setup for two-dimensional measurements has been demonstrated.
2. Ball lenses are versatile reflector targets that can be implemented in a variety of sample and lens mounts. Their disadvantage is that they are incapable to detect tilting errors.
3. The current implementation of the homodyne phase quadrature scheme leads to a periodic distortion of the position data. A novel wavelength modulation scheme might solve this issue in the near future.
4. For ptychograms measured under optimal experimental conditions, interferometer positions do not improve reconstruction quality over encoder positions. Algorithmic position refinement still yields the best reconstruction quality as it holistically incorporates all processes that affect the position of the focused beam on the sample, including instabilities of the x-ray beam.

Chapter 6

The in-vacuum detector device

The previous chapter described the efforts taken to determine where the focused beam hits the sample. There remains the task to transport the scattered beam to the area detector in the far field while maintaining as much as possible of the encoded information. In this section, we describe the design of the PtyNAMi detector device, present measurements of the scattering background, discuss the necessity of using beamstops and the effect of the in situ cell on the scattering background.

6.1 PtyNAMi detector device

6.1.1 Detector requirements

The detection of the diffraction patterns in the far field is technologically challenging:

1. The central part of the beam has a high flux of about 10^8 photons/s/mm², yet the central beam must be accurately detected to obtain a quantitative reconstruction.
2. At the same time, the scattered signal decreases rapidly with increasing scattering vector (Porods law: $I \sim q^{-4}$ [43–45]); high spatial resolution information of small or weak scatterers is mostly encoded in single photon events. These events should be accurately detected over a quasi noise-free background.
3. The pixels of the detector must be small enough to resolve individual speckles in the diffraction pattern.
4. Many experiments are only feasible if the detector has a fast read-out time, preferably of milliseconds or below.

These requirements cannot be met by traditional CCD and CMOS chips. Fortunately, over the past two decades, hybrid photon counting detectors developed in High Energy Physics were adapted for utilization at synchrotron facilities [126]. These area detectors

consist of an array of pixels that can determine the charge deposition of individual incoming x-ray photons.

As the energy of x-ray photons is in the range of keV, they can be effectively discriminated against visible light photons (eV) and thermal excitations (meV), therefore, the readout is essentially free of noise. When an event surpasses the configurable energy threshold it is counted in a digital register. As the deposited charge is not accumulated, the maximum number of photons per pixel is only limited by the maximum count rate, typically between 10^5 and 10^6 events per second and pixel. As such, the achievable dynamic range is far superior to conventional devices.

Photon-counting detectors are commercially available from various manufacturers, PtyNAMi uses the EIGER X 4M-PtyNAMi manufactured by DECTRIS. On this customized variant of the detector, the Mylar window can be removed to allow operation of the bare active area in vacuum [127, 128]. The detector features four million pixels, sized $75 \times 75 \mu\text{m}^2$, grouped in eight panels, and reaches frame rates of up to 750 Hz with readout times of 3 μs between frames.

The EIGER detector fulfills all of our requirements. The task of the detector device is to transport the beam from the sample position to this detector with minimal loss of signal quality.

6.1.2 Incoherent background scattering

As the area detector is noise-free, one might think that the dynamic range is unbounded and that scattering signals from all q-vectors can be collected. This is not the case as scattering of the beam on materials outside the sample produces an incoherent scattering background on the detector. This scattering background forms a noise floor in the detector image and thus weak scattering signals cannot be detected.

Decreasing the background scattering improves the signal-to-noise ratio (SNR), permitting to detect signals at higher q-values and thereby enlarging the virtual NA of the detector, directly leading to an improvement of the achievable spatial resolution (see section 2.3.1).

Background scattering from beamline elements upstream of the sample is blocked by the slits and the pinhole in place. As the pinhole is produced from crystalline material, it scatters dominantly to large angles, not hitting the detector.

Downstream from the sample position no further shielding can be used as any material in the beam path will scatter photons from the intense central beam to higher angles. Therefore, the detector device must be designed to minimize the amount of scattering material in the beam path.

In the past, this problem was solved by moving an evacuated flight tube with entrance windows at both ends between sample and detector. However, as was shown

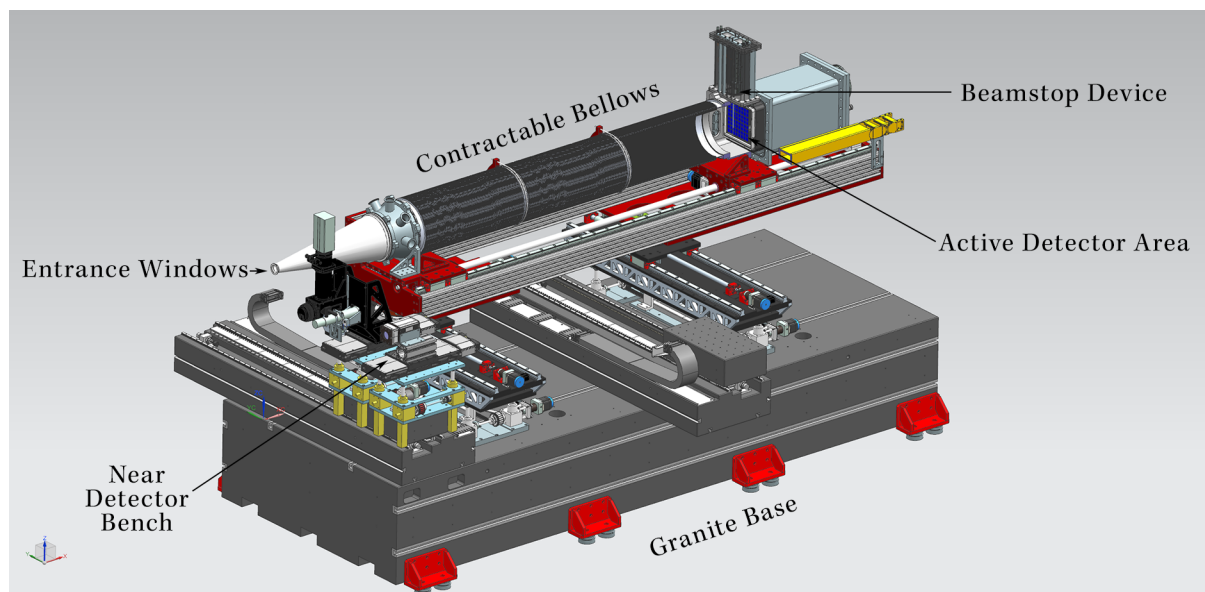


Figure 6.1: The PtyNAMi detector device with a virtual cut through the bellows to reveal the active area of the area detector (in blue). CAD rendering by Patrik Wiljes.

in previous work [129], the remaining air gap immediately in front of the detector has the largest impact on the scattering background. It was therefore essential to eliminate the exit window of the flight tube and the small air gap in front of the detector by installing a windowless detector directly into the vacuum.

6.1.3 Mechanical design

The design of the detector device is shown in figure 6.1. The evacuated flight tube on the top has an entrance window in the tip of the cone. A bellows system permits the flight tube to contract to a minimum length of 1440 mm and expand to a maximum of 3340 mm. In the CAD rendering the bellows have been cut open to expose the active area of the detector, rendered in dark blue. The protrusion just above the detector houses the positioning stages for the beamstop [130].

The stages permit the flight tube to move in five degrees of freedom, i.e. three translations as well as pitch and yaw. Since ptychography usually records the diffraction pattern along the optical axis, these are mostly used for other types of experiments at PtyNAMi, but they also have to be used when a KB or MLL focusing system is used that deflects the optical axis.

The flight tube is evacuated using a scroll pump, but the vacuum can be maintained by a single turbo pump (residual pressure 8×10^{-4} mbar). Additional vibration measurements have been performed to ensure that this turbo pump does not introduce additional vibrations to the setup, and no discernible contribution was found.

6.1.4 Beamstops

Scattering from the intense central beam can also be avoided by simply blocking the central beam with a small x-ray absorber¹ of appropriate size, placed into the beam path downstream of the sample. This is routinely done in conventional SAXS measurements, where the photon flux is much higher, to avoid damaging the detector.

In ptychography, blocking the central beam prevents the reconstruction of all low spatial frequencies, effectively applying a high-pass filter to all images and making quantitative imaging impossible. A second scan has then to be performed to measure the low frequencies in the central beam and in the reconstruction algorithm both measurements have to be combined.²

This measuring scheme has been explored in depth by Juliane Reinhardt [132, 133] and has proven to lead to a significant improvement of the SNR and reconstruction quality in experimental configurations with an air gap in front of the detector.

With the new PtyNAMi detector device and its windowless in-vacuum detector, the question now arises if such a measurement scheme is still necessary.

6.2 Background measurements

Three background measurements are presented: First, measurements at atmospheric pressure are compared to evacuated detector device and the effect of the beamstop is determined (6.2.1), second, the position of the entrance window is scanned (6.2.2), and third, the effect of the in situ cell on the background is discussed (6.2.3).

6.2.1 Evacuated flight path and beamstop

The background scattering was assessed in an experimental configuration at 9 keV photon energy using a focusing scheme with FZPs as in figure 3.5 on page 43. Without a sample, the empty beam was measured for ten counts à 60 s both with and without the beamstop. The beamstop was made by punching a disk of 10 mm diameter from lead tape and placed into the beamstop positioning device about 4 cm in front of the detector. The detector device was then flushed with dry nitrogen until ambient pressure was reached and the measurements were repeated. Additionally, a test sample of copper nanocubes was measured in both situations.

Figure 6.2 shows the detector images of these measurements. In the detector images measured under nitrogen the background scattering fills the entire detector. The beamstop is not capable to mitigate the background scattering, the improvement is

¹The beamstop can also contain a PIN diode to measure the intensity of the central beam.

²A possible compromise is a semi-transparent beamstop that attenuates but not fully blocks the central beam. This scheme has been demonstrated in the past [129, 131] but did not find widespread adaptation.

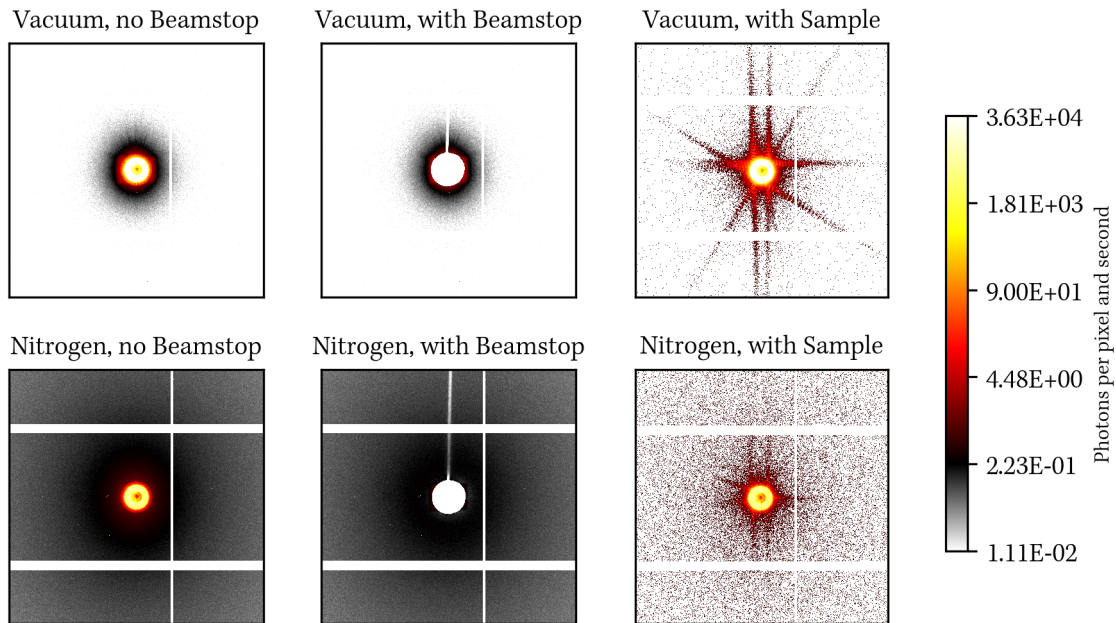


Figure 6.2: Comparison of the empty beams of an evacuated flight tube and a ventilated flight tube. All images are normalized to 1 s dwell time and displayed with identical LUT. Empty beam measurements are averaged over 600 s dwell time in total, images with sample are a single diffraction pattern of 2 s dwell time. Images are cropped to the size used in ptychography.

nearly null. On the other hand, the diffraction pattern measured in vacuum only shows background scattering in the vicinity of the direct beam, the outer areas appear clean.

The measurement with the sample was performed on the ultra-stable setup, therefore, diffraction patterns from identical sample positions could be obtained. In vacuum, the diffraction signal reaches the edges of the cropped diffraction pattern that are equivalent to 6.6 nm pixel size. In contrast, in the diffraction pattern measured under nitrogen, the scattering signal does not reach the edges, it quickly disappears into the shot noise of the background scattering. Therefore, any information at these high spatial frequencies is lost.

For a quantitative analysis, the collected empty beam images are azimuthally integrated and plotted as radial profiles in figure 6.3. A common figure of merit in such radial plots is the dynamic range, i.e. the ratio of the maximum to the minimum. The dynamic range is calculated for both the entire detector image and a cropping equivalent to 5 nm pixel size in table 6.1.

Starting at small scattering vectors, we see that the lead beamstop effectively blocks the central beam. The total intensity of the beam in nitrogen is reduced by an order of magnitude as expected for about 3 m of nitrogen at ambient pressure [134]. The scattering background is increased by an order of magnitude in nitrogen, in total, the dynamic range is reduced by a factor 88 at the edge of the detector and by a factor 162 at the 5 nm pixel size mark.

In nitrogen, the beamstop improves the scattering background close to the direct

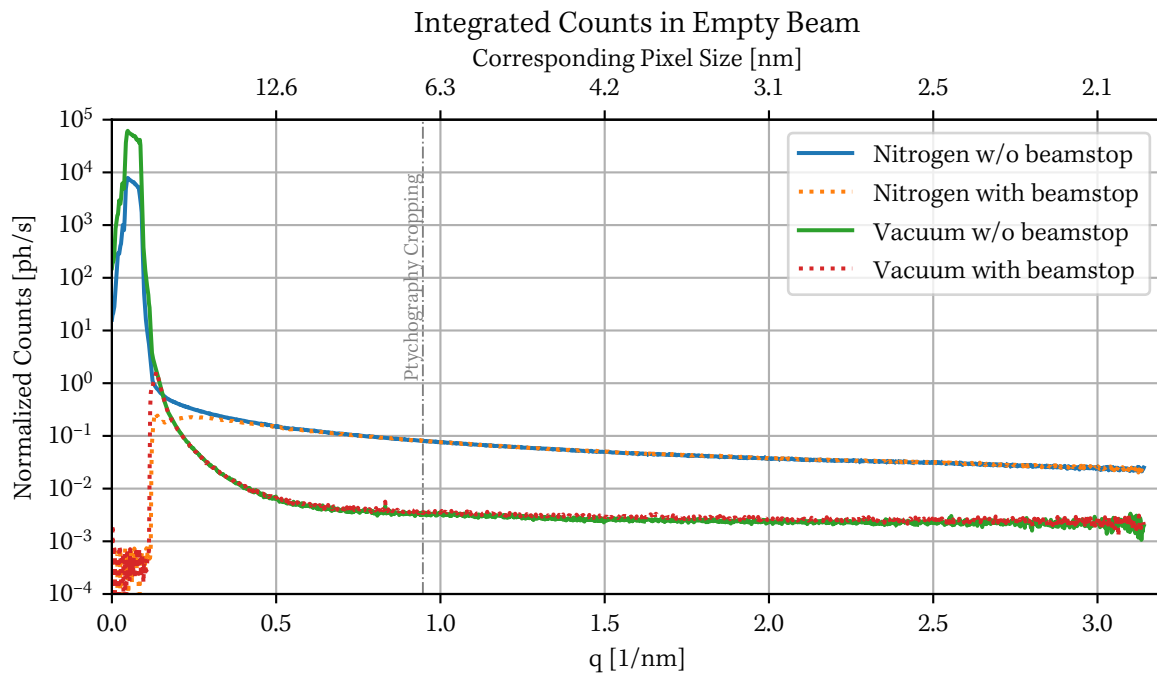


Figure 6.3: Radial profiles of the empty beams with nitrogen and vacuum as well as a beamstop. Measured at a photon energy of 9 keV and a detector distance of 3700 mm using FZPs for focusing.

Atmo- sphere	Beam- stop	Global			5 nm pixel size	
		Maximum	Minimum	Ratio	Minimum	Ratio
Vac.	Out	6.2×10^4	2.1×10^{-3}	2.9×10^7	2.9×10^{-3}	2.1×10^7
Vac.	In	-	2.3×10^{-3}	2.7×10^7	3.2×10^{-3}	2.0×10^7
N ₂	Out	7.9×10^3	2.4×10^{-2}	3.3×10^5	6.0×10^{-2}	1.3×10^5
N ₂	In	-	2.4×10^{-2}	3.2×10^5	6.0×10^{-2}	1.3×10^5

Table 6.1: Evaluation of radial profiles in figure 6.3. Maximum and minimum values are measured in photons per pixel and second. The global minimum is the average of all values of $q > 3 \text{ nm}^{-1}$, the minimum at the 5 nm pixel size mark is calculated as the average of the 10 data points nearest to $q = 2\pi/5 \text{ nm}$. The ratios of the beamstop measurements are calculated taking the maximum beam intensity from the equivalent measurement without beamstop.

beam at scattering vectors between 0.2 to 0.4 nm^{-1} . In vacuum and at higher q -ranges the beamstop has minuscule, negative effect on the scattering background that is probably caused by scattering on the edges of the beamstop itself.

The data clearly shows that, in the experimentally relevant vacuum case, the beamstop cannot improve the scattering background on the detector. Therefore, it is not necessary to combine two scans for a high-resolution ptychographic reconstruction, making experiments much quicker and simpler.

It is crucial to emphasize that this result can only be considered definitive for the tested experimental configuration. The material and make of the beamstop, especially of the edges, as well as the size and the placement along the beam path are all factors that are influence the effectiveness of the beamstop and that could not be tested. It

remains possible that a different beamstop, placed further upstream, could produce a notable improvement, but whether such an hypothetical improvement warrants using an increased amount of beamtime and a much more involved reconstruction process is an open question.

6.2.1.1 Ptychographic test measurements

As the evacuation of the flight path improves the scattering background by an order of magnitude, the resulting improvement of signal quality is clearly visible in ptychographic reconstructions.

Figure 6.4 shows the reconstructed object modulus and phase shift of two ptychographic measurements with identical parameters,³ during which the flight tube was once evacuated and once flushed with dry nitrogen at ambient pressure. The difference in spatial resolution is immediately visible, the image measured under nitrogen is softer throughout. In this next chapter, we will use Fourier ring correlation to estimate a resolution of 11 nm with the evacuated detector device and 22 nm in the nitrogen case.

In the zoomed-in region in figures 6.4e and 6.4f several smaller cubes lay in top of each other. This is only recognizable in the vacuum measurement, under nitrogen they appear as a single continuous body. Closer inspection of 6.4e reveals that, in addition to the decrease in spatial resolution, the image is also much noisier on the pixel level.

These differences are rather extreme as we were only able to measure with an either completely evacuated or fully vented detector device. A more relevant comparison would have been to include only a small air gap in front of the detector, such as was the case in the previous setup. With the detector inside the vacuum chamber, such a measurement could not be realized.

6.2.2 Position of the entrance window

Initially, the position of the entrance window was not considered as a significant factor, since prior work [129] had demonstrated that the dominating contributions of the background are produced by scattering close to the detector. However, in the absence of any scatterers in the vicinity of the detector, the entrance window of the flight tube is the closest source of background scattering.

In the measurements presented above, the kapton entrance window was placed about 300 mm downstream of the pinhole. To assess the influence of the window position along the beam path, the distance between pinhole and entrance window was reduced to 60 mm, the entrance window was then scanned in 100 mm steps downstream. The contractable bellow system was used to keep the position of the detector constant. This data is presented in figure 6.5.

³5 μm \times 5 μm field of view, 20 \times 20 steps, 2 s dwell time, ultra-stable setup, 9 keV photon energy.

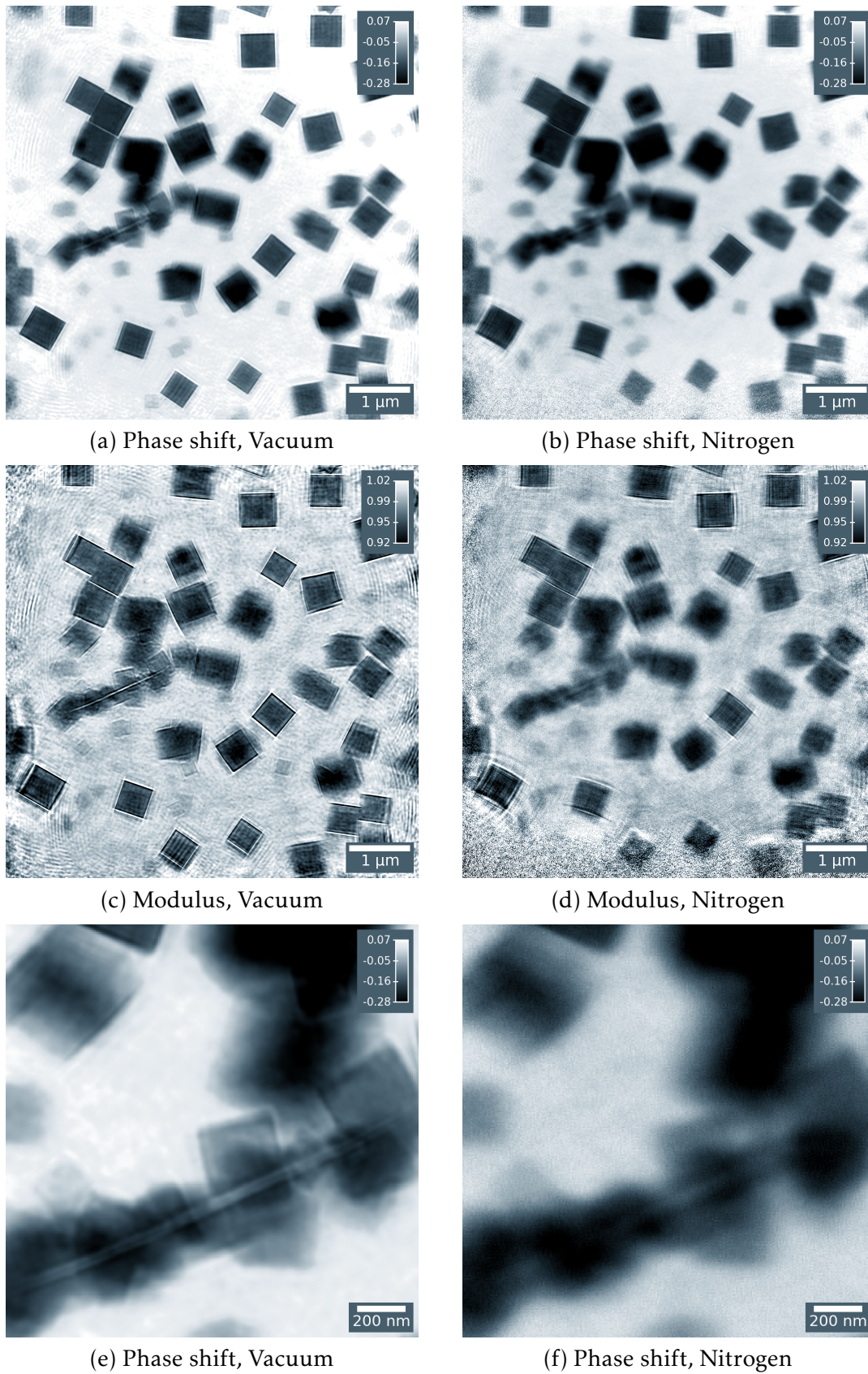


Figure 6.4: Ptychographic measurements on ultra-stable 2D setup to determine the influence of an evacuated flight path. a,c,e) Recorded with evacuated flight tube b,d,f) Flight tube flushed with dry nitrogen at ambient pressure a,b,e,f) Reconstructed phase shift c,d) Reconstructed modulus.

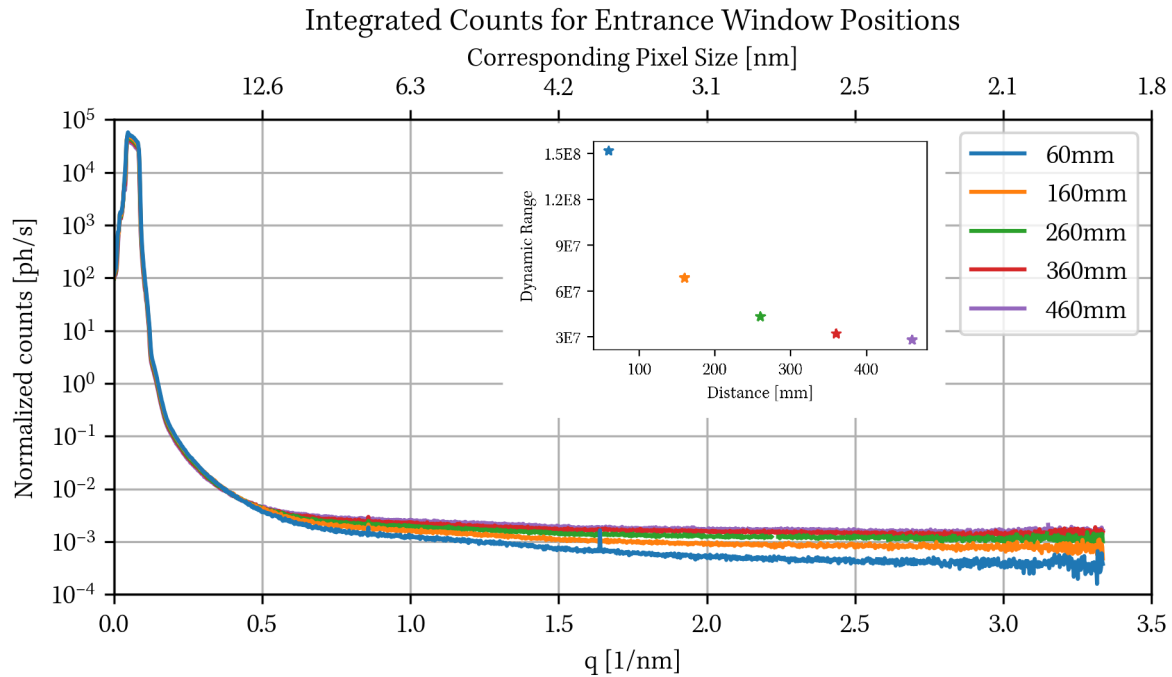


Figure 6.5: Effect of moving the entrance window of the evacuated flight tube, distances are measured from the pinhole to entrance window. The dynamic range is here defined as the maximum of the curve divided by the minimum, where the minimum is determined by averaging all values above 3 nm^{-1} . Measured at 9.3 keV photon energy and a constant detector distance of 3600 mm using FZPs.

It is evident that the scattering background can be improved significantly by moving the entrance window as close as possible to the sample position. Moving the entrance window 400 mm closer improves the dynamic range on the detector by a factor of 5. In this case, the dynamic range is now 1.5×10^8 or 27.2 bit.

6.2.3 Influence of the in situ cell

The effect of the in situ cell on the scattering background was measured at a later point in time under improved experimental conditions that positively affected the scattering background: The entrance window of the detector device was changed from kapton to diamond, the focusing optics were changed from FZPs to silicon refractive lenses (NFLs) and the photon energy was increased to 15 keV.⁴

The cumulative effect of these changes is an improvement of the dynamic range from 1.5×10^8 to 2.5×10^9 , i.e. 31.2 bit. The individual contributions to this improvement cannot be determined here, further studies at various experimental conditions are necessary.

The in situ cell was prepared in such a state that it was ready for the chemical synthesis, i.e. the kapton windows were installed, the cell was filled with the benzyl

⁴In the prior measurements, 9 keV photon energy was chosen for resonant measurements on the copper absorption edge. For the in situ measurements, 15 keV photon energy was chosen as a compromise of transmission through the cell and available coherent flux. The change of photon energy necessitated the change of focusing optics.

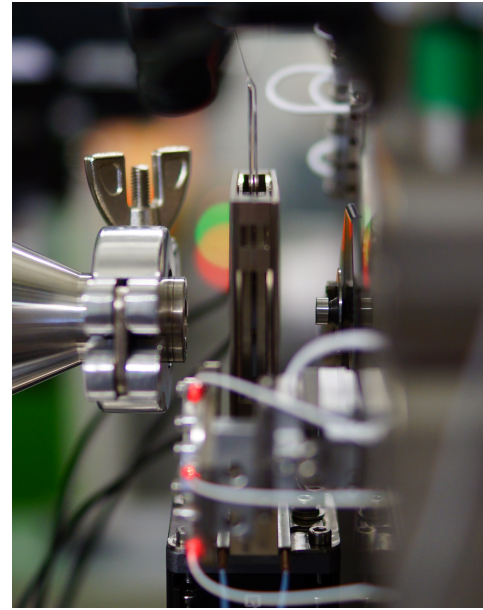
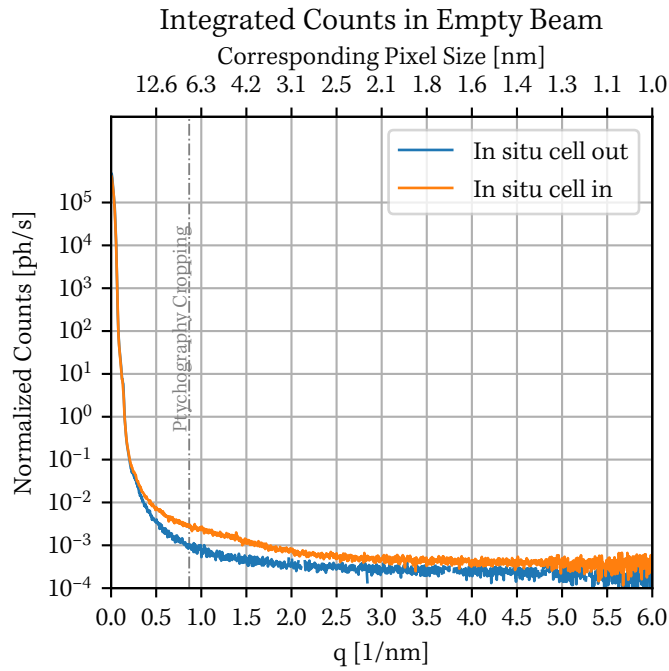


Figure 6.6: Effect of the in situ cell on the incoherent scattering background. Measured at 15 keV and a detector distance of 3370 mm using silicon NFLs. Different to the previous measurements, a diamond windows was used as the entrance window to the flight tube (left in the photo) instead of the kapton window.

In situ cell	Maximum	Global		5 nm pixel size	
		Minimum	Ratio	Minimum	Ratio
Out	4.8×10^5	1.9×10^{-4}	2.5×10^9	5.2×10^{-4}	9.3×10^8
In	4.2×10^5	3.9×10^{-4}	1.1×10^9	1.7×10^{-3}	2.8×10^8

Table 6.2: Evaluation of the dynamic range of the radial profiles in fig. 6.6. Maximum and minimum values are measured in photons per pixel and second. The global minimum was calculated as the average of all values of $q > 5 \text{ nm}^{-1}$.

alcohol solvent and the copper acetylacetonate precursor material in solution. As copper particles start to form as soon as the cell is heated, the scattering background was measured in the cold state before the synthesis was initiated.

Figure 6.6 shows the radial profiles acquired and a photograph of the setup, table 6.2 states the dynamic range in the empty beam measurements. The filled in situ cell attenuates the central beam by 12.5% which is close to the design value of 10%. The scattering background at high q -vectors at the edge of the detector is doubled by the in situ cell.

Regarding the background at $q = 1.25 \text{ nm}^{-1}$, i.e. at a equivalent pixel size of 5 nm, the increase in scattering background is larger, in total the dynamic range is reduced by a factor of 3.3 to 2.8×10^8 . This is still a comparatively small effect that does not suffice to explain the loss of resolution of the in situ measurements (chapter 8).

6.3 Summary

We can summarize this chapter in four points:

1. An in-vacuum, photon-counting detector is the ideal area detector for far-field ptychography, but it is challenging to suppress incoherent background scattering on the detector.
2. With the in-vacuum detector device of PtyNAMi, a dynamic range of 1.5×10^8 at 9 keV and 2.5×10^9 at 15 keV of the empty beam on the detector is achievable.
3. Using a beamstop to block the central beam close to the detector does not further improve the dynamic range. In consequence, additional scans with beamstops are not necessary, speeding up measurements and simplifying the data analysis.
4. The in situ cell constructed for measurements in heated solutions only decreases the dynamic range by a moderate factor of 3.3 at 15 keV.

Chapter 7

High-resolution ptychography

In this chapter, we present several ptychography measurements conducted under favorable conditions to reach high spatial resolution. All measurements have been performed on the ultra-stable setup with monitored sample vibrations in the order of 1 nm rms and with the evacuated detector device presented in the previous chapter. The samples of choice are copper cubes as presented in the previous chapters, giving us a strongly scattering object with sharp edges.

We begin this chapter with a short discussion about the necessity to use upsampling in the reconstructions of these measurements. In the next step, we estimate the resolution achieved in single-slice measurements, obtaining results around the 10 nm mark.

Before answering the question if this transversal resolution can be transferred to reconstructions with up to four slices, we discuss a method to determine the correct slice distance with contrast-based methods.

7.1 Upsampling and diffractive optics

Initially, the experiment presented here was planned as a multi-slice resonant ptychography measurement, i.e. the sample with particles on both sides of kapton substrate was scanned at several energies around the K-edge at copper at 8.98 keV [135] to determine the oxidation state. To this end, a zone plate of 125 μm diameter, 70 nm outer zone width and 64 mm focal length was chosen as the most efficient focusing optics. The zeroth order was blocked by a central stop of 50 μm diameter upstream of the zone plate and a 30 μm OSA close to the focus.

As a test at the beginning of the experiment, one side of a sample was cleaned of particles so that the conventional single-slice algorithm could be used. The amplitude

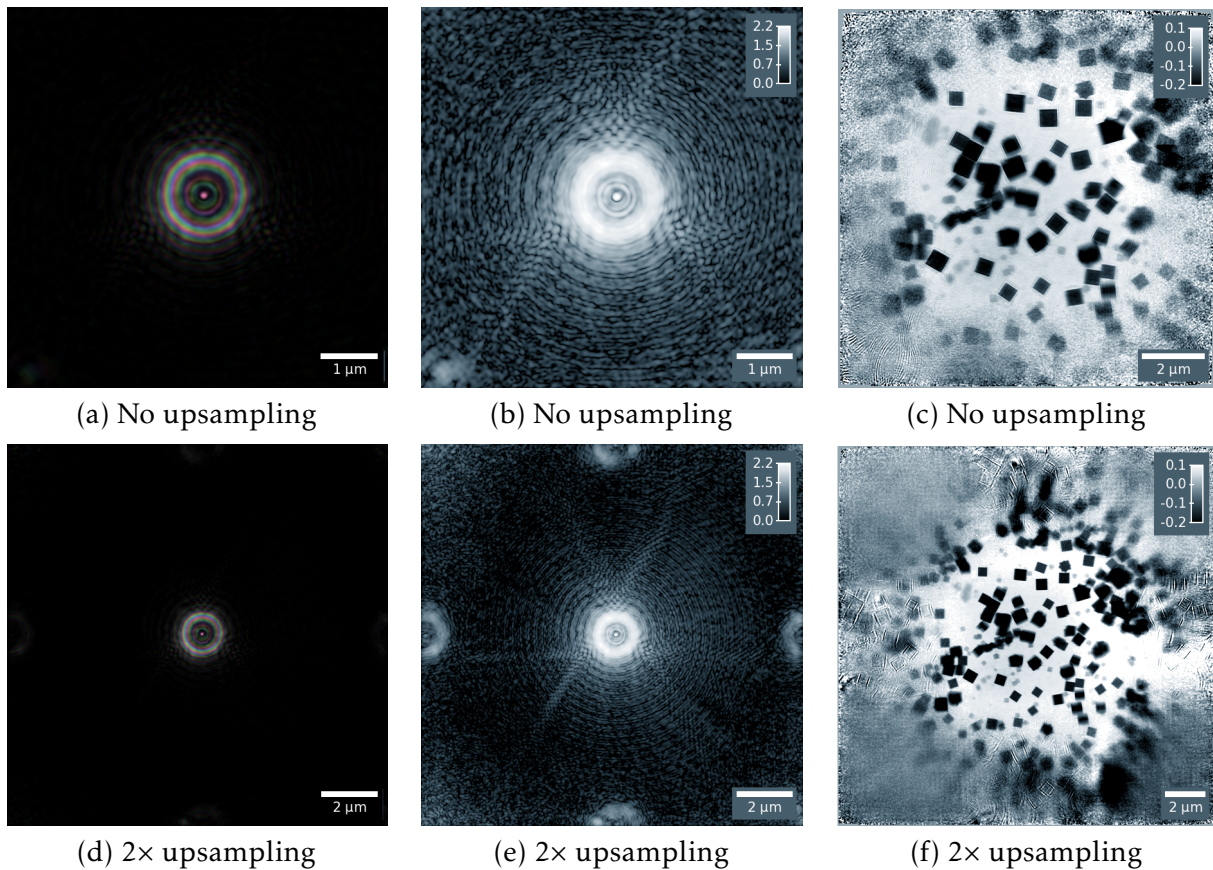


Figure 7.1: Comparison of single-slice reconstruction without upsampling (a,b,c) and with 2 \times upsampling (d,e,f). a,d) The probe function, displayed with the amplitude in linear scale as brightness and the phase as the hue. b,e) Logarithm of the amplitude of the probe function. The entire frame is filled with stray radiation from the diffractive optics. d,f) Uncropped reconstructed object. Conventionally, the center part of the upsampled image (f) is presented as the result of the reconstruction, here the full frame with all additional copies of the object at the edges of the field of view is shown.

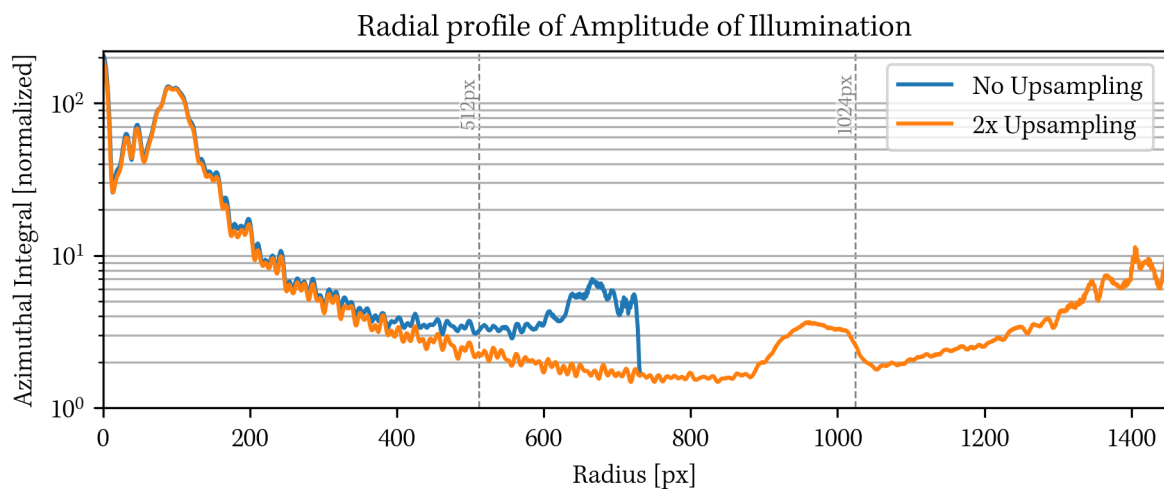


Figure 7.2: Azimuthal integration of the probe amplitudes shown in figure 7.1. The size of the probe field is 512 \times 512px without upsampling and 1024 \times 1024px with 2 \times upsampling; the azimuthal integral is calculated up to the corners of the field.

of the reconstructed probe field in this sample plane¹ is shown in fig. 7.1a in linear scale and in fig. 7.1b in logarithmic scale. As the FWHM of the probe is $1.6\ \mu\text{m}$ in a probe field of $6.8 \times 6.8\ \mu\text{m}^2$, the Nyquist condition (see section 2.2.2) should be fulfilled.

However, as is evident with logarithmic scaling, the beam intensity does not drop to zero outside the primary beam. The entire probe field is filled stray radiation that primarily originates from the central stop and the zone plate. This stray radiation is quantified in the azimuthal integration of the probe beam in figure 7.2; the probe amplitude falls by less than two orders of magnitude in the field of view. In comparison, the foci produced by refractive optics are cleaner, i.e. the intensity drops faster as a function of the radius [136].

By reconstructing the data set with $2\times$ upsampling, we virtually double the size of the probe field in both dimensions. With logarithmic scaling (fig. 7.1e), we can see that the diffraction of the zone plate, and in particular the hexagonal streaks caused by the central stop, extend far beyond the conventional probe field. In the reconstruction without upsampling, these outer features are not sampled correctly in the detector plane and are "reflected" back into the probe field by Fourier aliasing [8, p. 112]. In the multi-slice measurements presented below, the probe is larger in the additional planes, further increasing this effect.

However, the upsampled reconstruction is also not without flaws. On the edges of the probe field (fig. 7.1e), copies of the illumination appear that produce copies of the object (fig. 7.1f). Usually, these additional copies of the object are cropped out and not shown, as will be done in all following upsampled reconstructions.

The additional partial copies of the object, together with the low-frequency multi-slice artifacts discussed below, ultimately led to the loss of quantitative information in the reconstructions and with that to the incapability to extract useful spectroscopic information in the relevant XANES and EXAFS regions.

7.2 Transversal resolution of single-slice reconstructions

7.2.1 Fourier Ring Correlation

In figure 7.3, several reconstruction variants are shown that are used to estimate the transversal resolution with FRC. The measurement presented above is again reconstructed with and without upsampling, but this time as split data sets which are reconstructed independently from each other and correlated for a resolution estimation. Here, the figure shows the crop of the central region.

¹Here, the sample plane is not identical to the focus plane. As discussed in chapter 2, when not measuring complementary contrasts simultaneously, it is in general beneficial to move the sample out of the focus plane, thereby increasing the overlap and permitting longer dwell times at each of the fewer points of exposure.

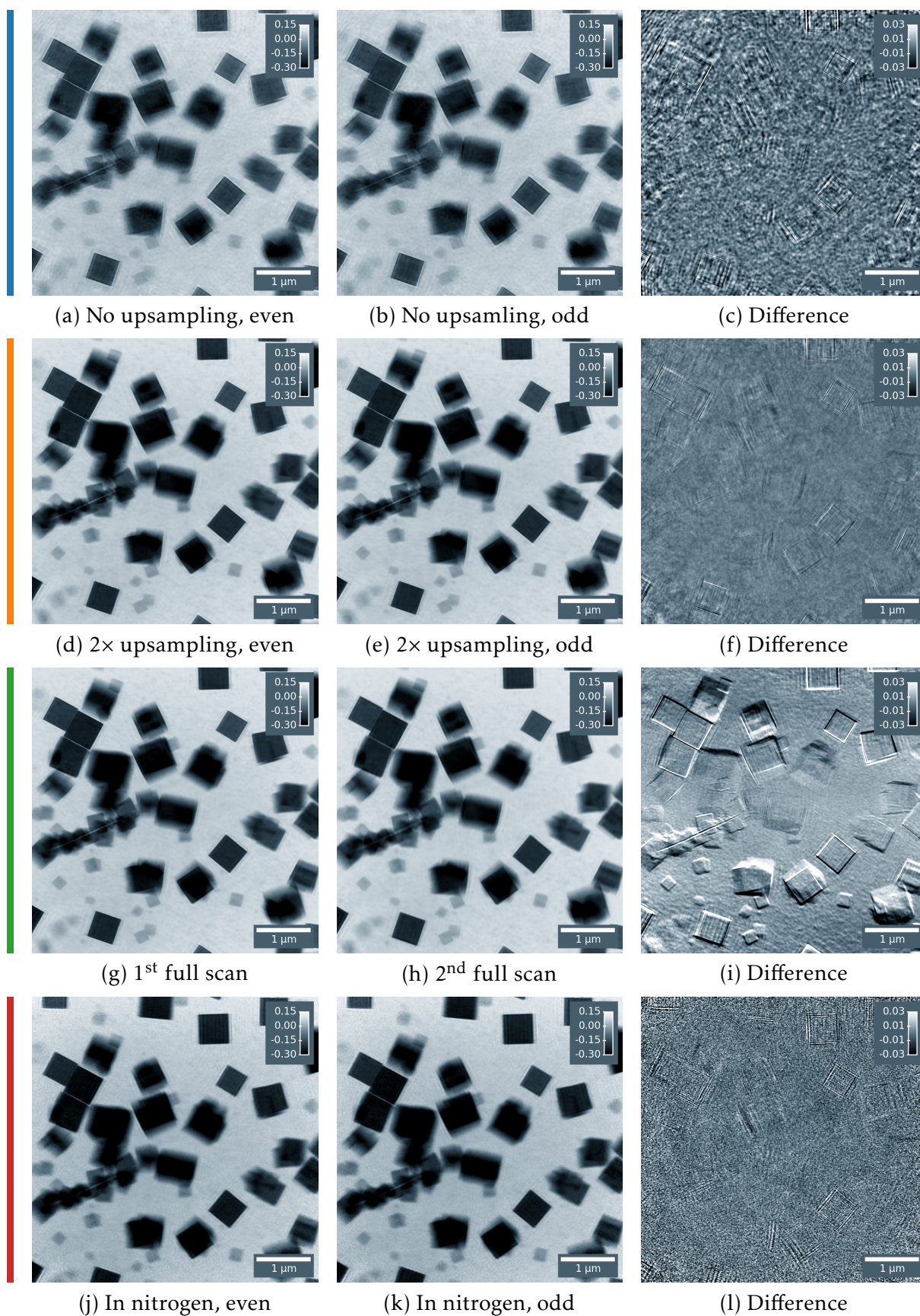


Figure 7.3: Reconstructions of single-slice sample for resolution estimation with FRC. a,b,c) Split data set reconstructed without upsampling. d,e,f) Split data set reconstructed with 2× upsampling. g,h,i) Reconstructions of full data sets of two consequent scans with identical scan parameters, with 2× upsampling. j,k,l) Split data set measured under nitrogen atmosphere, with 2× upsampling.

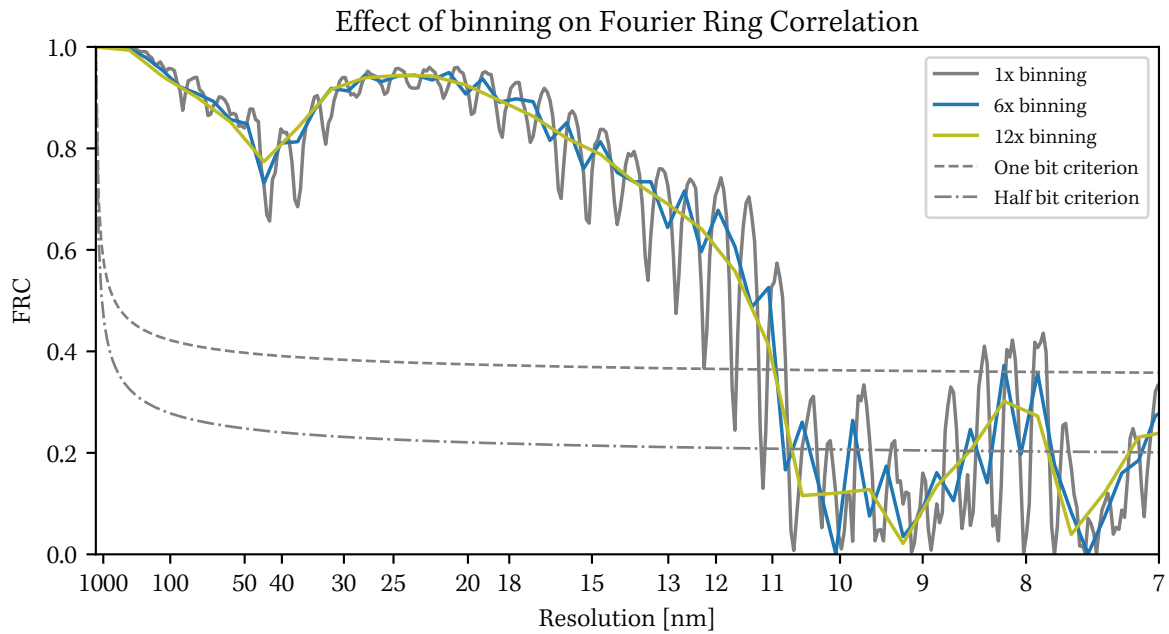


Figure 7.4: The effect binning in FRC, i.e. correlating rings of larger thickness in Fourier space. Here a moderate binning of 6× was selected for the following analysis.

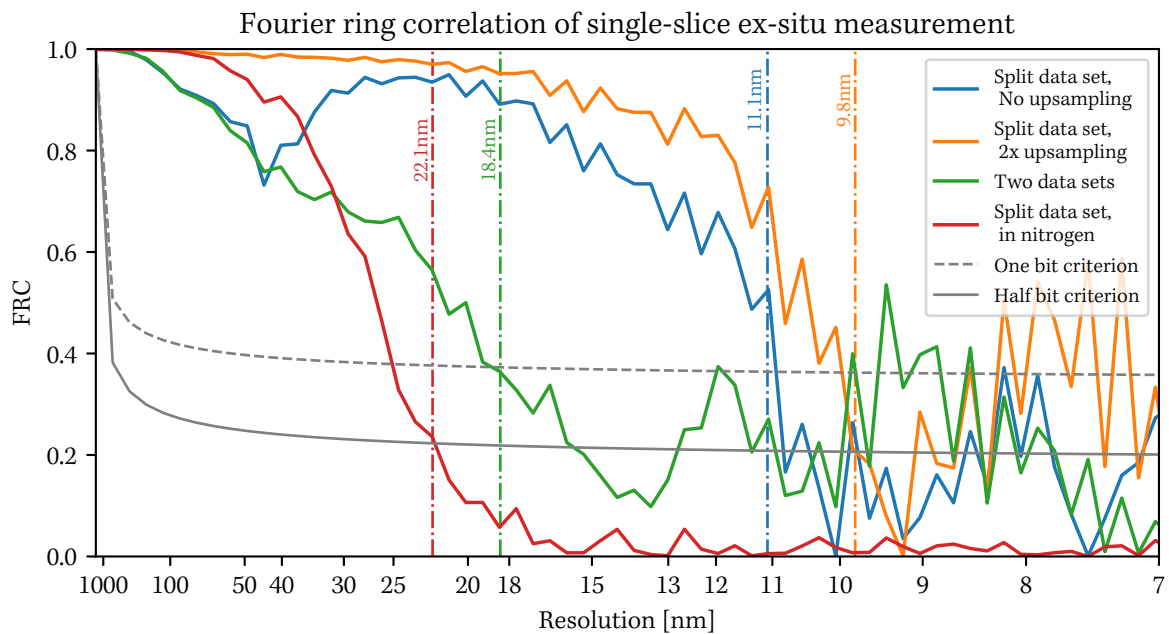


Figure 7.5: FRC curves of the reconstructions in figure 7.3. The correlation of the two full scans is evaluated at the one bit criterion, the split data sets are evaluated at the half bit criterion.

Even though the images are scaled identically, a difference in contrast between the reconstructions without upsampling (fig. 7.3a,b) and with $2\times$ upsampling (fig. 7.3d,e) is visible. This further illustrates the loss of quantitative information in upsampled reconstructions.

The difference image of the two split reconstructions show clear edge and ringing artifacts in the case without upsampling (fig. 7.3c) that are not present in the difference of the upsampled split reconstructions (fig. 7.3f). These edges and ringing artifacts are precisely what is found in the additional copies of the object in fig. 7.1f.

As a second variant of FRC, we also compare the reconstruction of the full scan with a second scan that was acquired immediately after the first one with identical parameters.² In the difference image in fig. 7.3i, the reconstructed images appear to be not correctly aligned. However, closer inspection reveals that the second image is compressed along the vertical axis. Therefore, both images cannot be aligned better by translation and rotation. This effect may be attributed to contraction of the kapton substrate which was observed on multiple occasions and may be caused by beam damage (see also appendix D), even though a vertical drift of the sample cannot be excluded conclusively.

The fourth data set (fig. 7.3j-l) is the case of the detector device being fully flushed with dry nitrogen. In this case the difference image is governed by noise.

7.2.1.1 FRC binning

When calculating the FRC of these reconstructions with the conventional method, i.e. correlating over rings in Fourier space that are 1 px in width, the resulting curve shows strong oscillations (fig. 7.4). As we define the resolution estimate as the first intersection of the FRC curve with the half-bit criterion, these oscillations can lead to non-representative results. To smoothen the curve, a binning can be applied in Fourier space, i.e. the width of rings that are correlated is increased to multiple pixels.

In figure 7.4, the curve is recalculated with both $6\times$ and $12\times$ binning. To my knowledge, there is no hard criterion which can be used to chose a "correct" binning, therefore, the $6\times$ binning was selected as a trade-off between determining a meaningful cut-off value and still maintaining some of the oscillating nature of the curve.

7.2.1.2 FRC results

In figure 7.5, the FRCs of all scans in figure 7.3 is plotted. Starting with the red curve, representing the measurement in nitrogen, we see the typically expected behavior of $FRC(k)$. The curve starts flat at full correlation close to $k = 0$, falls monotonously,

²All scans presented in this section were recorded at 9 keV photon energy, scanning a field of $5\times 5\ \mu\text{m}^2$ in 20×20 steps with 2 s dwell time. The positions in the grid were randomly jittered by up to 50% of the step width. Between scans fig. 7.3g and fig. 7.3h the position of the beam on the detector with respect to the panel gaps was altered.

crossing the half-bit criterion at the 22.1 nm resolution mark and then converges to 0 for large k . This is the expected form of the curve for a measurement limited by noise. Referring to the diffraction patterns in this experimental situation (fig. 6.2 on page 89), we see that the detectability of the scattering signal over the noise floor is the resolution-limiting factor in this case.

The three remaining curves, which were all measured with the evacuated detector device, do not converge towards 0 for large k . Even though all curves decline and cross the criterion line, giving us a number for the resolution estimate, the correlation increases afterwards again. This is an indication that the spatial resolution of these measurements is not limited by the strength of the scattering signal.

The worst result obtained with the evacuated detector device is produced by the correlation of the two consequent scans with an estimate of 18.4 nm due to the vertical contraction issues. This correlation is curve is evaluated at the one bit criterion as two full data sets are correlated. The reasoning is that two scans contain twice the signal of one split data set [137]. However, as we have indications that the reconstructed images are not signal-limited, that argument may not apply here.

Correlating the split data set yields much better results. In the reconstruction with $2\times$ upsampling, $FRC(k)$ crosses the half-bit criterion first at 9.8 nm, but several times more in the range from 8 nm to 7 nm. As the pixel size in this geometry is 6.6 nm, this indicates that the entire diffraction pattern is filled, at least at some positions, with detectable signal over the noise floor.

7.2.1.3 Estimation of the signal limit

Taking the $\delta_N = 22.1$ nm resolution estimate of the measurement in nitrogen, the dynamic range DR in the empty beam determined in section 6.2.1 and Porod's law, we can estimate the theoretical signal-limited resolution δ_s as

$$\delta_s = \frac{\delta_N}{\sqrt[4]{DR_{vac}/DR_N}} = \frac{22.1 \text{ nm}}{\sqrt[4]{2.1 \times 10^7/1.3 \times 10^5}} = 6.2 \text{ nm.} \quad (7.1)$$

This result seems realistic, in particular when compared with the diffraction patterns. The pixel size in the present reconstructions is 6.6 nm and diffraction signal reaches the edges of the cropped frame.

7.2.2 Line profiles

As a complementary method to estimate the resolution we take a full scan reconstructed with $2\times$ upsampling (fig. 7.3g) and fit line profiles in the form of

$$F(x) = a \cdot \operatorname{erf}\left(\frac{(x - x_0)}{\sqrt{2}\sigma}\right) + b \quad (7.2)$$

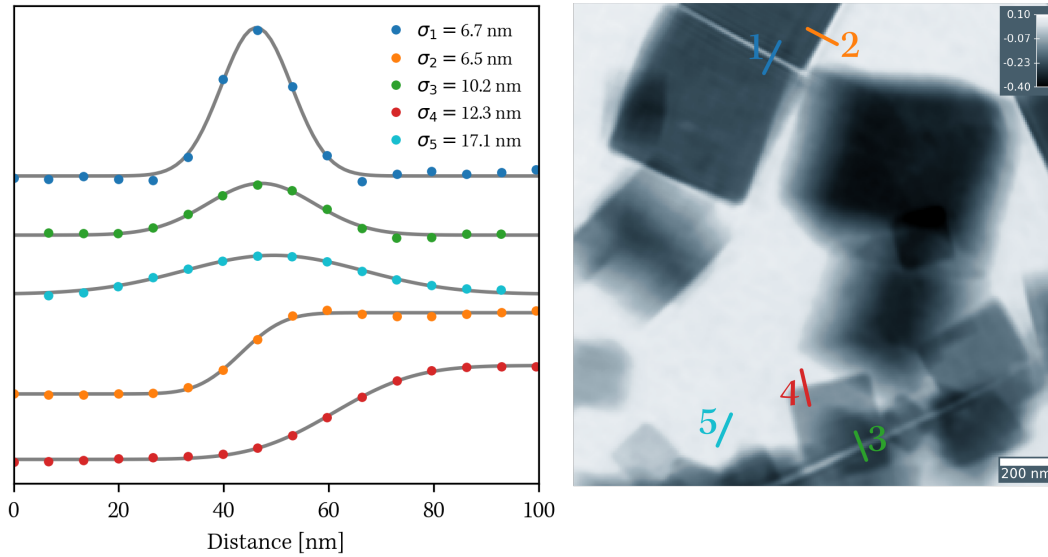


Figure 7.6: Line profiles on edges and other features, fitted with Gaussians and Gauss error functions. This is a reconstruction of a full ptychographic data set reconstructed with $2\times$ upsampling, also shown in fig. 7.3g, that achieved a resolution estimate of 9.8 nm with FRC as a split data set in fig. 7.5.

Line	1	2	3	4	5
σ	6.7 nm	6.5 nm	10.2 nm	12.3 nm	17.1 nm
FWHM	15.7 nm	15.3 nm	24.0 nm	29.0 nm	40.2 nm

Table 7.1: Resolution estimates obtained from the line profiles in figure 7.6. The FWHM is calculated from σ under the assumption of a Gaussian distribution as $\text{FWHM} = 2\sqrt{2\ln 2}\sigma$.

to the edges of the cube. As this sample has several narrow gaps, in particular between the two large cubes in the upper left corner, we can also fit these features with Gaussians of the form

$$G(x) = a \cdot \exp\left(\frac{-(x - x_0)^2}{2\sigma^2}\right) + b. \quad (7.3)$$

In both functions we are not interested in the scaling and offset parameters a , b and x_0 but only in the standard deviation σ .

The line profiles have been extracted from the image using ImageJ [138] and are shown in figure 7.6. The Gaussian profiles resp. Gaussian error functions describe the line plots well. Line plot 5 is fitted to a small feature on the substrate which is better visible in figure 7.7 below. In table 7.1 the FWHM of the line profiles are calculated from σ .

7.2.3 Discussion

We have seen clear indications that the achieved resolution in the single-slice reconstructions (FRC 9.8 nm, line profile FWHM = 15.3 nm) is not limited by the scattering signal on the detector for this strongly scattering test sample. At same time, laser-

interferometric monitoring showed vibrations of $0.8 \text{ nm} \times 1.2 \text{ nm}$ (horizontal \times vertical rms) during these measurements, so that vibrations of the sample mount are also not limiting the resolution.

At this point, we can only speculate what experimental factors limit the achievable spatial resolution. As neither vibration monitoring of the focusing optics nor quantitative monitoring of the beam steering was in place during this experiment, instabilities of the probe are a possible candidate. Another conceivable cause are vibrations of the sample that are locally induced on a microscopic or mesoscopic level by the sample-beam interactions and which are not measurable at the base of the sample mount. How such effects can be modeled or quantified may be the subject of future research.

7.3 Multi-slice measurements

Next, we measured a kapton substrate fresh out of the reaction chamber.³ According to the manufacturer, the thickness of this kapton substrate is $100 \mu\text{m}$. Taking the best resolution estimate of 9.8 nm and equation 2.11, we can calculate the expected DOF as

$$\text{DOF} = 2 \cdot \frac{\delta^2}{\lambda} = 2 \cdot \frac{(9.8 \text{ nm})^2}{0.1337 \text{ nm}} = 1.44 \mu\text{m}. \quad (7.4)$$

As such, the object is definitely a two-slice object and we expect that we have to find the correct slice distance to a precision of $1.4 \mu\text{m}$ for the best possible reconstruction.

7.3.1 Finding the slice distance

The search for the correct is distance is done iteratively by running reconstructions with various guesses of the correct distance. The resulting images can be evaluated by eye, but for a more reproducible result, an objective measure should be used. Reconstructing split scans at every distance and calculating the FRC may be a computationally expensive but precise method. With the present multi-slice data set, the reconstruction of two independent image planes was not possible when the data set was split, so that an alternative method had to be devised that works with reconstructions of the full data set.⁴

Similar to the contrast-based autofocus mechanism of digital photographic cameras, the images are first convolved with an edge-enhancing kernel⁵ and the spread of the distribution of the resulting gray values is analyzed. In figure 7.7, we see images of both object slice reconstructed at four different distances, including the manufacturer value of $100 \mu\text{m}$. Thanks to the edge contrast, we can also see a number of small particles

³This experiment was conducted before the in situ cell was available, the samples measured in this chapter were grown in a larger reaction chamber unsuitable for ptychographic imaging.

⁴With this data set in particular, the incapability to perform split reconstructions with two slices stems from the large dirt particle in the third slice. Therefore, split reconstructions with three or four slices are possible (see next section), but two slices can be only reconstructed by using the full data set.

⁵ $K \in \mathbb{R}^{5 \times 5}$, $K_{3,3} = 24$, $K_{i,j} = -1$ elsewhere. This is the default convolution Kernel in ImageJ [138].

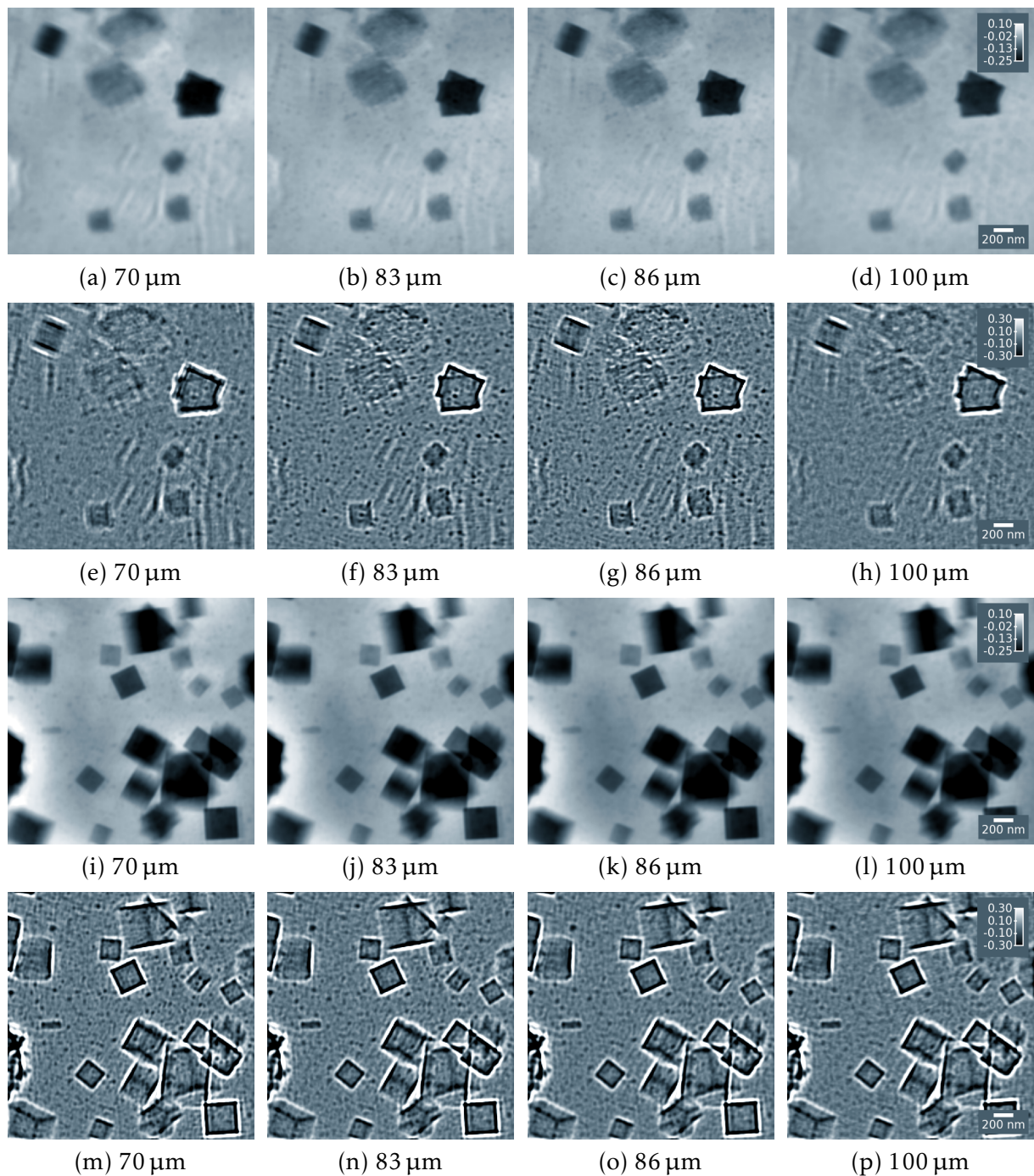


Figure 7.7: Multi-slice reconstructions with varying slice distances from 70 μm to 100 μm . Both the reconstructed phase image and an edge contrast image is shown. To make these images suitable for print, a high-pass filter was applied to remove long-range reconstruction artifacts. All phase images and edge contrast images are have respectively identical contrast and scale. a-d) Upstream slice. e-h) Edge contrast of upstream slice. i-l) Downstream slice. m-p) Edge contrast of downstream slice.

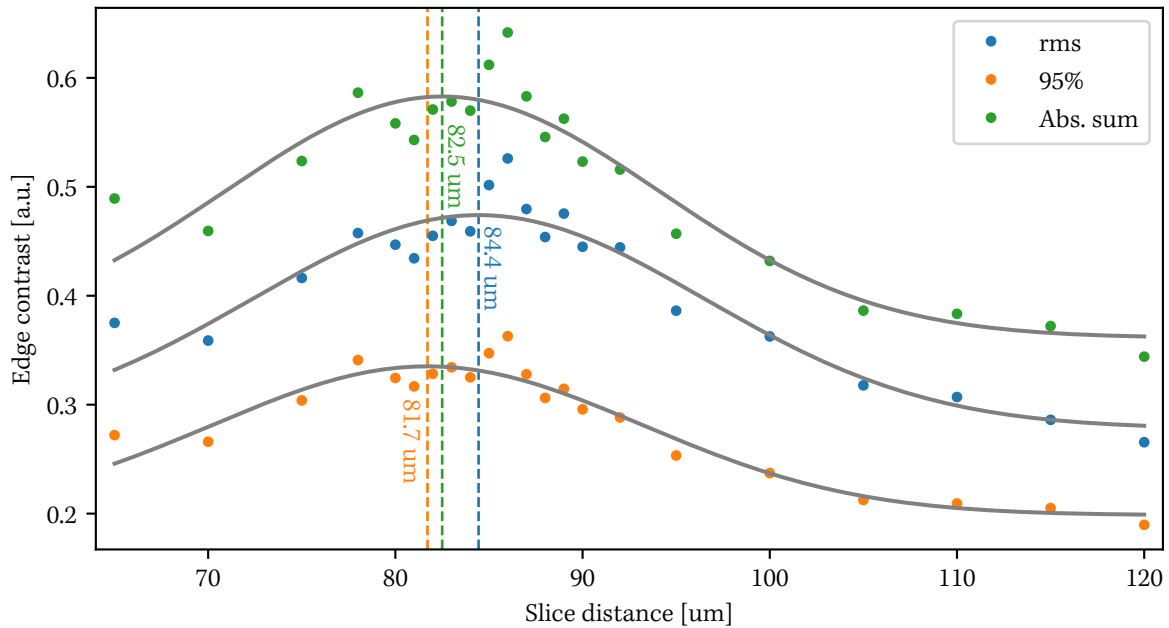


Figure 7.8: Evaluation of the edge contrast images. The rms, width of the 95%-interval and absolute sum of the pixel values are plotted and fitted with a Gaussian. The curves are rescaled along the ordinate axis to fit in the plot and are therefore in arbitrary units [a.u.].

appearing (fig. 7.7f,g) on the substrate when the slice distance is lowered to values between 80 and 90 μm . These small particles are also visible on some SEM images (e.g. in fig. 8.4b on page 122).

Comparing the amount of particles in the upstream and downstream slices of the object, the downstream slice is denser packed. As a result, the reconstruction of the downstream slice hardly changes with the slice distance while large changes are visible in the upstream slice. The reconstruction algorithm holds onto the strong scatterers in the downstream slice as a reference and lets the weak scatterers in the upstream slice go in and out of focus with changes of the slice distance.

In consequence, it suffices to analyze the distribution of gray values in the upstream slice. In figure 7.8, the rms, interquartile distance (50% of points) and sum of the absolute values of the gray values of the edge profile pictures are plotted for several slice distances and fitted with a Gaussian. The maxima of the fitted curve are between 81.7 μm and 84.4 μm , while the most contrast-rich reconstruction was achieved at 86 μm according to all three criteria. These results indicate that the DOF is larger than expected.

7.3.2 Reconstruction with four slices

While determining the inter-slice distance, we were looking at a cropped region of the object and applied a high-pass filter to remove low spatial frequency artifacts in the reconstruction that are not relevant for the edge contrast. The full object, without any filters, is shown in figures 7.9a and 7.9b. The images show a long-range artifact in the upper half that is in indicator of an object in an additional object slice.

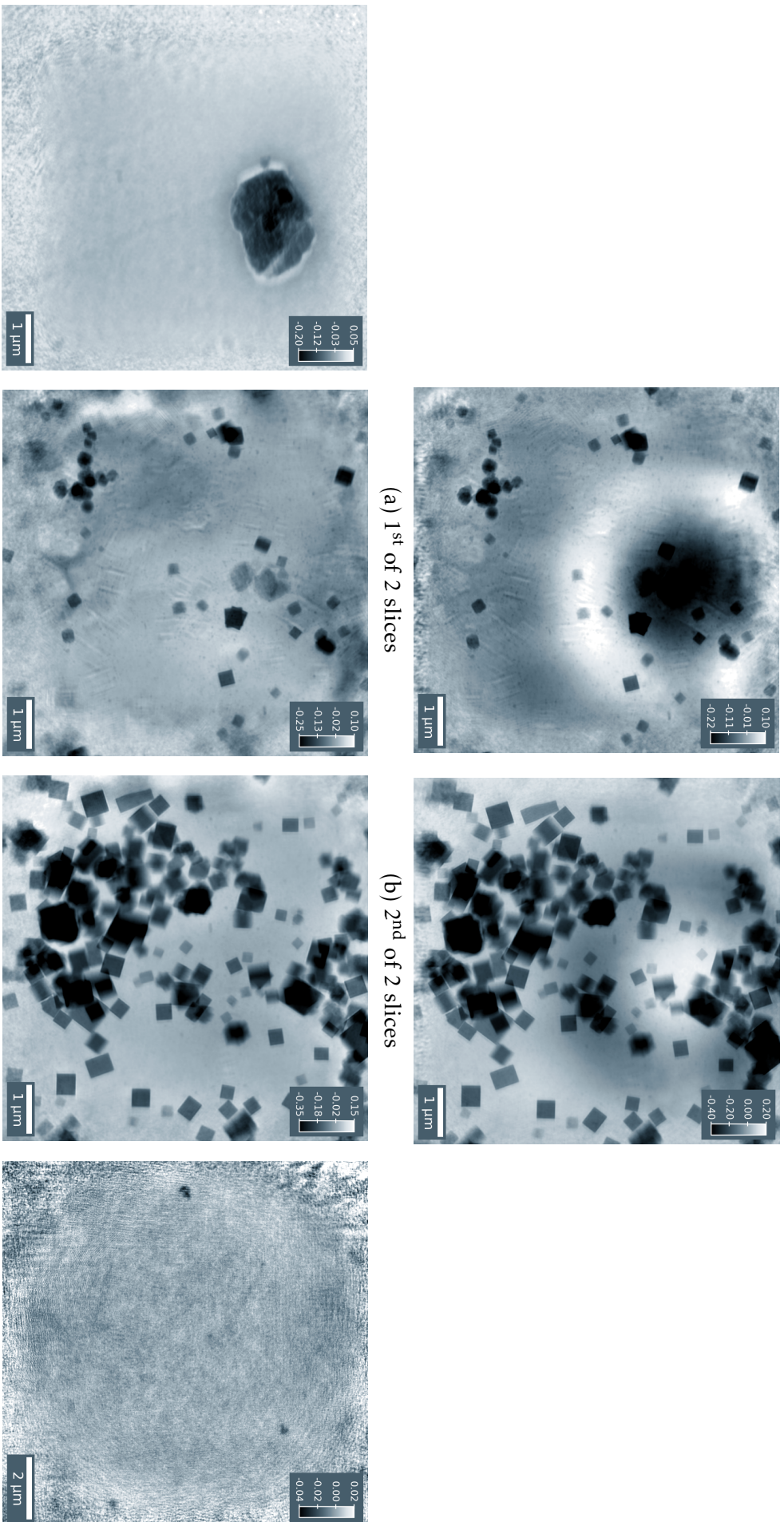


Figure 7.9: Multi-slice object reconstructed with $2\times$ upsampling. a,b) 2-slice reconstruction of both sample planes, i.e. the upstream and downstream surface of the kapton substrate. c,d,e,f) 4-slice reconstruction that also includes the entrance and exit window of the inert gas atmosphere chamber around the sample (see also appendix D). In f) a high-pass filter with a cut-off at $2\ \mu\text{m}$ was applied to the image. The figures 7.10j) and 7.10k) show this object without filter.

This sample was measured under a helium atmosphere to prevent carbon deposition on the sample (see appendix D). The helium atmosphere was contained in an enclosure around the sample with entrance and exit windows made from kapton. With a visible light microscope, the distances of the entrance and exit windows from the sample were determined roughly and then refined with the approach described above. With that, the object can be reconstructed in four slices, i.e. the entrance and exit windows and the two sample slices between them. Further separating the windows into their upstream and downstream sides yielded no result, even for other measurements not shown here with more dust on the windows.

The four reconstructed object slices are shown in figures 7.9c to 7.9f. A large dust particle is found on the entrance window of the helium enclosure (fig. 7.9c), but the exit window (fig. 7.9f) only shows sub-micron dust particles at the edges of the field of view. Even though this fourth slice is largely empty, it still reconstructs repeatably due to the constraints in the other three slices.

7.3.3 Multi-slicing artifacts

With the dust particles being separated into their own image planes, we can inspect the reconstruction of the sample closer. In the upstream object slice (fig. 7.9d) we can see two typical multi-slicing artifacts.⁶

There are clear imprints of particles from the downstream slice in the upstream slice that are in particular visible on sharp edges. Comparing the strength these edge artifact on various cubes, it is evident that the effect depends on the angular orientation. No artifacts are observed on horizontal edges, only edges that are close to vertical show the effect.

As vertical edges produce scattering in the horizontal direction and vice versa, an effect of partial coherence is clearly indicated. At PETRA III the horizontal emittance is $130\times$ worse than the vertical emittance (fig. 3.1 on page 36) which directly translates to an asymmetry of the lateral coherence in the beam. According to the P06 Unified Data Sheet [139], the nominal lateral coherence lengths are $\xi_h = 87\ \mu\text{m}$ and $\xi_v = 567\ \mu\text{m}$ at 100 m distance and 12 keV. As the experiment is positioned at 97.5 m and performed at 9 keV, we expect a horizontal coherence length of $113\ \mu\text{m}$ which slightly shorter than the $125\ \mu\text{m}$ diameter of the FZP.

However, as we do not have a measurement of the real source size and coherence length at the time of the experiment, the coherence might have been worse than expected, explaining the multi-slicing artifacts. With that in mind, further improvements of the reconstruction quality can be expected by decomposition of the probe into multiple coherent modes. However, at the time of writing, the author did not have

⁶During the experiment, four samples of this type have been measured in total, but only one is presented here as they all exhibit similar effects and features.

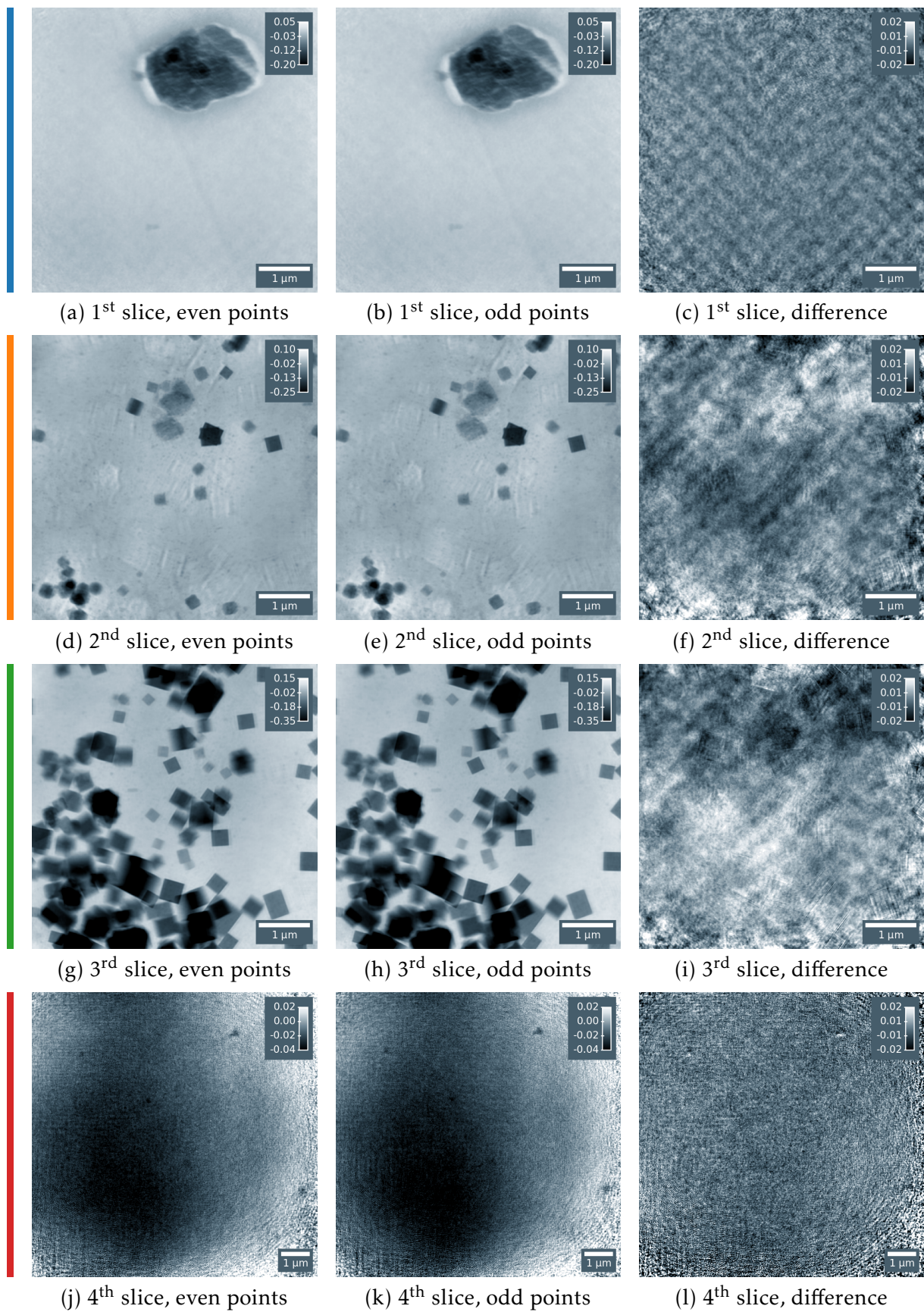


Figure 7.10: Four-slice reconstruction of a data set split in even- and odd-numbered scan points.

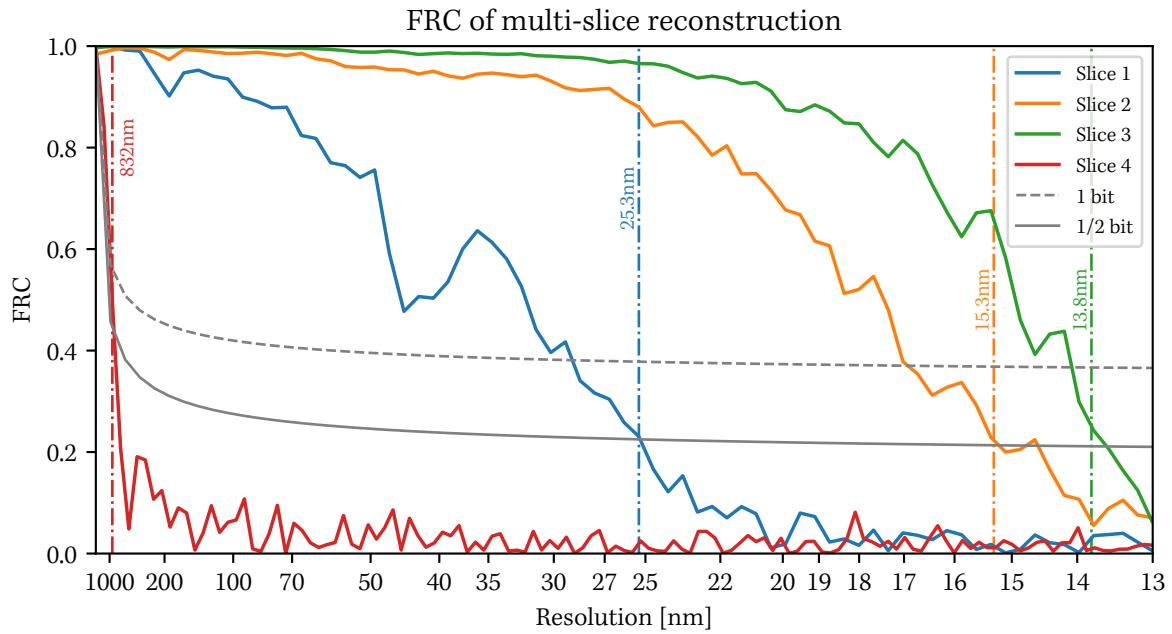


Figure 7.11: FRC curves of the four-slice reconstruction in figure 7.10. A single ptychographic scan was split in odd- and even-numbered diffraction patterns and separately reconstructed. From these two independent reconstructions, the phase shift images in each of the four object slices were independently correlated. The binning was reduced to $3\times$ as the oscillation artifacts are less present in these multi-slice reconstructions.

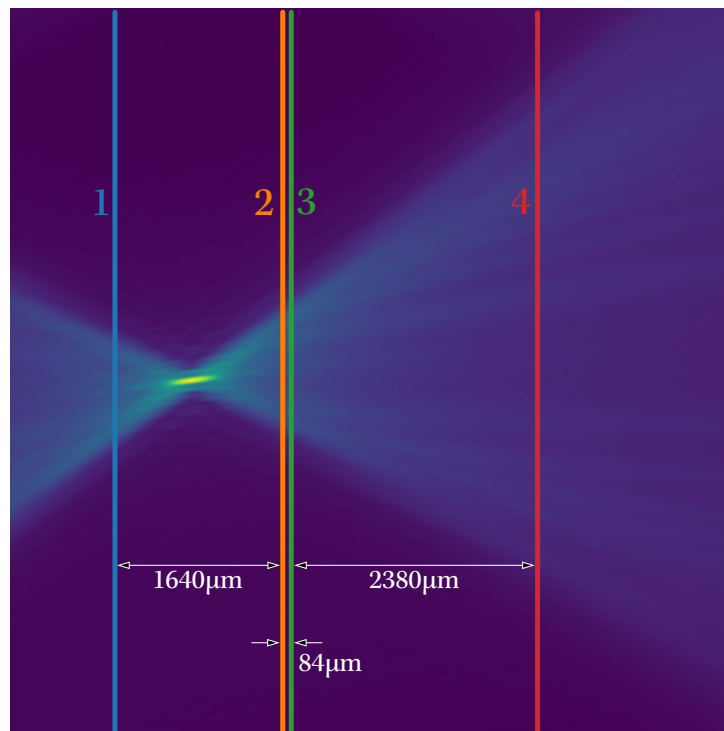


Figure 7.12: Position of the four object slices along the caustic of the focused beam. The beam caustic is displayed as the square root of the horizontal intensity profile. The lateral extent of shown probe is that of a reconstruction without upsampling, i.e. the probe field of the reconstructions in this section computed with $2\times$ upsampling is twice as large.

access to any multi-mode, multi-slicing, upsampling, position-refining ptychography implementation for such an endeavor.

The second effect visible are low spatial frequency artifacts. These have already been reported by other groups [47] and are more pronounced in the in situ measurements presented in the next chapter. Low spatial frequencies in the ptychographic microscope have a large DOF on their own, therefore, they cannot be separated uniquely when the distance between the slices is too small. They are, however, constrained by the size of the probe beam, only appearing at length scales larger than the probing beam.

In applications of multi-slicing in tomography as reported by Tsai et al., "sample rotation provides a significant redundancy of the low and middle spatial frequencies" [47, sec. 5.1]. In two-dimensional measurements, however, such a level of redundancy does not exist.

As the low frequency artifacts are fluctuating when the ptychographic reconstruction is repeated multiple times⁷ with different order of the subiterations, the measurements of the resonant series acquired at 29 energies around the copper K-edge were reconstructed 30 times each. In about a third of all reconstructions, the necessary usage of upsampling led to splitting of the probe and the object, mandating manual verification of all reconstructions and repetition of the failed attempts. This process had to be repeated six additional times until all reconstructions finished successfully.

Even with this considerable computational and labor effort, the averaged reconstructions still yielded no usable resonant signal. In consequence, it has to be concluded that quantitative ptychographic imaging in the presented case is not possible. The situation might improve when the probe is such that upsampling does not have to be used, or when the image slices have a larger distance.

7.3.4 Multi-slice FRC

In figure 7.10, the data set was split in odd and even numbered positions and reconstructed with four object slices. The position of the slices along the caustic of the focused beam is shown in figure 7.12, the FRC is plotted in figure 7.11.

The resulting resolution estimates vary greatly between the slices; while the resolution in the two slices of the sample are only moderately diminished from the single-slice case at 13.8 nm and 15.3 nm resolution, the entrance window yields a significantly worse values at 25.3 nm. The exit window in the fourth slice is essentially only noise, the value of 832 nm has to be understood with a large error bar as there are not many features in FRC at the low frequencies.

Even though FRC of the fourth slice (in red) shows hardly any correlation, the noise in the the difference image (7.10l) has an rms of 7.6 mrad. That is only slightly larger as

⁷This evaluation was also done on a second data set that could be reconstructed with only two planes at it had no large dust particles on the windows with similar results.

the fluctuations in the difference images of the downstream object (fig. 7.10i, 7.1 mrad rms) and the upstream object (7.10f, 6.0 mrad rms). However, the fourth object slice is mostly empty and the few objects in it produce an order of magnitude less phase shift than the copper cubes in the sample planes. As a result, the resolution estimates via FRC of a single measurement can be vastly different in the individual slices.

7.3.4.1 Evaluation of the DOF criterion

At the beginning of the section, we calculated an expected DOF of 1.44 μm based on the transversal resolution determined in the single-slice case. With the result of the multi-slice FRC, we can recalculate the DOF as

$$\text{DOF} = 2 \cdot \frac{\delta^2}{\lambda} = 2 \cdot \frac{(15.8 \text{ nm})^2}{0.1373 \text{ nm}} = 3.64 \mu\text{m}. \quad (7.5)$$

Here we take the resolution estimate of 15.4 nm of slice 2, the upstream sample plane, as we used the edge contrast in this plane to find the slice distance. Comparing this result with the edge contrast images, the resulting DOF of 3.64 μm appears to be underestimated.

Based on results of empirical studies, Tsai et al. [47] suggested that the prefactor 2 in equation 7.5 should be increased to 5.2 to obtain the true DOF in multi-slice ptychography. The resulting DOF of 9.5 μm agrees better with our experimental results.

7.4 Summary

Let us summarize the four most important points of this chapter.

1. A measurement with resolution estimates around 10 nm has been presented. There are indications that the achieved resolution is neither limited by sample vibrations nor by the SNR of the scattering signal.
2. Challenges in quantitative ptychographic imaging with multiple image slices arise from low frequency artifacts that can currently not be overcome in two-dimensional measurements.
3. There are indications that partial coherence effects limit the separability of the image planes.
4. The transversal resolution estimated by FRC in individual slices of multi-slice reconstruction can vary depending on the strength of the scatterers in each of the slices.

Chapter 8

In-solution ptychography

In this chapter, we take the in situ cell introduced in chapter 4 and perform in-situ multi-slice ptychography while the copper nanoparticles imaged in the previous chapter grow from solution. A full time series of a reaction is presented and the effects of beam damage is discussed. In comparison to the ex situ measurements, we observe a decrease in resolution and an increase of multi-slicing artifacts.

8.1 Ptychographic time series of a chemical reaction

For in-solution imaging at PtyNAMi, a photon energy of 15.25 keV was selected for increased transmission through the in situ chamber. At this increased photon energy, the beam was focused with silicon NFLs of 30 mm working distance. Mounting the in situ cell, attaching the necessary cables and aligning it to the x-ray beam is not feasible on the ultra-stable setup, the coarse translation stages of the tomography tower are required to gain access to all sides of the cell. The increased vibrations are negligible as the measured vibration of 9.9 nm rms of the tomography tower is a factor seven smaller than the resolution estimates presented below.

8.1.1 Temporal resolution

In the time series, an area of $12 \times 12 \mu\text{m}^2$ was scanned on a regular grid of 41×41 points, i.e. a step size of 300 nm, and a dwell time of 0.5 s per point. As the motion dead time from point to point with the heavy in situ cell on top of the tomography tower was 0.25 s,¹ these scan parameters result in an average total scan duration of 21.3 min.

¹A motion dead time of 33% means that the temporal resolution could be lowered to 15 min by switching to continuous scanning instead of the step scanning at the same photon dose. Continuous scanning requires to record more diffraction pattern with less photons in each of them, leading to less stable behavior in reconstructions using multi-slicing and position refinement while requiring proportionally more computing resources. More importantly, continuous scans require laser-interferometric position data as encoder positions are not available and the real positions deviate strongly from a regular grid. As the interferometers do not operate perfectly stable and sometimes require long rebooting and realignment procedures, continuous scanning increases the risk of missing parts of the time series due to technical problems.

Including overhead time to adjust for drifts, the average temporal resolution of the measurement is 22.5 min.

As the vertical direction was chosen as the fast scanning axis, the acquired images have a horizontal rolling shutter effect: The right edge of the image was acquired 21 min later than the left edge of the image. As no abrupt changes are visible in this time frame, the temporal resolution seems to be suitable for this particular sample system.

8.1.2 Sample drifts

In initial heating phase, the temperature was slowly increased from room temperature to 155 °C over a period of 25 min. During this period, the laser-interferometers measured a vertical thermal drift of the ball lens attached to the base plate of about 12 μm . From observations of the region of interest with a visible light microscope during this period, we determined a larger drift in the range of 50 μm . Therefore, the majority of the thermal expansion occurs inside the in situ cell, not in the underlying motor stack, thus, the interferometers are not suitable to track the thermal drifts of the imaged region in this configuration.

The thermal drifts continue for another 20 min after the target temperature has been reached so that the first usable measurement can be performed approximately 45 min after the beginning of heating. Once thermal equilibrium is reached, thermal drifts slow down to the 100 nm level between scans so that only minor adjustments are needed.

When viewing the time series as a movie of aligned images, we clearly observe that these residual thermal drifts occur on faster time scales. Comparing several consequent frames, the relative position of particles on the substrate with respect to each other oscillate. This effect can neither be observed nor corrected with interferometric monitoring of the base plate of the piezo scanner as the critical thermal effects occur above it, inside the in situ cell.

In order to quickly adjust for drifts between scans, one cannot wait for the ptychographic reconstruction of the scan. Instead, the software I developed for the beamline P06 renders lower resolution images based on Differential Phase Contrast, i.e. the horizontal and vertical centers of mass of the central beam in the diffraction pattern are displayed. These images can be rendered within a minute or less; characteristic large features of the sample can be used to adjust the field of view in the next scan if necessary.

After the initial heating up phase, the drifts observed in the two image planes (the entrance and exit windows of the reactor) are mostly independent, giving a first indication that the drifts are caused by deformations of the kapton substrate. As such, it is not possible to keep a given set of particles in both image planes in the field of view if they drift in opposite directions. Instead, one has to decide for one image plane that

is kept in place while the second image plane drifts. In the presented measurement, the overall drift of the upstream image slice was $6\ \mu\text{m}$ relative to the downstream image slice, i.e. half the field of view.

8.1.3 Experimental observations

In figure 8.1, the growth and dissolution of the copper particles is shown over a period of twenty hours. The presented measurements are not spaced equidistantly in time, the time frames are rather chosen such that each line represents a distinct phase of the reaction. These phases are color coded in figure 8.2.

In the first line, the precursor in solution begins to nucleate and cubes are formed that slowly grow in size. Reconstructing these early time frames without *ab initio* knowledge is not possible. Instead, both the slice distance and the complex probe function have to be determined from reconstructions of later time points and can then be applied to the early time points in retrospect. When the probe of a later scan is imported as the initial guess of the reconstruction, its update strength has to be reduced to 10% of the usual value.

Even with the *ab initio* information, the image quality of the early time frames is the worst in the entire time series. In particular, a periodic grid-like pattern overlays the image and many particles are not sufficiently resolved to determine their shape. For science cases in which this initial nucleation process is of interest, alternative imaging techniques, such as CDI or in-line holography at an XFEL, are probably preferable.

In the second line the cubic particles grow in size. As the larger cubes now produce sufficient scattering signal, the ptychograms can reconstruct unaidedly and the slice distance can be determined. From performing reconstruction with several slice distance guesses, it became immediately evident that the DOF is much larger than in the *ex situ* case at about $300\ \mu\text{m}$. Within the DOF laid the design value of $1000\ \mu\text{m}$ separation between the image planes, so that this value is chosen for the reconstructions.

In the third line the growth of the cubic particles slows down, but new particles appear from one frame to the other without any visible growth in between. These particles may have formed freely in solution, or they may have detached from the substrate outside the field of view. As we do not observe any particles disappearing from the field of view, the first hypothesis seems more plausible.

In the frames around the 12 h mark the reconstruction quality decreases; high-frequency artifacts appear in some regions of the image. The cause of these becomes more evident in the fourth line, from the 13th to the 16th hour of the reaction: The distance between the slices is changing gradually. We chose three time points and reconstructed them with a series of slice distance guesses, the distances of the time frames in between are interpolated. The time evolution of the slice distance is plotted in figure 8.2 as the gray curve.

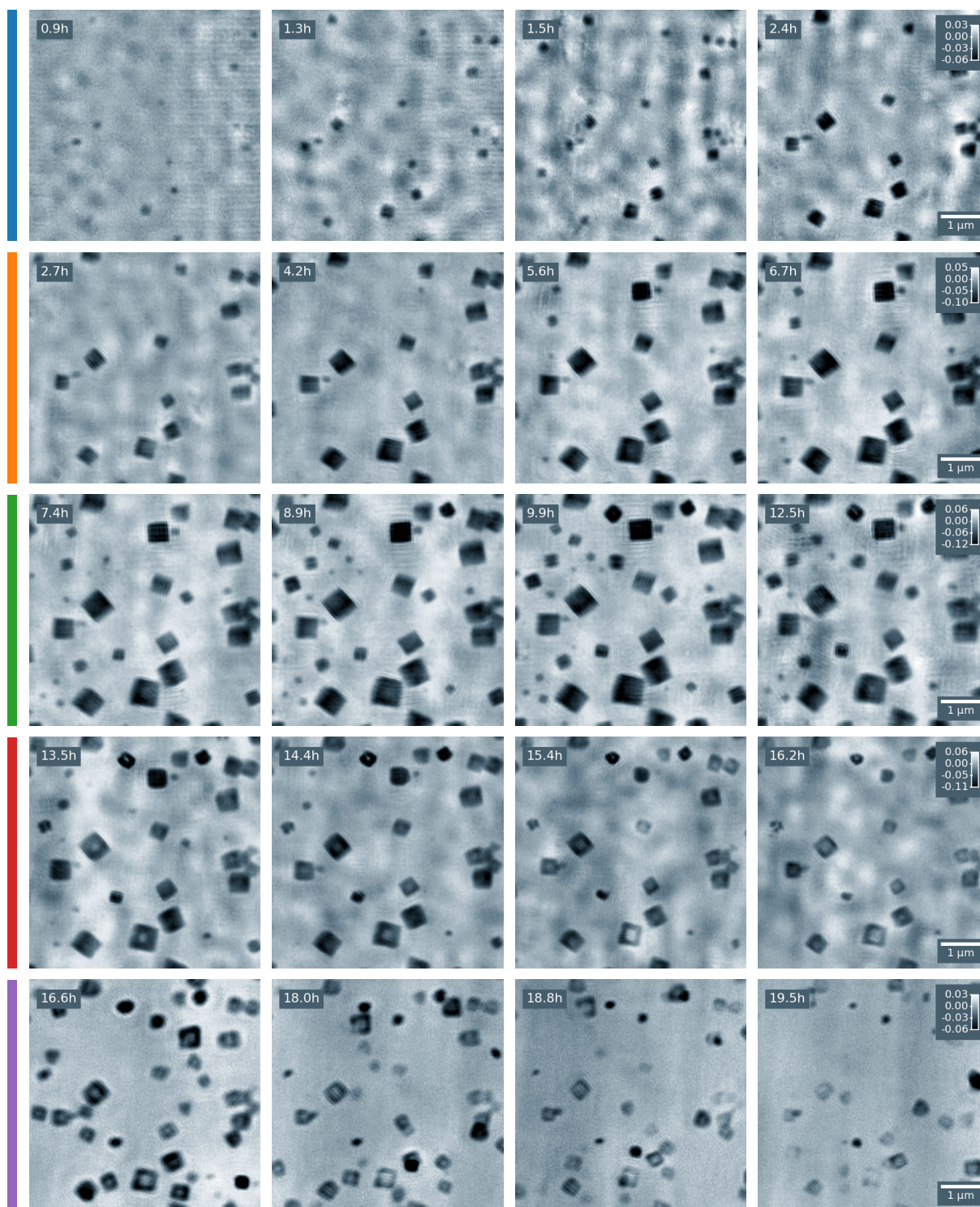


Figure 8.1: Time series of in situ measurement. The contrast in each line of images is constant and given in the colorbar of the rightmost image. The scale of all images is identical. The times are measured from the beginning of the heating process to the middle of the scan. The bottommost line shows single-slice reconstructions with the intensity refinement applied, the other lines show the upstream object slice of reconstructions with two image slices. The slice separation as function of time is plotted in fig. 8.2.

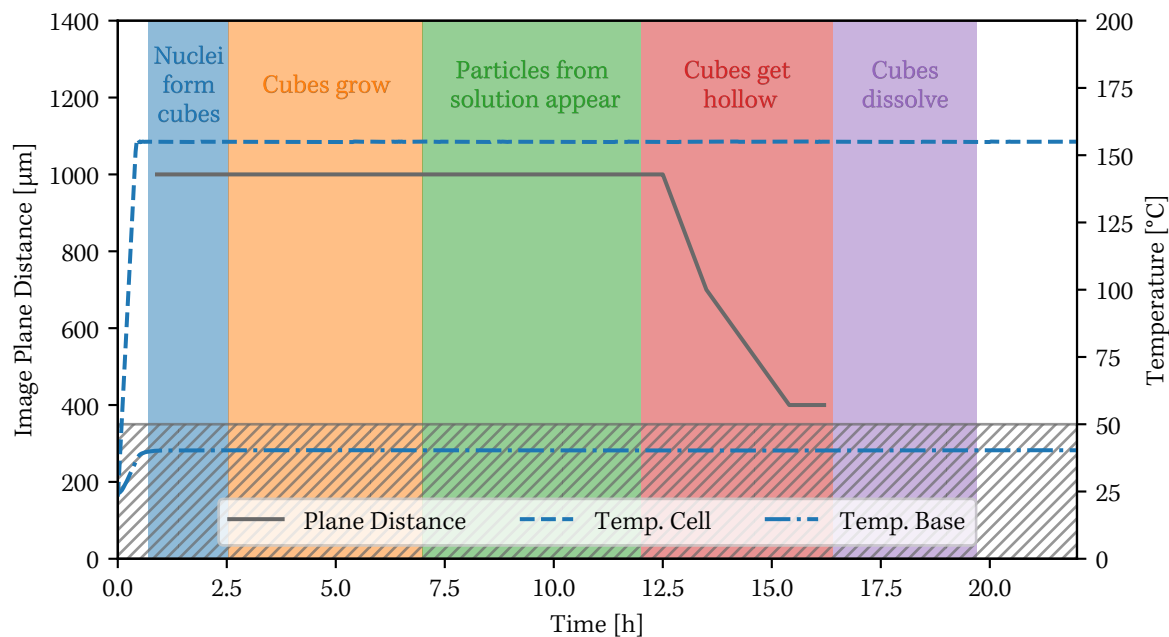


Figure 8.2: Timeline of in situ reaction with temperature curve and the image plane distance used for ptychographic reconstructions. The colored time periods correspond to the colors of the columns in figure 8.1. The hatched area on the bottom marks image plane distance where the multi-slice algorithm cannot be applied.

The observation of a decreasing slice separation was entirely unexpected. On the contrary, if the material properties of the 125 μm thick kapton substrate were to change to during the reaction, we expected it to bulge under the internal pressure inside the cell, thereby increasing the slice distance.

The most probable explanation is that the kapton expands with prolonged exposure to the heated solvent. The kapton windows are tightly clamped at the edges of the reactor and cannot expand outwards. Therefore, the material can only expand towards the center. As the parabolic shape of the heating covers (see chapter 4) already introduced a preferential direction to the shape of the substrate, an expansion of the material may well result in a narrowing of the slice distance.²

While the slice distance changes, the synthesis starts to strongly deviate from the expected behavior. Instead of further growing and transitioning into a metallic phase, the cubes start to shrink and form hollow voids inside them. In this work, there will be no attempt made to explain the underlying chemical processes, we limit ourselves to a description of the images obtained with in situ ptychography.

In the fifth row, spanning the time up to the 20 h mark, multi-slice ptychography fails completely and we have to resort to single-slice reconstructions. In consequence, we see now the particles from both kapton substrates and the low-frequency background

²In a very recent experiment, a second area detector was used to measure the kapton diffraction rings under similar conditions. In the same time frame in that a decrease of the slice distance was observed, the kapton rings changed their position, indicating a structural change of the polymer that is connected to changes of the mechanical material properties.

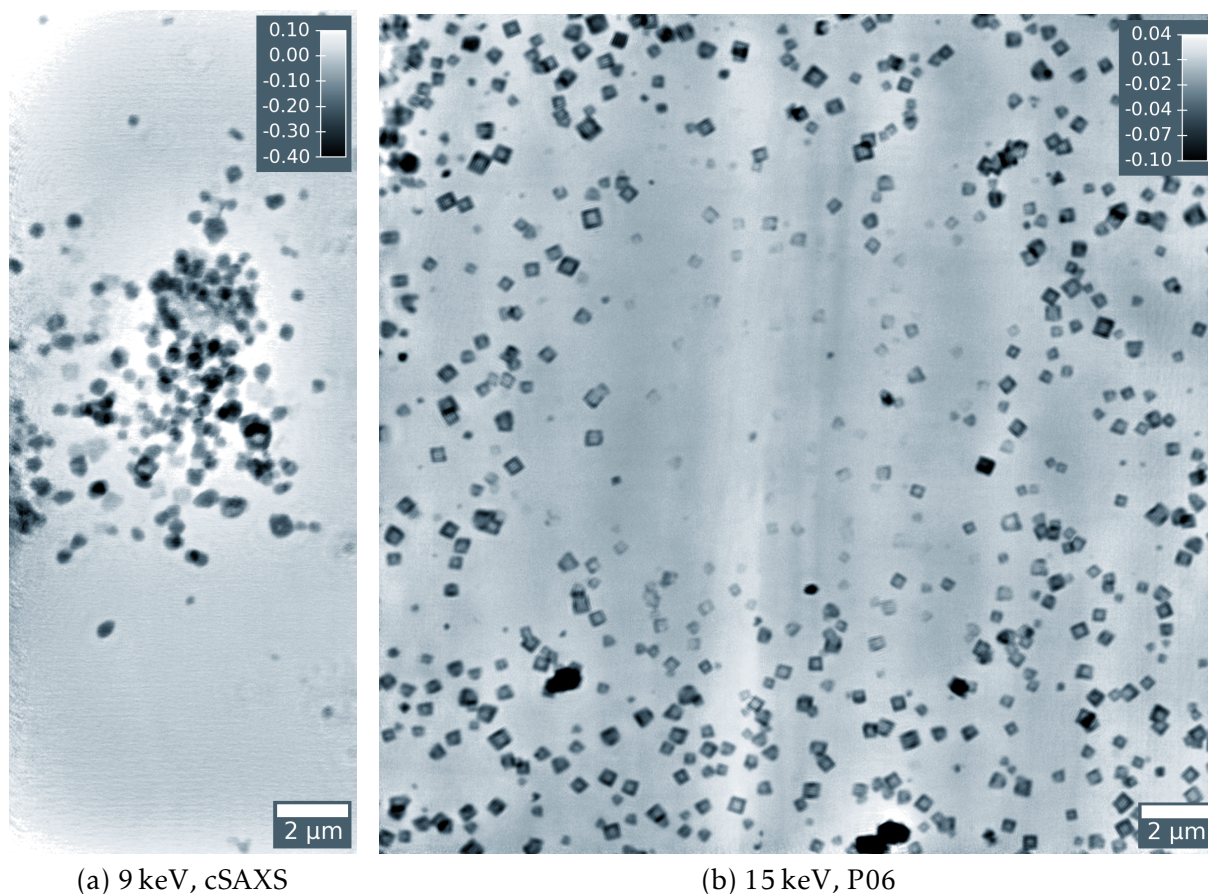


Figure 8.3: Large overview scan after the acquisition of the time series. a) Result obtained at cSAXS, SLS, at 9 keV. The particles are accumulated in the area that was repeatedly imaged. b) Result obtained at P06, PETRA III, at 15 keV. Particles have disappeared from the center region that was repeatedly imaged.

artifacts disappear (see discussion in the next section). The smallest slice distance for which multi-slicing still worked was 400 μm , for distances of 350 μm and below, only a single object slice yielded reasonable results. This is indicated in figure 8.2 as the hatched region.

We see two types of particles on the substrate: Cubic particles that are clearly hollow and round particles that appear to be solid. The difference of phase shift of the two particles types indicates that the hollow cubes are oxidic and the solid particles are metallic. With ongoing time, both particle types further shrink until they completely dissolve.

8.1.4 Beam damage

As the observed chemical reaction deviated completely from the expected behavior in the second half of the experiment, an effect caused by beam damage is indicated.

A larger scan around the region of interest was performed to assess the situation in the surrounding area (fig. 8.3b). The state in the surrounding area was essentially that of the region of interest three hours before, i.e. there were many hollow cubic particles and a few solid round particles. However, as these particles were close to the region

that was repeatedly scanned for 20 h, including some drifts, they might also have been affected by beam damage at a lower dose.

As the in situ cell has four cut-outs in the heating cover that can be used for imaging, we moved the cell by 1.7 mm to the neighboring cut-out, imaging a fresh region that was never touched by the x-ray beam. We observed the same hollow cubes in this fresh region, and they also started dissolving after within an hour of constant ptychographic imaging. We spent an additional 10 h scanning various regions in this second cut-out, always finding hollow cubes that started dissolving upon contact with the x-ray beam.

It is noteworthy that in experiments using the same setup performed at the Swiss Light Source, at the cSAXS beamline and 9 keV photon energy, we observed the opposite effect. While we observed only a few new particles appearing on the substrate between hours 7 and 10 in the P06 experiment, the amount of particles appearing in the cSAXS experiment was much larger and quickly resulting in complete coverage of the region of interest, hindering imaging of individual particles. A larger scan around the region of interest then revealed the surrounding substrate to be completely bare, all particles had accumulated in the center (fig. 8.3a). This effect was also much stronger on the substrate that was positioned closer to the focus of the beam.

A major difference between the experiments at P06 and cSAXS was that we were able to prepare the inner reaction container in the well-equipped labs of the CHyN on the Bahrenfeld campus in Hamburg, while we had to use what was available at the beamline at cSAXS. In particular, filling the cell under inert gas to exclude water and oxygen was a critical step. As such, the difference of the observed reaction dynamics may well have been caused by contamination and not necessarily by the difference in photon energy.

After the synchrotron experiment, the reaction cell was carefully disassembled and the kapton substrates were imaged with SEM. In figure 8.4a, a large bare spot on the substrate was found, the size of which corresponds to the large scan performed fig. 8.3b.

In some tens of micrometers distance from the bare spot hollow, split open cubes were found (figures 8.4c-e). Going back to the ptychographic images, there are a few cubes that possibly appear to be split or have less contrast on one of their edges. Distinguishing between whole hollow cubes and split hollow cubes is difficult, not least because of the strong low-frequency artifacts in the images.

8.2 Low frequency artifacts and intensity refinement

In the multi-sliced reconstructions of the first four rows in figure 8.1, many low-frequency artifacts are visible in the background. When watching the time series as movie, the artifacts are much more noticeable than in the printed version as they are fluctuating from frame to frame. On first glance, this effect does not seem to be different from the low-frequency multi-slicing artifacts observed in the previous chapter. On the

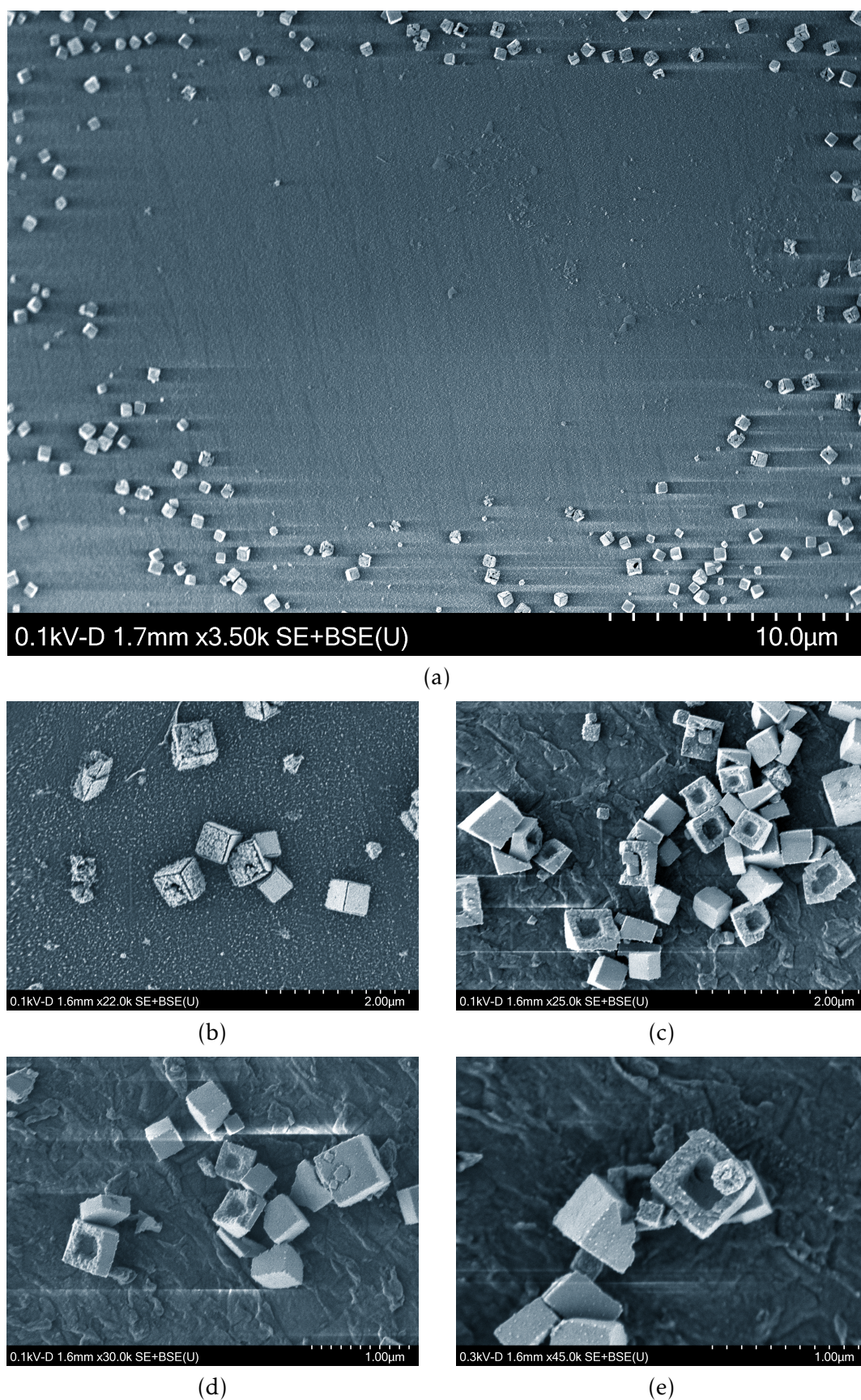


Figure 8.4: SEM images of kapton window after in situ synchrotron measurement. a) Overview around the $12 \times 12 \mu\text{m}^2$ region that was scanned at 15 keV for 20 hours. b) Particles at the edge of the empty region c,d,e) Hollow and cracked particles in some tens of micrometers distance from the edge of the empty region. SEM imaging by Lukas Grote and Emilis Kaziukenas in the group of Dorota Koziej at CHyN.

contrary, as the slice separation is now smaller in relation to the ptychographic DOF, we expect multi-slicing artifacts to be more pronounced.

8.2.1 Single-slice measurement

In figure 8.5, a measurement taken at 18.8 h, when the substrate had already collapsed and the slice distance had fallen below the DOF, is reconstructed with the single-slice algorithm. Subverting our expectations, we see distortions in the background that are similar to the known multi-slicing artifacts now also appearing in the reconstructions using the conventional single-slice algorithm (fig. 8.5a,b). In none of the previously presented single-slice data such an effect was observed (e.g. fig. 5.14 on page 82, fig. 6.4 on page 92, fig. 7.3 on page 100).

A possible explanation could be fluctuations of the incoming beam intensity; the beam might have been particularly unstable during this experiment. The diffraction patterns are normalized to the incoming beam current measured with the transmission diode and reconstructed again (fig. 8.5c,d).³ We see an improvement, but the effect persists.

Using algorithmic refinement of the intensity factors, i.e. normalizing the diffraction patterns during the reconstruction so that they best fit the model (section 2.2.4), yields a locally perfectly flat background and overall much improved image quality (8.5e,f). The refinement is not strong, the relative rms of the refined normalization values is 4.7 ‰ and the strongest correction of an individual normalization factor is 1.8 %.

Studying the modulus images (fig. 8.5b,d,f), there are evidently some cubes that exhibit a white edge contrast, i.e. a physical impossible increased transmission at the edges, while others do not show this effect. This is a strong indication that the sample is still in two slices, i.e. the kapton substrates have not collapsed so far that they touch each other. Still, the slice separation is smaller than the DOF and the slices cannot be separated.

Assuming that there is still solvent in between the substrates, the observed low-frequency artifacts may be explained with free particles floating in the solution. When particles traverse the illuminated volume during exposure of a scan point they are not steady in space, thus they cannot be imaged by ptychography, yet they still affect modulus and phase of the beam. As the core assumption of ptychography is that the object is not changing during the scan, free floating particles can intrinsically not be included in the model, leading to inconsistent data and that possibly results in background fluctuations from frame to frame.

³Normalizing to the transmission diode is not done by default as the readout is often noisier than the fluctuations of the beam current.

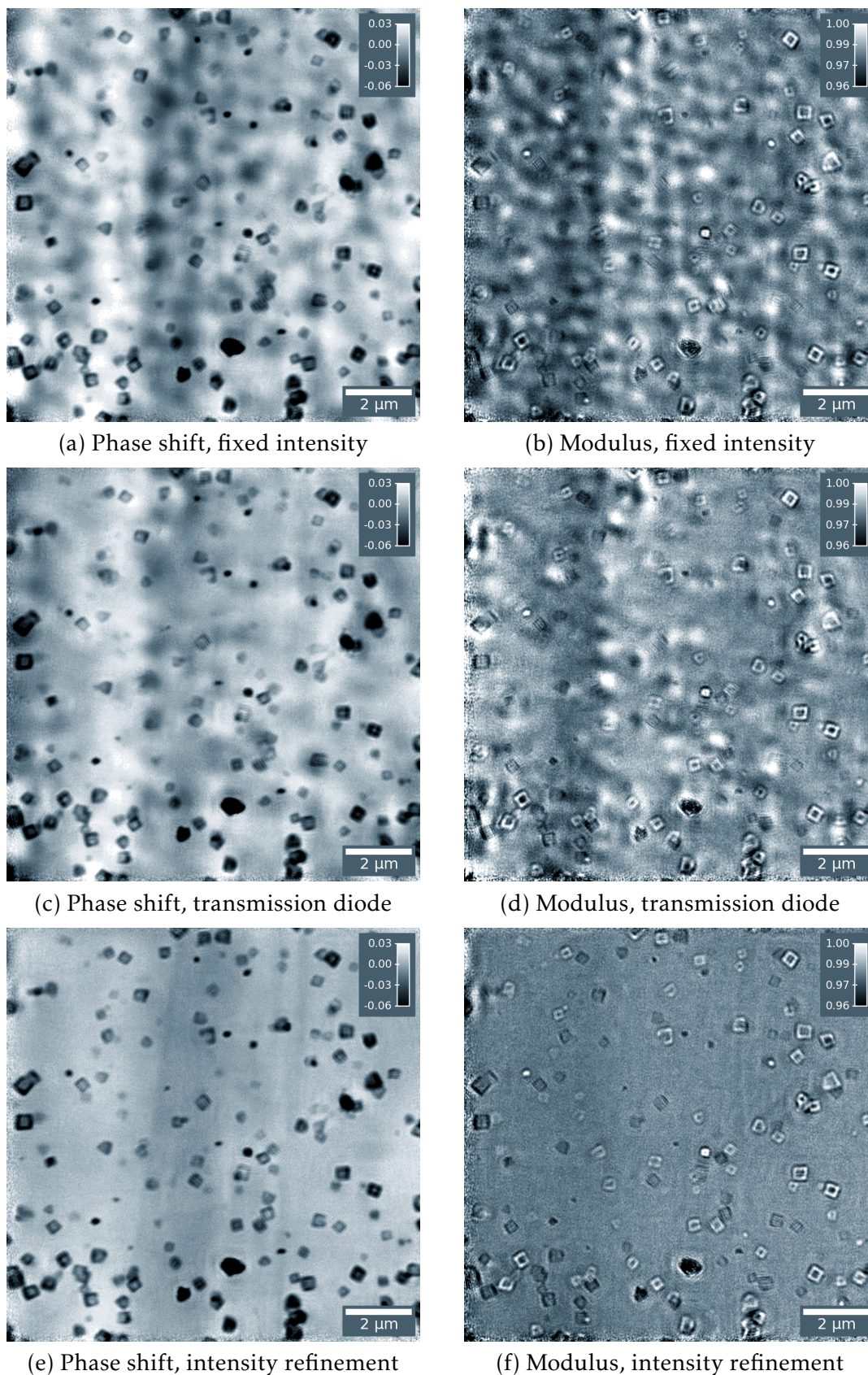


Figure 8.5: Single-slice reconstructions of the scan at 18.8 h in figure 8.1 with different normalization schemes. a,b) Diffraction patterns are not normalized. This is the default setting used in all reconstructions if not stated otherwise. c,d) Diffraction patterns are normalized to the current measured with the transmission diode positioned between slits and focusing optics (fig. 3.5, page 43). e,f) The normalization, i.e. the intensity factors, are algorithmically refined. After 500 iterations without refinement, the intensity factors are updated in each of the following 500 iterations.

8.2.2 Multi-slice measurement

Knowing that the refinement of the intensity factors, while not being an accurate model of the scattering processes inside the sample environment, can at least visually improve the results, we want to apply it to multi-slice measurements. To this end, several reconstructions variants of the scan at 5.6 h, when the slice separation was 1000 μm , are presented in figure 8.6.

Starting with fig. 8.6a, we reconstruct this two-slice object with the inapplicable single-slice algorithm. The algorithm converges to a solution in which the particles in the downstream slice are in focus, and the upstream particles form diffuse structures in the background. Under the application of intensity refinement (fig. 8.6b), the background is smoothed and the particles in the upstream slice now clearly appear as halos.

We can prove this conjecture with a false-color overlay (fig. 8.6c) of the single-slice reconstruction with intensity refinement (in red) with the multi-sliced image of the particles in the upstream slice (fig. 8.6d, in cyan). The images overlay perfectly, every cyan particles has a red halo and every red halo has cyan particle in it.

In a similar fashion, we can also create a false-color image of both images of the multi-sliced reconstruction (fig. 8.6f). This is the image we would see if we had a microscope with the current lateral resolution, but increased DOF. At this experimental configuration, such a microscope had to increase the photon energy to at least 45 keV (eqn. 2.11). As the multi-slice separation helps to follow the changes of individual particles, such a microscope is not desirable here from my point of view.

Applying refinement of the intensity factors to the multi-slice reconstruction (fig. 8.6g,h) hardly changes the reconstructed object. There are still long-range, low-frequency artifacts in both slices, and comparison to the shape of the probe in both slices (fig. 8.6i) reveals that these artifacts occur on the lengthscale defined by the size of the probe.

The failure of intensity refinement may be caused by insufficient constraints set by the experimental data. Changing the normalization of a diffraction pattern has a similar effect in the ptychographic forward model as changing the modulus in one of the slices. As only one diffraction pattern per position is measured, such local instabilities are not strongly constrained.

An attempt was made to reconstruct three consecutive scans together so that the effective scan grid is three times as dense, resulting in more local constraints. Such a reconstruction works for the steady phases of the reaction when strong position correction is applied and yields a reasonable result. However, the intensity factors obtained in this fashion still do not improve the result when applied to a single data set.

When reconstructing segments of the time series with such a *moving average* ap-

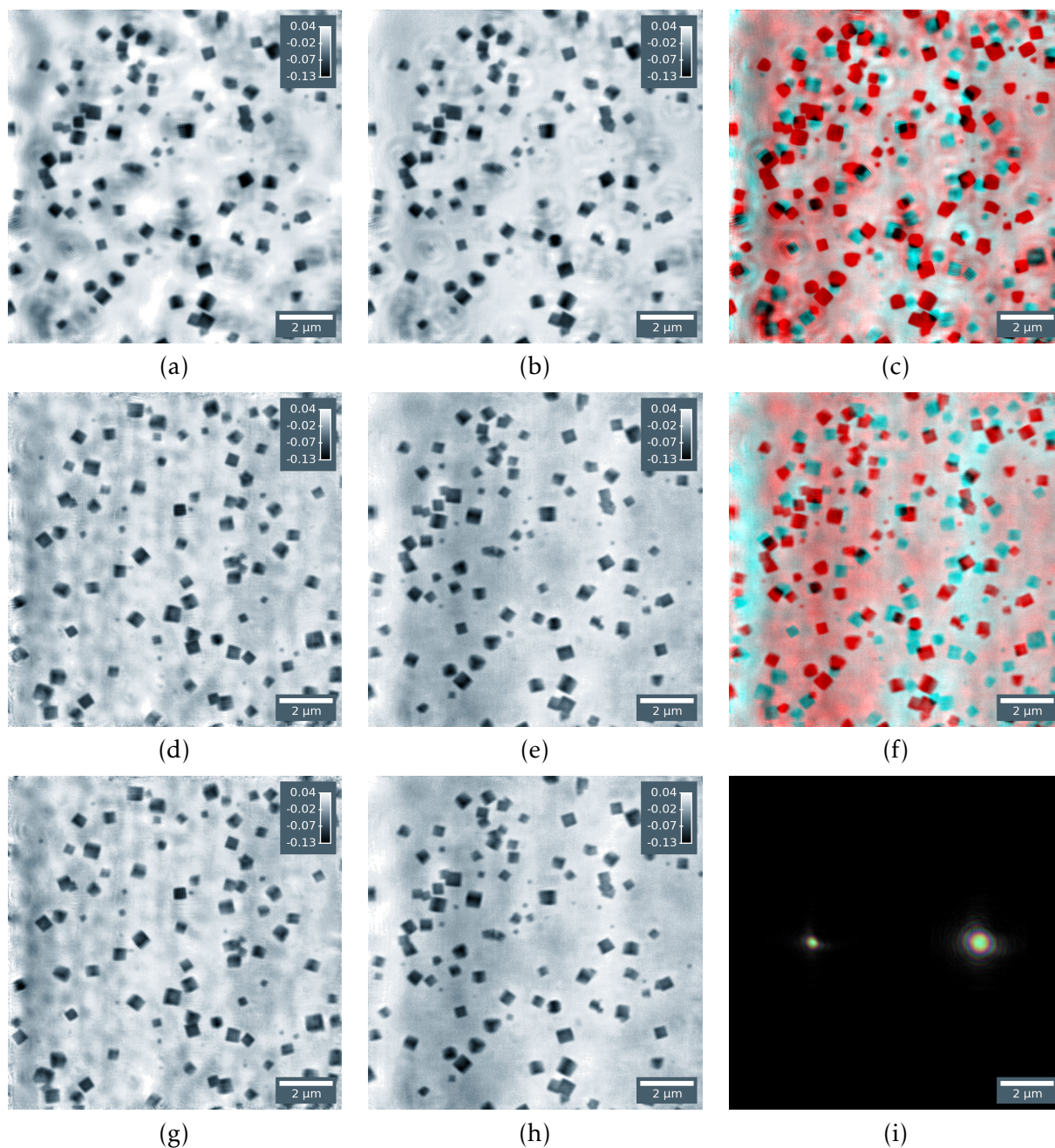


Figure 8.6: Various reconstructions of the scan at 5.6 h.

- a) Conventional single-slice reconstruction without refinement of intensity factors.
- b) Single-slice reconstruction with refinement of intensity factors.
- c) The particles in the upstream slice (in cyan, subfigure d) perfectly fit into the halos visible in the single-slice reconstruction with intensity refinement (in red, subfigure b).
- d) Upstream object slice of conventional multi-slice reconstruction.
- e) Downstream object slice of conventional multi-slice reconstruction.
- f) Colored overlay of upstream object (cyan) and downstream object (red).
- g) Upstream object reconstructed with intensity refinement during multi-slice reconstruction.
- h) Downstream object reconstructed with intensity refinement during multi-slice reconstruction.
- i) Empty probe beam in the upstream plane (left) and downstream plane (right).

proach, each scan appears in the first, second and third position of the triplet.⁴ If the intensity factors of a given scan represent a physical property of the measurement process, they will be refined to the same values in all three positions of the triplet. This is not the case, the intensity factors obtained in the three positions of the triplet are uncorrelated. A correlation is found instead between the intensity factors of the three different scans composing a triplet.

These observations are very clear signals that, in the present case, the intensity factors do not represent physical properties that can be interpreted in the ptychographic forward model in any meaningful manner. They are instead merely additional degrees of freedom that are misused to absorb some of the inconsistencies in the data set that are *not* explained in the forward model.

We have to emphasize that the present case is particularly difficult with the unknown amount of particles floating in the solvent and additional artifacts being introduced by multi-slicing. In measurements without these challenges, the refinement of the normalization remains a perfectly valid addition to the ptychographic algorithm.

8.3 Spatial resolution

As a final piece of the evaluation, we want to estimate the transversal spatial resolution of the various reconstruction variants discussed above with FRC. Since the sample is not in a steady state, two consequent time frames cannot be used and a single time frame has to be reconstructed twice from the two halves of a split data set instead. We choose the time frame from at the 12.5 h mark, i.e. the point in time when the hollowing of the particle began.

8.3.1 Transversal resolution

In figure 8.7 the split reconstructions are shown. In the two-slice reconstruction (fig. 8.7a-f) the most stable reconstruction variant was chosen, i.e. no intensity refinement was used. Furthermore, we regard two variants of single-slice reconstructions, one of them with the conventional algorithm (fig. 8.7g-i) and the other with refinement of the intensity factors (fig. 8.7j-l).

Even though the resulting images of these reconstructions and the difference images of the split data sets are distinctly different between these variants, the resulting FRC curves in figure 8.8 are almost identical. All curves exhibit a dip at low frequencies which is not surprising given the difficulties to reconstruct the low frequencies correctly. The curves then return to full correlation before decreasing monotonously, crossing the half-bit criterion at values between 74.5 nm and 68.4 nm.

Comparing the two variants of the single-slice reconstructions (red and green curves),

⁴For example, scan 3 appears in the triplets (1,2,3), (2,3,4) and (3,4,5).

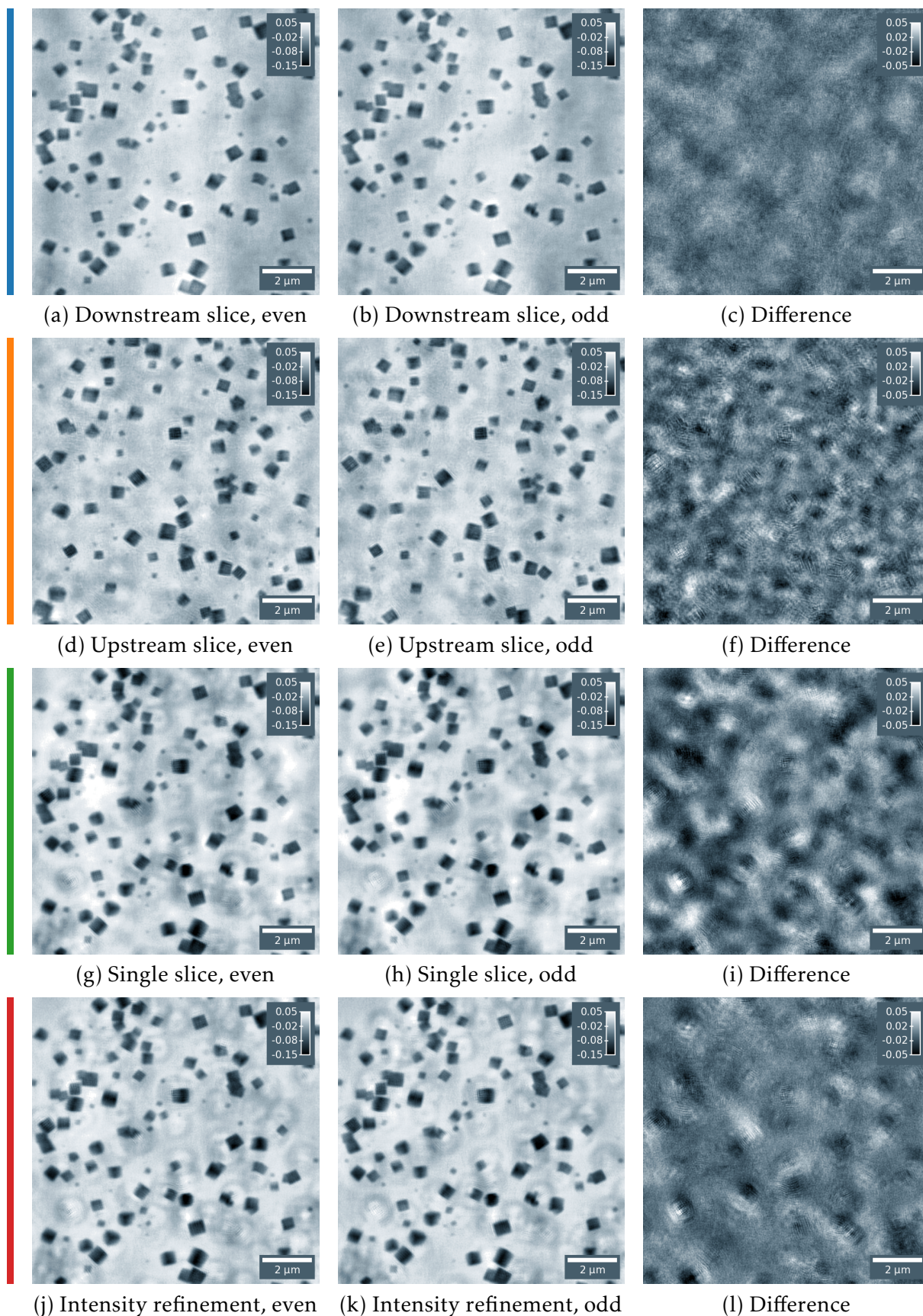


Figure 8.7: Reconstructions of split data set (12.5 h in fig. 8.1). a,b,c) Downstream object slice of multi-slice reconstruction. d,e,f) Upstream object slice of multi-slice reconstruction. g,h,i) Conventional single-slice reconstruction. j,k,l) Single-slice reconstruction with refinement of intensity factors.

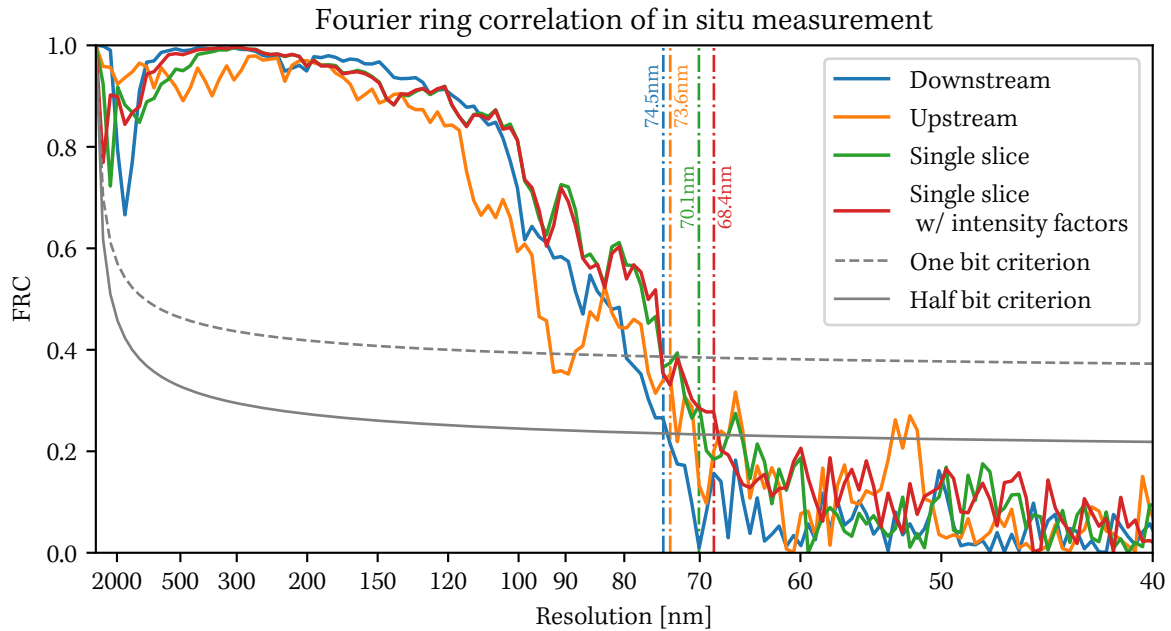


Figure 8.8: Fourier ring correlations of split data sets shown in figure 8.7. The correlation curves are evaluated at the half bit criterion. No additional binning was applied, i.e. rings of 1 px width were correlated.

their strong similarity is unexpected. Both in the split reconstruction and in the time series in its entirety, the refinement of the intensity leads to an immense visual improvement of the images (compare also again fig. 8.5a,8.5e). However, in the FRC, the entire curve is in almost perfect agreement, including the critical low frequencies that are supposedly corrected by the intensity refinement. This is an additional indication that a pure refinement of the normalization can only mask the inconsistencies of the data set visually, but it is not sufficient to explain in the ptychographic forward model the processes occurring inside the in situ cell.

8.3.2 Depth of field

Back in the first part of this chapter, we followed the collapse of the kapton substrate over time and empirically determined a minimum slice of $350\ \mu\text{m}$ that was necessary for successful multi-slicing. This analysis was performed while the experiment was running by reconstructing the measurements during the critical hours for many guesses of the slice distances, evaluating the resulting images subjectively by eye. In this subjective human evaluation, the ability of the algorithm to separate particles into two image slices, i.e. eliminating imprints or ghosts in the other slice, is perceived as much more critical than loss or gain of resolution.

After the experiment, we performed the reconstruction of split data sets and obtained FRC resolution estimates. Taking the resolution estimates of the multi-slice reconstruction, we can calculate the expected DOF of the ptychographic microscope. For this, we take the refined, less conservative formula discussed at the end of the

previous chapter:

$$\text{DOF} = 5.2 \cdot \frac{\delta^2}{\lambda} = 5.2 \cdot \frac{(73.6 \text{ nm})^2}{0.0813 \text{ nm}} = 346 \mu\text{m} \quad \text{Upstream slice} \quad (8.1)$$

$$= 5.2 \cdot \frac{(74.5 \text{ nm})^2}{0.0813 \text{ nm}} = 355 \mu\text{m} \quad \text{Downstream slice} \quad (8.2)$$

With this result, the DOFs determined with the two methods are in very good agreement. In future experiments, equation 8.1 can be used to predict the DOF more accurately.

The inverse relationship, as it was stated in equation 2.12 on page 32, does *not* hold. In the single slice reconstruction, we would expect the achievable resolution to be limited to

$$\delta_{\text{max}} = \sqrt{\frac{\lambda \cdot \text{DOF}}{5.2}} = \sqrt{\frac{0.0813 \text{ nm} \cdot 1000 \mu\text{m}}{5.2}} = 125 \text{ nm}. \quad (8.3)$$

This is clearly not the case as the FRC resolution estimates show. The single-slice ptychography algorithm does *not* function as a conventional microscope that is simply focused in between the image planes, thus imaging both planes slightly out of focus. Instead, the algorithm always converges to a solution in which one plane is in focus and the other is completely out of focus. This behavior was observed for all recorded data sets. The algorithm can be made to favor a certain slice by changing the initial probe function and activating the image slices in a different order, but it cannot be manipulated into mimicking the imaging characteristics of a traditional full-field microscope.

The methods to estimate the resolution are not constructed to notice additional objects in distant image planes as they cannot distinguish their out-of-focus features from low-frequency parts of the image plane in focus. In the future, PRTF should be considered as a method for resolution estimation of multi-slicing as it directly takes the entire forward model, including all image planes, into account.

8.4 Summary

We summarize the findings of this final chapter in four points.

1. We were able to image the nucleation and growth of copper particles in heated solvent with a transversal resolution of 73.6 nm, a longitudinal resolution of 350 μm and a temporal resolution of 22 min over a period of twenty hours.
2. During the second half of the synthesis, effects of beam damage led to a strong deviation from the expected reaction pathway.
3. Low-frequency image artifacts were observed in both single-slice and multi-slice measurements. In the single-slice case, algorithmic refinement of the normalization resulted in a visual improvement.
4. Albeit visually different, the FRC resolution estimates obtained with the algorithmic variants (single/multi-slice, normalization refined/fixed) are very similar. The DOF could be accurately calculated from the FRC resolution estimates.

Chapter 9

Outlook

In chapter 5 about interferometry, we arrived at two major conclusions. First, laser-interferometry was proven to be an excellent tool for vibration measurements down to the Ångström level, but second, no significant improvement of image quality was observed when using interferometer positions instead of encoder positions. We stated that several measurement uncertainties may contribute to this second point, including x-ray beam instabilities and the periodic error of the homodyne phase quadrature scheme. We expect the latter problem to be solved in the near future by switching to interference spectroscopy (section 5.6.4).

In chapter 7, we optimized the setup to push the spatial resolution as high as possible and reached 9.8 nm FRC resolution estimate as the best result. From the onset, we had identified sample vibrations and incoherent background scattering as two limiting factors of the achievable resolution. In the experiment performed, both of these factors have been optimized so far that we are confident that they are no longer limiting. Discussing probable new limiting factors, incoherence effects and beam vibrations were the first that came to mind.

This leads us back to the point that the beam characteristics are in general not well known. While we now have thousands of sample vibration data sets, collected over years under various experimental and environmental conditions, the number of source size, monochromator vibration or focusing optics vibration measurements can be counted on one hand. In fact, the only measurement of the beam in regular operation is the steering measured by the QBPMs, data that is only qualitative as no quantitative calibration exists.

Even if the flat beam was adequately monitored, characterizing the focused beam is much more difficult. The lens interferometers are available and have been used to measure vibrations between 2 and 3 nm rms, but their alignment is time-consuming; time that no user wants to spend. Moreover, measurements of lens vibrations along a single axis tells us nothing about rotational vibrations of the focusing optics. In the

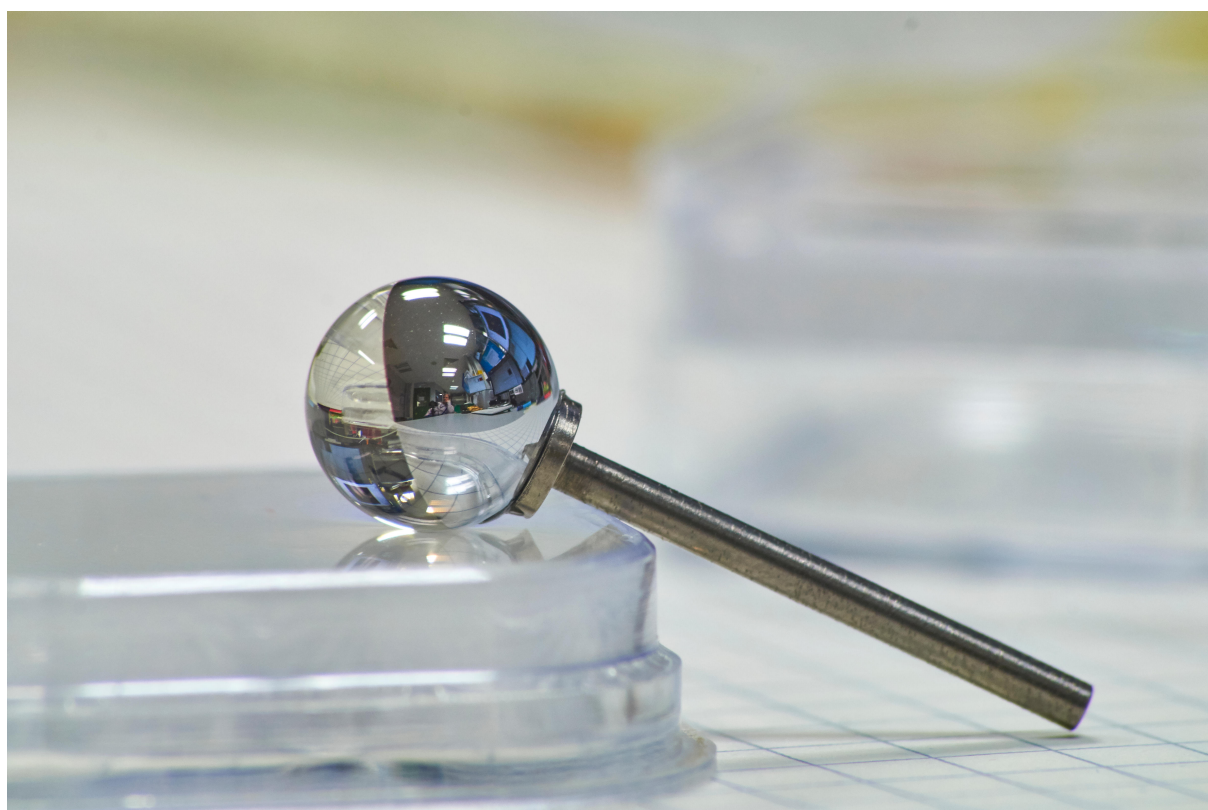
optimal case, the beam should be characterized downstream of the focusing optics. How this can be achieved is not clear, and as focusing optics of high numerical aperture and short focal length are growing in popularity, it is probably unfeasible in many cases.

With so many unknowns about the x-ray beam, it is impossible to decide here if the effects observed can really be attributed to beam instabilities, or if other sources of measurement uncertainties have been neglected. In any case, the beam stability is a central point in this discussion. With these arguments in mind, I arrive at the conclusion that *the same attention that has been paid to sample positioning should now also be paid to the monitoring of the x-ray beam.*

In chapter 7, we concluded that quantitative data enabling resonant ptychography could not be obtained from the multi-slice reconstructions. However, this conclusion was explicitly stated only for the measured data set and not in general. The experiment should be repeated with refractive optics producing a clean focus, and careful attention should be paid that at all energies, full quality reconstructions can be performed without virtual enlargement of the probe. In addition, the diversity of the data set could be increased, e.g. by measuring at two positions along the beam caustic or tilting the sample [140]. Furthermore, as a complete quantitative measurement should contain quantitative data of both the phase shift and modulus, the I_0 monitoring needs to be improved.

In all parts of this thesis that showed ptychographic reconstructions, one or several of the extensions of the ptychographic model introduced in chapter 2 were applied, and often the discussion revolved around comparisons between variants in which certain extensions were used or not used. Even though these additional degrees of freedom in the model permit great improvements of image quality in a direct comparison, they also contribute to incapability to retrieve quantitative information. Furthermore, as they always need to be tailored to the individual measurement by a knowledgeable person, they greatly reduce the accessibility of ptychography to synchrotron users and hinder the implementation of automatic data processing pipelines. Therefore, experiments should be set up such that these algorithmic extensions are not necessary. Multi-slicing is the exception here, as it is sometimes inherently required by the fundamental physical working principle of the microscope.

The presented in situ measurement in solution was only a first demonstration and one of many more to come, multiple avenues for future research present themselves. There is the possibility to add complementary scanning microscopy contrasts (XRF, WAXS). The temporal resolution can be improved moderately by optimizing the scanning mechanics and x-ray geometry. At fourth generation synchrotron radiation sources, the temporal resolution can probably be increased to less than a minute, and much faster time scales can be accessed at XFELs with single-shot imaging techniques. Furthermore, the coherent radiation available at higher energies at fourth generation sources can be used to reduce the induced beam damage. The opportunities are manifold.



Appendix A

Monochromator vibrations

The original mechanical design of the DCMs at the PETRA III beamlines made them susceptible to vibrations induced by the cryogenic nitrogen cooling system [141]. In normal operation, vertical beam vibrations of $0.3 \mu\text{rad rms}$ were regularly observed; lowering the frequency of the cryogenic pumps would half this value. At that time, the channel cut monochromators with measured beam vibrations of $0.045 \mu\text{rad rms}$ [142] offered a significant advantage, the beamline P06 therefore decided to install one of them.

As an improved design of the cryogenic cooling system became available, the DCMs of microscopy beamlines were upgraded. After the upgrade, some measurements showed stability as good as the CC ($0.05 \mu\text{rad rms}$) or slightly higher ($0.07 \mu\text{rad rms}$) while others still observed up to 400% more vibrations with the DCM. Kristiansen et al. [143] demonstrated that beam vibrations may change up to 40% with changes of the Bragg angle while deviations higher than that indicate a higher sensitivity to external excitations of the DCM than the CC.

In general, the findings about the repeatability of vibration measurements presented in section 5.4.3 also applies here, i.e. isolated measurements do not suffice to characterize the vibrations in general. Different to the sample vibration measurements, only a handful of data points are available to assess monochromator vibrations.

In operation, the additional beam steering possibilities of the DCM outweigh the stability advantages of the CC; the DCM is therefore used for most measurements, including those presented in this work.

In addition to the vertical vibrations introduced by the monochromator, the higher-order suppressing mirrors can also introduce horizontal vibrations for which no quantification can be presented here.

Appendix B

Coordinate transformation for laser-interferometry

We want to derive an algebraic expression to transform a motion measured by interferometers under arbitrary directions into arbitrary target coordinates. This problem may seem identical to the base decomposition of a vector in a linear space, but it is not as a displacement collinear to one of the base vectors can still result in non-zero observations along other, non-orthogonal observation axes.

B.1 General problem

Let the displacement of the target reflector be

$$\Delta \mathbf{r} = \sum_{k=1}^3 r_k \cdot \hat{\mathbf{e}}_k \quad (\text{B.1})$$

where the r_k are scalar factors and the $\hat{\mathbf{e}}_k$ form an orthogonal, normalized base $\hat{\mathbf{e}}_i \cdot \hat{\mathbf{e}}_j = \delta_{ij}$. In a similar fashion, we define the observation axes $\hat{\mathbf{I}}_n$ of several interferometer axes as

$$\hat{\mathbf{I}}_n = \sum_{k=1}^3 a_{n,k} \cdot \hat{\mathbf{e}}_k \quad (\text{B.2})$$

with $\|\hat{\mathbf{I}}_n\| = 1$. The displacement we measure along with such an axes with an ideal interferometer is

$$\Delta l_n = \Delta \mathbf{r} \cdot \hat{\mathbf{I}}_n = \sum_{k=1}^3 r_k \cdot a_{n,k}. \quad (\text{B.3})$$

We are interested to find the component of the displacement $\Delta \mathbf{r}$ along

$$\hat{\mathbf{d}} = \sum_{k=1}^3 d_k \cdot \hat{\mathbf{e}}_k \quad (\text{B.4})$$

with $\|\hat{\mathbf{d}}\| = 1$. The value we are looking for is simply

$$\Delta d = \Delta \mathbf{r} \cdot \hat{\mathbf{d}} = \sum_{k=1}^3 r_k \cdot d_k. \quad (\text{B.5})$$

B.2 Two-dimensional case

Let us assume that we have two observation axes $\hat{\mathbf{I}}_n$ that are not colinear. In this case, we can describe the displacement $\Delta \mathbf{r}$ in the plane spanned by $\hat{\mathbf{I}}_1$ and $\hat{\mathbf{I}}_2$ as a linear combination:

$$\exists! (\alpha, \beta) \in \mathbb{R}^2 : \alpha \cdot \hat{\mathbf{I}}_1 + \beta \cdot \hat{\mathbf{I}}_2 = \Delta \mathbf{r}_n \quad (\text{B.6})$$

Inserting this linear combination into equations B.3 and B.5 yields

$$\Delta l_1 = \sum_k (\alpha \cdot a_{1,k} + \beta \cdot a_{2,k}) a_{1,k} \quad (\text{B.7})$$

$$\Delta l_2 = \sum_k (\alpha \cdot a_{1,k} + \beta \cdot a_{2,k}) a_{2,k} \quad (\text{B.8})$$

$$\Delta d = \sum_k (\alpha \cdot a_{1,k} + \beta \cdot a_{2,k}) d_k. \quad (\text{B.9})$$

This is a system of three equations with three unknowns α, β and Δd . Using the distributive property we get

$$\Delta l_1 = \alpha \sum_k a_{1,k}^2 + \beta \sum_k a_{1,k} a_{2,k} \quad (\text{B.10})$$

$$\Delta l_2 = \alpha \sum_k a_{1,k} a_{2,k} + \beta \sum_k a_{2,k}^2 \quad (\text{B.11})$$

where the $a_{n,k}$ are normalized

$$\sum_k a_{1,k}^2 = \sum_k a_{2,k}^2 = 1 \quad (\text{B.12})$$

and we define the scalar product as

$$A := \sum_k a_{1,k} a_{2,k}. \quad (\text{B.13})$$

The system of equations of reduced to

$$\Delta l_1 = \alpha + A\beta \quad (\text{B.14})$$

$$\Delta l_2 = A\alpha + \beta \quad (\text{B.15})$$

which is solved as

$$\alpha = \frac{\Delta l_1 - A\Delta l_2}{1 - A^2} \quad (\text{B.16})$$

$$\beta = \frac{\Delta l_2 - A\Delta l_1}{1 - A^2}. \quad (\text{B.17})$$

This solution can be inserted into equation B.9 to solve the problem in general. When the target coordinate axes are the Cartesian coordinate axes the solution is simplified to

$$\Delta x = a_{x,1}\alpha + a_{x,2}\beta \quad (\text{B.18})$$

$$\Delta y = a_{y,1}\alpha + a_{y,2}\beta. \quad (\text{B.19})$$

We leave the three-dimensional case as an exercise to the reader.

Appendix C

Homodyne Phase Quadrature

Here the derivation of the homodyne phase quadrature signal is reproduced from my prior work [10].

In a conventional Michelson interferometer, the intensity I of the observed interference pattern scales with the wave vector \mathbf{k} and the displacement Δx of the sample mirror:

$$I \sim \cos(2k\Delta x). \quad (\text{C.1})$$

This dependency is inconvenient as the sensitivity drops to zero at the extrema of the cosine; furthermore, the direction of the motion at the extrema cannot be distinguished. Therefore, it is desirable to measure a second signal that is proportional to the sine of the displacement. Sine and cosine complement each other perfectly and assure constant displacement sensitivity over an arbitrarily large distance.

There are a number of experimental methods to obtain this second signal; in one possible setup a second reference arm that is $\lambda/8$ longer is introduced. Modern commercial interferometers [82, 83] use rapid modulation (in the order of megahertz) of the laser's wavelength:

$$k = k_0 + \delta_k \cdot \cos(\omega t) \quad (\text{C.2})$$

We can insert this time-dependency into equation (C.1) and obtain

$$I \sim \cos(2\Delta x [k_0 + \delta_k \cdot \cos(\omega t)]) \quad (\text{C.3})$$

$$\sim \cos(2\Delta x k_0) \cos[2\Delta x \delta_k \cdot \cos(\omega t)] - \sin(2\Delta x k_0) \sin[2\Delta x \delta_k \cdot \cos(\omega t)]. \quad (\text{C.4})$$

We chose the amplitude of the modulation δ_k sufficiently small, such that we can apply a second-order Taylor approximation:

$$I \sim \cos(2\Delta x k_0) \left[1 - 2(\Delta x \delta_k)^2 \cos^2(\omega t) \right] - \sin(2\Delta x k_0) \cdot 2\Delta x \delta_k \cos(\omega t) \quad (\text{C.5})$$

With the theorem $\cos^2 x = \frac{1}{2}[1 + \cos(2x)]$, the observed intensity separates into three summands

$$I_C \sim \cos(2\delta x k_0) \left[1 - (\Delta x \delta_k)^2 \right] \quad (\text{C.6})$$

$$I_\omega \sim -\sin(2\Delta x k_0) \cdot 2\Delta x \delta_k \cdot \cos(\omega t) \quad (\text{C.7})$$

$$I_{2\omega} \sim -\cos(2\Delta x k_0) \cdot (\Delta x \delta_k)^2 \cos(2\omega t) \quad (\text{C.8})$$

Hence we see that demodulation of the time-dependent intensity yields us signals proportional to the sine and cosine of the displacement Δx .

In equations C.7 and C.8, the unknown displacement Δx is still contained in the prefactors $2\Delta x \delta_k$ and $(\Delta x \delta_k)^2$. Therefore, the quadrature signal $Z_q = I_\omega + iI_{2\omega}$ forms an ellipse of unknown (and potentially changing) eccentricity in the complex plane. As one of the prefactors is quadratic and the other is linear, the ellipse is in general strongly eccentric.

During the alignment procedure of the interferometers, the interferometer controllers vary the diode laser's wavelength over a large region so that the number of waves in the interferometer changes by several full waves, sampling the entire shape ellipse of the ellipse and fitting parameters to describe the shape. During measurement, the modulation of the wave length is so small that only a small arc-segment of the ellipse is sampled. When the vibrations are strong, or the reflector target is moved around, the entire ellipse is sampled during the measurement and the controller can adapt the fitting parameters.

However, when the vibrations are small, and the sample moves slowly, the controller cannot adapt the fitting parameters during the measurement, or adapts them wrongly, resulting on a strong periodic measurement error as shown fig. 5.13 on page 79.

Interference spectroscopy works with similar hardware, but constantly performs large wavelength sweeps that result in changes of about 10 waves in the interferometer. Instead of an ellipse, the resulting sinusoidal modulation is simply fitted, and an internal gas standard is used as an absolute wave length reference at which the fitted phase is evaluated.¹ With this method, fitting an ellipse and obtaining a periodic error can be avoided.

¹This information is published in parts in the European Patent [124], I was told some additional aspects of the working principle and implementation by the inventor Björn Habrich in person.

Appendix D

Carbon deposition and beam damage

During some experiments we noticed that prolonged scanning of a sample region can lead to material deposition on the sample. As the sample in PtyNAMI is in air, we suspect that this deposition is carbon [132], but no definite proof of the elemental composition has been obtained so far.

For unknown reasons, the samples of copperoxide cubes on kapton substrate seem to be particularly susceptible to material deposition. In a test measurement (fig. D.1, sample in air, not in situ), we scanned a fresh region of the substrate that was never exposed to the beam before. Afterwards, we let the focused beam rest on the sample and opened the shutter for 30 min, and repeated the scan afterwards. In the difference image (fig. D.1c) the imprint of the beam is clearly visible, about 70 mrad of material was deposited.

The first attempt to combat this effect was to build a large tent of about one cubic meter around the setup that was to be flushed with helium. However, due to leaks, only a 50% helium-air mixture could be achieved. Repeating the test measurement as described above showed that the phase shift of the material deposition had halved. Figure D.2 shows that the effect of prolonged exposure in such gas mixture is not only material deposition but apparently also deformation of the substrate as the particles clearly move closer together.

The material deposition could only be successfully suppressed by mounting the sample in a gas-tight cell (fig. D.3). This cell is a nanoreactor developed by Yakub Fam, Thomas Sheppard et al. at KIT in collaboration with the beamline P06 for complementary x-ray and electron imaging of catalytic processes [74]. By design, samples are mounted in the cell on TEM chips that provide heating capabilities as well as gas flow through windows in the membrane. We simply mounted a strip of sample with double-sided tape and flushed the cell continuously with helium. The entrance and exit windows of this cell are the third and fourth image planes shown in figures 7.9 and 7.12.

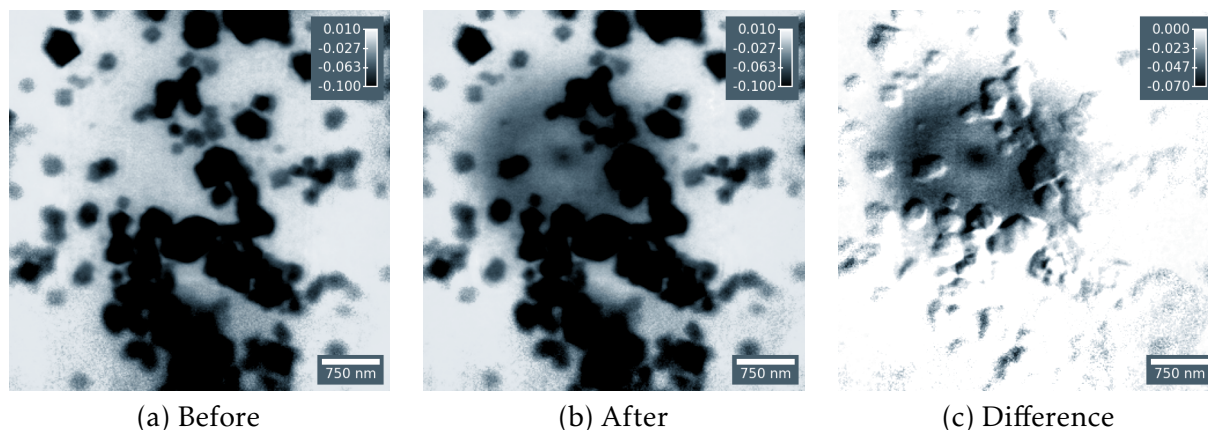


Figure D.1: Experiment to determine the effect of carbon deposition on samples of copper cubes on kapton substrate, conducted at room temperature in air. a) Ptychographic scan of a fresh region of the sample. b) Ptychographic scan after the focused beam rested for 30 min on a fixed spot on the sample. c) Difference of (a) and (b).

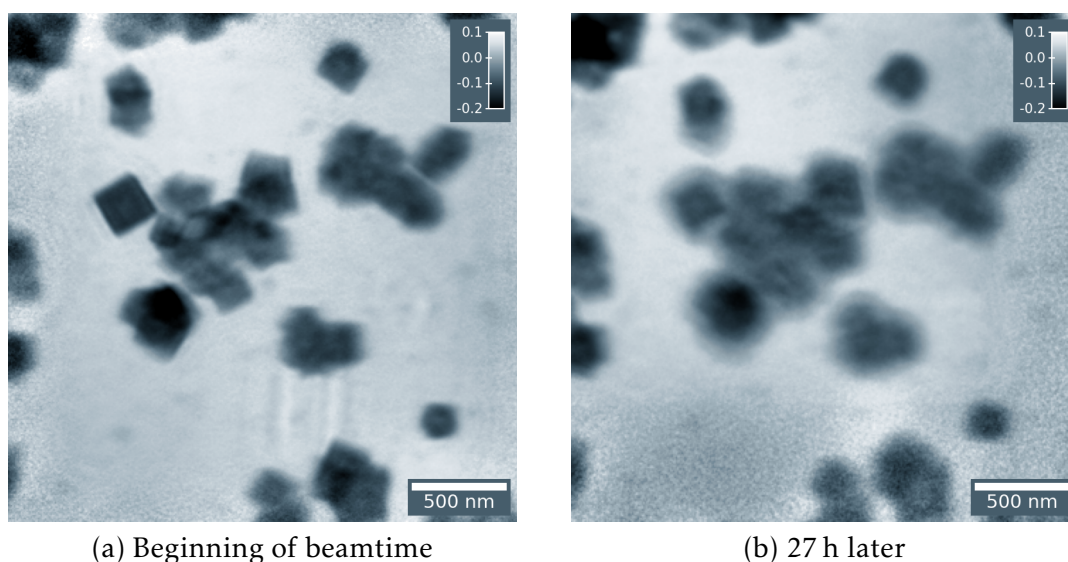


Figure D.2: Observation of beam damage in ex situ measurement under an atmosphere of approx. 50% helium and 50% air. Both images are one object slice of a two-slice reconstruction. a) First scan in this region. b) After 27 h of ptychographic imaging in this region. Besides softening of all in features in the sample the particles also moved closer to the center of the region of interest, indicating that the kapton substrate contracted in the beam.

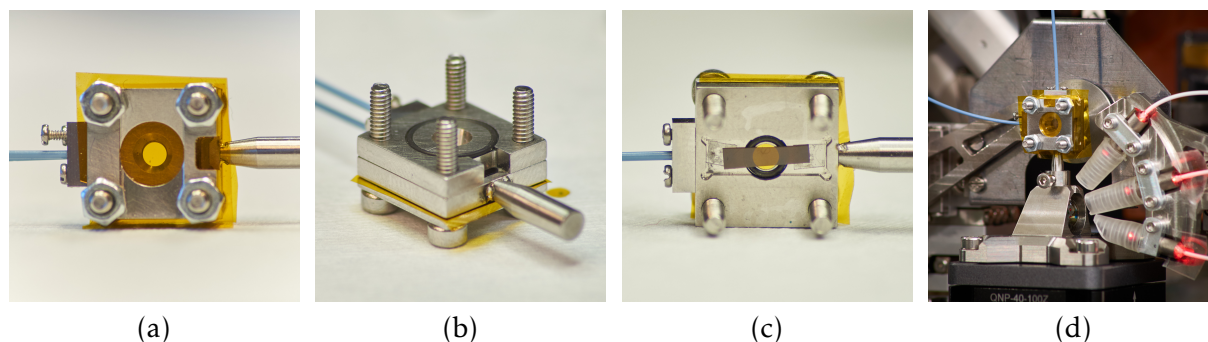


Figure D.3: Nanoreactor for gaseous reagents developed by KIT [74]. This reactor was used for all multi-slice measurements in chapter 7 and prevented beam damage of the kind shown above. a) View through empty cell. b) Rubber o-ring for gas-tight seal. c) Sample glued into the reactor with double-sided adhesive tape. d) Mounted in PtyNAMi.

Bibliography

- [1] Wikipedia The Free Encyclopedia. *List of countries by GDP (nominal)*. 2020. URL: [https://en.wikipedia.org/wiki/List_of_countries_by_GDP_\(nominal\)](https://en.wikipedia.org/wiki/List_of_countries_by_GDP_(nominal)) (visited on 12/15/2020) (cit. on p. 12).
- [2] Lightsources.org. *Light sources of the world*. 2020. URL: <https://lightsources.org/lightsources-of-the-world/> (visited on 12/15/2020) (cit. on p. 12).
- [3] Christian G. Schroer. *PETRA IV: upgrade of PETRA III to the Ultimate 3D X-ray microscope. Conceptual Design Report*. Ed. by Ralf Roehlsberger, Edgar Weckert, Rainer Wanzenberg, Ilya Agapov, Reinhard Brinkmann, and Wim Leemans. Hamburg: Deutsches Elektronen-Synchrotron DESY, 2019, 259 pages : illustrations, diagrams. DOI: 10.3204/PUBDB-2019-03613 (cit. on pp. 12, 36).
- [4] J. Als-Nielsen and D. McMorrow. *Elements of Modern X-Ray Physics*. John Wiley & Sons, 2011 (cit. on pp. 13, 16, 36).
- [5] Eugene Hecht. *Optics*. Second Edition. Addison-Wesley, 1987 (cit. on pp. 13, 74).
- [6] J.W. Goodman. *Introduction to Fourier Optics*. McGraw-Hill physical and quantum electronics series. W. H. Freeman, 2005 (cit. on p. 13).
- [7] D.C. Champeney. *Fourier transforms and their physical applications*. Ed. by N.H. March. Academic Press, 1973 (cit. on p. 13).
- [8] Tilman Butz. *Fouriertransformation für Fußgänger*. 7th. Vieweg+Teubner Verlag, 2011 (cit. on pp. 13, 99).
- [9] Chris Jacobsen. *X-ray Microscopy*. Advances in Microscopy and Microanalysis. Cambridge University Press, 2019. DOI: 10.1017/9781139924542 (cit. on pp. 13, 16, 29, 31, 43).
- [10] Martin Seyrich. “An Interferometric Positioning System for High Resolution 3D Ptychography”. MA thesis. Technische Universität Dresden, Oct. 2015 (cit. on pp. 13, 14, 57, 58, 60, 73, 75, 143, 160).
- [11] W. Hoppe. “Beugung im inhomogenen Primärstrahlwellenfeld. I. Prinzip einer Phasenmessung von Elektronenbeugungsinterferenzen”. In: *Acta Crystallographica Section A* 25.4 (July 1969), pp. 495–501. DOI: 10.1107/S0567739469001045 (cit. on p. 15).
- [12] W. Hoppe and G. Strube. “Beugung in inhomogenen Primärstrahlenwellenfeld. II. Lichtoptische Analogieversuche zur Phasenmessung von Gitterinterferenzen”. In: *Acta Crystallographica Section A* 25.4 (July 1969), pp. 502–507. DOI: 10.1107/S0567739469001057 (cit. on p. 15).

- [13] W. Hoppe. “Beugung im inhomogenen Primärstrahlwellenfeld. III. Amplituden- und Phasenbestimmung bei unperiodischen Objekten”. In: *Acta Crystallographica Section A* 25.4 (July 1969), pp. 508–514. doi: 10.1107/S0567739469001069 (cit. on p. 15).
- [14] R. Hegerl and W. Hoppe. “Dynamische Theorie der Kristallstrukturanalyse durch Elektronenbeugung im inhomogenen Primärstrahlwellenfeld”. In: *Berichte der Bunsengesellschaft für physikalische Chemie* 74.11 (1970), pp. 1148–1154. doi: 10.1002/bbpc.19700741112 (cit. on p. 15).
- [15] John Rodenburg and Andrew Maiden. “Ptychography”. In: *Springer Handbook of Microscopy*. Ed. by Peter W. Hawkes and John C. H. Spence. Cham: Springer International Publishing, 2019, pp. 819–904. doi: 10.1007/978-3-030-00069-1_17 (cit. on pp. 15, 18).
- [16] David M. Paganin. *Coherent X-Ray Optics*. Oxford Science Publications. Oxford University Press, 2006 (cit. on p. 16).
- [17] Henry Chapman et al. “Femtosecond diffractive imaging with a soft-X-ray free-electron laser”. In: *Nature Physics* 2 (Nov. 2006), pp. 839–843. doi: 10.1038/nphys461 (cit. on p. 17).
- [18] Johannes Hagemann. “X-Ray Near-Field Holography: Beyond Idealized Assumptions of the Probe”. Dissertation, University of Goettingen, 2017. Dissertation. Göttingen: University of Goettingen, 2017, p. 138. doi: 10.3204/PUBDB-2017-11971 (cit. on p. 17).
- [19] Andreas Schropp et al. “PtyNAMi: ptychographic nano-analytical microscope”. In: *Journal of Applied Crystallography* 53.4 (Aug. 2020), pp. 957–971. doi: 10.1107/S1600576720008420 (cit. on pp. 18, 36, 160).
- [20] Bjoern Enders, Kasra Nowrouzi, Harinarayan Krishnan, Stefano Marchesini, Jungjin Park, Young-Sang Yu, and David A. Shapiro. “Dataflow at the COSMIC Beamline - Stream Processing and Supercomputing”. In: *Microscopy and Microanalysis* 24.S2 (2018), pp. 56–57. doi: 10.1017/S1431927618012710 (cit. on p. 18).
- [21] Andrew M. Maiden and John M. Rodenburg. “An improved ptychographical phase retrieval algorithm for diffractive imaging”. In: *Ultramicroscopy* 109.10 (2009), pp. 1256–1262. doi: <https://doi.org/10.1016/j.ultramicroscopy.2009.05.012> (cit. on p. 18).
- [22] Wolfgang Hönig. *Portierung einer Ptychographie-Anwendung auf das CUDA GPU-Modell*. Großer Beleg, Technische Universität Dresden, Fakultät Informatik. 2010 (cit. on p. 19).
- [23] Robert Hoppe. “Anpassung und Optimierung des ptychographischen Modells für die quantitative Mikroskopie mit kohärenter Röntgenstrahlung und sichtbarem Laserlicht”. Dissertation, Universität Hamburg, 2019. Dissertation. Universität Hamburg, 2019, p. 203 (cit. on pp. 19, 21, 28).
- [24] Tobias Witt. “Multi-Slicing in der optischen Ptychographie”. MA thesis. Technische Universität Hamburg, 2016 (cit. on p. 19).
- [25] A. Schropp et al. “Hard x-ray nanobeam characterization by coherent diffraction microscopy”. In: *Applied Physics Letters* 96.9 (2010), p. 091102. doi: 10.1063/1.3332591 (cit. on pp. 20, 60).

- [26] Frank Seiboth et al. “Perfect X-ray focusing via fitting corrective glasses to aberrated optics”. In: *Nature Communications* 8 (Mar. 2017), p. 14623. doi: 10.1038/ncomms14623 (cit. on p. 20).
- [27] Esther H. R. Tsai et al. “High-Resolution Ptychographic Tomography with Extended Depth of Field”. In: *Imaging and Applied Optics 2017 (3D, AIO, COSI, IS, MATH, pcAOP)*. Optical Society of America, 2017, CW3B.2. doi: 10.1364/COSI.2017.CW3B.2 (cit. on p. 21).
- [28] Maik Kahnt. “3D nano-tomography using coherent X-rays”. eng. PhD thesis. Universität Hamburg, 2019 (cit. on p. 21).
- [29] T. M. Godden, R. Suman, M. J. Humphry, J. M. Rodenburg, and A. M. Maiden. “Ptychographic microscope for three-dimensional imaging”. In: *Opt. Express* 22.10 (May 2014), pp. 12513–12523. doi: 10.1364/OE.22.012513 (cit. on p. 21).
- [30] A. M. Maiden, M. J. Humphry, and J. M. Rodenburg. “Ptychographic transmission microscopy in three dimensions using a multi-slice approach”. In: *J. Opt. Soc. Am. A* 29.8 (Aug. 2012), pp. 1606–1614. doi: 10.1364/JOSAA.29.001606 (cit. on p. 23).
- [31] Jiantai Dou, Zhishan Gao, Jun Ma, Caojin Yuan, Zhongming Yang, and Lei Wang. “Iterative autofocusing strategy for axial distance error correction in ptychography”. In: *Optics and Lasers in Engineering* 98 (2017), pp. 56–61. doi: <https://doi.org/10.1016/j.optlaseng.2017.06.003> (cit. on p. 24).
- [32] Felix Wittwer. “Untersuchung der Auflösung der Beugungsbilder in der Ptychographie”. MA thesis. Technische Universität Hamburg, 2015 (cit. on p. 24).
- [33] D. J. Batey, T. B. Edo, C. Rau, U. Wagner, Z. D. Pe šić, T. A. Waigh, and J. M. Rodenburg. “Reciprocal-space up-sampling from real-space oversampling in x-ray ptychography”. In: *Phys. Rev. A* 89 (4 Apr. 2014), p. 043812. doi: 10.1103/PhysRevA.89.043812 (cit. on p. 24).
- [34] Felix Wittwer, Robert Hoppe, Frank Seiboth, Juliane Reinhardt, Maria Scholz, and Christian Schroer. “Ptychography with a Virtually Enlarged Illumination”. In: vol. 24. S2. © Microscopy Society of America. 14th International Conference on X-ray Microscopy, Saskatoon (Canada), 20 Aug 2018 - 24 Aug 2018. New York, NY: Cambridge University Press, Aug. 2018, pp. 48–49. doi: 10.1017/S1431927618012667 (cit. on p. 24).
- [35] H.M.L. Faulkner and J.M. Rodenburg. “Error tolerance of an iterative phase retrieval algorithm for moveable illumination microscopy”. In: *Ultramicroscopy* 103.2 (2005), pp. 153–164. doi: <https://doi.org/10.1016/j.ultramicro.2004.11.006> (cit. on p. 26).
- [36] A.M. Maiden, M.J. Humphry, M.C. Sarahan, B. Kraus, and J.M. Rodenburg. “An annealing algorithm to correct positioning errors in ptychography”. In: *Ultramicroscopy* 120 (2012), pp. 64–72. doi: <https://doi.org/10.1016/j.ultramicro.2012.06.001> (cit. on p. 26).
- [37] Edgar Weckert. “The potential of future light sources to explore the structure and function of matter”. In: *IUCrJ* 2.2 (Mar. 2015), pp. 230–245. doi: 10.1107/S2052252514024269 (cit. on pp. 28, 36).

- [38] Max Rose. “Coherent X-ray diffractive imaging of biological samples in 2D and 3D with synchrotron and XFEL radiation”. Dissertation, Universität Hamburg, 2018. Dissertation. Hamburg: Universität Hamburg, 2018, p. 203. doi: 10.3204/PUBDB-2018-05474 (cit. on pp. 28, 33).
- [39] Lord Rayleigh F.R.S. “XXXI. Investigations in optics, with special reference to the spectroscope”. In: *The London, Edinburgh, and Dublin Philosophical Magazine and Journal of Science* 8.49 (1879), pp. 261–274. doi: 10.1080/14786447908639684. eprint: <https://doi.org/10.1080/14786447908639684> (cit. on p. 29).
- [40] Ernst Abbe. “Beiträge zur Theorie des Mikroskops und der mikroskopischen Wahrnehmung”. In: *Archiv für mikroskopische Anatomie* 9.1 (1873), pp. 413–418 (cit. on p. 29).
- [41] Saša Bajt and Christian Schroer. “Sub-micrometer Focusing and High-Resolution Imaging with Refractive Lenses and Multilayer Laue Optics”. In: *Synchrotron Light Sources and Free-Electron Lasers*. Cham: Springer International Publishing, 2019, pp. 1–28. doi: 10.1007/978-3-319-04507-8_62-1 (cit. on p. 29).
- [42] Diana Duarte. “Edge effects in a pixelated CdTe radiation detector”. PhD thesis. Aug. 2016. doi: 10.13140/RG.2.2.20470.86081 (cit. on p. 29).
- [43] Günther Porod. “Theorie der diffusen Röntgenkleinwinkelstreuung an kolloiden Systemen”. In: *Zeitschrift für Naturforschung A* 4.6 (1949), pp. 401–414. doi: <https://doi.org/10.1515/zna-1949-0601> (cit. on pp. 30, 85).
- [44] S. K. Sinha, E. B. Sirota, S. Garoff, and H. B. Stanley. “X-ray and neutron scattering from rough surfaces”. In: *Phys. Rev. B* 38 (4 Aug. 1988), pp. 2297–2311. doi: 10.1103/PhysRevB.38.2297 (cit. on pp. 30, 85).
- [45] D. Starodub et al. “Dose, exposure time and resolution in serial X-ray crystallography”. In: *Journal of Synchrotron Radiation* 15.1 (Jan. 2008), pp. 62–73. doi: 10.1107/S0909049507048893 (cit. on pp. 30, 85).
- [46] J. M. Rodenburg and R. H. T. Bates. “The theory of super-resolution electron microscopy via Wigner-distribution deconvolution”. In: *Philosophical Transactions of the Royal Society of London. Series A: Physical and Engineering Sciences* 339.1655 (1992), pp. 521–553. doi: 10.1098/rsta.1992.0050. eprint: <https://royalsocietypublishing.org/doi/pdf/10.1098/rsta.1992.0050> (cit. on p. 31).
- [47] Esther H. R. Tsai, Ivan Usov, Ana Diaz, Andreas Menzel, and Manuel Guizar-Sicairos. “X-ray ptychography with extended depth of field”. In: *Opt. Express* 24.25 (Dec. 2016), pp. 29089–29108. doi: 10.1364/OE.24.029089 (cit. on pp. 31, 112, 113).
- [48] Andreas Schropp and Christian G Schroer. “Dose requirements for resolving a given feature in an object by coherent x-ray diffraction imaging”. In: *New Journal of Physics* 12.3 (Mar. 2010), p. 035016. doi: 10.1088/1367-2630/12/3/035016 (cit. on p. 33).
- [49] R. N. Wilke, M. Priebe, M. Bartels, K. Giewekemeyer, A. Diaz, P. Karvinen, and T. Salditt. “Hard X-ray imaging of bacterial cells: nano-diffraction and ptychographic reconstruction”. In: *Opt. Express* 20.17 (Aug. 2012), pp. 19232–19254. doi: 10.1364/OE.20.019232 (cit. on p. 33).

- [50] Peter Modregger, Daniel Lübbert, Peter Schäfer, and Rolf Köhler. “Spatial resolution in Bragg-magnified X-ray images as determined by Fourier analysis”. In: *physica status solidi (a)* 204.8 (2007), pp. 2746–2752. doi: 10.1002/pssa.200675685 (cit. on p. 33).
- [51] Marin van Heel and Michael Schatz. “Fourier shell correlation threshold criteria”. In: *Journal of Structural Biology* 151.3 (2005), pp. 250–262. doi: <https://doi.org/10.1016/j.jsb.2005.05.009> (cit. on p. 33).
- [52] Pawel A. Penczek. “Chapter Three - Resolution Measures in Molecular Electron Microscopy”. In: *Cryo-EM, Part B: 3-D Reconstruction*. Ed. by Grant J. Jensen. Vol. 482. Methods in Enzymology. Academic Press, 2010, pp. 73–100. doi: [https://doi.org/10.1016/S0076-6879\(10\)82003-8](https://doi.org/10.1016/S0076-6879(10)82003-8) (cit. on p. 33).
- [53] Marin van Heel and Michael Schatz. “Reassessing the Revolution’s Resolutions”. In: *bioRxiv* (2017). doi: 10.1101/224402. eprint: <https://www.biorxiv.org/content/early/2017/11/24/224402.full.pdf> (cit. on p. 33).
- [54] Niccolò Banterle, Khanh Huy Bui, Edward A. Lemke, and Martin Beck. “Fourier ring correlation as a resolution criterion for super-resolution microscopy”. In: *Journal of Structural Biology* 183.3 (2013), pp. 363–367. doi: <https://doi.org/10.1016/j.jsb.2013.05.004> (cit. on p. 33).
- [55] Frank Grotelüschen, Barbara Warmbein, Ute Wilhelmsen, Thomas Zoufal, and Ilke Flegel. *50 Jahre DESY*. Deutsches Elektronen-Synchrotron DESY, 2009 (cit. on p. 35).
- [56] R. Brandelik et al. “Evidence for planar events in e+e- annihilation at high energies”. In: *Physics Letters B* 86.2 (1979), pp. 243–249. doi: [https://doi.org/10.1016/0370-2693\(79\)90830-X](https://doi.org/10.1016/0370-2693(79)90830-X) (cit. on p. 35).
- [57] K. Balewski, W. Brefeld, U. Hahn, J. Pflüger, and R. Rossmanith. “An undulator at PETRA II—a new synchrotron radiation source at DESY”. In: *Proceedings Particle Accelerator Conference*. Vol. 1. 1995, 275–277 vol.1 (cit. on p. 35).
- [58] Christian G. Schroer et al. “PETRA IV: the ultralow-emittance source project at DESY”. In: *Journal of Synchrotron Radiation* 25.5 (Sept. 2018), pp. 1277–1290. doi: 10.1107/S1600577518008858 (cit. on p. 36).
- [59] Pedro F. Tavares et al. “Commissioning and first-year operational results of the MAXIV 3GeV ring”. In: *Journal of Synchrotron Radiation* 25.5 (Sept. 2018), pp. 1291–1316. doi: 10.1107/S1600577518008111 (cit. on p. 36).
- [60] Andraut D. et al. *The orange Book: ESRF UPGRADE PROGRAMME PHASE II (2015 - 2022)*. 2019. doi: 10.1515/ESRF-DC-186715732 (cit. on p. 36).
- [61] C. G. Schroer et al. “Hard X-ray nanoprobe at beamline P06 at PETRA III”. In: *Nuclear instruments & methods in physics research / A* 616 (2010), pp. 93–97. doi: 10.1016/j.nima.2009.10.094 (cit. on pp. 36, 38).
- [62] C. G. Schroer et al. “Hard x-ray nanoprobe of beamline P06 at PETRA III”. In: *AIP Conference Proceedings* 1741.1 (2016), p. 030007. doi: 10.1063/1.4952830. eprint: <https://aip.scitation.org/doi/pdf/10.1063/1.4952830> (cit. on p. 36).
- [63] K. Balewski, W. Brefeld, W. Decking, H. Franz, R. Rohlsberger, and E. Weckert. *PETRA III: A low emittance synchrotron radiation source (Technical design report)*. Tech. rep. DESY-04-035. ISSN: 0418-9833. 2004, p. 558 (cit. on p. 37).

- [64] R. W. Alkire, G. Rosenbaum, and G. Evans. “Design of a vacuum-compatible high-precision monochromatic beam-position monitor for use with synchrotron radiation from 5 to 25keV”. In: *Journal of Synchrotron Radiation* 7.2 (Mar. 2000), pp. 61–68. doi: 10.1107/S090904959901568X (cit. on p. 38).
- [65] Mikhail Lyubomirskiy. “High energy X-ray inline interferometry based on refractive lenses”. PhD thesis. Mar. 2016. doi: 10.13140/RG.2.1.2460.4560 (cit. on p. 38).
- [66] Mikhail Lyubomirskiy, Irina Snigireva, and Anatoly Snigirev. “Lens coupled tunable Young’s double pinhole system for hard X-ray spatial coherence characterization”. In: *Opt. Express* 24.12 (June 2016), pp. 13679–13686. doi: 10.1364/OE.24.013679 (cit. on p. 38).
- [67] Gavin B. M. Vaughan, Jonathan P. Wright, Aleksei Bytchkov, Michel Rossat, Henri Gleyzolle, Irina Snigireva, and Anatoly Snigirev. “X-ray transfocators: focusing devices based on compound refractive lenses”. In: *Journal of Synchrotron Radiation* 18.2 (Mar. 2011), pp. 125–133. doi: 10.1107/S0909049510044365 (cit. on p. 38).
- [68] Nobelstiftelsen. *Les Prix Nobel en 1919-1920*. French. 1922 (cit. on p. 41).
- [69] C. G. Schroer et al. “Hard x-ray nanoprobe based on refractive x-ray lenses”. In: *Applied Physics Letters* 87.12 (2005), p. 124103. doi: 10.1063/1.2053350 (cit. on p. 43).
- [70] Adam Kubec et al. “Ptychography with multilayer Laue lenses”. In: *Journal of Synchrotron Radiation* 21.5 (Sept. 2014), pp. 1122–1127. doi: 10.1107/S1600577514014556 (cit. on p. 44).
- [71] Saša Bajt et al. “X-ray focusing with efficient high-NA multilayer Laue lenses”. In: *Light: Science & Applications* 7.3 (2018), pp. 17162–17162 (cit. on pp. 44, 70).
- [72] Shaul Barkan, Jan Iwanczyk, Bradley Patt, Liangyuan Feng, and Carolyn Tull. “Vortex™ - A new high performance silicon drift detector for XRD and XRF Applications”. In: *Adv. X-Ray Anal.* 46 (Jan. 2003) (cit. on p. 44).
- [73] M. Holler et al. “OMNY—A tOMography Nano crYo stage”. In: *Review of Scientific Instruments* 89.4 (2018), p. 043706. doi: 10.1063/1.5020247. eprint: <https://doi.org/10.1063/1.5020247> (cit. on pp. 47, 60).
- [74] Yakub Fam et al. “A versatile nanoreactor for complementary *in situ* X-ray and electron microscopy studies in catalysis and materials science”. In: *Journal of Synchrotron Radiation* 26.5 (Sept. 2019), pp. 1769–1781. doi: 10.1107/S160057751900660X (cit. on pp. 47, 145, 146).
- [75] Claire Donnelly et al. “Time-resolved imaging of three-dimensional nanoscale magnetization dynamics”. In: *Nature Nanotechnology* 15 (May 2020). doi: 10.1038/s41565-020-0649-x (cit. on p. 47).
- [76] Malwina Staniuk, Daniel Zindel, Wouter van Beek, Ofer Hirsch, Niklaus Kränzlin, Markus Niederberger, and Dorota Koziej. “Matching the organic and inorganic counterparts during nucleation and growth of copper-based nanoparticles – *in situ* spectroscopic studies”. In: *CrystEngComm* 17 (36 2015), pp. 6962–6971. doi: 10.1039/C5CE00454C (cit. on p. 47).

- [77] Niklaus Kränzlin, Wouter van Beek, Markus Niederberger, and Dorota Koziej. “Mechanistic Studies as a Tool for the Design of Copper-Based Heterostructures”. In: *Advanced Materials Interfaces* 2.9 (2015), p. 1500094. doi: 10.1002/admi.201500094. eprint: <https://onlinelibrary.wiley.com/doi/pdf/10.1002/admi.201500094> (cit. on p. 47).
- [78] Shengda Pu, Chen Gong, and Alex W. Robertson. “Liquid cell transmission electron microscopy and its applications”. In: *Royal Society Open Science* 7.1 (2020), p. 191204. doi: 10.1098/rsos.191204. eprint: <https://royalsocietypublishing.org/doi/pdf/10.1098/rsos.191204> (cit. on p. 49).
- [79] Aerotech Inc. *Piezo Engineering Tutorial*. 2014. URL: <https://www.aerotechgmbh.de/media/851554/aerotech%20piezo%20engineering%20tutorial.pdf> (visited on 10/29/2020) (cit. on p. 49).
- [80] Schott AG. *ZERODUR® Glaskeramik mit extrem niedriger thermischer Ausdehnung*. 2020. URL: https://www.schott.com/advanced_optics/german/products/optical-materials/zerodur-extremely-low-expansion-glass-ceramic/zerodur/index.html (visited on 11/01/2020) (cit. on p. 51).
- [81] Ulrich Teubner, (author.) Brückner Hans Josef, and ProQuest (Firm). *Optical imaging and photography : introduction to science and technology of optics, sensors and systems*. English. Includes bibliographical references (pages 571-572) and index. Berlin : De Gruyter, 2019 (cit. on p. 54).
- [82] *User Manual attoFPSX010 Version 1.11*. attocube systems AG. Jan. 2015 (cit. on pp. 55, 143).
- [83] Smaract GmbH. *PicoScale User Manual*. Version 2.1.4. 2018 (cit. on pp. 55, 143).
- [84] M. Kahnt et al. “Simultaneous Hard X-ray Ptychographic Tomography and X-ray Fluorescence Tomography of Isolated Hollow Core-Shell GaN Rods”. In: *Microscopy and Microanalysis* 24.S2 (2018), pp. 32–33 (cit. on p. 55).
- [85] SmarAct GmbH. *PicoScale sensor head type F01 - Specification Sheet*. Version 1.10. 2019 (cit. on p. 56).
- [86] SmarAct GmbH. *PicoScale sensor head type C01*. Version 1.12. 2019 (cit. on p. 56).
- [87] SmarAct GmbH. *PicoScale sensor head type L01 - Specification Sheet*. Version 1.16. 2020 (cit. on p. 56).
- [88] Simionovici Alexandre, Pierre Bleuet, and Bruno Golosio. “Advanced Tomographic Methods in Materials Research and Engineering”. In: ed. by John Banhart. Oxford: Oxford University Press, 2008. Chap. 8.1, pp. 202–210, 235–243 (cit. on p. 57).
- [89] Florian Schaff, Martin Bech, Paul Zaslansky, Christoph Jud, Marianne Liebi, Manuel Guizar-Sicairos, and Franz Pfeiffer. “Six-dimensional real and reciprocal space small-angle X-ray scattering tomography”. In: *Nature* 527 (Nov. 2015), pp. 353–356. doi: 10.1038/nature16060 (cit. on p. 57).
- [90] M. Holler, J. Raabe, A. Diaz, M. Guizar-Sicairos, C. Quitmann, A. Menzel, and O. Bunk. “An instrument for 3D x-ray nano-imaging”. In: *Review of Scientific Instruments* 83.7, 073703 (2012), pp. -. doi: <http://dx.doi.org/10.1063/1.4737624> (cit. on p. 57).

- [91] Mirko Holler and Jörg Raabe. “Error motion compensating tracking interferometer for the position measurement of objects with rotational degree of freedom”. In: *Optical Engineering* 54.5 (2015), p. 054101. DOI: 10.1117/1.0E.54.5.054101 (cit. on p. 57).
- [92] Jungdae Kim, K. Lauer, H. Yan, Y. S. Chu, and E. Nazaretski. “Compact prototype apparatus for reducing the circle of confusion down to 40 nm for x-ray nanotomography”. In: *Review of Scientific Instruments* 84.3 (2013), p. 035006. DOI: 10.1063/1.4798546. eprint: <https://doi.org/10.1063/1.4798546> (cit. on p. 57).
- [93] Tomaš Stankevič et al. “Interferometric characterization of rotation stages for X-ray nanotomography”. In: *Review of Scientific Instruments* 88.5 (2017), p. 053703. DOI: 10.1063/1.4983405. eprint: <https://doi.org/10.1063/1.4983405> (cit. on p. 57).
- [94] Christian G. Schroer et al. “PtyNAMI: ptychographic nano-analytical microscope at PETRA III: interferometrically tracking positions for 3D x-ray scanning microscopy using a ball-lens retroreflector”. In: *X-Ray Nanoimaging: Instruments and Methods III*. Ed. by Barry Lai and Andrea Somogyi. Vol. 10389. International Society for Optics and Photonics. SPIE, 2017, pp. 8–17. DOI: 10.1117/12.2273710 (cit. on pp. 57, 73, 160).
- [95] OHARA GmbH. *S-LAH79 Data Sheet*. 2019. URL: https://www.ohara-gmbh.com/fileadmin/user_upload/export-data/pdf/product_datasheets/S-LAH79_English_.pdf (visited on 05/25/2020) (cit. on p. 57).
- [96] Yi-Ting Tu. *Ray Optics Simulation*. Version 2. Google Chrome App. 2015. URL: <https://chrome.google.com/webstore/detail/ray-optics-simulation/egamlemiiddmmccadndbjjihkcfiobh> (cit. on p. 58).
- [97] Mirko Landmann. *Entwicklung und Konstruktion von hochpräzisen Justierungsmechanismen für Interferometerachsen und Probenkörper*. Hamburg University of Applied Sciences. Bachelorarbeit. 2018 (cit. on p. 58).
- [98] Christian Schroer et al. “Hard x-ray nano-beam characterization by ptychographic imaging”. In: vol. 8141. *Advances in Computational Methods for X-Ray Optics II*, San Diego (USA), 21 Aug 2011 - 21 Aug 2011. Bellingham, Wash.: SPIE, Aug. 21, 2011, pp. 814103-814103-10. DOI: 10.1117/12.893055 (cit. on p. 60).
- [99] Inc. Aerotech. *QNP-XY Series Product Sheet*. 2018. URL: <https://www.aerotechgmbh.de/media/3196518/qnp-xy.pdf> (visited on 08/17/2020) (cit. on p. 61).
- [100] Inc. Aerotech. *QNP-Z Series Product Sheet*. 2018. URL: <https://www.aerotechgmbh.de/media/3196560/qnp-z.pdf> (visited on 08/17/2020) (cit. on p. 61).
- [101] Richard Leach. “Abbe Error/Offset”. In: *CIRP Encyclopedia of Production Engineering*. Ed. by Luc The International Academy for Produand Laperrière and Gunther Reinhart. Berlin, Heidelberg: Springer Berlin Heidelberg, 2014, pp. 1–4. DOI: 10.1007/978-3-642-35950-7_16793-1 (cit. on p. 61).
- [102] Sasa Bajt et al. “X-ray focusing with efficient high-NA multilayer Laue lenses”. In: *Light: Science & Applications* 7 (Mar. 2018), p. 17162. DOI: 10.1038/lsa.2017.162 (cit. on p. 62).

- [103] Charles Bevis et al. “Multiple beam ptychography for large field-of-view, high throughput, quantitative phase contrast imaging”. In: *Ultramicroscopy* 184 (2018), pp. 164–171. doi: <https://doi.org/10.1016/j.ultramic.2017.08.018> (cit. on p. 62).
- [104] SmarAct GmbH. *PicoScale Interferometer Noise and Resolution*. Version 1.5. 2020 (cit. on p. 63).
- [105] Imke Greving et al. “P05 imaging beamline at PETRA III: first results”. In: *Proceedings of SPIE* 9212 (Aug. 18, 2014). Ed. by Stuart R. Stock, 92120O. doi: 10.1117/12.2061768 (cit. on p. 65).
- [106] Nobert Schell, Ann-Christian Dippel, and Martin von Zimmermann. *Unified Data Sheet P07 - High Energy Materials Science Beamline*. 2020. URL: https://photon-science.desy.de/facilities/petra_iii/beamlines/p07_high_energy_materials_science/unified_data_sheet_p07/index_eng.html (visited on 05/26/2020) (cit. on p. 65).
- [107] Torben Reuß. *Analyse und Optimierung der Schwingungseigenschaften der Experimentierumgebung am Teilchenbeschleuniger PETRA III*. Bachelor’s Thesis, Hamburg University of Applied Sciences. Bachelorarbeit. 2018 (cit. on p. 66).
- [108] Martin Seyrich. *2016 PtyNAMi comparison construction site*. 2020. URL: https://ptychography.com/video/2016_ptynami_comparison_construction_site.mp4 (visited on 11/06/2020) (cit. on p. 69).
- [109] Martin Seyrich. *2017 Vibrations Cryo Chamber 3D*.mp4. 2020. URL: https://ptychography.com/video/2017_vibrations_cryo_chamber_3D.mp4 (visited on 11/06/2020) (cit. on p. 69).
- [110] Martin Seyrich. *2019 PtyNAMi comparison tomo vs ultrastable*. 2020. URL: https://ptychography.com/video/2019_comparison_ptynami_tomo_vs_ultrastable.mp4 (visited on 11/06/2020) (cit. on p. 69).
- [111] Jens Patommel et al. “Focusing hard x rays beyond the critical angle of total reflection by adiabatically focusing lenses”. In: *Applied Physics Letters* 110.10 (2017), p. 101103. doi: 10.1063/1.4977882. eprint: <https://doi.org/10.1063/1.4977882> (cit. on p. 70).
- [112] Bengt Edlén. “The Dispersion of Standard Air*”. In: *J. Opt. Soc. Am.* 43.5 (May 1953), pp. 339–344. doi: 10.1364/JOSA.43.000339 (cit. on p. 73).
- [113] Bengt Edlén. “The Refractive Index of Air”. In: *Metrologia* 2.2 (1966), p. 71 (cit. on p. 73).
- [114] Karolina Stachnik et al. “Multimodal X-ray imaging of nanocontainer-treated macrophages and calcium distribution in the periacicular bone matrix”. In: *Scientific Reports* (Feb. 2020). doi: 10.1038/s41598-020-58318-7 (cit. on p. 74).
- [115] Mirko Landmann. “Thermische Simulation zweier Designvarianten für einen Probenaufbau mit In-Situ-Heizung.” Master’s Project. MA thesis. Hamburg University of Applied Sciences, 2020 (cit. on p. 74).
- [116] Anthony Dandridge, Alan Tveten, and Thomas Giallorenzi. “Homodyne demodulation scheme for fiber optic sensors using phase generated carrier”. In: *IEEE Journal of Quantum Electronics* 18.10 (1982), pp. 1647–1653 (cit. on p. 75).

- [117] U. Minoni, E. Sardini, E. Gelmini, F. Docchio, and D. Marioli. “A high-frequency sinusoidal phase-modulation interferometer using an electro-optic modulator: Development and evaluation”. In: *Review of Scientific Instruments* 62.11 (1991), pp. 2579–2583. DOI: 10.1063/1.1142233. eprint: <https://doi.org/10.1063/1.1142233> (cit. on p. 75).
- [118] Klaus Thurner, Francesca Paola Quacquarelli, Pierre-François Braun, Claudio Dal Savio, and Khaled Karrai. “Fiber-based distance sensing interferometry”. In: *Appl. Opt.* 54.10 (Apr. 2015), pp. 3051–3063. DOI: 10.1364/AO.54.003051 (cit. on p. 75).
- [119] Khaled Karrai. “Apparatus for determining a position”. EP2045572. Attocube Systems AG. 2007 (cit. on p. 75).
- [120] Khaled Karrai and Pierre-François Braun. “Positioning device with confocal Fabry-Perot interferometer”. EP2363685. Attocube Systems AG. 2010 (cit. on p. 75).
- [121] Kakao Kobayashi and Kuroe Akio. “Optical Measurement Instrument”. JPH07-49922B2. Matsushita Electric Industrial Co. Ltd. 1987 (cit. on p. 75).
- [122] Klaus Thurner, Pierre-François Braun, and Khaled Karrai. “Fabry-Pérot interferometry for long range displacement sensing”. In: *Review of Scientific Instruments* 84.9, 095005 (2013), pp. -. DOI: <http://dx.doi.org/10.1063/1.4821623> (cit. on p. 75).
- [123] qutools GmbH. *quDIS - Interferometric distance measurement Whitepaper*. 2020. URL: https://www.qutools.com/files/quDIS/qutools_quDIS_Whitepaper.pdf (visited on 08/11/2020) (cit. on p. 80).
- [124] Björn Habrich. “Measuring a cavity by means of interference spectroscopy”. WO2017144567A1. 2016 (cit. on pp. 80, 144).
- [125] Maria Scholz. “3D Multimodal X-ray Imaging of a Microchip: Correlating Structure, Composition and Orientation at the Nanoscale”. Dissertation. Universität Hamburg, 2021. Forthcoming (cit. on p. 80).
- [126] Christian Brönnimann and Peter Trüb. “Hybrid Pixel Photon Counting X-Ray Detectors for Synchrotron Radiation”. In: *Synchrotron Light Sources and Free-Electron Lasers: Accelerator Physics, Instrumentation and Science Applications*. Ed. by Eberhard J. Jaeschke, Shaukat Khan, Jochen R. Schneider, and Jerome B. Hastings. Cham: Springer International Publishing, 2016, pp. 995–1027. DOI: 10.1007/978-3-319-14394-1_36 (cit. on p. 85).
- [127] DECTRIS Ltd. *Technical Specifications EIGER X 4M Detector Systems*. Version v1.3.8. 2019 (cit. on p. 86).
- [128] DECTRIS Ltd. *Specific Solutions - X-ray Diffraction*. 2020. URL: <https://www.dectris.com/products/specific-solutions/diffraction/> (visited on 03/23/2020) (cit. on p. 86).
- [129] Susanne Klare. “Der Einfluss des Messuntergrundes auf die Ptychographische Bildgebung”. University of Hamburg, 2017. PhD thesis. University of Hamburg, 2017 (cit. on pp. 87, 88, 91).
- [130] Hendrik Lindemann. “Entwicklung eines Positioniersystems für ein Absorptionselement im Hochvakuum.” MA thesis. Hamburg University of Applied Sciences, 2018 (cit. on p. 87).

- [131] R. N. Wilke, M. Vassholz, and T. Salditt. “Semi-transparent central stop in high-resolution X-ray ptychography using Kirkpatrick–Baez focusing”. In: *Acta Crystallographica Section A* 69.5 (Sept. 2013), pp. 490–497. doi: 10.1107/S0108767313019612 (cit. on p. 88).
- [132] Juliane Reinhardt. “Resonant Hard X-ray Ptychography for High-Sensitivity Imaging with Chemical Contrast”. University of Hamburg, 2017. PhD thesis. University of Hamburg, 2017 (cit. on pp. 88, 145).
- [133] Juliane Reinhardt et al. “Beamstop-based low-background ptychography to image weakly scattering objects”. In: *Ultramicroscopy* 173 (2017), pp. 52–57. doi: <https://doi.org/10.1016/j.ultramicro.2016.11.005> (cit. on p. 88).
- [134] Eric Gullikson. *X-Ray Interactions with Matter*. 2010. url: http://henke.lbl.gov/optical_constants/ (visited on 05/19/2020) (cit. on p. 89).
- [135] David Attwood et al. *X-ray Data Booklet*. Berkeley, CA: Lawrence Berkeley National Laboratory, University of California, 2009 October 2009 (cit. on p. 97).
- [136] Christian G. Schroer et al. “Hard x-ray nanofocusing with refractive x-ray optics: full beam characterization by ptychographic imaging”. In: *Advances in X-Ray/EUV Optics and Components VIII*. Ed. by Ali Khounsary, Shunji Goto, and Christian Morawe. Vol. 8848. International Society for Optics and Photonics. SPIE, 2013, pp. 38–47. doi: 10.1117/12.2024127 (cit. on p. 99).
- [137] Marin [van Heel] and Michael Schatz. “Fourier shell correlation threshold criteria”. In: *Journal of Structural Biology* 151.3 (2005), pp. 250–262. doi: <https://doi.org/10.1016/j.jsb.2005.05.009> (cit. on p. 103).
- [138] National Institutes of Health. *ImageJ*. 2018. url: <https://imagej.nih.gov/ij/index.html> (visited on 08/22/2020) (cit. on pp. 104, 105).
- [139] Gerald Falkenberg. *Unified Data Sheet P06 - Micro and Nano-Probe Beamline*. 2020. url: https://photon-science.desy.de/facilities/petra_iii/beamlines/p06_hard_x_ray_micro_nano_probe/unified_data_sheet_p06/PETRAExp_eng.html (visited on 12/18/2020) (cit. on p. 109).
- [140] Kei Shimomura, Akihiro Suzuki, Makoto Hirose, and Yukio Takahashi. “Precession x-ray ptychography with multislice approach”. In: *Phys. Rev. B* 91 (21 June 2015), p. 214114. doi: 10.1103/PhysRevB.91.214114 (cit. on p. 134).
- [141] Ralph Döhrmann, Ilya Sergeev, Joachim Heuer, Jan Horbach, and Horst Schulte-Schrepping. *Investigation of the vibrational stability of synchrotron X-Ray optics using a differential interferometer*. MEDSI. 2016. url: https://www.meds2016.org/event/42/contributions/615/attachments/476/763/TUCA01_TALK.PDF (visited on 07/21/2020) (cit. on p. 137).
- [142] A V Zozulya et al. “Wavefront preserving channel-cut optics for coherent x-ray scattering experiments at the P10 beamline at PETRAIII”. In: *Journal of Physics: Conference Series* 499 (), p. 012003. doi: 10.1088/1742-6596/499/1/012003 (cit. on p. 137).
- [143] Paw Kristiansen, Jan Horbach, Ralph Döhrmann, and Joachim Heuer. “Vibration measurements of high-heat-load monochromators for DESY PETRA III extension”. In: *Journal of Synchrotron Radiation* 22.4 (July 2015), pp. 879–885. doi: 10.1107/S1600577515005664 (cit. on p. 137).

- [144] Christian G. Schroer et al. “Ptychographic Nano-Analytical Microscope (Pty-NAMi) at PETRA III: signal-to-background optimization for imaging with high sensitivity”. In: *X-Ray Nanoimaging: Instruments and Methods IV*. Ed. by Barry Lai and Andrea Somogyi. Vol. 11112. International Society for Optics and Photonics. SPIE, 2019, pp. 42–50. doi: 10.1117/12.2529096 (cit. on p. 160).

Experimental Data

Experimental data taken at PETRA III from 2015 onward is stored and archived by DESY IT on the central ASAP3 storage system. Beamtimes are identified with an eight-digit beamtime ID and have a responsible principal investigator (PI). Furthermore, it is the convention at P06 to structure a beamtime with sessions, a session contains all scans and counts pertaining to a part of the beamtime. With beamtime ID, session name and scan number experimental, data can be uniquely identified.

The following table lists these identifiers for all figures containing experimental data in the thesis.

Figure	Date	ID	Session	Scan	PI
2.1, 2.2, 2.4	2017/09	11004697	0002_balcony_siemens_star	00187 [†]	Falkenberg
2.5, 2.7	2017/10	11003668	0002_CuOx_60min_23052017	00037	Seyrich
2.8	2013/09	10010678	0001_Si-Saphir	00089*	Seiboth
2.9	2018/12	11005161	0011_multislice_sample	00350	Seyrich
2.10	2015/09	11001693	0004_wd10_h00_v01	00004 ^{†v}	Falkenberg
2.12	2018/12	11005161	0003_beamstop_tests	00078	Seyrich
5.5	2018/12	11005161	0003_beamstop_tests	00078	Seyrich
5.5	2020/09	11008166	0009_GR03	00288	Grote
5.5, 5.8	2016/10	11002410	0003_infineon_chip	00006 [‡]	Schropp
5.5, 5.8	2016/10	11002410	0003_infineon_chip	00106	Schropp
5.7	2016/10	11002410	0003_infineon_chip	00006 [‡]	Schropp
5.7	2017/10	11003668	0002_CuOx_60min_23052017	00041	Seyrich
5.7	2017/09	11004697	0002_balcony_siemens_star	00171	Falkenberg
5.7	2016/11	11002307	0006_microchip_alignment	00046	Scholz
5.12	2017/10	11003747	0003_Monolith_1_tomo	00297	Sheppard
5.13	2018/06	11004545	0001_alignment	00136	Kahnt
5.14a,b	2016/10	11002410	0003_infineon_chip	00103 [‡]	Schropp
5.14c	2015/09	11001693	0004_wd10_h00_v01	00004 ^{†v}	Falkenberg
5.14d-f	2017/09	11004697	0002_balcony_siemens_star	00187 [†]	Falkenberg

Figure	Date	ID	Session	Scan	PI
6.2, 6.3	2018/12	11005161	0003_beamstop_tests	¶	Seyrich
6.4a,c,e	2018/12	11005161	0003_beamstop_tests	00078	Seyrich
6.4b,d,f	2018/12	11005161	0003_beamstop_tests	00085	Seyrich
6.5	2018/12	11005161	0014_flighttube_test	00416	Seyrich
6.6	2020/09	11008166	0005_background_scattering	¶	Grote
7.1, 7.2	2018/12	11005161	0003_beamstop_tests	00078	Seyrich
7.3a-g,i	2018/12	11005161	0003_beamstop_tests	00077	Seyrich
7.3h,i	2018/12	11005161	0003_beamstop_tests	00078	Seyrich
7.3j-l	2018/12	11005161	0003_beamstop_tests	00085	Seyrich
7.4-7.6	2018/12	11005161	0003_beamstop_tests	00077	Seyrich
7.5	2018/12	11005161	0003_beamstop_tests	00078	Seyrich
7.5	2018/12	11005161	0003_beamstop_tests	00085	Seyrich
7.7 - 7.12	2018/12	11005161	0004_LG044	00138	Seyrich
8.1, 8.2	2019/05	11005902	0006_insitu_3	¶	Grote
8.3a	2019/05	50000260	-	00347 [§]	Grote
8.3b	2019/05	11005902	0006_insitu_3	00289	Grote
8.5	2019/05	11005902	0006_insitu_3	00285	Grote
8.6	2019/05	11005902	0006_insitu_3	00247	Grote
8.7	2019/05	11005902	0006_insitu_3	00250	Grote
8.8	2019/05	11005902	0006_insitu_3	00250	Grote
D.1a,c	2017/09	11004697	0007_FZP_CuOx_60min_...	00455	Falkenberg
D.1b,c	2017/09	11004697	0007_FZP_CuOx_60min_...	00456	Falkenberg
D.2a	2017/10	11003668	0002_CuOx_60min_23052017	00037	Seyrich
D.2b	2017/10	11003668	0002_CuOx_60min_23052017	00097	Seyrich

† This data set was also published in [19].

‡ This data set was also published in [94].

∨ This data set was also published in [10].

|| This data set was also published in [144].

* I have not personally participated in this beamtime.

§ Data acquired at cSAXS at SLS, data archived at DESY.

¶ Multiple counts or scans in the session that are too many to list.

List of Publications

- Björn De Samber, Tom Vanden Berghe, Eline Meul, Stephen Bauters, Martin Seyrich, Joël Smet, Boel De Paepe, Julio Cesar da Silva, Sylvain Bohic, Peter Cloetens, Rudy Van Coster, Peter Vandenabeele, and Laszlo Vincze. “Nanoscopic X-ray imaging and quantification of the iron cellular architecture within single fibroblasts of Friedreich’s ataxia patients”. In: *Journal of Synchrotron Radiation* 27.1 (Jan. 2020), pp. 185–198. DOI: 10.1107/S1600577519015510.
- Andreas Schropp, Ralph Döhrmann, Stephan Botta, Dennis Brückner, Maik Kahnt, Mikhail Lyubomirskiy, Christina Ossig, Maria Scholz, Martin Seyrich, Michael E. Stuckelberger, Patrik Wiljes, Felix Wittwer, Jan Garrevoet, Gerald Falkenberg, Yakub Fam, Thomas L. Sheppard, Jan-Dierk Grunwaldt, and Christian G. Schroer. “PtyNAMi: ptychographic nano-analytical microscope”. In: *Journal of Applied Crystallography* 53.4 (Aug. 2020), pp. 957–971. DOI: 10.1107/S1600576720008420.
- Yakub Fam, Thomas L. Sheppard, Johannes Becher, Dennis Scherhauser, Heinz Lambach, Satishkumar Kulkarni, Thomas F. Keller, Arne Wittstock, Felix Wittwer, Martin Seyrich, Dennis Brueckner, Maik Kahnt, Xiaogang Yang, Andreas Schropp, Andreas Stierle, Christian G. Schroer, and Jan-Dierk Grunwaldt. “A versatile nanoreactor for complementary *in situ* X-ray and electron microscopy studies in catalysis and materials science”. In: *Journal of Synchrotron Radiation* 26.5 (Sept. 2019), pp. 1769–1781. DOI: 10.1107/S160057751900660X.
- M. Lyubomirskiy, F. Koch, K. A. Abrashitova, V. O. Bessonov, N. Kokareva, A. Petrov, F. Seiboth, F. Wittwer, M. Kahnt, M. Seyrich, A. A. Fedyanin, C. David, and C. G. Schroer. “Ptychographic characterisation of polymer compound refractive lenses manufactured by additive technology”. In: *Opt. Express* 27.6 (Mar. 2019), pp. 8639–8650. DOI: 10.1364/OE.27.008639.
- Christian G. Schroer, Martin Seyrich, Andreas Schropp, Ralph Döhrmann, Stephan Botta, Patrik Wiljes, Dennis Brückner, Maik Kahnt, Felix Wittwer, Lukas Grote, Dorota Koziej, Jan Garrevoet, and Gerald Falkenberg. “Ptychographic Nano-Analytical Microscope (PtyNAMi) at PETRA III: signal-to-background optimization for imaging with high sensitivity”. In: *X-Ray Nanoimaging: Instruments and Methods IV*. Ed. by Barry Lai and Andrea Somogyi. Vol. 11112. International Society for Optics and Photonics. SPIE, 2019, pp. 42–50. DOI: 10.1117/12.2529096.
- Frank Seiboth, Maik Kahnt, Mikhail Lyubomirskiy, Martin Seyrich, Felix Wittwer, Tobias Ullsperger, Stefan Nolte, Darren Batey, Christoph Rau, and Christian G. Schroer. “Refractive hard x-ray vortex phase plates”. In: *Opt. Lett.* 44.18 (Sept. 2019), pp. 4622–4625. DOI: 10.1364/OL.44.004622.

- M. Kahnt, G. Falkenberg, J. Garrevoet, J. Hartmann, T. Krause, M. Niehle, M. Scholz, M. Seyrich, A. Trampert, A. Waag, and et al. “Simultaneous Hard X-ray Ptychographic Tomography and X-ray Fluorescence Tomography of Isolated Hollow Core-Shell GaN Rods”. In: *Microscopy and Microanalysis* 24.S2 (2018), pp. 32–33. doi: 10.1017/S143192761801259X.
- Juliane Reinhardt, Andreas Schropp, Mikhail Lyubomirskiy, Martin Seyrich, Dennis Bruckner, Thomas F. Keller, Vedran Vonk, Sergey Volko, Andreas Stierle, Edvinas Navickas, and et al. “Hard X-ray Resonant Ptychography for Chemical Imaging at the Sensitivity Limit”. In: *Microscopy and Microanalysis* 24.S2 (2018), pp. 26–27. doi: 10.1017/S1431927618012564.
- Frank Seiboth, Felix Wittwer, Maria Scholz, Maik Kahnt, Martin Seyrich, Andreas Schropp, Ulrich Wagner, Christoph Rau, Jan Garrevoet, Gerald Falkenberg, and Christian G. Schroer. “Nanofocusing with aberration-corrected rotationally parabolic refractive X-ray lenses”. In: *Journal of Synchrotron Radiation* 25.1 (Jan. 2018), pp. 108–115. doi: 10.1107/S1600577517015272.
- Christian G. Schroer, Martin Seyrich, Maik Kahnt, Stephan Botta, Ralph Döhrmann, Gerald Falkenberg, Jan Garrevoet, Mikhail Lyubomirskiy, Maria Scholz, Andreas Schropp, and Felix Wittwer. “PtyNAMi: ptychographic nano-analytical microscope at PETRA III: interferometrically tracking positions for 3D x-ray scanning microscopy using a ball-lens retroreflector”. In: *X-Ray Nanoimaging: Instruments and Methods III*. Ed. by Barry Lai and Andrea Somogyi. Vol. 10389. International Society for Optics and Photonics. SPIE, 2017, pp. 8–17. doi: 10.1117/12.2273710.
- C. G. Schroer, C. Baumbach, R. Döhrmann, S. Klare, R. Hoppe, M. Kahnt, J. Patommel, J. Reinhardt, S. Ritter, D. Samberg, M. Scholz, A. Schropp, F. Seiboth, M. Seyrich, F. Wittwer, and G. Falkenberg. “Hard x-ray nanoprobe of beamline P06 at PETRA III”. In: *AIP Conference Proceedings* 1741.1 (2016), p. 030007. doi: 10.1063/1.4952830. eprint: <https://aip.scitation.org/doi/pdf/10.1063/1.4952830>.
- Frank Seiboth, Maik Kahnt, Maria Scholz, Martin Seyrich, Felix Wittwer, Jan Garrevoet, Gerald Falkenberg, Andreas Schropp, and Christian G. Schroer. “Quantitative characterization of aberrations in x-ray optics”. In: *Advances in X-Ray/EUV Optics and Components XI*. Ed. by Ali M. Khounsary, Shunji Goto, and Christian Morawe. Vol. 9963. International Society for Optics and Photonics. SPIE, 2016, pp. 88–95. doi: 10.1117/12.2237646.

Danksagung

Zuerst möchte ich meinem Doktorvater Prof. Christian Schroer danken. Noch als Oberstufenschüler lernte ich Christian kennen, als ich an der TU Dresden die Veranstaltung *Physik am Samstag* besuchte und ihn dort zum Thema Röntgen-Freie-Elektronen-Laser vortragen hörte. Ein halbes Jahr später war ich dann eingeschriebener Student im Studiengang Physik, Christian hielt die Erstsemestervorlesung der Experimentalphysik und begeisterte uns mit zahlreichen Demonstrationen im Hörsaal.

Als ich dann im fünften Semester an einer Informationsveranstaltung zu möglichen Themen der Bachelorarbeit teilnahm, berichtete er von einer wunderschönen neuen Mikroskopiemethode, der "Ptychographie", an der er in seiner Gruppe arbeitete. Ich war sofort interessiert und er bot mir ein Thema an, so dass ich in den nächsten Wochen dann die Optische Ptychographie im Laserlabor des Institutes erforschte.

Im Jahr darauf erkundigte ich mich dann bei ihm nach einem Folgethema, worauf hin er mir anbot, ihn zu seiner neuen Stelle am DESY zu begleiten. Ohne jemals in Hamburg gewesen zu sein, sagte ich sofort zu und nahm in seiner Gruppe am DESY meine Arbeit auf, die mich bis zum heutigen Tag beschäftigt.

So hat mich Christian von der Wahl meines Studienganges bis zur Einreichung meiner Dissertation in weiten Teilen meines Studiums begleitet, wofür ich ihm hier herzlich danken möchte.

An zweiter Stelle möchte ich Felix Wittwer danken. Schon seit Beginn meiner Arbeit war Felix mir eine große Hilfe in unzähligen Dingen, insbesondere in Allem was die Programmierung betrifft. Ohne seine kontinuierliche Arbeit an *ptycho* hätten viele Ergebnisse in der Arbeit nicht erlangt werden können. Auch sähe dieses Dokument ohne Felix' Rat zu Layout und zur Typographie deutlich schlechter aus. Als ich meinen kreativen Ausgleich zu meiner wissenschaftlichen Arbeit in der Fotografie suchte, war Felix mir auch dort ein treuer Begleiter; mit gegenseitiger Kritik und Lob spornten wir uns immer weiter an. Unvergessen sind auch unsere Mühen zur Röntgendiffraktions-ptychographie.

Maik Kahnt hat in vielen kleinen und großen Dingen zum Gelingen dieser Arbeit beigetragen. Schon frühzeitig arbeiteten wir zusammen an den Interferometern, erst in Vorarbeiten im Metrologielabor und später in zahlreichen Messzeiten an PtyNAMi.

Auch war er der Stein des Anstoßes für die Anwendung der Mehrschichtptychographie auf die Kupferwürfelproben. Maik war der treibende Faktor hinter unseren Bemühungen, eine gut dokumentierte Codebasis für unsere Arbeit aufzubauen und schrieb viele Skripte, die mir recht nützlich waren und sind. Auch schreibt Maik die umfangreichsten und bestorganisiertesten wissenschaftlichen Dokumentationen und sollte somit uns Allen zum Vorbild gereichen.

Keines der Messergebnisse in den Kapiteln 7 und 8 hätte ohne Lukas Grote zu Stande kommen können. Nicht nur bereitete er alle Proben und chemischen Reaktionen vor, er arbeitete auch unbeirrt an dem Bau der Reaktionszelle weiter, als mir doch die Zweifel kamen, ob sich so etwas in den gegebenen Rahmenbedingungen überhaupt umsetzen ließe. Meinen verhaltenen Optimismus zum Trotz baute eine Probenumgebung, die sich bereits im ersten Versuch als voller Erfolg erwies; eine Errungenschaft, die gewiss vielen anderen verwehrt geblieben wäre.

Mein herzlicher Dank geht auch an Juliane Reinhardt, aus deren Arbeit ich einige Aspekte weitergeführt habe. Diese umfassen die Bestimmung des Messuntergrundes, die Verwendung von Beamstops und die resonante Ptychographie. Und auch wenn auf diesen Gebieten nicht alle Blüenträume reiften, so stand sie mir stets hilfreich bei, unter anderem auch als Telekonsulantin während meiner Messzeiten.

Maria Scholz begleitete meine Arbeit am DESY ab dem ersten Tag und hat mir in der Anfangszeit oft geholfen, mich zurecht zu finden. In den letzten Monaten meiner Promotion war sie mir eine besonders große Stütze, denn wir arbeiteten zeitgleich auf das Ende hin und konnten uns so immer wieder gegenseitig motivieren.

Andreas Schropp hat meine Promotion als Zweitbetreuer begleitet. Noch gut kann ich mich die Anfangstage erinnern, als wir uns in der 455 gegenüber saßen und auf den freien Schreibtischen die Interferometer aufgebaut hatten. Seit dieser Zeit habe ich sehr viel von ihm gelernt und möchte ihm hier dafür danken.

Mikhail Lyubomirskiy danke ich für die vielen interessanten Messzeiten jenseits des Gewöhnlichen, an denen er mich teilhaben ließ, und für seine Effizienz, mit der er deren Ergebnisse zu Publikationen werden ließ, und auch für seine Hilfe während meiner Messzeiten. Auch sind die kulinarischen Gaben aus seiner Heimat nicht zu verachten.

An Christina Ossig schätze ich ihre positive Aura, mit der sie unsere Arbeit und unser Gruppenleben immer wieder erquickt. Auch hat sich Christina in der letzten Zeit in unser Softwarepaket *PetraPy* eingearbeitet und konnte mir so Arbeit und viele Supportanfragen abnehmen.

Mit Johannes Hagemann zog ein Querulant in die Gruppe ein, der die Ptychographie verkannte und seine Nahfeldmethoden propagierte. Ich lernte ihn bald als Kollegen sehr schätzen und wir hatten so manche interessanten Gespräche zu unser beiden Fachgebiete, die in mir die Neugier auf das Nahfeld geweckt haben.

Auch Frank Seiboth hat mich mehrmals auf seine Messzeiten mitgenommen. Des Öfteren waren wir in England an der Diamond Light Source, besonders spannend aber war unsere Reise zum PAL-XFEL in Südkorea.

Auch dem Rest der immer größer werdenden Gruppe möchte ich hier für die schöne und interessante Zeit am DESY danken, die sie mir mit ihren wissenschaftlichen und persönlichen Gesprächen bereitet hat.

Mein Dank ist auch unserem Ingenieursteam gewidmet, ohne das wir uns der theoretischen Physik zuwenden müssten.

Zuerst ist hier Ralph Döhrmann zu nennen, der von der ersten beschichteten Kugellinse bis zum letzten Langloch an PtyNAMi das ganze Projekt begleitet hat und dabei viele der wesentlichen Entwürfe entwickelte. Auch musste Ralph oft als mein Einkäufer agieren, da die Doktoranden dieses Privileg nicht genießen. Ihm zur Seite stand Stephan Botta, der uns oft am Experiment half und viel Zeit damit verbrachte, die Linseninterferometer nachträglich in den Linsenkäfig einzufügen.

Patrik Wiljes hat sich auch des Interferometer- und Stabilitätsthemas angenommen und hat dazu viele weitere Messungen durchgeführt, die unser Verständnis über das Thema weiter vertieft haben. Zur Bändigung unseres Positionierers waren seine Kenntnisse der Regeltechnik von großem Wert.

Hendrik Lindemann stand mir bei meiner ersten Messzeit im Oktober 2017 tatkräftig zur Seite und musste dabei so einiges über sich ergehen lassen. Auch konstruierte er das Positioniersystem für den Strahlfänger. Torben Reuß unternahm weitere Vibrationsmessungen, die zur Entdeckung der großen Bedeutung des Luftschalls führten und errechnete weiterhin einige sehr aufschlussreiche FEM-Simulationen. Mirko Landmann konstruierte die Festkörpergelenkhalterung zur Interferometerjustage und simulierte die thermischen Eigenschaften der Insituzelle.

Von der Mannschaft der Beamline P06 möchte ich vor allem Jan Garrevoet danken. Seine Arbeit an der Beamline in den letzten Jahren resultierte in so tiefgreifenden Verbesserungen, dass viele Experimente ohne ihn schlicht nicht möglich gewesen wären. Auch möchte ich Gerald Falkenberg danken, der mir sowohl in seiner Funktion als Beamlinemanager als auch als Mentor meines Promotionsvorhabens zur Seite stand. Vielen Dank auch an den Rest des Beamlineteams.

Ich danke auch den Gutachtern und den Mitgliedern der Prüfungskommission für ihre Zeitaufwendung.

Abschließend möchte ich meinen Eltern danken, deren Erziehung in mir schon früh das naturwissenschaftliche Interesse erweckte und welche mir das Abitur, das Studium und die Übersiedlung nach Hamburg ermöglichten.

Martin Seyrich im Dezember 2020

Abschnitte dieses Dokumentes wurden korrekturgelesen von Maik Kahnt, Patrick Kneschke, Christian Schroer, Maria Scholz, Felix Wittwer, Christina Ossig, Barbara Seyrich, Gerald Falkenberg, Lukas Grote, Juliane Reinhardt und Johannes Hagemann.

I would also like to take this opportunity to thank the many volunteer developers of open source software around the world. In particular, I would like to thank the developers of python, ImageJ and L^AT_EX. I spend countless hours using their software.

Eidesstattliche Versicherung

Hiermit versichere ich an Eides statt, die vorliegende Dissertationsschrift selbst verfasst und keine anderen als die angegebenen Hilfsmittel und Quellen benutzt zu haben.

Die eingereichte schriftliche Fassung entspricht der auf dem elektronischen Speichermedium.

Die Dissertation wurde in der vorgelegten oder einer ähnlichen Form nicht schon einmal in einem früheren Promotionsverfahren angenommen oder als ungenügend beurteilt.

Hamburg, den 23.12.2020

Martin Seyrich

“And he that breaks a thing to find out what it is
has left the path of wisdom.”

*Gandalf the White to Saruman of Many Colours,
in J.R.R. Tolkien's *The Lord of the Rings**